

People's Democratic Republic of Algeria  
Ministry of Higher Education and Scientific Research  
University of 08 Mai 1945 Guelma



Faculty of Mathematics, Computer Science, and Sciences of Matter  
Department of Sciences of Matter  
Materials Physics Laboratory (L.2.P.M)

**DISSERTATION**  
**SUBMITTED IN CANDIDACY FOR THE DEGREE**  
**OF DOCTORATE IN 3<sup>rd</sup> CYCLE**

Field: **Sciences of Matter** Branch: **Physics**  
Specialty: **Condensed Matter Physics**

**Presented by**

**ELAGGOUNE Warda**

*Entitled*

*Ab-initio study of the properties of the 3D SrS-based mono-doped and co-doped compounds.*

*A comparative study of the 2D and 3D mono-doped compounds.*

Defended on: 22/02/2024

Before the Jury composed of:

<b>Hakima Yahi</b>	<b>Prof</b>	Univ. of 8 May 1945-Guelma	President
<b>Athmane Meddour</b>	<b>Prof</b>	Univ. of 8 May 1945-Guelma	Supervisor
<b>Chahrazed Bourouis</b>	<b>MCB</b>	Univ. of 8 May 1945-Guelma	Co-supervisor
<b>Hakim Baaziz</b>	<b>Prof</b>	Univ. of Mohamed Boudiaf-M'sila	Examiner
<b>Hocine Meradji</b>	<b>Prof</b>	Univ. of Badji Mokhtar-Annaba	Examiner
<b>Hayet Moumeni</b>	<b>Prof</b>	Univ. of 8 May 1945-Guelma	Examiner

**Academic Year: 2023/2024**

*Excerpt from a letter to Richard Phillips, editor of the  
Philosophical Magazine, 3 weeks after the discovery of the  
Electro-magnetic induction in 1831:*

*“I am busy just now again on electro-magnetism, and  
Think I have got hold of a good thing.”*

---

*Michael Faraday (1791-1867)*

# Acknowledgements

First and foremost, I would like to thank almighty God, to whom I express my gratitude, for granting me health, courage, and strength to successfully complete this work until the end.

This dissertation would not have been possible without the guidance and support of numerous individuals who in one way or another contributed and extended their valuable assistance in the completion of this study. It is with deep gratitude that I take this moment to extend my sincere thanks to those who made it a possibility.

My heartfelt thanks go to the person behind this work, who is my dissertation supervisor, **Mr. Athamne Meddour**, Professor at the University of Guelma. He entrusted me with his confidence and provided guidance and support throughout this dissertation. It is by his side that I truly understood the meaning of rigor and precision. I also value his human qualities; he has been like a second father to me in my academic journey. Next, I would like to express my gratitude to **Dr. Chahrazed Bourouis**, MCB at the University of Guelma, my co-supervisor, for always being approachable and for inspiring me to delve into new realms of physics. Her invaluable advice, encouragement, and insightful discussions have been instrumental.

I wish to express my deepest gratitude to **Ma'am Hakima Yahi**, Professor at the University of Guelma, for the honor she grants to me by accepting to chair the jury and evaluate my dissertation.

I extend my warmest thanks to Mrs. / Ma'am the members of the jury; **Mr. Hakim Baaziz**, Professor at the University of M'sila, **Mr. Hocine Meradji**, Professor at the University of Annaba, and **Ma'am Hayet Moumeni** Professor at the University of Guelma, for the time and effort that they have devoted to evaluate my dissertation and to be part of the jury members.

I gratefully acknowledge **Dr. Hadi Med Gous**, **Dr. Zeyneb Bordjiba**, and **Prof. Abdelhak Elaggoune**, from the University of Guelma, **Prof. Abdelaziz Boukra** from the University of Mostaganem, and **the authors of**

BoltzTrap team for their invaluable help and contributions to my work, which have been honored with two publications of good impact factor.

I convey my sincere gratitude to **Prof. Fatih Ersan** from Aydin Adnan Menderes University, Turkey, for accepting to be the guest of honor for my dissertation, and also for graciously welcoming me and generously granting access to a high-performance computational facility for conducting simulations. I would also like to thank **Dr. Yusuf Zuntu** and all the members of laboratory and staff administration of the University of Aydin Adnan Menderes, who have made the Internship period enjoyable for me.

I am highly thankful to Professor **Bariza Ellagoune** from the University of Guelma, for her constant availability and numerous encouragements she has provided me since my master's degree, which greatly boosted my morale at various stages of this work.

Big thanks go to the Director of our research Laboratoire de Physique des Matériaux (L.2.P.M), **Pr. Sabah Chettibi**, to the entire team of our research Laboratory, and my colleagues Ph.D. **Khawla Chaoui** and **Dr. Nassima Gueshi** for their invaluable help and support. My thanks cannot be concluded without thanking **every member** of the physics department's teaching faculty and the dedicated administrative staff. I could not have done it without you.

Finally, behind every achievement, there is a family that stands as the bedrock of support, and I am blessed to have such a family. I must thank all **my family** members, specially my second mother Malouka, my parents, and my siblings Imen and Wail, for their love, support, and motivation across all the time. I record my affection for my grandmother, aunts, uncles, and cousins for their encouragements given to me.

It is impossible for me to compile an exhaustive list of all the individuals without the risk of forgetting someone. Please know that I associate you with this work and I cannot thank you enough for your aid.

*W. Elagoune*



# List of International Publications

During this Ph.D., the content of the dissertation was contributed by the following publications:

1. **Elaggoune, W.**, Meddour, A., Bourouis, C., Gous, M. H., & Bordjiba, Z. (2023). Influence of 3d-Fe substitution on structural, mechanical, electronic, and magnetic properties in rock-salt SrS: Insights from the first-principles study. *Solid State Communications*, 361, 115060.
2. **Elaggoune, W.**, Meddour, A., & Bourouis, C. (2023). p<sup>0</sup>-d co-doping alloys as prospective half-semiconductors for optoelectronic, spintronic, and thermoelectric applications. *Materials Science in Semiconductor Processing*, 165, 107684.

## *Abstract*

In this dissertation, we aim to predict the evolution of the various physical properties of the binary semiconductor SrS after its doping with iron (Fe) and *sp*-type metals. In this context of study, we consider ternary compounds (SrS mono-doped with iron) and quaternary compounds (SrS co-doped with iron and *sp*-type alkali metals), some of which are studied in volume (3D) and others in monolayer form (2D). Properties calculations are based on the Full Potential Linearized Augmented Plane Wave (FP-LAPW) method and on the PBE and PBE + mBJ approximations implemented in the WIEN2K simulation program. The work involves assessing the impact of elements added to the SrS semiconductor host matrix on the properties of final compounds produced by doping and co-doping.

Initially, we investigated the structural, mechanical, electronic and magnetic properties of single-doped  $\text{Sr}_{1-x}\text{Fe}_x\text{S}$  compounds in the rock-salt structure, considering the following Fe concentrations: 0%, 12.5%, 25%, 50% and 75%. The study is carried out at 3D and the main objective is to investigate new potential half-metallic ferromagnets (HMF) for spintronic applications. The results obtained show that the compounds containing 12.5%, 25% and 50% iron are half-metallic ferromagnets with a total magnetic moment value equal to  $4\mu_B$ , and are thermodynamically and mechanically stable; nevertheless, the iron-rich compound (75% Fe) is metallic.

We then turned our attention to co-doping the SrS matrix to produce quaternary compounds. The latter are realized by doping the ternary compound (12.5% Fe) with alkali metals (Li, Na and K). The aim is to see the effect of the *sp* metals on the properties of the ternary compounds. The study of these new compounds, also in 3D, is based on density functional theory (DFT) and semi-classical Boltzmann theory (BT), and covers structural, electronic, magnetic, optical and thermoelectric properties. The results obtained show that the incorporation of alkali metals into the SrS: 12.5% Fe compound renders them half-semiconducting (HSC) with narrower energy gap values than those of HMF ternary compound (SrS: Fe). The Curie temperature ( $T_c$ ) values obtained are higher than room temperature. In addition, the magnetic moment of quaternary compounds is higher than that of ternary compounds, having a value of  $5\mu_B$ . Examination of the optical properties revealed a shift of the spectra towards the visible region, accompanied by a broadening of the compounds' absorption band. Investigation of the thermoelectric properties of *p*-type compounds showed that their figure of merit ( $ZT$ ) values are greater than unity at 1200K, underlining their exceptional transport efficiency and making them highly promising candidates for optoelectronics and high-temperature thermoelectric applications.

The 2D study focused on the structural, electronic and magnetic properties of ternary compounds. The calculations are based on a plane-wave pseudopotential (PAW) method using the PBE and

PBE+HSE06 functionals, integrated into the VASP simulation software. The effect of dimensionality reduction was mainly observed at the level of electronic structures, where the character of ternary compounds becomes HSC instead of HMF observed in their 3D counterparts. This result has a positive impact on the optical and transport properties of ternary compounds. Under these conditions, the total magnetic moment resulting from  $p$ - $d$  hybridization is  $4\mu_B$  per unit cell.

**Keywords:** Ab-initio calculations, SrS, Half-metallic ferromagnetic, Alkali co-doping, 3D-bulk materials, 2D-monolayers, Spintronics, Optical properties, Thermoelectric properties.

## Résumé

Dans cette thèse, nous visons à prédire l'évolution des différentes propriétés physiques du semi-conducteur binaire SrS après son dopage au fer (Fe) et aux métaux de type *sp*. Dans ce contexte d'étude, nous considérons des composés ternaires (SrS mono-dopé au fer) et des composés quaternaires (SrS co-dopé au fer et aux métaux alcalins de type *sp*) dont certains composés sont étudiés en volume (3D) et d'autres sous forme de monocouche (2D). Le calcul des propriétés est basé sur la méthode d'ondes planes augmentées linéarisées à potentiel plein (FP-LAPW) ainsi que sur les approximations PBE et PBE+mBJ implémentées dans le programme de simulation WIEN2K. Le travail consiste à évaluer l'impact des éléments ajoutés à la matrice semi-conductrice SrS sur les propriétés des composés finaux réalisés par dopage et par co-dopage.

Dans un premier temps, nous nous sommes intéressés aux propriétés structurales, mécaniques, électroniques et magnétiques des composés mono-dopés de type  $Sr_{1-x}Fe_xS$  dans la structure rock-salt en considérant les concentrations de Fe suivantes : 0 %, 12,5 %, 25 %, 50 % et 75 %. L'étude est faite à 3D et l'objectif principal est d'investiguer de nouveaux ferromagnétiques semi-métalliques (HMF) potentiels pour des applications dans le domaine de la spintronique. Les résultats obtenus ont montré que les composés contenant 12,5%, 25% et 50% de fer sont demi-métalliques ferromagnétiques avec une valeur du moment magnétique total égale à  $4\mu_B$  et sont thermodynamiquement et mécaniquement stables ; néanmoins, le composé riche en fer (75% Fe) s'avère métallique.

Dans un deuxième temps, nous nous sommes intéressés au co-dopage de la matrice SrS pour réaliser des composés quaternaires. Ces derniers sont réalisés par le dopage du composé ternaire (12,5% Fe) par les métaux alcalins (Li, Na et K). Le but est de voir l'effet des métaux *sp* sur les propriétés des ternaires. L'étude de ces nouveaux composés, toujours à 3D, repose sur la méthode de la théorie de la fonctionnelle de la densité (DFT) et sur la théorie semi-classique de Boltzmann (BT) et concerne les propriétés structurales, électroniques, magnétiques, optiques et thermoélectriques. Les résultats obtenus montrent que l'incorporation des métaux alcalins dans le composé SrS : 12,5% Fe les rend demi-conducteur (HSC) avec des valeurs du gap énergétique plus étroites que celles du composé ternaire HMF (SrS : Fe). Les valeurs de la température de Curie ( $T_c$ ) obtenues sont supérieures à la température ambiante. En outre, la valeur du moment magnétique des composés quaternaires est supérieure à celle des composés ternaires, elle vaut  $5\mu_B$ . L'examen des propriétés optiques a révélé un décalage des spectres vers la région du visible accompagné d'un élargissement de la bande d'absorption des composés. L'étude des propriétés thermoélectriques des composés de type *p* a montré que les valeurs de leurs figures de mérite (ZT) sont supérieures à l'unité à la température 1200K, soulignant l'efficacité exceptionnelle de leur

transport et faisant d'eux des candidats très prometteurs pour l'optoélectronique et pour les applications thermoélectriques à haute température.

L'étude à 2D a concerné les propriétés structurales, électroniques et magnétiques des composés ternaires. Les calculs effectués reposent sur une méthode de pseudo-potential à ondes planes (PAW) en utilisant les fonctionnelles PBE et PBE+HSE06, intégrées dans le logiciel de simulation VASP. L'effet de la réduction de la dimensionnalité a été principalement observé au niveau des structures électroniques, où le caractère des composés ternaires devient HSC au lieu de HMF observé dans leurs homologues à 3D. Ce résultat impacte positivement les propriétés optiques et de transport des composés ternaires. Dans ces conditions, le moment magnétique total résultant de l'hybridation  $p-d$ , vaut  $4\mu_B$  par cellule unitaire.

**Mots-clés :** Calculs ab-initio, SrS, Demi-métaux Ferromagnétiques, Co-dopage alcalin, Matériaux en bulk-3D, Monocouches-2D, Spintronique, Propriétés optiques, Propriétés thermoélectriques.

## المخلص

في هذه الأطروحة، نهدف إلى التنبؤ بتطور الخصائص الفيزيائية المختلفة لأشباه الموصلات الثنائية SrS بعد تطعيمها بالحديد (Fe) والمعادن من النوع  $sp$ . في سياق هذه الدراسة، نأخذ بعين الاعتبار المركبات الثلاثية (SrS أحادي المطعم بالحديد) والمركبات الرباعية (SrS المطعمة بالحديد والمعادن القلوية من نوع  $sp$ ) والتي تتم دراسة بعض المركبات في الحجم (3D) والبعض الآخر في شكل طبقة أحادية (2D). يعتمد حساب الخصائص على طريقة الموجة المستوية الصاعدة الخطية الكاملة المحتملة (FP-LAPW) وكذلك على تقريب PBE + mBJ و PBE المطبق في برنامج محاكاة WIEN2K. يتمثل العمل في تقييم تأثير العناصر المضافة إلى مصفوفة أشباه الموصلات SrS على خصائص المركبات النهائية الناتجة عن المركبات الأحادية والمركبات المشتركة.

أولاً، ركزنا على الخواص الهيكلية والميكانيكية والإلكترونية والمغناطيسية للمركبات أحادية التطعيم من نوع  $Sr_{1-x}Fe_xS$  في بنية الملح الصخري من خلال النظر في تركيزات Fe التالية: 0% و 12.5% و 25% و 50% و 75%. تتم الدراسة في 3D والهدف الرئيسي هو التحقيق في المغناطيسات الحديدية شبه المعدنية الجديدة المحتملة (HMFs) للتطبيقات في مجال spintronics. أظهرت النتائج التي تم الحصول عليها أن المركبات التي تحتوي على 12.5% و 25% و 50% من الحديد هي أشباه معدنية مغناطيسية حديدية ذات قيمة عزم مغناطيسية إجمالية تساوي  $4\mu_B$  وهي مستقرة ديناميكياً، حرارياً وميكانيكياً. ومع ذلك، تبين أن المركب الغني بالحديد (75% Fe) معدني. في الخطوة الثانية، ركزنا على المركبات المشتركة لمصفوفة SrS لإنتاج مركبات رباعية. يتم إجراء هذا الأخير عن طريق تطعيم المركب الثلاثي (12.5% Fe) بواسطة المعادن القلوية (Li و Na و K). الهدف هو رؤية تأثير المعادن  $sp$  على خصائص الثلاثيات. تعتمد دراسة هذه المركبات الجديدة، دائماً في 3D، على طريقة نظرية الكثافة الوظيفية (DFT) وعلى نظرية بولتزمان شبه الكلاسيكية (BT) وتتعلق بالخصائص الهيكلية والإلكترونية والمغناطيسية والبصرية والكهروحرارية. أظهرت النتائج التي تم الحصول عليها أن دمج الفلزات القلوية في مركب Fe/SrS: 12.5 يجعلها نصف أشباه موصلات (HSC) بقيم فجوة طاقة أصبغ من قيم مركب HMF الثلاثي (SrS: Fe). قيم درجة حرارة كوري ( $T_c$ ) التي تم الحصول عليها أعلى من درجة حرارة الغرفة. بالإضافة إلى ذلك، فإن قيمة العزم المغناطيسي للمركبات الرباعية أعلى من قيمة المركبات الثلاثية، بإجمالي مقدر ب  $5\mu_B$ . كشف فحص الخصائص البصرية عن انزياح الأطياف نحو المنطقة المرئية مصحوباً بتوسيع نطاق امتصاص المركبات. أظهرت دراسة الخواص الكهروحرارية للمركبات من النوع  $p$  أن قيم أرقام الجدارة (ZT) أكبر من الوحدة عند درجة حرارة 1200 كلفن، مما يسلط الضوء على الكفاءة الاستثنائية لنقلها ويجعلها مرشحة واعدة للغاية للإلكترونيات الضوئية وللتطبيقات الكهروحرارية ذات درجة الحرارة العالية.

تتعلق دراسة 2D بالخصائص الهيكلية والإلكترونية والمغناطيسية للمركبات الثلاثية. تستند الحسابات التي تم إجراؤها إلى طريقة الجهد الزائف للموجة المستوية (PAW) باستخدام وظائف PBE و PBE + HSE06، المدمجة في برنامج محاكاة VASP. لوحظ تأثير خفض الأبعاد بشكل رئيسي على مستوى الهياكل الإلكترونية، حيث تصبح طبيعة المركبات الثلاثية HSC بدلاً من HMF التي لوحظت في نظيراتها 2D. هذه النتيجة لها تأثير إيجابي على الخصائص البصرية والنقل للمركبات الثلاثية. في ظل هذه الظروف، يكون إجمالي العزم المغناطيسي الناتج عن تهجين  $p-d$  هو  $4\mu_B$  لكل خلية وحدة.

**الكلمات المفتاحية:** حسابات المبادئ الأولى، SrS، مركبات نصف معدنية، دمج الفلزات القلوية، مواد ثلاثية الأبعاد، طبقات ثنائية الأبعاد، سبينترونيك، الخواص البصرية، الخواص الكهروحرارية.

# Contents

List of International Publications . . . . .	I
Abstract . . . . .	II
List of Figures . . . . .	XI
List of Tables . . . . .	XV
Symbols and Abbreviations . . . . .	XVII
General Introduction . . . . .	1
References for General Introduction . . . . .	5

## Chapter 1: Literature Background

<b>1.1 Introduction</b> . . . . .	7
<b>1.2 Spintronics and Related Devices</b> . . . . .	8
1.2.1 Definition and Historical Development of Spintronic Phenomena. . . . .	8
1.2.2 Spin Devices . . . . .	10
1.2.3 Spin Generation. . . . .	11
<b>1.3 Opportunities at the Frontiers of Spintronics</b> . . . . .	12
1.3.1 Thermoelectric Effects. . . . .	13
1.3.2 Transport Equations. . . . .	15
1.3.3 Optimization Parameters for $ZT$ . . . . .	18
1.3.4 Boltzmann Transport Theory. . . . .	20
1.3.5 Spin-driven Thermoelectrics. . . . .	22
<b>1.4 Wide Bandgap Semiconductors: host base for different applications</b> . . . . .	24
1.4.1 Bulk SrS Monochalcogenide. . . . .	27
1.4.2 Tuning the Properties of SrS Monochalcogenide . . . . .	29
1.4.2.1 Diluted Magnetic Semiconductors (DMSs) . . . . .	31
1.4.2.2 $d^0$ vs. Conventional Magnetism. . . . .	37
<b>1.5 Low-Dimensional Nanomaterials</b> . . . . .	39
1.5.1 Two-Dimensional (2D) Nanomaterials. . . . .	40
1.5.2 Synthesis Approaches for 2D Nanomaterials. . . . .	41
1.5.2.1 Top-Down Approach. . . . .	42
1.5.2.2 Bottom-Up Approach. . . . .	42

1.5.3 Categorization of 2D Nanomaterials. . . . .	46
<b>1.6 An Overview of Bibliography . . . . .</b>	<b>47</b>
<b>1.7 Simulation Studies and Their Scope. . . . .</b>	<b>48</b>
<b>1.8 Conclusion. . . . .</b>	<b>49</b>
<b>References for Chapter 1. . . . .</b>	<b>50</b>

## \_\_\_\_\_Chapter 2: Theory and Computational Techniques\_\_\_\_\_

<b>2.1 Introduction . . . . .</b>	<b>63</b>
<b>2.2 Theoretical Formulation. . . . .</b>	<b>64</b>
2.2.1 Many Body Problem within Schrödinger Wave Equation . . . . .	64
2.2.1.1 The Born-Oppenheimer Approximation (1927). . . . .	65
2.2.1.2 Variational Principle: Ground State of the System. . . . .	66
2.2.1.3 Independent Electrons Approximations . . . . .	67
a) Hartree Approach (1928) . . . . .	67
b) Hartree-Fock Approach (1930) . . . . .	67
2.2.1.4 Early Density Functional Theories: The Thomas-Fermi Model . . . . .	69
2.2.1.5 Density Functional Theory: An Ab-initio Approach (1964) . . . . .	70
2.2.1.6 The Kohn-Sham Formalism (1965) . . . . .	70
2.2.1.7 Exchange and Correlation . . . . .	74
2.2.1.7.1 Exchange-correlation Hole. . . . .	74
2.2.1.7.2 Exchange-Correlation Energy Approximation. . . . .	75
a) Local Density Approximation (LDA) . . . . .	75
b) Generalized Gradient Approximation (GGA) . . . . .	76
c) Modified Becke and Johnson Potential (mBJ) . . . . .	78
d) Heyd-Scuseria-Ernzerhof Functional (HSE) . . . . .	79
2.2.2 Augmented Plane Wave (APW) Basis Set . . . . .	80
2.2.2.1 Augmented Plane Wave (APW) Method. . . . .	80
2.2.2.2 Linearized Augmented Plane Wave (LAPW) Method . . . . .	83
2.2.2.3 Development of LAPW into Local Orbitals . . . . .	84
2.2.2.3.1 LAPW+LO Method . . . . .	85
2.2.2.3.2 APW+LO Method . . . . .	85
2.2.2.4 FP-LAPW Method . . . . .	86
2.2.3 Projector Augmented Wave (PAW) Method . . . . .	87



<b>2.3 Computational Formulation</b> .....	90
2.3.1 WIEN2k Code .....	91
2.3.2 VASP Code .....	91
2.3.3 BoltzTraP2 Code .....	92
<b>2.4 Conclusion</b> .....	94
<b>References for Chapter 2</b> .....	95

## \_\_\_\_\_Chapter 3: Effect of Doping and CO-Doping on the SrS Bulk Properties\_\_\_\_\_

<b>3.1 Structural, Mechanical, Electronic, and Magnetic Properties of mono-doped SrS: Fe Alloy</b>	
3.1.1 Introduction .....	100
3.1.2 Computational Details .....	101
3.1.3 Results and Discussion .....	102
3.1.3.1 Structural Properties .....	102
3.1.3.2 Mechanical Properties .....	106
3.1.3.3 Electronic Properties .....	114
3.1.3.3.1 <i>Electronic Band Structure Analysis</i> .....	114
3.1.3.3.2 <i>Total and Partial Densities of States Analysis</i> .....	118
3.1.3.4 Magnetic Properties .....	123
3.1.3.4.1 <i>Magnetic Moment</i> .....	123
3.1.3.4.2 <i>Exchange Constants</i> .....	124
3.1.4 Conclusion .....	126
<b>3.2 Structural, Electronic, Magnetic, Optical, and Thermoelectric Properties of co-doped SrS: Fe Alloy</b>	
3.2.1 Introduction .....	127
3.2.2 Computational Details .....	128
3.2.3 Results and Discussion .....	128
3.2.3.1 Structural Properties .....	128
3.2.3.2 Electronic Properties and Chemical Bonding Analysis .....	131
3.2.3.2.1 <i>Electronic Band Structure Analysis</i> .....	131
3.2.3.2.2 <i>Total and Partial Densities of States Analysis</i> .....	134
3.2.3.2.3 <i>Electron Density Difference and Chemical Bonding Analysis</i> .....	135

3.2.3.3	Magnetic Properties .....	137
3.2.3.3.1	<i>Magnetic Moment</i> .....	137
3.2.3.4.2	<i>Exchange Constants</i> .....	138
3.2.3.4	Optical Properties .....	138
a.	<i>Real and Imaginary Parts of Complex Dielectric Function</i> .....	140
b.	<i>Absorption Coefficient</i> .....	142
c.	<i>Optical Conductivity</i> .....	143
3.2.3.5	Thermoelectric Properties .....	144
a.	<i>Electrical Conductivity</i> .....	152
b.	<i>Seebeck Coefficient</i> .....	153
c.	<i>Thermal Conductivity</i> .....	154
d.	<i>Figure of merit</i> .....	155
3.2.4	Conclusion .....	156
<b>References for Chapter 3</b> .....		157
<b>__ Chapter 4: Effect of Dimensionality Reduction on Fe-Doped SrS Monolayer Properties __</b>		
<b>4.1</b>	<b>Introduction</b> .....	164
<b>4.2</b>	<b>Computational Details</b> .....	165
<b>4.3</b>	<b>Results and Discussion</b> .....	166
4.3.1	Structural Properties .....	166
4.3.2	Electronic Properties and Bader Charge Analysis .....	172
4.3.2.1	<i>Band Structures Analysis</i> .....	172
4.3.2.2	<i>Bader Charge Analysis</i> .....	173
4.3.2.3	<i>Total and Partial Densities of States Analysis</i> .....	176
4.3.3	Magnetic Properties .....	180
<b>4.4</b>	<b>Conclusion</b> .....	182
<b>References for Chapter 4</b> .....		183
<b>General Conclusion and Future Perspectives</b> .....		185
<b>Appendices</b> .....		188
Appendix. A	.....	188
Appendix. B	.....	192
<b>References for Appendices</b> .....		202

# List of Figures

---



---

<b>Figure 1.</b> Annual publications on spintronics over the past decade.....	9
<b>Figure 2.</b> Catalog of spintronics devices .....	10
<b>Figure 3.</b> Methods for generating spin-polarized electrons in non-magnetic media. ....	11
<b>Figure 4.</b> An illustrative depiction of the concept of spin caloritronics.....	12
<b>Figure 5. (a)</b> Key pioneers in thermoelectricity. <b>(b)</b> The representation of Seebeck, Peltier, and Thomson effects, respectively.....	15
<b>Figure 6.</b> Evolving thermoelectric parameters with charge carrier concentration, $n$ , at 300 K.....	19
<b>Figure 7.</b> Degrees of freedom affecting the figure of merit.....	20
<b>Figure 8.</b> A network topology diagram illustrating the diverse material categories within WBG semiconductors.....	26
<b>Figure 9. a)</b> The Unit-cell of the semiconductor SrS, which adopts a rock-salt structure. Green spheres represent the Sr atoms, while orange spheres depict the S atoms. <b>b)</b> The first brillouin zone of an FCC crystal, with the irreducible wedge enclosed by orange lines. The special points within the brillouin zone are identified by their common names, and the reciprocal base vectors are labeled as $b_1$ , $b_2$ , and $b_3$ .....	29
<b>Figure 10.</b> Visualizing the covered elements in this dissertation within the periodic table.....	31
<b>Figure 11.</b> Schematic illustration of different types of semiconductors based on their magnetic properties: <b>(a)</b> Magnetic semiconductor, <b>(b)</b> Diluted magnetic semiconductor, and <b>(c)</b> Non-magnetic semiconductor. Green circles represent the magnetic ion.....	32
<b>Figure 12.</b> Schematic representation of the difference in density of states between a non-magnetic metal, magnetic metal, non-magnetic semiconductor, and half-metal.....	34
<b>Figure 13.</b> Alignment of the magnetic spin of each individual iron atom.....	34
<b>Figure 14.</b> Taxonomy of nanoscale dimensions.....	39
<b>Figure 15.</b> Annual publications on 2D nanomaterials over the past decade.....	41
<b>Figure 16.</b> Widely utilized top-down and bottom-up approaches to synthesize the 2D materials.....	42
<b>Figure 17.</b> Schematic illustration of the different 2D nanomaterials families.....	43
<b>Figure 18.</b> Categorization of 2D chalcogenides.....	44
<b>Figure 19. a)</b> The Unit cell of the monolayer SrS, which adopts a hexagonal structure. Green spheres represent the Sr atoms, while orange spheres depict the chalcogen S atoms. The image was generated using VESTA software [76]. <b>b)</b> The first brillouin zone of a hexagonal crystal, with the irreducible wedge identified by their common names, and the reciprocal base vectors labeled as $b_1$ , and $b_2$ .....	45

---

<b>Figure 1.</b> Pseudo potential approach – pseudo wave function and pseudo potential representation.....	72
<b>Figure 2.</b> Flowchart illustrating the various steps within the Kohn-Sham iterative loop in Density Functional Theory (DFT) codes.....	73
<b>Figure 3.</b> Illustration of muffin tin spheres and the interstitial region where potential singularities occur at the core positions. The Augmented Plane Waves (APW), shown in red lines, must transition smoothly exactly at the boundaries of the spheres and coincide with the plane waves in the interstitial region, shown by the blue line.....	81
<b>Figure 4.</b> A schematic representation of the PAW method is shown. (a) Pseudo-quantities are established using a uniform, flat wave grid covering the entire space. (b) Pseudowave functions are reconstructed inside spheres and the respective single-center terms are subtracted. (c) The all-electron wave functions are reconstructed and the corresponding single-center energies are included.....	89

---

<b>Figure 1.</b> Supercell models showing the cubic structure of $\text{Sr}_{1-x}\text{Fe}_x\text{S}$ compounds with different x values (a) $x = 0.125$ , (b) $x = 0.25$ , (c) $x = 0.50$ and (d) $x = 0.75$ . The Sr atom is shown in gray color, iron in red color, and sulfur in yellow color.....	103
<b>Figure 2.</b> Change in total energy with volume for $\text{Sr}_{1-x}\text{Fe}_x\text{S}$ compounds ( $x = 0.125, 0.25, 0.50$ , and $0.75$ ) in spin-polarized and unpolarized states.....	104
<b>Figure 3.</b> The directional dependencies of three-dimensional (3D) contour plots of (a) bulk modulus (B), (b) shear modulus (G), and (c) Young's modulus (E) for SrS pristine compound.....	111
<b>Figure 4.</b> The Directional Dependencies of Three-Dimensional (3D) Contour Plots of (a) Bulk Modulus (B), (b) Shear Modulus (G), and (c) Young's Modulus (E) for $\text{Sr}_{1-x}\text{Fe}_x\text{S}$ Compounds [(1) $x=0.125$ , (2) $x=0.25$ , (3) $x=0.50$ , and (4) $x=0.75$ ].....	111
<b>Figure 5.</b> The dependence of melting temperature ( $T_m$ ) and Debye temperature ( $\theta_D$ ) on Fe content for $\text{Sr}_{1-x}\text{Fe}_x\text{S}$ Compounds ( $x = 0, 0.125, 0.25, 0.50$ , and $0.75$ ).....	113
<b>Figure 6.</b> Electronic band structure of rock-salt SrS with mBJ-PBE method.....	115
<b>Figure 7.</b> Spin-resolved electronic band Structures of $\text{Sr}_{1-x}\text{Fe}_x\text{S}$ compounds ( $x = 0.125, 0.25, 0.50$ , and $0.75$ ) with mBJ-PBE.....	116
<b>Figure 8.</b> Spin-resolved total and partial densities of states of $\text{Sr}_{1-x}\text{Fe}_x\text{S}$ compounds ( $x = 0.125, 0.25, 0.50$ , and $0.75$ ) with mBJ-PBE.....	119
<b>Figure 9.</b> Spin-resolved total and partial densities of states of $\text{Sr}_{1-x}\text{Fe}_x\text{S}$ compounds ( $x = 0.125, 0.25, 0.50$ , and $0.75$ ) with mBJ-PBE.....	120

<b>Figure 10.</b> Schematic diagram of the distribution of electrons in the $e_g$ and $t_{2g}$ levels of the $Fe^{2+}$ ion situated in an octahedral crystal field.....	122
<b>Figure 11. (a)</b> Polyhedral view of the SrS: (Fe, $p^0$ ) [ $p^0 = Li, Na, \text{ and } K$ ] crystal structures <b>(b)</b> The stable FM configuration.....	128
<b>Figure 12.</b> An illustration of the total energy and cell volume of the Fe- $p^0$ co-doped systems in comparison to the Fe mono-doped system.....	130
<b>Figure 13. (a-c)</b> Spin-resolved electronic band structures of (Fe, Li), (Fe, Na), and (Fe, K) co-doped SrS with mBJ-PBE method.....	133
<b>Figure 14. (a-c)</b> Spin-resolved total and partial densities of states of of (Fe, Li), (Fe, Na), and (Fe, K) co-doped SrS with the mBJ-PBE method.....	134
<b>Figure 15. (a-c)</b> The bonding contour profiles of electron density difference for (Fe, Li), (Fe, Na), and (Fe, K) co-doped SrS Systems, respectively.....	136
<b>Figure 16. (a-d)</b> Real part of the complex dielectric function $\epsilon_1(\omega)$ , Imaginary part of the complex dielectric function $\epsilon_2(\omega)$ , Absorption coefficient $\alpha(\omega)$ , and Optical conductivity $\sigma(\omega)$ spectra, respectively, of pristine SrS, Fe-single doped and (Fe, $p^0$ ) co-doped systems.....	140
<b>Figure 17.</b> Band energy edge ( $E_{edge}$ ) as a function of uniaxial strain ( $\frac{\Delta a}{a_0}$ ) for the pristine SrS.....	146
<b>Figure 18.</b> Band energy edge ( $E_{edge}$ ) as a function of uniaxial strain ( $\frac{\Delta a}{a_0}$ ) for: <b>(a)</b> Fe mono-doped and <b>(b-d)</b> (Fe, Li), (Fe, Na), and (Fe, K) co-doped systems, respectively.....	147
<b>Figure 19.</b> Total energy as a function of uniaxial strain ( $\frac{\Delta a}{a_0}$ ) for the pristine SrS.....	147
<b>Figure 20.</b> Total energy as a function of uniaxial strain ( $\frac{\Delta a}{a_0}$ ) for: <b>(a)</b> Fe mono-doped and <b>(b-d)</b> (Fe, Li), (Fe, Na), and (Fe, K) co-doped systems, respectively.....	148
<b>Figure 21.</b> Measured relaxation time ( $\tau$ ) of holes and electrons as temperature dependence for Pristine SrS.....	149
<b>Figure 22.</b> Measured relaxation time ( $\tau$ ) of holes and electrons as temperature dependence for SrS.....	149
<b>Figure 23.</b> Measured spin-resolved relaxation time ( $\tau$ ) of holes and electrons as temperature dependence for <b>(a)</b> Fe-single doped and <b>(b-d)</b> (Fe, $p^0$ ) co-doped systems, respectively.....	150

---

<b>Figure 1.</b> Top and side views of the repeated unit-cells of <b>(a)</b> the bare $h$ -SrS and <b>(b)</b> $s$ -FeS monolayers.....	166
<b>Figure 2.</b> Phonon Dispersion Spectra of the bare $h$ -SrS and $s$ -FeS, respectively.....	168
<b>Figure 3.</b> The Variation of the total energy with time during AIMD simulation at 300k over a 3000 fs.....	168
<b>Figure 4.</b> The ground-state configurations of predicted energetically stable $Sr_{1-x}Fe_xS$ monolayers (Sr atom is designated by brown color, S by yellow, and Fe by grey).....	170

<b>Figure 5.</b> Spin-polarized electronic band structures of the bare <i>h</i> -SrS, <i>s</i> -FeS and Sr <sub>1-x</sub> Fe <sub>x</sub> S monolayer alloys calculated with the HSE06 method. The E <sub>F</sub> is set to zero.....	174
<b>Figure 6.</b> Visualization of the bandgap fluctuation of the bare <i>h</i> -SrS, <i>s</i> -FeS and Sr <sub>1-x</sub> Fe <sub>x</sub> S monolayer alloys.....	175
<b>Figure 7.</b> Electronic total (TDOS) and partial (PDOS) densities of states of the bare <i>h</i> -SrS and <i>s</i> -FeS monolayers.....	177
<b>Figure 8.</b> Electronic TDOS of Sr <sub>1-x</sub> Fe <sub>x</sub> S (x= 0.125, 0.25, 0.50, and 0.75) monolayer alloys. The positive and negative values represent the spin-up and spin-down channels, respectively.....	178
<b>Figure 9.</b> Electronic PDOS of Sr <sub>1-x</sub> Fe <sub>x</sub> S (x= 0.125, 0.25, 0.50, and 0.75) monolayer alloys.....	180
<b>Figure 10.</b> Schematic diagram representation of the crystal field splitting of the Fe <sup>2+</sup> sites.....	181

# List of Tables

---



---

<b>Table 1.</b> The optimized lattice parameters $a$ (Å), bulk moduli $B$ (GPa), and formation energies $E_f$ (eV/atom) for both binary SrS and ternary $Sr_{1-x}Fe_xS$ ( $x = 0, 0.125, 0.25, 0.50, \text{ and } 0.75$ ) compounds.....	106
<b>Table 2.</b> The calculated values of elastic constants $C_{ij}$ (GPa), bulk modulus $B$ (GPa), shear modulus $G$ (GPa), Young's modulus $E$ (GPa), Pugh $B/G$ ratio, Poisson's ratio $\nu$ , Zener anisotropy factor $A$ , longitudinal $v_l$ (m/s), transverse $v_t$ (m/s), and average $v_m$ (m/s) elastic sound velocities, Debye $\theta_D$ (K) and melting $T_m$ (K) temperatures of SrS and $Sr_{1-x}Fe_xS$ ( $x = 0.125, 0.25, 0.50, \text{ and } 0.75$ ) compounds.....	114
<b>Table 3.</b> The calculated spin-majority bandgaps $E_g$ (eV), half-metallic bandgaps $G_{HM}$ (eV), and partial density of states (PDOS) at the Fermi level (states/eV) of $Sr_{1-x}Fe_xS$ compounds ( $x = 0.125, 0.25, 0.50, \text{ and } 0.75$ ).....	121
<b>Table 4.</b> Calculated values of exchange-splitting $\Delta_x(d)$ , majority-spin $N_\uparrow(E_F)$ and minority-spin $N_\downarrow(E_F)$ states at $E_F$ , and the spin polarization $P$ of $Sr_{1-x}Fe_xS$ ( $x=0.125, 0.25, 0.50, \text{ and } 0.75$ ) compounds.....	123
<b>Table 5.</b> The calculated values of total magnetic moment $M_{tot}$ (in $\mu_B$ ) per Fe atom, local magnetic moments (in $\mu_B$ ) of Fe ( $M_{Fe}$ ), Sr ( $M_{Sr}$ ), and S ( $M_S$ ), and magnetic moment in the interstitial sites $M_i$ ( $\mu_B$ ), spin-splitting edges of conduction $\Delta E_c$ (eV) and valence $\Delta E_v$ (eV) bands, and exchange constants $N_{0\alpha}$ , and $N_{0\beta}$ of $Sr_{1-x}Fe_xS$ compounds ( $x = 0.125, 0.25, 0.50, \text{ and } 0.75$ ).....	125
<b>Table 6.</b> The calculated values of crystal lattice parameter $a$ (Å), bulk modulus $B$ (GPa), energy difference ( $\Delta E$ ), Curie temperature ( $T_C$ ), and formation energy ( $E_f$ ) of (Fe, $p^0$ ) co-doped SrS systems. The Fe mono-doped SrS data are included in the Table from the preceding section, to facilitate further analysis and comparison.....	131
<b>Table 7.</b> The calculated bandgap values of co-doped SrS: (Fe, $p^0$ ) systems. The data of Fe mono-doped SrS are included in the Table from the previous section to facilitate further analysis and comparison.....	132
<b>Table 8.</b> The calculated values of total magnetic moment ( $M^{tot}$ ), interstitial magnetic moment ( $M^i$ ), magnetic moment on each Sr, S, Fe, and $p^0$ atoms, band edges splitting $\Delta E_c$ and $\Delta E_v$ , and exchange constants $N_{0\alpha}$ and $N_{0\beta}$ of co-doped SrS systems. The data of Fe mono-doped SrS are included in the Table from the previous section for further analysis and comparison.....	138

**Table 9.** The calculated elastic constant  $C_{\alpha}$ , the DP constant  $E_d$ , and the effective mass  $m^*$  of the pristine, doped and co-doped SrS systems.....149

---

**Table 1.** The equilibrium optimized structural parameters of bare  $h$ -SrS,  $s$ -FeS, and doped monolayers  $\text{Sr}_{1-x}\text{Fe}_x\text{S}$ : lattice constant ( $a$ ), shortest bond length ( $d$ ), formation energy( $E_f$ ), and elastic constants ( $C_{ij}$ ).....171

**Table 2.** The calculated electronic properties of bare  $h$ -SrS,  $s$ -FeS, and doped monolayer alloys  $\text{Sr}_{1-x}\text{Fe}_x\text{S}$ , including bandgap values for up-spin channel, down-spin channel, and total gap within both PBE and HSE functionals, along with Bader charge ( $\Delta q$ ) transfer from Sr (Fe) to S atoms.....176

**Table 3.** Total magnetic moment ( $M_{\text{TOT}}$ ) and local magnetic moment on each Sr, S, and Fe atoms of  $\text{Sr}_{1-x}\text{Fe}_x\text{S}$  ( $x=0.125, 0.25, 0.50,$  and  $0.75$ ) monolayer alloys.....181



# SYMBOLS and ABBREVIATIONS

---

---

DMS	Diluted Magnetic Semiconductor
3D	Three Dimensional
2D	Two Dimensional
1D	One Dimensional
0D	Zero Dimensional
TMR	Tunnel Magneto-Resistance
GMR	Giant Magnetoresistance
$T_C$	Curie Temperature
FM	Ferromagnetic
AFM	Anti-Ferromagnetic
FIM	Ferrimagnetic
NM	Non-Magnetic
HMF	Half-Metallic Ferromagnetic
SC	Semiconductor
S	Seebeck Effect
$\Delta V$	Electric Potential Difference
$\Delta T$	Temperature Difference
$\pi$	Peltier Coefficient
$Q$	Thermal Power
$I$	Electric Current
$\rho$	Electrical Resistivity
$J$	Joule Effect
$\tau$	Thomson Coefficient
$W$	Dissipated Power
ZT	Figure of Merit
$\sigma$	Electrical conductivity
$S^2\sigma$	Power Factor
$\kappa$	Thermal Conductivity
$\kappa_e$	Electronic Thermal Conductivity
$\kappa_l$	Lattice Thermal Conductivity
$e$	Electronic Charge
$E$	Electric Field
$\hbar$	Planck Constant
$K_B$	Boltzman Constant

SDSE	Spin-Dependent Seebeck Effect
SDPE	Spin-Dependent Peltier Effect
WBG	Wide Band Gap
EG	Energy Gap
EF	Fermi Level
TCO	Transparent Conductive Oxides
ITO	Tin-Doped Indium Oxides
AES	Alkaline Earth Sulfides
LED	Light Emitting Diodes
RS	Rock-Salt
FCC	Face Centered Cubic
P	Polarizability
$H_{ex}$	Heisenberg Exchange Hamiltonian
$N_0\alpha$	Valence Band Exchange
$N_0\beta$	Conduction Band Exchange
TM	Transition Metal
BN	Boron Nitride
TMD	Transition Metal Dichalcogenide
DFT	Density Functional Theory
MD	Molecular Dynamic
QMC	Quantum Monte Carlo

---

$\hat{H}$	The Hamiltonian
$\psi$	Wave Function
$\hat{T}_e$	Kinetic Energy of Electrons
$\hat{T}_N$	Kinetic Energy of Nuclei
$\hat{V}_{eN}$	Energy Potential Characterizing the Electron-Nuclear Potential
$\hat{V}_{ee}$	Energy Potential Characterizing the Electron-Electron Potential
$\hat{V}_{NN}$	Energy Potential Characterizing the Nuclear-Nuclear Potential
$\chi(\vec{R})$	Nuclear Wave Function
$\varphi(\vec{r}, \vec{R})$	Electronic Wave Function
$E_{HF}$	Hartree Fock Energy
$K_{ij}$	Exchange Integral
$J_{ij}$	Coulomb Integral
$E_{TF}$	Thomas Fermi Energy
$V_{ext}$	The External Potential

$E_{xc}$	Exchange-Energy Potential
LDA	Local Density Approximation
GGA	Generalized Gradient Approximation
PBE	Perdew, Burke, and Ernzerhof
WC	Wu and Cohen
TB-mBJ	Tran-Blaha Modified Beck Johnson
HSE	Heyd–Scuseria–Ernzerhof
APW	Augmented Plane Wave
LAPW	Linearized Augmented Plane Wave
FP-LAWP	Full-Potential Linearized Augmented Plane Wave
APW+LP	Augmented Plane Waves in conjunction with Local Orbitals
LAPW+LP	Linearized Augmented Plane Waves in conjunction with Local Orbitals
$R_{mt}$	Muffin-Tin Spheres Radius
$Y_{lm}$	Spherical Harmonics
$E_l$	Energy of Linearization
PAW	Projector Augmented Waves
DFPT	Density Functional Perturbation Theory

---

EOS	Equation of States
$E_0$	Minimum Energy
$V_0$	Equilibrium Volume
a	Lattice Parameter
B	Bulk Modulus
$E_f$	Formation Energy
$C_{ij}$	Elastic Constant
G	Shear Modulus
E	Young Modulus
B/G	Bulk to Shear ratio
A	Anisotropy Zener Factor
$\nu$	Poisson's ratio
$v_l$	Longitudinal Elastic Sound Velocity
$v_t$	Transverse Elastic Sound Velocity
$v_m$	Average Sound Velocity
$\theta_D$	Debye Temperature
$T_m$	Melting Temperature
BS	Band Structure
DOS	Density of States

TDOS	Total Density of States
PDOS	Partial Density of States
CBM	Conduction Band Minima
VBM	Valence Band Maxima
$G_{HM}$	Half-Metallic Gap
$\Delta\chi(d)$	Direct Exchange Splitting Energy
$\mu_B$	Bohr Magnetron
$\Delta E_c$	Spin-Splitting Edge of the Conduction Band
$\Delta E_v$	Spin-Splitting Edge of the Valence Band
MFA	Mean Field Approximation
$\Delta E_{crys}$	Crystal Field Energy
$M_{TOT}$	Total Magnetic Moment
$M_I$	Interstitial Magnetic Moment
HSC	Half-Semiconductor
$\varepsilon(\omega)$	Complex Dielectric Function
$\varepsilon_1(\omega)$	Real Part of the Complex Dielectric Function
$\varepsilon_2(\omega)$	Imaginary Part of the Complex Dielectric Function
$n(\omega)$	Refractive Index
$k(\omega)$	Extinction Coefficient
$\alpha(\omega)$	Absorption Coefficient
$\sigma(\omega)$	Optical Conductivity
RTA	Relaxation Time Approximation
$E_d$	Deformation Potential Energy
$\tau$	Relaxation Time
$m^*$	Effective Mass

---

VASP	Vienna Ab-initio Simulation Package
$d$	The Bond Length
$\Delta q$	Bader Charge
$\varepsilon$	Strain Ratio
fs	Femto Second
ps	Pico Second
AIMD	Ab-Initio Molecular Dynamic

---

# General Introduction

The inception of the transistor in 1947 sparked a pivotal turning point in the evolution of communication and technology [1]. With the ability to digitize information on-chip, the world entered the information age, where knowledge and communication became the driving forces of economic prosperity, surpassing dependence on physical effort and natural resources. In today's world, we witness persons communicating through cell phones, working on laptops, and utilizing the World Wide Web for various tasks. Integrated circuits and high-performance electronics have become integral to our lives, powering applications in drones, recording devices, contemporary cars, and manufacturing machinery, and more. This remarkable growth and evolution of technology has revolutionized the global economy, profoundly affecting all aspects of everyday life, science, industry, and technology.

The continuous growth of technology-based semiconductors has been driven by the ever-growing data processing capabilities, rapid integration density, and faster speeds. Advancements in magnetic materials and optical have further facilitated the seamless transmission, processing, and storage of vast amounts of information. Despite these impressive achievements, the semiconductor-based technology is now facing significant challenges. According to the International Technology Roadmap for Semiconductors (ITRS), further downsizing and power reduction will be hindered as the miniaturization of elements size and operational speed approach their limits [2]. Additionally, electronics inherently generate waste heat during switching, leading to higher power consumption in electronic devices. To overcome these obstacles, the focus is on developing innovative particle-less technologies to handle the growing information demands. Simultaneously, researchers are exploring new ways to efficiently manage and organize information in this rapidly evolving technological landscape.

Exploring alternative integrated circuits presents a promising path forward, and one such example is the realm of all-optical devices utilizing photons as information carriers - the fundamental quanta of electromagnetic waves. This exciting field has given rise to photonic crystals, a subset of optical materials characterized by their periodically adjusted refractive index [3–5]. Just as a semiconductor's periodic atoms lattice creates energy bands and bandgaps for electrons, photonic crystals introduce frequency bands and bandgaps for electromagnetic waves, known as photonic bandgaps. When light (or photons) falls within these bandgaps, the photonic crystals efficiently reflect it, regardless of the incident angle. What makes photonic crystals truly fascinating is their ability to control and manipulate their

properties. By modulating physical parameters such as the dielectric constant or lattice parameters, the characteristics of the photonic bandgaps can be finely tuned. This unique selectivity has resulted in various applications, from photonic waveguides to integrated circuits, unleashing the potential for advanced optical devices [6–10].

In recent times, nano-magnetism and magnetization dynamics [11] have emerged as compelling subfields within the realm of spintronics [12], capturing significant attention by virtue of their promise in revolutionizing nanoscale signal processing and information exchange mechanisms [13–15], like filters, transistors, and storage elements [16–18]. Spintronics, originally abbreviated as "SPIN Transport Electronics," revolves around transmitting, processing, and storing informations hinged on the magnetization state of a given system. A pivotal breakthrough in spintronics occurred with the discovery of the giant magnetoresistance (GMR) effect in Fe/Cr multilayered systems by Fert and Grunberg [19, 20], for which they were honored with the Nobel Prize in 2007. The GMR effect, dependent on the relative orientation of two ferromagnetic layers when subjected to a spin-polarized current, revolutionized magnetic hard disk drives and paved the way for novel non-volatile magnetic memories like Magnetoresistive Random Access Memory (MRAM) [13]. Since then, additional discoveries, such as Spin Transfer Torque (STT) [21], facilitating current-assisted magnetization switching, and the (Inverse) Spin Hall Effect ((I)SHE) [22], enabling the generation and detection of spin currents, have further propelled the field. The Spin Pumping Effect [23], the Spin Seebeck Effect (SSE) [24], and the Dzyaloshinskii-Moriya Interaction (DMI) [25] have also introduced fascinating possibilities to the world of spintronics.

Besides spintronics, the SSE gives rise to the nascent scientific field of so-called spin-caloritronics, in which transport design methodologies have been considered as future independent power sources since they enable the generation of electricity from waste heat in magnetic materials, thus positioning it supplementary to the well established domains of spintronics and thermoelectricity [26]. The field of spin-caloritronics, derived from the term "calor" (Latin for heat), and which came into existence following the significant discovery of the spin Seebeck effect (SSE) in 2008 by Uchida, Saitoh, and their colleagues [24] emerges from the intricate coupling of spin, charge, entropy, and energy transport in predominantly magnetic structures and devices [27]. This quickly developing sector finds several uses in coolers, power generators, and thermometers [28].

In light of these compelling factors, the pursuit of advanced and efficient spintronic, photonic and thermoelectric materials gains even greater significance for the emergence of eco-friendly energy devices in the realm of materials science and technology. Diluted Magnetic Semiconductors (DMSs) that are semiconducting materials doped with magnetic impurities, typically transition metals (TM), and that demonstrate room temperature ferromagnetism, are widely employed in spintronics due to their

remarkable half-metallic ferromagnetic nature (HMF), exhibiting a 100% spin-polarization in both their bulk form (3D) and monolayer form (2D) [29]. Interest in the utilization of DMSs is further fueled by the prospect of finely tuning the bandgap through different processes such as doping, co-doping, alloying, etc., thereby providing the ability to precisely control light absorption at specific energy levels, tailored to suit the desired application [30]. Another important feature is the high carrier mobility resulting from the quantum confinement [30], which is widely desirable for thermoelectric devices.

The extensive findings and in-depth comprehension of the physical characteristics of these materials owe much to ab-initio calculations utilizing Density Functional Theory (DFT). This computational approach minimizes the time, risks, and expenses associated with experimental studies. Furthermore, the results obtained through ab-initio calculations generally align with experimental observations. At the very least, such calculations can predict material properties, thus providing valuable guidance for experimental investigations. A notable example is in the field of spintronics, where the captivating property of half-metallicity, as documented in the literature [29], was initially revealed through ab-initio calculations [29], subsequently confirmed through experimental validation [31]. In the realm of photonic and optoelectronic materials, the groundbreaking concept of "valleytronics" in 2D materials, which enables precise control of light emission and absorption through manipulation of the valley degrees of freedom, has also taken the same path [32]. In recent times, ab-initio calculations have experienced remarkable advancements, primarily due to significant progress in computational techniques and computing power.

Given the significance of DMSs materials and their potential applications in the various desired domains, we employ, in this dissertation, ab-initio calculations to systematically investigate spin-dependent structural, mechanical, electronic, magnetic, optical, and thermoelectric properties of selected host matrix semiconductor SrS-based DMSs using different processes.

The layout of the dissertation is structured as follows:

**Chapter 1** entitled "*Literature Background*", serves as concise introduction to the domains of spintronics and spin caloritronics, providing an overview of diluted magnetic semiconductors (DMSs) that includes a diverse array of materials, spanning from 3D bulk semiconductors to low-dimensional 2D materials. Additionally, the chapter delves into a comprehensive bibliographic research on the fascinating realm of doped and co-doped structures, where elements ranging from alkali to transition metals are integrated into the host SrS to amplify the different physical properties of the materials under investigation.

**Chapter 2** entitled “*Theoretical and Computational Formulation*”, is dedicated to an in-depth exploration of the Density Functional Theory (DFT), which forms a fundamental basis for the ab-initio calculations. It delves into the PAW (Projector Augmented Wave), LAPW (Linearized Augmented Plane Wave), and FP-LAPW (Full Potential Linearized Augmented Plane Wave) methods, elucidating their significance in our research. Various approximations used in our study are thoroughly examined and discussed. Moreover, this chapter provides a comprehensive overview of the functionalities of the WIEN2K and VASP codes, both of which were crucial tools employed in our research.

### **Chapter 3 and 4**

In each of chapters 3 and 4, a comprehensive compilation of the calculation parameters, the obtained results, and their insightful interpretations is presented.

**Chapter 3** entitled “*Effect of Doping and CO-Doping on the SrS Bulk Properties*”, focuses on investigating the spin-resolved structural, mechanical, electronic, and magnetic properties of bulk rock-salt  $\text{Sr}_{1-x}\text{Fe}_x\text{S}$  at various concentrations, namely  $x = 0, 0.125, 0.25, 0.50,$  and  $0.75$ . Additionally, the chapter delves into the structural, electronic, mechanical, magnetic, optical, and thermoelectric properties of bulk SrS: Fe co-doped with alkali metals Li, Na, and K, while maintaining a fixed concentration of  $x = 0.125$ . The chapter further compares the properties of these co-doped materials to those of singly doped  $\text{Sr}_{0.875}\text{Fe}_{0.125}\text{S}$ .

**Chapter 4** entitled “*Effect of Dimensionality Reduction on Fe-Doped SrS Properties*”, deals with the structural, electronic, and magnetic properties of monolayers  $\text{Sr}_{1-x}\text{Fe}_x\text{S}$  at various concentrations, including  $x = 0, 0.125, 0.25, 0.50, 0.75,$  and  $1$ . The chapter further compares the properties of these doped-monolayers to their bulk counterparts.

Finally, the dissertation concludes with a comprehensive summary covering the most important findings and future perspectives.



## References for General Introduction

- [1] Bardeen, J., & Brattain, W. H. (1948). The transistor, a semi-conductor triode. *Physical Review*, 74(2), 230.
- [2] Semiconductor Industry Association. (2009). International technology roadmap for semiconductors. <http://www.itrs.net>.
- [3] Oh, S. S., Kee, C. S., Kim, J. E., Park, H. Y., Kim, T. I., Park, I., & Lim, H. (2000). Duplexer using microwave photonic band gap structure. *Applied Physics Letters*, 76(16), 2301-2303.
- [4] D'Orazio, A., De Sario, M., Petruzzelli, V., & Prudenzano, F. (2003). Photonic band gap filter for wavelength division multiplexer. *Optics Express*, 11(3), 230-239.
- [5] Lončar, M., Doll, T., Vučković, J., & Scherer, A. (2000). Design and fabrication of silicon photonic crystal optical waveguides. *Journal of lightwave technology*, 18(10), 1402.
- [6] Li, J., & Chiang, K. S. (2007). Guided modes of one-dimensional photonic bandgap waveguides. *JOSA B*, 24(8), 1942-1950.
- [7] Li, X., Wang, Y., Su, Y., Yan, M., & Qiu, M. (2008). *Opt. Express*, 16(2), 880-888.
- [8] Gruszecki, P., Banerjee, C., Mruczkiewicz, M., Hellwig, O., Barman, A., & Krawczyk, M. (2019). The influence of the internal domain wall structure on spin wave band structure in periodic magnetic stripe domain patterns. In *Solid State Physics* (Vol. 70, pp. 79-132). Academic Press.
- [9] Petrov, A. Y., & Eich, M. (2005). Dispersion compensation with photonic crystal line-defect waveguides. *IEEE journal on selected areas in communications*, 23(7), 1396-1401.
- [10] Van Laere, F., Stomeo, T., Cambournac, C., Ayre, M., Brenot, R., Benisty, H., & Baets, R. (2009). Nanophotonic polarization diversity demultiplexer chip. *Journal of lightwave technology*, 27(4), 417-425.
- [11] Barman, A., & Sinha, J. (2018). *Spin dynamics and damping in ferromagnetic thin films and nanostructures* (Vol. 1). Cham: Springer International Publishing.
- [12] Wolf, S. A., Awschalom, D. D., Buhrman, R. A., Daughton, J. M., von Molnár, V. S., Roukes, M. L., & Treger, D. M. (2001). Spintronics: a spin-based electronics vision for the future. *Science*, 294(5546), 1488-1495.
- [13] Tehrani, S., Chen, E., Durlam, M., DeHerrera, M., Slaughter, J. M., Shi, J., & Kerszykowski, G. (1999). High-density submicron magnetoresistive random access memory. *Journal of Applied Physics*, 85(8), 5822-5827.
- [14] Imre, A., Csaba, G., Ji, L., Orlov, A., Bernstein, G. H., & Prood, W. (2006). Majority logic gate for magnetic quantum-dot cellular automata. *Science*, 311(5758), 205-208.
- [15] Allwood, D. A., Xiong, G., Faulkner, C. C., Atkinson, D., Petit, D., & Cowburn, R. P. (2005). Magnetic domain-wall logic. *Science*, 309(5741), 1688-1692.

- [16] Lee, K. S., Han, D. S., & Kim, S. K. (2009). Physical origin and generic control of magnonic band gaps of dipole-exchange spin waves in width-modulated nanostrip waveguides. *Physical review letters*, 102(12), 127202.
- [17] Etko, Y. L., & Ustinov, A. B. (2011). Broadband spin-wave delay lines with slot antennas. *Technical Physics Letters*, 37, 1015-1017.
- [18] Kumar, D., Barman, S., & Barman, A. (2014). Magnetic vortex based transistor operations. *Scientific reports*, 4(1), 4108.
- [19] Baibich, M. N., Broto, J. M., Fert, A., Van Dau, F. N., Petroff, F., Etienne, P., & Chazelas, J. (1988). Giant magnetoresistance of (001) Fe/(001) Cr magnetic superlattices. *Physical review letters*, 61(21), 2472.
- [20] Binasch, G., Grünberg, P., Saurenbach, F., & Zinn, W. (1989). Enhanced magnetoresistance in layered magnetic structures with antiferromagnetic interlayer exchange. *Physical review B*, 39(7), 4828.
- [21] Berger, L. (1996). Emission of spin waves by a magnetic multilayer traversed by a current. *Physical Review B*, 54(13), 9353.
- [22] Hirsch, J. E. (1999). Spin Hall Effect. *Physical review letters*, 83(9), 1834.
- [23] Brataas, A., Kent, A. D., & Ohno, H. (2012). Current-induced torques in magnetic materials. *Nature materials*, 11(5), 372-381.
- [24] Uchida, K. I., Takahashi, S., Harii, K., Ieda, J., Koshibae, W., Ando, K., & Saitoh, E. (2008). Observation of the spin Seebeck effect. *Nature*, 455(7214), 778-781.
- [25] Dzyaloshinskii, I. E. (1957). Thermodynamic theory of weak ferromagnetism in antiferromagnetic substances. *Journal of Physics and Chemistry of Solids*, 5(6), 1259-1272.
- [26] Petsagkourakis, I., Tybrandt, K., Crispin, X., Ohkubo, I., Satoh, N., & Mori, T. (2018). Thermoelectric materials and applications for energy harvesting power generation. *Science and technology of advanced materials*, 19(1), 836-862.
- [27] Bauer, G. E., MacDonald, A. H., & Maekawa, S. (2010). Spin caloritronics. *Solid State Communications*, 150(11-12), 459-460.
- [28] Johnson, M., & Silsbee, R. H. (1987). Thermodynamic analysis of interfacial transport and of the thermomagnetolectric system. *Physical Review B*, 35(10), 4959.
- [29] De Groot, R. A., Mueller, F. M., van Engen, P. V., & Buschow, K. H. J. (1983). New class of materials: half-metallic ferromagnets. *Physical review letters*, 50(25), 2024.
- [30] Jain, M. K. (1991). *Diluted magnetic semiconductors*. World Scientific.
- [31] Borca, C. N., Komesu, T., Jeong, H. K., Dowben, P. A., Ristoiu, D., Hordequin, C., & Idzerda, Y. U. (2001). Evidence for temperature dependent moments ordering in ferromagnetic NiMnSb (100). *Physical Review B*, 64(5), 052409.
- [32] Schaibley, J. R., Yu, H., Clark, G., Rivera, P., Ross, J. S., Seyler, K. L., & Xu, X. (2016). Valleytronics in 2D materials. *Nature Reviews Materials*, 1(11), 1-15.

# Chapter 1

## Literature Background

**T**his chapter provides a concise yet comprehensive introduction to the fields of spintronics and spin caloritronics as well as dilute magnetic semiconductors (DMS), which include various 3D bulk semiconductor groups as well as low-dimensional 2D materials. Furthermore, it explores the fascinating area of doped/codoped structures, in which alkali to transition metals are incorporated to improve structural, mechanical, electronic, magnetic, optical and thermoelectric properties. By exploring the fascinating properties and diverse uses of these materials, this chapter helps in selecting suitable compounds for this dissertation.



### 1.1 Introduction

The ever-increasing energy demand of human activities has become an urgent global problem and requires the introduction of advanced techniques for research and development of sustainable and environmentally friendly energy resources. The scientific and industrial community is extremely curious to find an ideal renewable energy source that can be practically translated into the development of useful products and mitigate the harmful effects of anthropogenic carbon emissions on the global climate. Among the various options, the thermoelectric phenomenon stands out as an excellent source of renewable energy. As electronic devices continue to shrink toward the nanometer and their operating speed increases, dissipating heat or waste energy has become a critical issue. To achieve energy savings and improve the performance and reliability of electronic devices, it is imperative to either reduce or effectively utilize wasted energy. In this context, spintronics proves to be a promising path to significantly lower energy consumption [1]. On the other hand, thermoelectrics explores the direct conversion of waste heat into electrical power and represents a fascinating avenue for research and development. A fascinating and novel research area known as spin caloritronics is currently gaining significant attention as it combines the strengths of spintronics and thermoelectrics [2]. Semiconductor materials, whether in their bulk form or as 2D counterparts, with their intrinsic properties and well-suited electronic structures emerge as perfect candidate bases for this purpose. Based on their energy bandgap, semiconductor materials are divided into three different categories, of which we are interested and will only discuss the wide bandgap semiconductor (WBG) category.

## 1.2 Spintronics and Related Devices

### 1.2.1 Definition and Historical Development of Spintronic Phenomena

Spintronics (or spin electronics) has revolutionized electronic data storage by actively manipulating the spin degrees of freedom of electrons interacting with their orbital moments, ushering in a new era of possibilities [3]. Magnetic layers act as spin polarizers or analyzers and determine spin polarization through spin-orbit coupling. This complicated interaction leads to the generation of a spin current, which is further driven by fascinating spin waves.

Every electron possesses two possible states known as spin-up  and spin-down , meaning they can rotate either clockwise or counterclockwise. These majority-up and majority-down domains are randomly distributed. However, when an external magnetic field is applied, it aligns the domains in the direction of the electric field. This phenomenon enables precise control and manipulation of electron spins and forms the basis for various fast and energy-efficient spintronic applications and innovations in electronic data storage and processing [4].

The attractive field of spintronics began in 1922 with the discovery of the magnetic moment of electrons [5]. Wolfgang Pauli's groundbreaking research validated the quantization of electron spin and introduced the idea of Pauli matrices. A crucial moment came in 1973 when the conversion of electron spin to spin current between ferromagnetic films was observed [6] and shortly afterwards D'yakonov and Perel predicted the spin Hall effect [7], which was later confirmed experimentally.

In 1975, Julliere and his team conducted the first experiment on the tunneling magnetoresistance effect (TMR), revealing the fascinating phenomenon of electron tunneling between two ferromagnets separated by a thin insulator [8].

In 1976, the concept of generating spin-polarized current in a semiconductor by passing a current through a ferromagnet/semiconductor junction was first proposed [9].

In the 1980s, the idea of spintronics emerged, which explores spin-dependent electron transport in solid-state devices. The journey continued with the discovery of spin-polarized electron injection from one ferromagnetic metal to another by Johnson and Silsbee [10]. This was followed by the independent giant magnetoresistance (GMR) breakthrough, observed in ferro/metal/ferro multilayer structures, reported by Fert et al. and Grünberg et al. Their pioneering work earned them the Nobel Prize in Physics in 2007 [11, 12].

A milestone in the practical application of spintronics was the introduction in 1997 of spin valve sensors in read heads of hard disk drives, which were developed by an IBM researcher [13]. This

breakthrough enabled an impressive storage capacity of 16.8 GB, setting the stage for other manufacturers to follow suit and continually improve performance and storage capacities.

However, despite remarkable progress, spintronics has faced several challenges. The search remains for low-cost, abundant, and lightweight ferromagnetic materials with 100% spin-polarized current, longer spin lifetime, high magnetic anisotropy, and easy manipulation of spin currents. Furthermore, it is important to consider the influence of strain and temperature on spin properties to exploit the full potential of spintronic devices [14].

During the late 20<sup>th</sup> century, heavy transition metals such as iron (Fe), nickel (Ni), and cobalt (Co) gained recognition as important components of spintronic materials due to their high Curie temperatures (TC) and intrinsic ferromagnetic (FM) nature. These properties make them ideal for generating and controlling spin polarization, which is fundamental to various spintronic applications. Due to their remarkable contributions, these materials have laid the foundation for remarkable advances in this field [15].

As a result, the field of spintronics experienced rapid growth, driven by the growing interest and contributions of numerous research groups. This trend can be seen in the significant increase in publication numbers over the years, as shown in Figure 1.

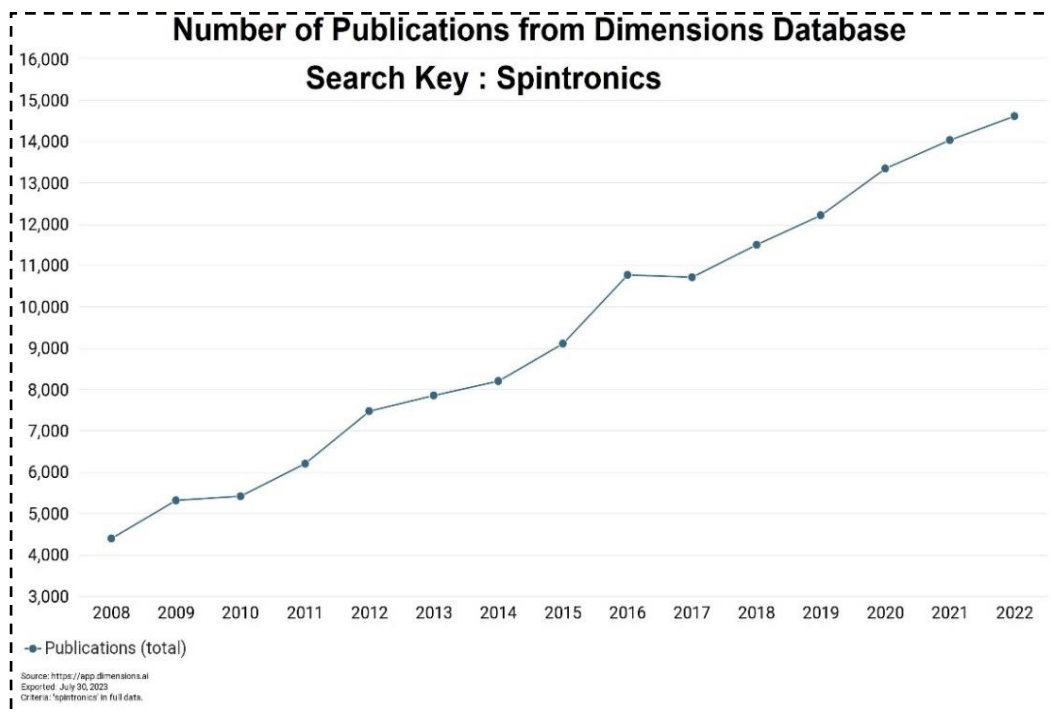


**Figure 1.** Annual publications on spintronics over the past decade.

### 1.2.2 Spin Devices

Figure 2 provides a comprehensive and insightful overview of spintronic devices, which can be conveniently divided into two distinct categories: Mott-type and Dirac-type, with each category characterized by its unique use of electron spins, spin waves, and spin/orbit moments. In the Mott-type devices, the most important phenomena are giant magnetoresistance (GMR) and tunneling magnetoresistance (TMR), while the Dirac-type devices exploit the fundamental spin-orbit interactions [16].

To better understand the evolutionary progress of these spintronic devices, we can divide them into three generations, each with a notable leap in their capabilities and applications. The first generation revolves around spin transport, with electrical spin generation playing a central role. The second generation includes devices that exploit spin dynamics, making skilful use of spin-orbit effects, electric fields and electromagnetic wave applications. These advances have significantly expanded the horizons of spintronics and led to transformative functionalities and innovative possibilities. Finally, the groundbreaking developments of the third generation pushed the boundaries of spintronics even further to include three-dimensional structures and quantum technology. This development has catapulted spintronics into the realm of quantum computation and promises a revolutionary paradigm shift in the field.

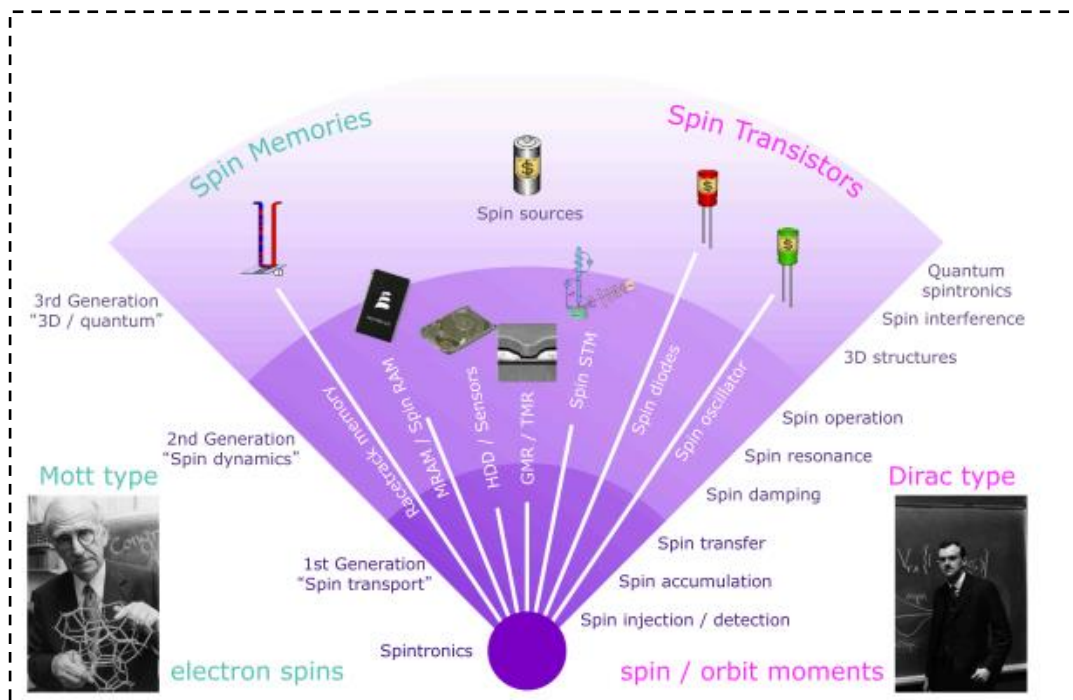


**Figure 2.** Catalog of spintronics devices. After Ref [16].

### 1.2.3 Spin Generation

The generation of spin-polarized electrons in non-magnetic (NM) materials can be achieved by various methods [16]. These techniques include spin injection from ferromagnetic (FM) materials, application of magnetic or electric fields, introduction of electromagnetic waves, Zeeman splitting, spin driving force, thermal gradients, and mechanical rotation (see Figure 3). A commonly used approach is spin injection through FM materials such as conventional FM metals (Fe, Co, and Ni), half-metallic ferromagnets (HMF), and dilute magnetic semiconductors (DMS).

Besides, spin-polarized electrons in an NM material may exhibit a population difference due to a stray field near the edge of an FM. Electromagnetic waves such as circularly polarized light and microwaves can also excite spin-polarized electrons in SC materials, where the optical selection rule plays a crucial role. Conversely, a spin-polarized electron current can produce circularly polarized light emission. These principles can be extended to spin generation by other electromagnetic waves, including spin pumps and high-frequency spin induction.

Furthermore, the application of a thermal gradient due to the spin-Seebeck and Nernst effects has been shown to be effective in generating spin-polarized carrier currents and offers valuable opportunities for energy harvesting and other potential applications.

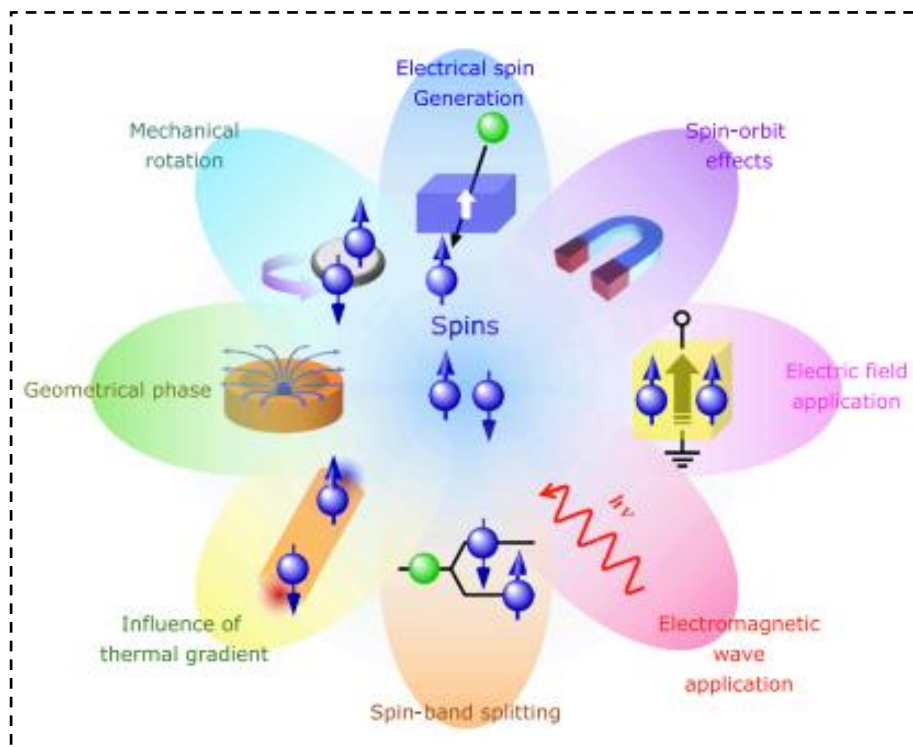


**Figure 3.** Methods for generating spin-polarized electrons in non-magnetic media. After Ref [16].

### 1.3 Opportunities at the Frontiers of Spintronics

As mentioned in the previous section, an effective method for generating spin-polarized electrons is through the application of a thermal gradient, which leads to the emergence of a new field at the forefront of spintronics, known as “spin caloritronics”.

Spin caloritronics deals with the study of thermoelectric transport effects in material systems in which magnetic spin moments are introduced. The inclusion of additional spin degrees of freedom not only opens up a wealth of conceptually innovative mechanisms and functionalities, but also ushers in a new era of transformative breakthroughs in the conversion of thermal to electrical energy in solids. In Figure 4 we present a clear representation of the concept of spin caloritronics.

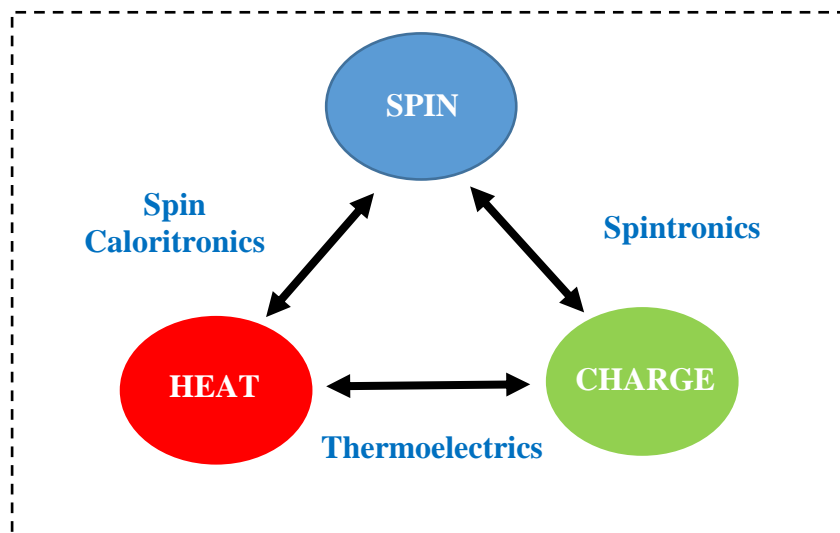


**Figure 4.** An illustrative depiction of the concept of spin caloritronics.

Since its founding in 2009 through an international workshop, the field of spin caloritronics has attracted considerable attention. Annual meetings of specialists in the field have become the norm as the research topic attracts more and more researchers. In particular, the twelfth “Spin Caloritronics” workshop took place in 2023 [17].

The German Physical Society (DFG) has recognized the importance of this emerging field and initiated a priority program to support further research [18]. In addition, the US Department of Energy has provided funding for the SHINES (Spins and Heat in Nanoscale Electronic Systems) research cluster, which includes 14 research groups from 7 different institutions across the country.

The interdisciplinary nature of spin caloritronics, combining magnetism, thermoelectrics and microelectronics, ensures that it will continue to captivate the global scientific community and generate immense interest in cutting-edge research [19].



Before continuing our discussions in this new area, it is first necessary to look at the history of thermoelectricity to better understand the role of spin in our study.

### 1.3.1 Thermoelectric Effects

Thermoelectricity is an intrinsic property of materials that gives them the ability to convert thermal energy into electrical energy. Over time, this fascinating area has experienced two significant periods of development:

The first stretched from 1821 to 1851, the second lasted from the late 1930s to the early 1960s. In 1821, the pioneering German physicist Thomas Johann Seebeck made a significant discovery, revealing one of the fundamental thermoelectric effects [20]. His observation involved a metal needle placed between two different metal conductors connected at their ends by junctions at different temperatures, resulting in a noticeable deflection. He originally incorrectly attributed this phenomenon to a magnetic field induced by the temperature differences at the metal junctions and suggested that this could explain the earth's magnetic field.

However, in 1825, Oersted corrected this misunderstanding by showing that the effect was due to the emergence of a potential difference at the junction of two materials with temperature contrast. This discovery became known as the “Seebeck effect.” Consequently, this effect allows the use of a temperature gradient to generate an electric current, as described by the equation:

$$\Delta V = S_{AB} \cdot \Delta T \quad (\text{eq.1})$$

With  $S_{AB}$  being the Seebeck coefficient or thermoelectric power of the two materials A and B, typically expressed in  $\mu\text{V}\cdot\text{K}^{-1}$ , and  $\Delta V$  representing the electric potential difference generated by the temperature difference  $\Delta T$ .

In 1834, physicist and watchmaker Jean-Charles Peltier made the groundbreaking discovery that a temperature difference occurs at the junctions of two different materials when they are exposed to an electric current [21]. However, it took until 1838 for Lenz to fully explain the phenomenon [22]. Through a convincing experiment, Lenz showed that the direction of heat transfer depends on the direction of current flow. He crystallized water around a bismuth-antimony compound and by reversing the direction of the current; he managed to melt the ice. This phenomenon became known as the “*Peltier effect*.”

Since each material has its own Peltier coefficient  $\pi$ , flowing a current through the junction results in an interruption in the flow of heat at that point. For example, as current flows from material  $a$  to material  $b$ , the junction heats up (if  $\pi_a > \pi_b$ ) or cools (if  $\pi_a < \pi_b$ ), as described by the equation:

$$Q = \pi_{AB} \cdot I \quad (\text{eq.2})$$

With  $Q$  representing the generated thermal power,  $I$  denoting the electric current, and  $\pi_{AB}$  being the Peltier coefficients of the two materials.

In 1840, a crucial breakthrough occurred when James Prescott Joule revealed his groundbreaking discovery. He showed that whenever an electric current flows through a material, an amount of heat is generated that is directly proportional to the intensity of that current [23]. This remarkable phenomenon became known as the ‘‘Joule effect’’ and its expression is captured by the following equation:

$$q_J = \rho \cdot \vec{J}^2 \quad (\text{eq.3})$$

With  $\rho$  representing the electrical resistivity of the material.

It is obvious that the square of the current flux density and the positive nature of the electrical resistivity contribute to the inevitable positivity of the amount of heat,  $q_J$ . Unlike the reversible Peltier and Seebeck effect, the Joule effect is irreversible as it merely produces the production of heat without the ability to absorb it. In addition, the physicist William Thomson established the crucial connection between the Seebeck and Peltier effects in 1851 [24]. Consequently, when a temperature difference and an electric current are applied at the same time, a dynamic heat exchange with the environment occurs. Conversely, a material exposed to a thermal gradient and with heat flowing through it produces an electric current, a process known as the ‘‘Thomson effect.’’

The heat output or absorbed per unit volume can be expressed using the following formula:

$$Q_T = -\tau \cdot \vec{J} \cdot \vec{\nabla} T \quad (\text{eq.4})$$

$\tau$  denotes the Thomson coefficient. The Thomson coefficient is closely linked to the Seebeck and Peltier coefficients, as expressed in the following relationship:

$$\pi_{AB} = S_{AB} \cdot T \quad (\text{eq.5})$$

$$\tau = \rho \cdot \frac{dS_{AB}}{dT} \quad (\text{eq.6})$$

The Peltier, Seebeck and Thomson effects have a fundamental difference: the latter phenomenon manifest itself within a single material, eliminating the need for a connection between different materials, as in the case with other two.

The timeline of discovery of these various thermoelectric effects by their respective pioneers is shown in Figure 5(a), along with schematic representations of each effect (Figure 5(b)).

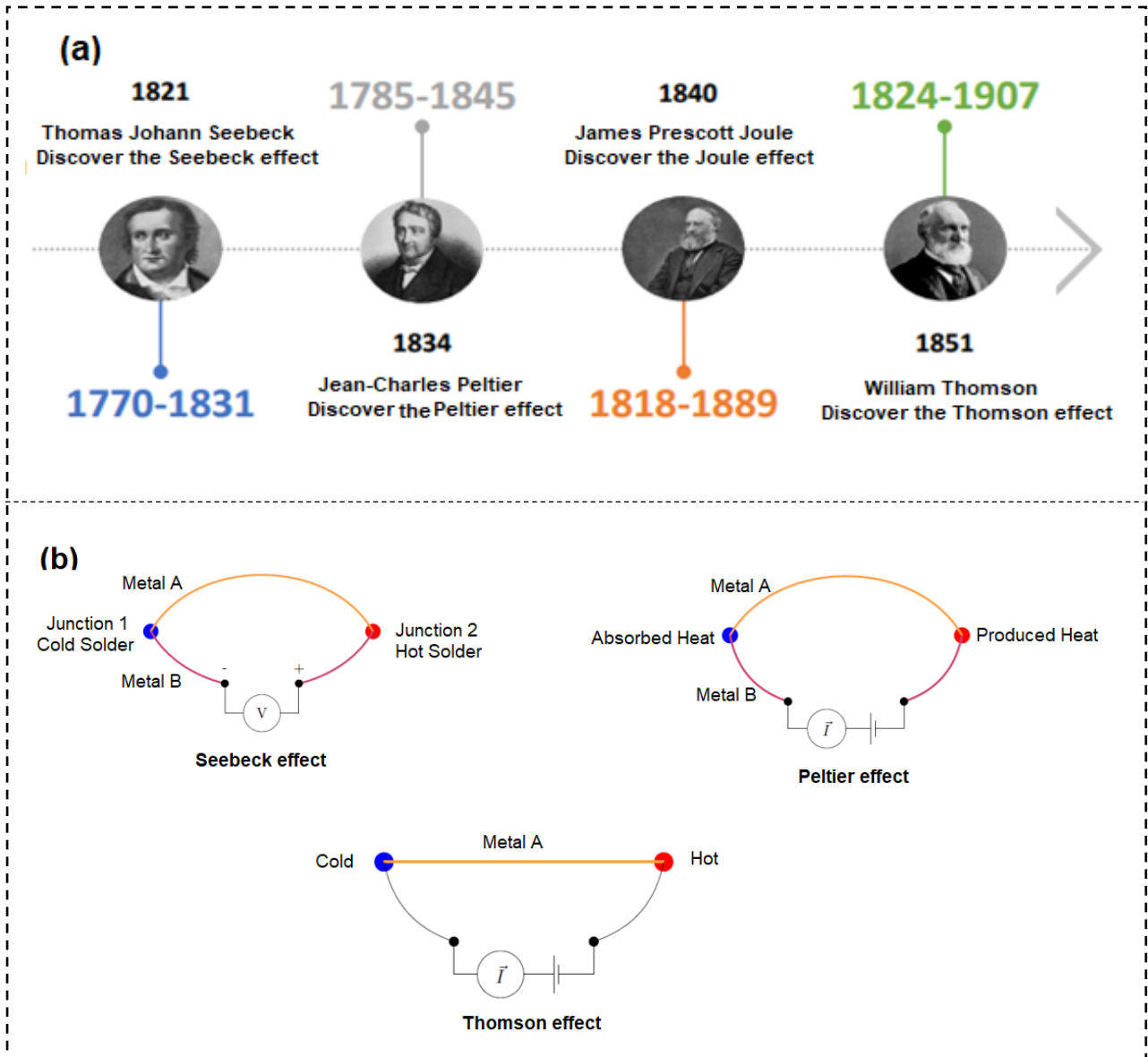


**Figure 5.** (a) Key pioneers in thermoelectricity. (b) The representation of Seebeck, Peltier, and Thomson effects, respectively.

### 1.3.2 Transport Equations

Thermoelectric devices are based on the connection of two pairs of materials, one of type  $p$  with  $S > 0$  and the other of type  $n$  with  $S < 0$ . When electric current is applied, charge carriers move from the

cold to the hot source. More specifically, electrons in the  $n$ -type branch migrate toward the hot source, while holes in the  $p$ -type branch also migrate toward the same heat reservoir. This concerted action results in both charge carriers transporting entropy from the cold source to the hot source, ultimately inducing a heat flow that actively counteracts heat conduction [25].

Within each branch, the total flow is expressed by:

$$Q_p = S_p IT - \kappa_p A_p \frac{dT}{dz} \quad (\text{eq.7})$$

$$Q_n = S_n IT - \kappa_n A_n \frac{dT}{dz} \quad (\text{eq.8})$$

Where  $\kappa_p$  and  $\kappa_n$  are the thermal conductivities of the  $p$ -type and  $n$ -type materials,  $A_p$  and  $A_n$  are their respective cross-sectional areas,  $S_p$  and  $S_n$  are the Seebeck coefficients, and  $z$  represents the spatial coordinate.

Heat is dynamically transported from the cold source to the hot source, resulting in a total flux  $Q_t$  [25]:

$$Q_t = (Q_p + Q_n)|_{z=0} \quad (\text{eq.9})$$

At the same time, the Joule effect comes into play in the circuit due to the flow of the electrical current  $I$ . The heat generated by this effect is given by  $\rho I^2/A$ . Conservation of energy can be aptly described for both branches of the circuit, taking into account the balance achieved by a non-constant thermal gradient:

$$\kappa_p A_p \frac{d^2 T}{dz^2} = \frac{I^2 \rho_p}{A_p} \quad (\text{eq.10})$$

$$\kappa_n A_n \frac{d^2 T}{dz^2} = \frac{I^2 \rho_n}{A_n} \quad (\text{eq.11})$$

When analyzing the system, we must carefully consider the boundary conditions. Let  $L_n$  and  $L_p$  denote the lengths of the individual branches. At the cold source ( $z = 0$ ), the temperature remains the same as the cold source, ensuring a consistent thermal interface. Similarly, at the hot source ( $z = L_p$  or  $z = L_n$ ), the temperature is maintained at the hot source level, thereby maintaining thermal equilibrium.

The boundary conditions can therefore be formulated precisely as follows [25]:

$$T = T_c \text{ at } z = 0 \quad (\text{eq.12})$$

$$T = T_h \text{ at } z = L_n \text{ or } z = L_p \quad (\text{eq.13})$$

The eq.10 and eq.11 yield:

$$\kappa_p A_p \frac{dT}{dz} = -\frac{I^2 \rho_p (z - \frac{1}{2} L_p)}{A_p} + \frac{\kappa_p A_p (T_h - T_c)}{L_p} \quad (\text{eq.14})$$

$$\kappa_n A_n \frac{dT}{dz} = -\frac{I^2 \rho_n (z - \frac{1}{2} L_n)}{n} + \frac{\kappa_n A_n (T_h - T_c)}{L_n} \quad (\text{eq.15})$$

By substituting these formula into eq.7 and eq.8 and employing eq.9, we reveal the comprehensive expression for the total thermal flux  $Q_t$ :

$$Q_t = (S_p - S_n)IT_f - \kappa \Delta T - \frac{1}{2} I^2 R \quad (\text{eq.16})$$

Where  $\kappa$  is the thermal conductivity and  $R$  is the electrical resistance of the circuit, both defined as follows:  $\kappa$

$$\kappa = \frac{\kappa_p A_p}{L_p} + \frac{\kappa_n A_n}{L_n} \quad (\text{eq.17})$$

$$R = \frac{L_p \rho_p}{A_p} + \frac{L_n \rho_n}{A_n} \quad (\text{eq.18})$$

The combined Joule and Seebeck effects play a crucial role in determining the dissipated power  $W$  [26]:

$$W = I \cdot [(S_p - S_n) \cdot \Delta T + IR] \quad (\text{eq.19})$$

The efficiency  $\epsilon_c$  of the thermoelectric cooler is defined as the ratio between the extracted heat  $Q_t$  and the dissipated electrical power  $W$ . By utilizing equations eq.16 and eq.19, it follows [26]:

$$\epsilon_c = \frac{Q_t}{W} = \frac{(S_p - S_n)IT_f - \kappa \Delta T - \frac{1}{2} I^2 R}{I \cdot [(S_p - S_n) \cdot \Delta T + IR]} \quad (\text{eq.20})$$

In addition, it is possible to determine the efficiency of a  $p-n$  device specifically designed for electricity generation from a temperature difference. The efficiency  $\epsilon_c$  is defined as the ratio of the useful electrical power delivered to a load resistance  $r$  and the thermal flux through the device:

$$\varepsilon_e = \frac{W_{\text{useful}}}{Q} = \frac{I \cdot [(S_p - S_n) \Delta T + IR]}{(S_p - S_n) I T_f - \kappa \Delta T - \frac{1}{2} I^2 (R + r)} \quad (\text{eq.21})$$

This profound expression provides a way to discover the electrical current that maximizes efficiency. Both cooling and power generation have two different values of electrical current  $I$ , each optimizing either the conversion efficiency or the electrical energy generated by using heat.

When both efficiencies reach their peak, an interesting observation occurs that shows their dependence exclusively on the temperatures  $T_c$  and  $T_h$  and the dimensionless figure of merit  $Z_{pn} \cdot T_A$  [27]. Here  $T_A = (T_c + T_h)/2$  represents the average temperature, a crucial parameter in this thermoelectric context. The figure of merit factor  $Z_{pn} \cdot T_A$  is a critical factor that is defined specifically for the particular pair of materials used in the device. The  $Z_{pn} \cdot T_A$  formulation includes the intrinsic absolute parameters of the materials constituting the thermoelectric couple [27]:

$$Z_{pn} T = \frac{(S_n - S_p)^2}{(\sqrt{\kappa_p \rho_p} + \sqrt{\kappa_n \rho_n})^2} T \quad (\text{eq.22})$$

The maximum occurs when the efficiency reaches its peak.

Similarly, individual  $p$ -type and  $n$ -type materials each have their own intrinsic factor, commonly known as the figure of merit:

$$ZT = \frac{S^2}{\rho \kappa} T = \frac{S^2 \sigma}{\kappa} T = \frac{S^2 \sigma}{\kappa_e + \kappa_l} T \quad (\text{eq.23})$$

The figure of merit factor  $ZT$  is of utmost importance when assessing the thermoelectric properties of a material and serves as a crucial indicator of its suitability for thermoelectric applications. This dimensionless factor plays a critical role in whether a material has desirable thermoelectric properties or does not meet the criteria. In order to achieve the greatest possible efficiency of thermoelectric conversion, a maximum value of  $ZT$  must be aimed [28]. This requires maximizing the Seebeck coefficient and achieving the highest possible electrical conductivity and hence the numerator  $S^2 \sigma$ , called the power factor, while at the same time minimizing the denominator, which represents the sum of the electronic contribution to thermal conductivity,  $\kappa_e$ , and the lattice contribution,  $\kappa_l$ .

### 1.3.3 Optimization Parameters for $ZT$

We have just seen the importance of the quality factor in identifying high-performance thermoelectric materials, whether they belong to the  $n$ -type or  $p$ -type semiconductors. To realize the greatest potential of  $ZT$ , these materials must have distinct and precise thermal and electrical transport properties. However, we face a challenge because these transport phenomena have strong correlations.

Notably, a material with excellent thermal conductivity often also has exceptional electrical conductivity [29].

The insightful Figure 6 illustrates the overall evolution of thermoelectric properties with respect to carrier concentration and provides valuable insights into the complex relationship between thermal and electrical properties in thermoelectric materials.

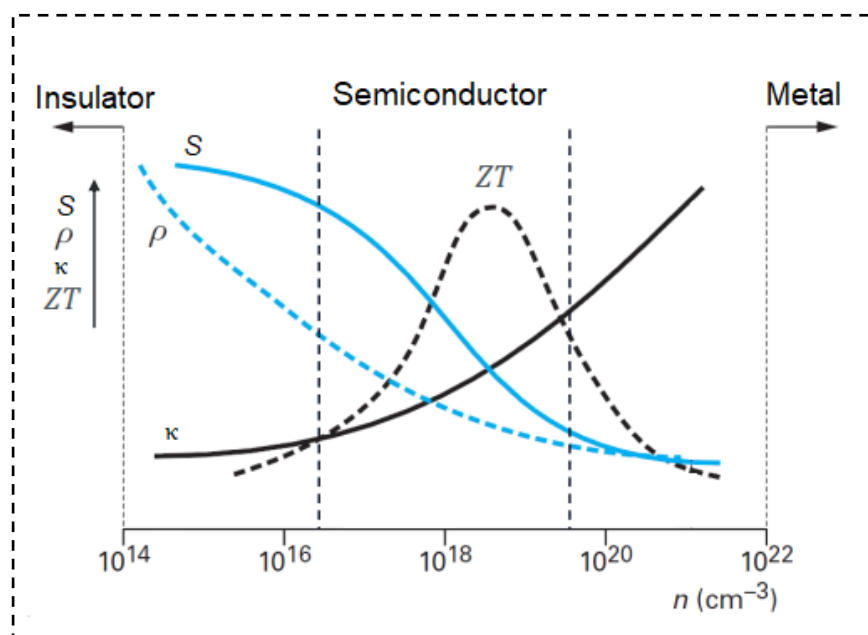


**Figure 6.** Evolving thermoelectric parameters with charge carrier concentration,  $n$ , at 300 K. After Ref [30].

This figure provides a compelling insight into the complex interdependence of thermoelectric parameters on carrier concentration. As the concentration of charge carriers varies, a delicate equilibrium is created in which the Seebeck coefficient decreases while the electrical and thermal conductivity increases. It becomes clear that there is an optimal carrier concentration that maximizes the figure of merit typically found in heavily doped semiconductors. Remarkably, this optimal concentration is in the range of  $10^{19}$  to  $10^{20}$   $\text{cm}^{-3}$ , although each semiconductor has its own optimum.

When exploring the fascinating material properties described in the literature, a promising thermoelectric material should manifest itself as a glass due to its low thermal conductivity to phonons and as a crystal to electrons due to its exceptional electrical properties [31]. Achieving peak performance requires a complex crystal structure that hinders the propagation of phonons. Cutting-edge research has identified numerous degrees of freedom, allowing researchers to influence the figure of merit and shape material performance [32]. These critical factors are illustrated in Figure 7.

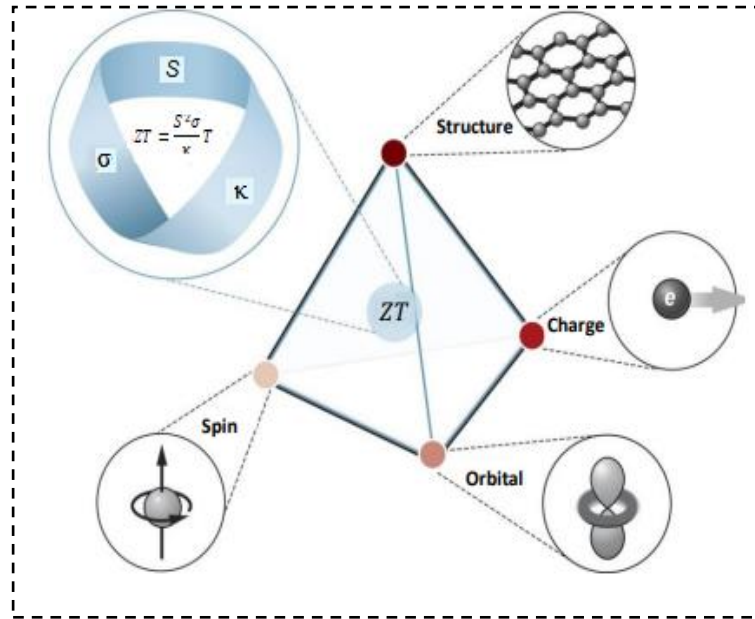


**Figure 7.** Degrees of freedom affecting the figure of merit. After Ref [30].

These four degrees of freedom make it possible to optimize the quality factor. These mechanisms, which are crucial for charge carrier transport, are the key to understanding the complex interactions between charge, orbitals, spin, and lattice structure [33]. For example, by manipulating the crystal complexity of the semiconductor, the proportion of optical phonons increases compared to acoustic phonons. Since acoustic phonons mainly transport heat, a more complex structure leads to reduced thermal conductivity [34]. The incorporation of impurities or point defects increases phonon scattering and effectively reduces thermal conductivity [35]. At the same time, doping improves the electrical properties of the semiconductor [36]. Furthermore, heat transport through dimensionality reduction to limit the phonon mean free path and approximate the interatomic distance follows a mode of random thermal diffusion known as Einstein's model [37]. Furthermore, dimensionality reduction leads to significant fluctuations in electron density, favoring a high Seebeck coefficient without affecting the electrical conductivity of the material [38].

### 1.3.4 Boltzmann Transport Theory

The simulation of electrical conductivity and the Seebeck coefficient can be achieved by applying first principles calculations alongside the use of the Boltzmann transport equation. Charge transport occurs in the presence of an electric field and/or a temperature gradient. This phenomenon is described in the following equation [39]:

$$J = e \sum f \cdot v = \sigma E \quad (\text{eq.24})$$



In this context,  $\mathbf{J}$  represents the flow of charge;  $e$  stands for the electronic charge;  $\mathbf{f}$  denotes the charge distribution;  $\sigma$  denotes the electrical conductivity;  $\mathbf{E}$  represents the electric field, and  $\mathbf{v}$  corresponds to the charge velocity. By understanding the temporal and spatial distribution of charges, we can determine the flow of charges. The temporal development of the charge distribution can be illustrated as follows [40]:

$$\frac{\partial \mathbf{f}}{\partial t} + \frac{d\mathbf{r}}{dt} \cdot \nabla_{\mathbf{r}} \mathbf{f} + \frac{d\mathbf{p}}{dt} \cdot \nabla_{\mathbf{p}} \mathbf{f} = \left(\frac{\partial \mathbf{f}}{\partial t}\right)_{\mathbf{c}} \quad (\text{eq.25})$$

Here,  $\mathbf{r}$  represents the electron's position;  $\mathbf{p}$  signifies momentum, and  $\mathbf{c}$  denotes collision index. More specifically, eq.25 illustrates the change in charge distribution after a collision.

$$\frac{\partial \mathbf{f}}{\partial t} = \frac{\mathbf{f} - \mathbf{f}_0}{\tau} \quad (\text{eq.26})$$

$$\mathbf{f} - \mathbf{f}_0 = \mathbf{c} e^{-\frac{t}{\tau}} \tau \quad (\text{eq.27})$$

By utilizing eq.25, eq.26, and eq.27, we can derive:

$$\mathbf{f} = \mathbf{f}_0 + e \left( -\frac{\partial \mathbf{f}_0}{\partial \varepsilon} \right) \tau \mathbf{v} \cdot \mathbf{E} \quad (\text{eq.28})$$

Upon substituting eq.24 with the expression provided in eq.28, the conductivity can be effectively described as follows:

$$\sigma = e^2 \sum -\left(\frac{\partial \mathbf{f}_0}{\partial \varepsilon}\right) \mathbf{v}^2 \tau \quad (\text{eq.29})$$

This equation can be reconfigured into tensor form as part of electronic structure calculations:

$$\sigma(\varepsilon) = \frac{e^2}{N\Omega} \int d\varepsilon - \left(\frac{\partial \mathbf{f}_0}{\partial \varepsilon}\right) \sum_{n,k} \tau_{n,k} \vec{\mathbf{v}}_{n,k} \vec{\mathbf{v}}_{n,k} \delta(\varepsilon - \varepsilon_{n,k}) \quad (\text{eq.30})$$

In this context,  $\Omega$  signifies the volume of the unit cell;  $e$  denotes the charge of the carrier;  $\varepsilon$  represents the energy of the group;  $N$  stands as the count of  $k$ -points employed in the computation;  $\mathbf{f}_0$  corresponds to the Fermi-Dirac distribution function;  $\tau$  denotes the relaxation time, which represents the average time elapsed between two collisions;  $\mathbf{v}$  signifies the charge group velocity, and  $\delta$  is the delta function [41]. The indices  $\mathbf{k}$  and  $n$  refer to the crystal momentum and band index, respectively.

The velocity,  $\mathbf{v}$ , can be estimated from the band structure through the following relationship:

$$\vec{v}_{n,k} = \frac{1}{\hbar} \frac{\partial \varepsilon_{n,k}}{\partial \mathbf{k}} \quad (\text{eq.31})$$

Here,  $\hbar$  is the reduced Planck constant.

In the presence of a temperature gradient, the total electric field deviates from the expression in eq.24 due to the influence of the Seebeck effect. This change results in the adjusted formulation of eq. 24 as shown below:

$$\mathbf{J} = \sigma \mathbf{E} - \sigma \mathbf{S} \nabla T \quad (\text{eq.32})$$

Moreover, the heat flux ( $\mathbf{Q}$ ) generated from the temperature difference can be defined as follows:

$$\mathbf{Q} = T \mathbf{J}_s = \mathbf{S} T \mathbf{J} - \kappa \nabla T \quad (\text{eq.33})$$

Where  $\mathbf{J}_s$  represents the entropic flow. Eq. 32 and eq. 33 are recognized as Onsager relationships [42].

Using the Onsager equations, we can derive the Seebeck coefficient and electronic thermal conductivity from band structure calculations:

$$\mathbf{S} = \frac{e k_B}{N \Omega} \sigma^{-1} \int d\varepsilon - \left( \frac{\partial f_0}{\partial \varepsilon} \right) \left( \frac{\varepsilon - \mu}{k_B T} \right) \sum_{n,k} \tau_{n,k} \vec{v}_{n,k} \vec{v}_{n,k} \delta(\varepsilon - \varepsilon_{n,k}) \quad (\text{eq.34})$$

$$\kappa_e = \frac{k_B^2 T}{N \Omega} \sigma^{-1} \int d\varepsilon - \left( \frac{\partial f_0}{\partial \varepsilon} \right) \left( \frac{\varepsilon - \mu}{k_B T} \right)^2 \sum_{n,k} \tau_{n,k} \vec{v}_{n,k} \vec{v}_{n,k} \delta(\varepsilon - \varepsilon_{n,k}) - T \sigma \mathbf{S}^2 \quad (\text{eq.35})$$

Here,  $\mu$  denotes the chemical potential, and  $k_B$  stands for the Boltzmann constant.

Based on the above equations, we can define electrical conductivity, Seebeck coefficient and electronic thermal conductivity. The two unknown parameters are the lattice thermal conductivity and the value of the relaxation time. How to determine them is already discussed in Chapter 3.

### 1.3.5 Spin-Powered Thermoelectrics

With thermo-spin effects, energy transfer is controlled by the spin current instead of the conventional charging current. This fascinating phenomenon has revealed several novel thermo-spin conversion processes in magnetic materials and their complex interconnecting structures. Notably, notable phenomena such as the spin-dependent Seebeck-Peltier effect [43, 44] have come to the fore, offering enormous potential for revolutionizing spintronics and applications in thermal energy conversion.

The spin-dependent Seebeck-Peltier effect is a fascinating thermo-spin conversion phenomenon in ferromagnetic materials (FMMs). Its essence arises from the inequality of the Seebeck-Peltier coefficients between electrons with spin-up and spin-down orientation. To understand the transport phenomena within FMMs, a two-current model that treats spin-up and spin-down electrons as different entities is required [45]. The electron density of states (DOS) within FMMs depends on spin, leading to spin-sensitive variations in transport properties, including thermopower, electrical conductivity, and electronic thermal conductivity.

Using the two-current model, a comprehensive picture of the transport properties is created, which includes the entire electrical conductivity, the Seebeck coefficient and the electronic part of the thermal conductivity. This is achieved by combining the relevant information from the two spin channels, as given in the following equations [45]:

For electrical conductivity, the formula is as follows:

$$\sigma = \sigma \uparrow + \sigma \downarrow \quad (\text{eq.36})$$

Accounting for the complicated nature of the spin-Seebeck coefficient requires careful consideration of the up- and down-spin coefficients in relation to their respective electrical conductivities:

$$S = (\sigma \uparrow S \uparrow + \sigma \downarrow S \downarrow) / (\sigma \uparrow + \sigma \downarrow) \quad (\text{eq.37})$$

The electronic part of thermal conductivity can be expressed by the following simple summation:

$$\kappa_e = \kappa_e \uparrow + \kappa_e \downarrow \quad (\text{eq.38})$$

However, the lattice thermal component works independently of spin considerations. We use a separate model to calculate this aspect. Further details will be explained in a later discussion.

In today's applications, the Peltier and Seebeck effects are of central importance for power generation and cooling. Semiconductors are playing a pioneering role in exploiting these phenomena. At absolute zero temperature (0 K), these materials exhibit electrical properties similar to those of insulators. However, as temperature increases, electrons acquire significant ability to generate electric currents [46]. Essentially, semiconductors occupy an intermediate position, having electrical conductivity levels that span the spectrum between metals and insulators. A semiconductor is classified as intrinsic if it maintains a pure state, although achieving absolute purity is virtually unattainable. In such cases, charge carriers arise exclusively from crystal defects and thermal excitation [29]. Consequently, these semiconductors have minimal electrical conductivity and have limited application

in thermoelectric scenarios. To address this challenge, doping becomes a crucial technique by introducing impurities into the intrinsic semiconductor matrix. In addition, the semi-metallic property, which is vital for spintronics, can only be realized through the process of doping semiconductors.

Subsequently, our goal will shift to the classification of wide bandgap semiconductors, a special category that is the focus of our research and piques our great interest.

#### **1.4 Wide Bandgap Semiconductors : Host Base for Different Applications**

Wide-gap (WBG) semiconductors are a fascinating class of semiconductor materials characterized by their relatively large energy band gap ( $E_g > 2$  eV). Due to their exceptional properties, these materials have become essential components of today's electronic devices and energy applications. They feature adjustable electrical conductivity, controlled carrier concentration and high optical transparency, making them extremely versatile and desirable. Among the prominent wide bandgap semiconductors, transparent conductive oxides (TCOs) have been intensively studied since the 1950s [47]. Materials such as tin-doped indium oxide (ITO) and amorphous In-Ga-Zn-O (IGZO) are extensively used in display technologies and solar cells [48]. These TCOs exhibit a remarkable combination of transparency and conductivity, allowing their use as transparent electrodes, enabling efficient light transmission while enabling effective electrical conduction.

While much of the research and device integration efforts have been directed toward wide bandgap oxide materials, it is important to note that the scope of transparent semiconductors extends beyond oxides. Since the early 20<sup>th</sup> century, numerous classes of non-oxide semiconductors have been experimentally demonstrated to exhibit both transparency and conductivity. In this context, the following classes have acquired particular importance:

- Carbides with group IV anions [49] such as silicon carbide (SiC) and nitrides with group V anions [50] such as gallium nitride (GaN) have revolutionized power electronics due to their excellent electronic properties. SiC and GaN offer significant advantages, including high breakdown voltages, excellent thermal stability, and impressive electron mobilities. These properties make them ideal for power conversion and control applications, enabling more efficient energy management and improved performance in a range of electronic systems.
- Halides like  $\gamma$ -CuI with anions from group VII [51] and IV two-dimensional (2D) materials [52] like graphene have shown great promise in various optoelectronic devices. These materials have unique properties that can be exploited for applications such as advanced sensors, ultra-fast electronics, and next-generation photonic devices. Their exploration opens up exciting possibilities for the development of innovative and powerful optoelectronic technologies.

• Furthermore, extensive research efforts have been dedicated to group-based VI chalcogenide (Ch = S, Se, Te) semiconductors, encompassing various material compositions. This includes binary II-VI MCh semiconductors, such as ZnS [53], and CdS [54], as well as other binary  $M_xCh_y$  semiconductors (e.g.,  $SnS_2$ ,  $In_2S_3$ , where M represents a metal). Ternary chalcopyrite I-III- $Ch_2$  semiconductors, predominantly based -copper, have also received significant attention. Examples of this class include  $CuAlS_2$  [55], as well as other ternary compounds like  $\alpha$ - $BaCu_2S_2$  [56] and  $Cu_3TaS_4$  [57]. Moreover, multinary-layered mixed-anion compounds, such as  $LaCuOCh$  [58], have been investigated for their unique properties. Additionally, research has extended to 2D chalcogenides, both binary and ternary materials, including  $MoS_2$ , further broadening the scope of exploration in this field.

The particular chemistries and properties of WBG chalcogenide semiconductors distinguish them from other compounds, particularly their oxide counterparts, and offer specific advantages for optoelectronic applications and as *p*-type semiconductors. This distinction can be understood by considering factors such as the covalency of metal–VI (M–VI) bonds, which tend to increase as we move down group VI in the periodic table. This increase in covalency leads to larger orbital overlaps and lower hole effective masses. Heavier chalcogenides, with elements such as sulfur (S), selenium (Se), and tellurium (Te), possess higher-lying *p* orbitals (S-3*p*, Se-4*p*, Te-5*p*) that can hybridize with metal (M) orbitals, such as copper (Cu) 3*d* orbitals. This hybridization results in the formation of more disperse and delocalized valence bands compared to oxides [59]. Consequently, *p*-type chalcogenides exhibit the potential for achieving higher mobilities than their oxide counterparts. For example, Cu-based chalcogenides have demonstrated *p*-type mobilities of up to  $20 \text{ cm}^2 \text{ V}^{-1} \text{ s}^{-1}$  [56], while Cu-based wide bandgap oxides typically exhibit mobilities lower than  $1 \text{ cm}^2 \text{ V}^{-1} \text{ s}^{-1}$ .

Figure 8 provides a comprehensive network diagram architecture highlighting various WBG material classes, with particular emphasis on chalcogenides, which are clearly shown in a brown gradient. The classes are systematically organized and sorted according to their respective anion groups.

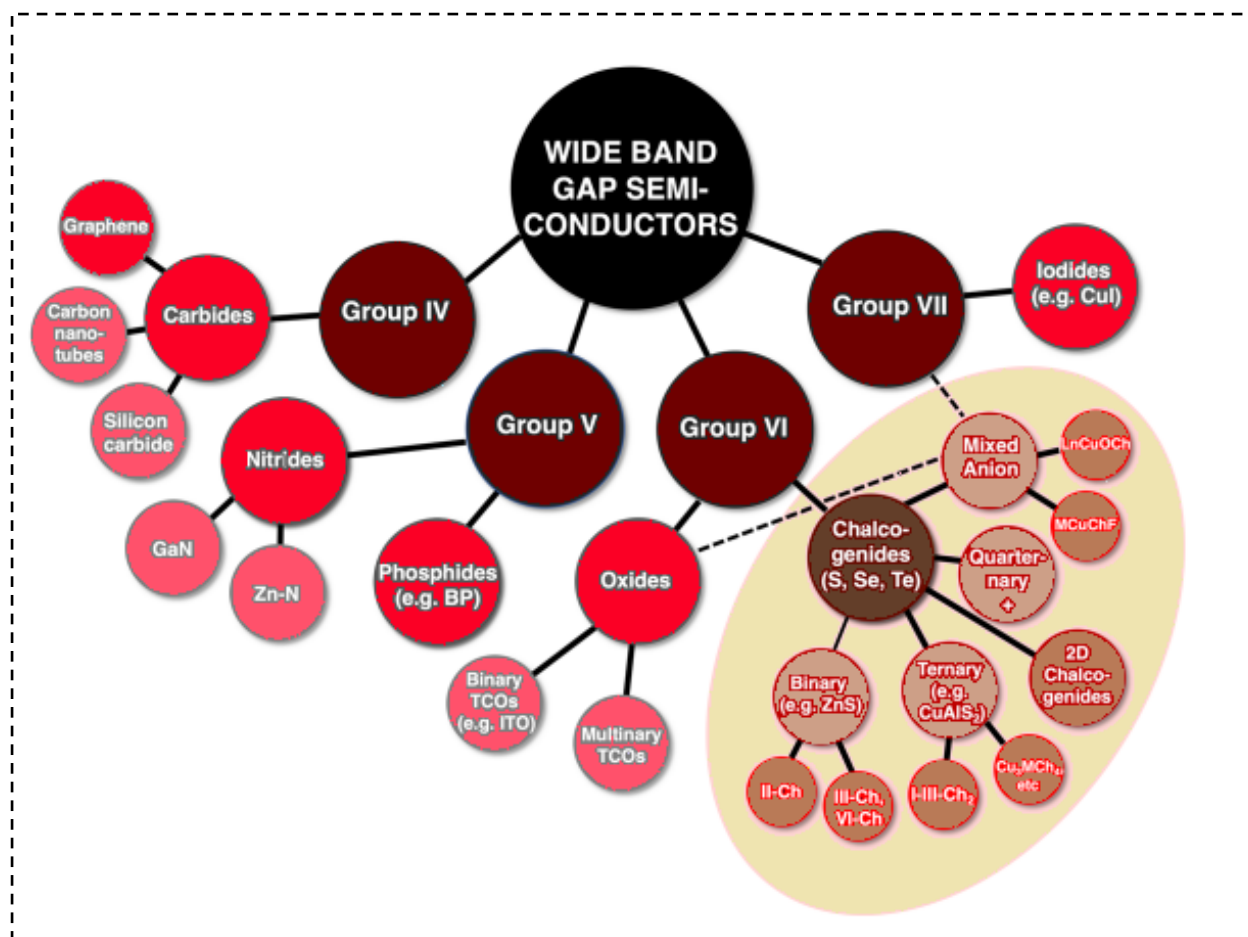


**Figure 8.** A network topology diagram illustrating the diverse material categories within WBG semiconductors. After Ref [60].

On the other hand, the simplest class of WBG chalcogenide semiconductors in terms of their respective cation groups consists of binary divalent metal chalcogenides designated  $M^{+2}Ch^{-2}$  ( $Ch = S, Se, Te$ ). Among these, the II-VI chalcogenide materials (referred to as II-Ch) are the most commonly used binary materials for electronic and optical applications. They typically contain cations of groups IIA and IIB, including elements such as Mg, Ca, Sr, Ba, Zn or Cd, among others.

The family of strontium chalcogenides  $SrX$  ( $X = S, Se, Te$ ) has recently attracted considerable attention in both experimental and theoretical studies due to their intriguing physical properties [61, 62, 63]. Their chemical composition leads to a number of fascinating properties, including the ability to tune their band gaps, exhibit high electrical conductivity, exhibit exceptional thermal stability, and display excellent optical properties spanning a wide spectrum of electromagnetic waves. In addition, strontium chalcogenides offer significant advantages compared to other materials, making them extremely attractive for scientific research and technological applications. Their abundance in nature, cost-effectiveness and environmental friendliness contribute to the growing interest in harnessing their potential for various advances in science and technology.

Furthermore, the versatile SrX chalcogenide family offers a compelling opportunity for extrinsic doping with both isostructural and non-isostructural binary systems. This opens up a wealth of possibilities that enable the exchange of cations and anions as well as the formation of ternary and/or quaternary compounds within the common crystal structure. A particular focus in research on SrX chalcogenides is the addition of extrinsic elements to the matrix in different concentrations [64–68]. This has become a fascinating area of research with the aim of modifying the inherent indirect nature of the electronic band gap and improving the optical absorption properties. By reducing the large band gap, these materials can be individually tailored to the specifications of optoelectronic devices. This trend was inspired by the successes observed in related technologies such as CIGS (copper indium gallium selenide) and CdTe (cadmium telluride), where the integration of extrinsic species to passivate intrinsic defects, the introduction of flat dopants, and the use of substitution doping (alloying) for band gap technology has led to impressive solar cell efficiencies of over 22% [69]. The integration of extrinsic species into the SrX chalcogenide family also offers exciting prospects for state-of-the-art spintronic devices and efficient spin caloritronic systems [70–72].

From revolutionizing and advancing various fields to enabling efficient energy storage and facilitating the right path to energy conservation, research into strontium-based chalcogenides promises to address critical challenges and promote innovation in multiple areas.

For this dissertation we chose strontium monochalcogenide (SrS). Recognizing the importance of a comprehensive review, the following section delves into an in-depth study of both pure and SrS-based dilute magnetic semiconductors (DMS). In particular, we investigate their properties and applications in three-dimensional (3D) bulk structures as well as two-dimensional (2D) monolayer structures to highlight their importance in the fields of spintronics, optoelectronics, and thermoelectronics.

#### **1.4.1 Bulk SrS Monochalcogenide**

Strontium sulfide (SrS), a promising member of the alkaline earth sulfide (AES) family, has proven to be a highly sought-after phosphor in various fields. Extensive research efforts have been devoted to exploring its applications in various fields, revealing its extraordinary potential. SrS has demonstrated superior performance and versatility in both bulk form and thin films, making it an attractive material for numerous practical applications. One of the main strengths of SrS lies in its luminescence properties, which have been extensively studied and exploited. Its indirect wide bandgap of 4.32 eV in bulk form [73] makes it an ideal choice for luminescence applications. This band gap allows SrS to create suitable luminescence centers and emit visible light without the undesirable effect of self-absorption [74]. This property ensures efficient light emission and improves the overall performance of SrS as a phosphor. The remarkable versatility of SrS phosphor is evident in its wide range of applications. In the field of optoelectronics, SrS is used in the development of efficient blue-emitting diodes (LEDs), displays and

radiation dosimetry. In addition, SrS is used in medical imaging to improve image quality and precision and enable more accurate diagnoses and treatments.

In addition, SrS has applications in various other areas, such as lighting technology, where it contributes to energy-efficient and long-lasting lighting solutions. SrS's versatility extends to quantum technologies and advanced sensing systems, where its luminescence properties play a critical role in the development of next-generation devices. SrS exhibits polymorphism, meaning it can crystallize in different phases depending on temperature and pressure conditions. At room temperature and ambient pressure, SrS adopts a rock salt crystal structure, also known as B1 structure (Figure 9(a)). Alternatively, it can be represented as a regular face-centered cubic (FCC) lattice arrangement of anions, with cations occupying the octahedral holes in the lattice. Both types of ions (strontium cations  $\text{Sr}^{2+}$  and sulfide anions  $\text{S}^{2-}$ ) have a coordination number of 6 with an overall compactness of 74%. This makes it an open structure and offers the possibility of introducing both light and heavy atoms. Figure 9(b) also presents a comprehensive representation of the Brillouin zone belonging to the FCC Bravais lattice. In this figure, the irreducible part of the Brillouin zone is highlighted and surrounded by prominent orange lines.

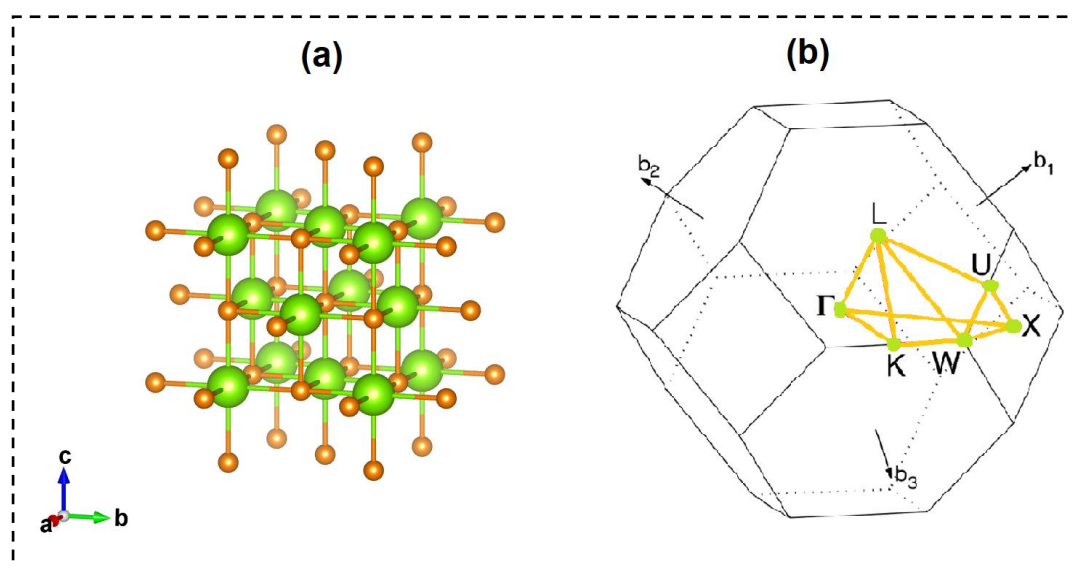


**Figure 9.** a) The Unit-cell of the semiconductor SrS, which adopts a rock-salt structure. Green spheres represent the Sr atoms, while orange spheres depict the S atoms. The image was generated using VESTA software [76]. b) The first Brillouin zone of an FCC crystal, with the irreducible wedge enclosed by orange lines. The special points within the Brillouin zone are identified by their common names, and the reciprocal base vectors are labeled as  $b_1$ ,  $b_2$ , and  $b_3$ . After Ref [77].

In the B1 structure, each strontium cation is surrounded by six sulfide anions and vice versa, resulting in six-fold coordination. The FCC lattice ensures a symmetrical and densely packed structure and gives the crystal stability. This arrangement of atoms enables efficient charge transport and favorable electronic properties and contributes to the usefulness of SrS as a semiconductor material. The



six-fold coordination in the rock salt structure ensures the optimal balance between electrostatic interactions and the packing efficiency of the atoms within the crystal lattice, contributing to optimized electrical conductivity. This coordination arrangement influences the mechanical, optical, electronic and thermoelectric properties of the material and plays a crucial role in determining its behavior in various applications.

However, fascinating phenomena occur in SrS under high pressures. Syassen et al. conducted X-ray diffraction experiments and discovered a pressure-induced structural phase transition in SrS at around 18 GPa [73]. This transition involves a transformation from the NaCl-type structure (B1) with six-fold coordination to the CsCl-type structure (B2) with eight-fold coordination.

Furthermore, it was predicted that after the B1-B2 phase transition, the non-metallic nature of SrS would give way to metallic behavior at even higher pressures. This transition from a non-metallic to a metallic state is attributed to a mechanism known as bandgap overlap [75].

#### 1.4.2 Tuning the Properties of SrS Monochalcogenide

The properties of bulk SrS can be fine-tuned and optimized using a variety of methods, allowing properties to be tailored to specific applications. Doping [64-68], co-doping [78, 79], alloying [80], defect engineering [81], dimensionality reduction [82, 83] and external stimuli [84] are powerful techniques for manipulating and improving the properties of these binary connection.

- **Doping:** involves the introduction of foreign atoms into the SrS lattice to change its properties. By selectively adding dopants, we can change the electronic and optical properties of SrS. Doping can influence the band gap, carrier concentration and conductivity, enabling the optimization of SrS for applications in optoelectronics, photovoltaics, thermoelectrics and sensing.
- **Co-doping:** refers to the simultaneous introduction of two or more dopants into SrS. This technique allows for more precise control of material properties by combining the effects of multiple dopants.
- **Alloying:** Solid solutions are created by alloying SrS with other materials, which expands the range of properties that can be achieved. By incorporating different elements, researchers can change the lattice structure, band gap and physical properties of SrS.
- **Defect engineering:** involves the targeted manipulation of defects within the SrS crystal lattice. By controlling the concentration and type of defects, researchers can fine-tune the electrical, optical and mechanical properties of SrS. Defect engineering plays a crucial role in improving the thermoelectric efficiency, luminescence properties and mechanical strength of SrS.

- **Dimensional reduction:** refers to the reduction of bulk dimensionality of SrS into low dimensional structures such as 2D monolayers and their derivatives, i.e. nanotubes (1D), nanoribbons (1D) and nanoflakes (0D). At low dimension, SrS exhibits unique properties due to quantum confinement effects and an increased surface area to volume ratio. Reducing the dimensionality of SrS provides improved electronic and optical properties, improved charge transport, and increased surface reactivity, making it valuable for applications in nanoelectronics, catalysis, and energy storage.
- **External stimuli:** such as temperature, pressure and electric fields can be used to modify the properties of SrS. By exposing SrS to certain environmental conditions, its physical properties can be changed. External stimuli also enable exploration of SrS behavior under different conditions.

Although a lot of work has been done using these methods, especially in the area of doping and alloying, there is still a need for a systematic study of this compound and its derivatives using different approaches. In this dissertation, we chose doping, co-doping and dimensionality reduction as the primary techniques to tune the properties of rock salt SrS. These techniques have proven effective in improving material performance in optoelectronics, spintronics, spin caloritronics and nanoelectronics, which are indeed the future technological trends. The basic building blocks of spintronics, dilute magnetic semiconductors (DMS), were selected by doping with transition metals and studied in both 3D bulk configurations and 2D monolayers. Alkaline metals were also selected as co-dopants due to their three-dimensional volume structure.

Figure 10 provides a representation of the extrinsic elements examined in this dissertation. The binary host elements are marked in green, the dopant elements in red, and the elements that form substitutional co-dopants are shown in blue. Certain elements such as Sr, S and Fe are considered for both 3D and 2D doping scenarios (in yellow).

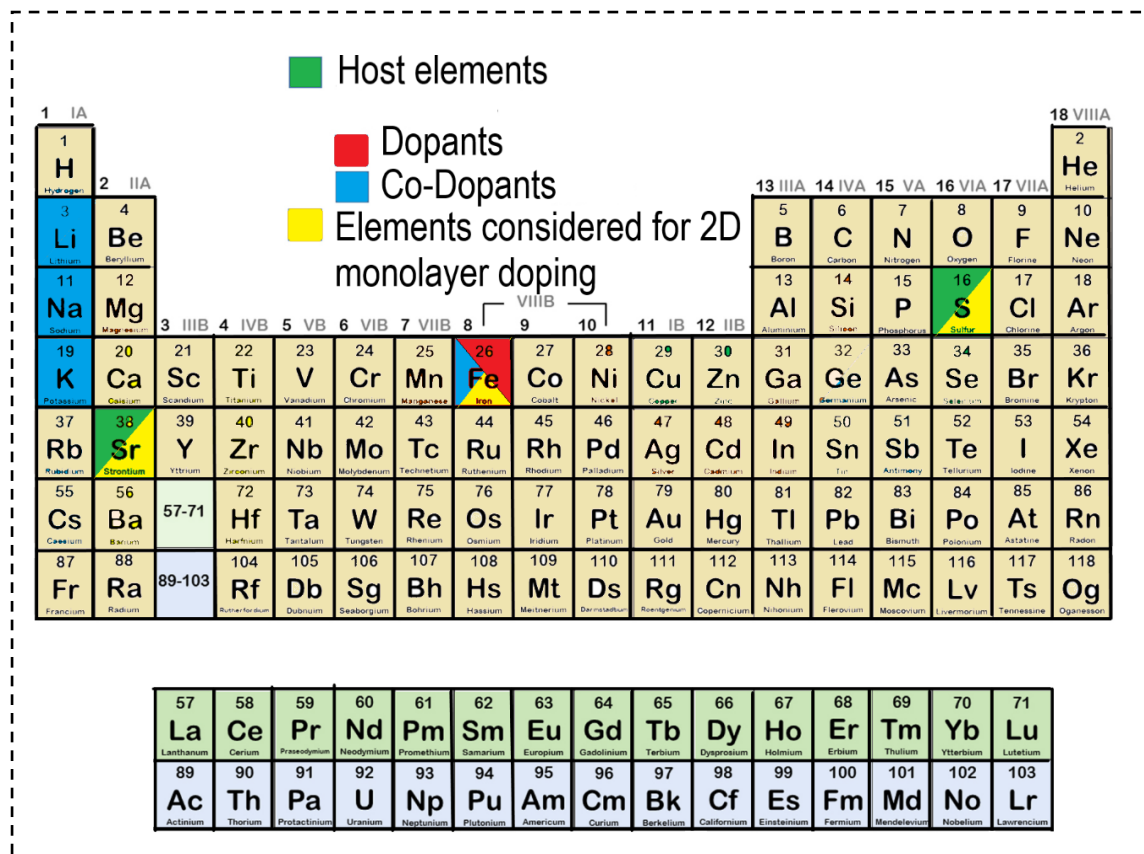


**Figure 10.** Visualizing the covered elements in this dissertation within the periodic table.

Moving forward, we will continue our discussion about DMS and alkali-substituted elements, highlighting their specific and exceptional properties as well as their applications.

#### 1.4.2.1 Diluted Magnetic Semiconductors (DMSs)

Magnetic semiconductors are unique materials with both intrinsic semiconductor properties and magnetic properties. These substances provide a rich platform for theoretical and experimental investigations, allowing researchers to explore core ideas in condensed matter physics. The focus of magnetic semiconductor research is the complex interplay between semiconductor band electrons, such as charge carriers or impurity states, and the magnetic moments of the constituent ions. This unique interaction leads to a variety of electronic phenomena, including giant magnetoresistance, robust magneto-optical rotation, magnetically driven semiconductor-metal transitions, and fascinating magnetic polaron effects, among others [85]. These phenomena are missing from conventional semiconductors, making magnetic semiconductors a fascinating subject of research.

While rare earth chalcogenide compounds, particularly those containing europium, have attracted considerable attention, the initial fascination with these materials stemmed from the discovery of EuO, a structurally simple semiconductor ferromagnet. At that time, EuO was only the second known semiconductor ferromagnet [86]. The ferromagnetic behavior of these compounds was explained by the

indirect coupling between local moments on the europium ions and the conduction band states. Nevertheless, the reported Curie temperature ( $T_C$ ) of about 170 K, which is the temperature at which the metal loses its spontaneous magnetization - that is, the temperature at which the ferromagnetic phase changes to the paramagnetic phase - remains well below room temperature when it is endowed with Gd. This represents a significant obstacle in the search for improvements in this regard.

Subsequent studies have focused their attention primarily on dilute magnetic semiconductors (DMS), which are currently among the most extensively studied systems. These DMSs are composed of alloys in which transition metal ions, including  $\text{Cr}^{2+}$ ,  $\text{Mn}^{2+}$ ,  $\text{Fe}^{2+}$ ,  $\text{Co}^{2+}$ , etc., are randomly incorporated in place of specific group II elements in II-VI semiconductor compounds, as explained in Figure 11.

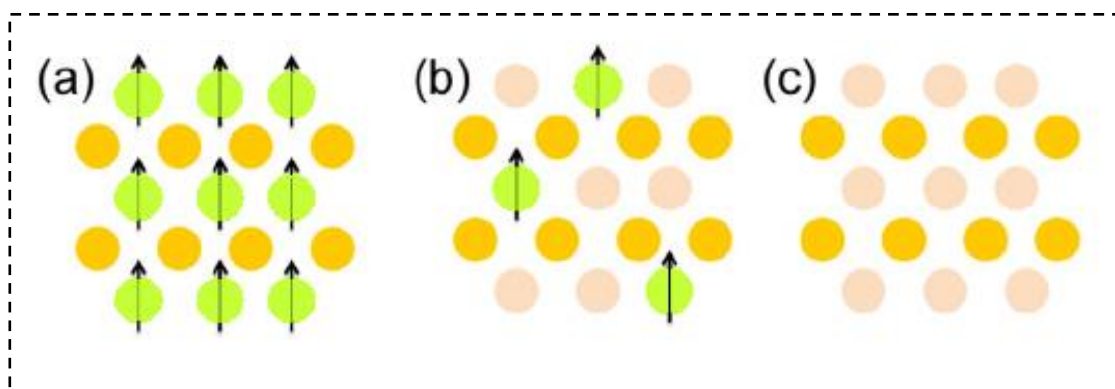


**Figure 11.** Schematic illustration of different types of semiconductors based on their magnetic properties: (a) Magnetic semiconductor, (b) Diluted magnetic semiconductor, and (c) Non-magnetic semiconductor. Green circles represent the magnetic ion. After Ref [87].

On the semiconductor side, the multicomponent nature of DMS allows continuous tuning of structural and electronic parameters by adjusting the composition. On the magnetic side, they exhibit phenomena such as spin-glass transitions, antiferromagnetic short-range ordering, and anisotropic exchange interactions, making them fascinating random magnetic systems. Beyond their scientific appeal, DMSs hold promise for various technological applications. The ability to grow DMS in multilayer form with atomic precision using methods such as molecular beam epitaxy (MBE) opens opportunities for the integration of these materials into II-VI based integrated semiconductor structures [88]. This not only promotes their scientific research, but also enables practical advances in areas such as optoelectronics, spintronics, magnetoelectronics and spin caloritronics.

The main goal of doping conventional semiconductors with magnetic ions is to make them ferromagnetic at room temperature without changing their semiconductor properties, and thus make them usable in spintronics. Although almost all materials have some degree of magnetism, only three are capable of maintaining permanent magnetization with  $T_C$  above 600 K: Fe, Ni and Co. These materials have high magnetic susceptibility, about 200 for Fe, and are called ferromagnetic. On a

microscopic scale, they consist of tiny regions in which each atom exhibits the characteristics of magnetic dipoles that are naturally oriented in a uniform direction. When exposed to an external magnetic field, these areas align with the field, resulting in significant overall magnetization of the material. Furthermore, this magnetization persists even when the external excitation is removed, a phenomenon known as hysteresis [89].

In fact, these materials represent typical *ferromagnetic* metals, but with a unique twist as they manifest as new semi-metallic ferromagnetic materials (HMF). The prediction of such materials dates back to 1983, when de Groot et al. [90] conducted a theoretical study on the band structure of the half-Heusler alloy NiMnSb. This alloy exhibited an intriguing property at the Fermi level ( $E_F$ ), where it had a zero electronic density of states for minority spins and a nonzero density of states for majority spins. Consequently, it conducts electricity for one spin direction (up), while for the other spin direction (down), it behaves like a semiconductor or insulator. This fascinating behavior allows achieving a remarkable 100% spin polarization, as indicated by the following relationship:

$$P = \frac{N_{EF}^{\uparrow} + N_{EF}^{\downarrow}}{N_{EF}^{\uparrow} - N_{EF}^{\downarrow}} \quad (\text{eq.39})$$

Where:  $N_{EF}^{\uparrow}$  and  $N_{EF}^{\downarrow}$  are the values of electronic density of states at the  $E_F$  for spin-up and spin-down electrons, respectively.

The difference in density of states between a non-magnetic metal, magnetic metal, non-magnetic semiconductor, and half-metal is schematically depicted in Figure 12.

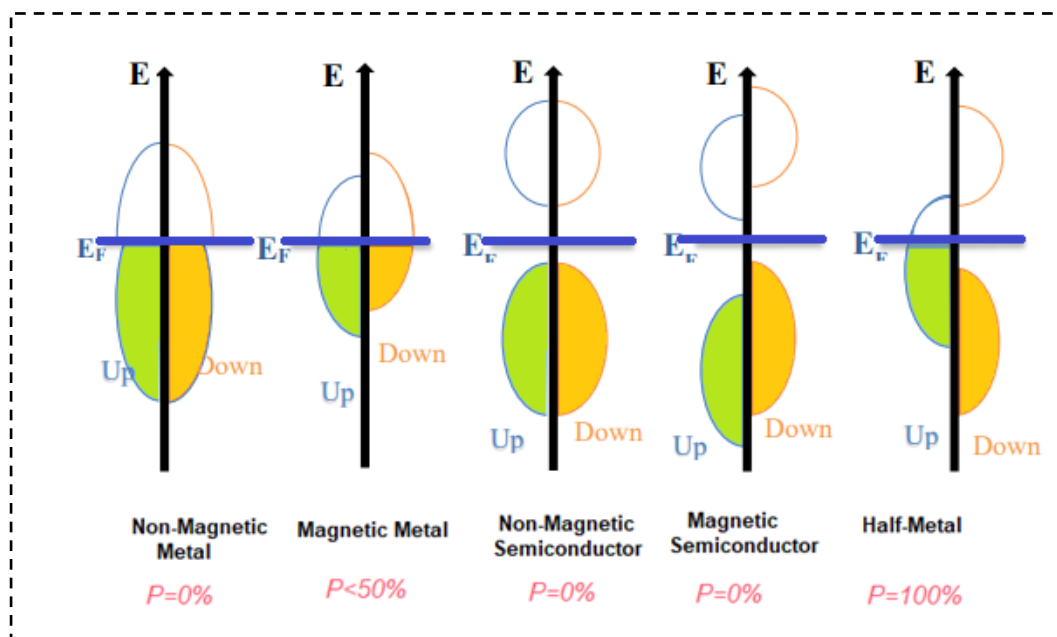


**Figure 12.** Schematic representation of the difference in density of states between a non-magnetic metal, magnetic metal, non-magnetic semiconductor, and half-metal. After Ref [91].

In certain DMS, interactions between electrons tend to align adjacent atomic magnetic dipoles antiparallel, resulting in two sublattices with opposite magnetization. The French physicist Louis Néel developed the first relevant model of this “*anti-ferromagnetism*” in 1936 [92]. In a “*ferrimagnetic*” material, neighboring atoms, due to their different natures, form magnetic dipoles with opposite orientations but different amplitudes (e.g. an  $\text{Fe}^{2+}$  ion and an  $\text{Fe}^{3+}$  ion), resulting in incomplete compensation. The spontaneous magnetization of such materials is non-zero below their Curie temperature [92]. Another visualization can be found in Figure 13.

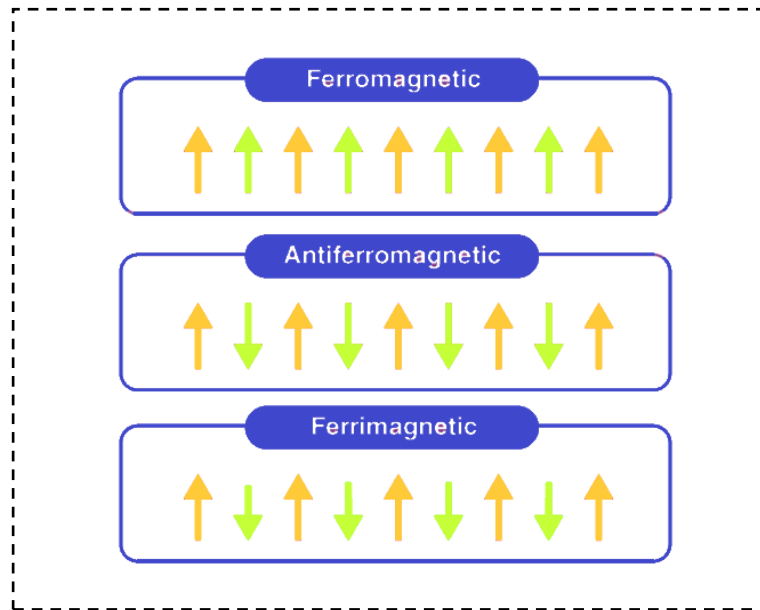


**Figure 13.** Alignment of the magnetic spin of each individual iron atom.

It is generally accepted that the presence of partially filled *d* or *f* bands is a prerequisite for a material to exhibit magnetism. These partially filled bands lead to complex exchange interactions that are crucial for the emergence of magnetic order. The exchange interaction, a cornerstone of quantum mechanics, plays a crucial role in determining the long-range magnetic order in ferromagnets [93]. However, its influence extends beyond ferromagnets and profoundly affects ferrimagnets and antiferromagnets, where neighboring magnetic ions are subjected to forces that align their individual moments into parallel or antiparallel configurations. This profound interaction results from the delicate interplay of Coulomb forces and the Pauli exclusion principle. Their effects can be effectively captured and are given by the Hamiltonian of the Heisenberg exchange as follows:

$$\mathbf{H}_{ex} = -2J \sum_{i \neq j} \mathbf{S}_i \cdot \mathbf{S}_j \quad (\text{eq.40})$$

In this context,  $\mathbf{S}_i$  represents the spin operator of the  $i^{\text{th}}$  atom, and the parameter  $J$  is commonly referred to as the exchange integral. The above equation may be expressed as follows in the continuum model,

which takes into account the exchange interaction only between nearest neighbors inside the cubic lattice:

$$E_{ex} = A_{ex} \int (\nabla \mathbf{m})^2 dV \quad (\text{eq.41})$$

Where,  $\mathbf{m} = \mathbf{M}/M_s$  is the continuous vector of reduced magnetization. The parameter  $A_{ex}$ , referred to as the exchange stiffness constant for the cubic lattice of spins, assuming the following form:

$$A_{ex} = \frac{2JS^2}{a} \quad (\text{eq.42})$$

Where  $a$  is the lattice constant.

The previously mentioned interaction is referred to as *direct exchange interaction*, which encompasses the interaction of electrons between magnetic atoms and their closest neighbors. However, this exchange can also take place *indirectly*, linking magnetic moments across relatively greater distances. There are several noteworthy types of indirect exchange mechanisms, such as the *Ruderman–Kittel–Kasuya–Yosida (RKKY)* exchange, which involves the coupling of metallic ions through itinerant electrons; *super-exchange*, occurring through various nonmagnetic ions mediating the exchange; and *anisotropic exchange* interaction (also known as *Dzyaloshinskii-Moriya* interaction) [94], where the spin-orbit interaction exerts significant influence and often results in a slight canting of neighboring spins. Additionally, there is the *double exchange* that arises between ions in different oxidation states.

Other important interactions are the *s-d* and *p-d* exchange interactions, which refer to the interaction between the conduction and the valence bands, respectively, with the *d* electron states of the magnetic atom in a material. This interaction is crucial in confirming and reinforcing the ferromagnetic order in DMSs.

The *s-d* and *p-d* exchange interactions in DMSs, arises from intentional doping of magnetic impurities (TM ions) into a non-magnetic semiconductor matrix. The *s* and *p* electrons of the host atoms interact with the *d* electrons of the magnetic impurities, creating local magnetic moments in the material.

The Heisenberg exchange Hamiltonian in this case can be written as follow:

$$H_{ex} = \sum_i J(\mathbf{r} - \mathbf{R}_i) \cdot \mathbf{S}_i \cdot \mathbf{s} \quad (\text{eq.43})$$

Where  $\mathbf{S}_i$  and  $\mathbf{s}$  represent the spin of the localized electrons and the delocalized carriers at  $R_i$  and  $r$  belonging to the magnetic ions and the semiconductor matrix, respectively.

With the mean field approximation [95], the Hamiltonian exchange can be expressed in two forms:

For the symmetry  $s$  electrons in the conduction band and those localized on the magnetic ion:

$$H_{ex} = -xN_0\alpha < S > s \quad (\text{eq.44})$$

For the symmetry  $p$  electrons in the valence band and those localized on the magnetic ion:

$$H_{ex} = -xN_0\beta < S > s \quad (\text{eq.45})$$

$N_0\alpha$  and  $N_0\beta$  are the exchange constants corresponding to the  $s$ - $d$  and  $p$ - $d$  exchange interactions, respectively. In the case of a positive exchange constant, the interaction between the spins is ferromagnetic else, it is antiferromagnetic.

During the past ten years, these DMSs have been extensively studied, but there have been limited experimental investigations conducted, in contrast to the existing theoretical works available in the literature. Some notable examples include  $\text{Ca}_{0.75}\text{Cr}_{0.25}\text{S}$  and  $\text{Ca}_{0.75}\text{V}_{0.25}\text{Se}$  [96],  $\text{Zn}_{1-x}\text{Cr}_x\text{S}$  and  $\text{Cd}_{1-x}\text{Cr}_x\text{S}$  [97],  $\text{Mg}_{1-x}\text{V}_x\text{Se}$  [98],  $\text{Be}_{0.75}\text{Mn}_{0.25}\text{X}$  ( $X = \text{S}, \text{Se}, \text{Te}$ ) [99], and  $\text{Sr}_{0.75}\text{TM}_{0.25}\text{S}$  (TM is 3d transition metals) [100]. More remarkably, Fe-based DMSs have garnered considerable attention as ferromagnetic semiconductors because of their high Curie temperatures, low power consumption, and suitability for high-speed spin devices [101]. Researchers have been inspired by these intriguing characteristics and have dedicated efforts to unraveling the ferromagnetic mechanism in Fe-based DMSs. Several notable studies have contributed to our understanding of these materials. We mention, Fe-doped ZnO by Zhang et al. [102], Fe-doped CdS by Bourouis et al. [103], Fe-doped CdSe by Singh et al. [104], Fe-doped ZnTe by Mahmood et al. [105], Fe-doped ZnSe by Li et al. [106], and Fe-based CaS by Amari et al. [107]. The results of these studies showed that the materials exhibited their highest strength when incorporated with the Fe impurity, exhibited ferromagnetic behavior at room temperature, and allowed tuning of mechanical, magnetic, and optical properties through different Fe dopant concentrations.

The co-doping process has shown even greater improvement in such DMS, as it has been demonstrated that the addition of other impurities besides the Fe atoms not only improves the physical properties but also introduces new properties different from those obtained by single doping can be achieved. An example of this is the addition of Fe alongside Mn in CdTe [108], which not only improves the magneto-optical properties but also changes the DMS type from  $n$ -type to  $p$ -type. Another example is the co-doping of CdS with (Cu, Fe) [109], which results in a transformation of its character from metallic to semi-metallic in nature with an increase in magnetic moment value, making it useful for spintronic applications. Furthermore, unlike other transition metals such as Cr and Co, the addition of Fe to  $\text{Cd}_x\text{Hg}_{1-x}\text{Se}$  [110] results in a significant change in thermoelectric properties, which could be manipulated by adjusting the composition.



On the other hand, the presence of TM clustering, the complexity of controlling stoichiometry, and the challenges associated with d-d transitions make the use of both TM- co-dopants difficult [111]. Nowadays, co-doping with other substituents such as non-magnetic elements, called d0, has emerged as a viable approach to improve and tailor the properties of DMS materials and offers exciting opportunities for advancements in various technological applications. Further discussion of this type of material can be found in the following section.

### 1.4.2.2 $d^0$ vs. Conventional Magnetism

$d^0$  magnets include a category of materials that lack magnetic ions with  $d$  or  $f$  orbitals and should theoretically not exhibit ferromagnetic properties. However, these materials often exhibit ferromagnetism with a  $T_c$  of over 300 K [112]. In this fascinating category of materials, the first materials discovered were doped non-magnetic oxides, thin films of  $\text{HfO}_2$ , non-stoichiometric  $\text{CaB}_6$  and irradiated graphite, with observation revealing that these materials exhibit small ferromagnetic moments and possess Curie points well above room temperature despite the absence magnetic atoms [113]. The magnetism in these materials has been attributed to the interaction between localized magnetic moments and traveling charge carriers. Even though  $d^0$  elements do not have partially filled  $d$  or  $f$  electron shells, they can still exhibit ferromagnetism due to the double exchange mechanism discussed previously.

In some cases, the formation of resonant donor levels in  $d^0$  ferromagnets can also contribute to their magnetic properties. These resonant donor values can be controlled by varying the composition of the solid solution, allowing tuning of the magnetic behavior [114]. From now on, a significant part of the work was devoted to the study of ferromagnetism, which arises from the incorporation of non-magnetic elements into wide bandgap semiconductors [115–117]. This increase in interest can be attributed to the remarkable effects of metal-free magnetism, which offers the potential for the further development of lightweight, biocompatible and environmentally friendly magnetic materials [118]. A widely discussed scenario for  $d^0$ -based DMSs involves magnetic polarization of valence states by doping with  $sp$ -type impurities. To maximize HM ferromagnetism and improve structural and optoelectronic properties, for example, to increase luminance, facilitate charge injection, and achieve better energy band alignment, the most promising approach is to selectively dope the cation sites with the  $s$ -type, also known as  $p^0$  elements from the first row of the periodic table, such as  $\text{Li}^+$ ,  $\text{Na}^+$  and  $\text{K}^+$  [119].

The alkali metals  $\text{Li}^+$ ,  $\text{Na}^+$  and  $\text{K}^+$  have one valence electron and are therefore electron donors when incorporated into a host material. This means that they provide the host material with additional charge carriers (electrons), effectively increasing its electrical conductivity. Doping with alkali metals can improve the electrical and thermal properties of the material, making it more suitable for various electronic and energy applications. In addition to changing the electrical conductivity, doping with alkali metals can also influence the optical properties of the material. For example, there may be changes in

the bandgap, allowing the material to absorb and emit light of different wavelengths. This property is crucial for the development of optoelectronic devices such as LEDs and solar cells. The monovalent elements  $\text{Li}^+$ ,  $\text{Na}^+$  and  $\text{K}^+$  are also in close proximity to the position of Sr in the periodic table. Due to their similar atomic size, they are well suited for incorporation into the rock-salt SrS lattice, which represents a high probability for co-doping with transition metals (TM) and has a significant influence on its properties. Surprisingly, investigations into alkali doping at the Sr site are relatively new. In an experimental study by Chang et al.  $\text{Na}^+$ -doped SrS phosphor has been shown to produce high-quality solid-state light-emitting diodes (SS-LEDs) with improved emission intensity over the wavelength range of 430–700 nm [120]. Furthermore, the ferromagnetism in the compound  $(\text{Sr}_{0.75}\text{K}_{0.25})_2\text{MnGe}_2\text{S}_6\text{O}$  was increased by replacing  $\text{Sr}^{2+}$  with  $\text{K}^+$ , as theoretically predicted [121], resulting in a  $T_c$  of 300 K. Studies by Yang et al. [122] proved the effectiveness of cation doping in  $\text{Li}^+$ -ion and  $\text{Na}^+$ -ion batteries and showed promising results for large-scale electrical energy storage.

While extensive experimental and theoretical studies have been carried out on the co-doping of alkali elements with transition metals in other matrices [123–126], the study of the SrS matrix provided with both co-dopings is completely missing. Therefore, it is crucial to study in depth the co-doping process within these elements and its effects on various SrS properties.

After explaining the basic methods used in this dissertation to tune SrS bulk properties, we now provide a brief summary of dimensionality reduction, focusing on the 2D monolayer configuration.

## 1.5 Low-Dimensional Materials

Changing material properties on the way to the nanoscale is a field of intensive research. With its focus on materials and structures ranging in size from 1 to 100 nm, nanotechnology opens up a world of possibilities [127]. While the term “nanomaterial” may only conjure up thoughts of size, it encompasses much more. Nanotechnology deals with the manipulation of structures at the atomic and molecular levels and the development of materials that are precisely tailored to specific applications [128]. The advanced application of nanomaterials highlights that dimensions and shapes are critical aspects that have a profound impact on performance [129]. Nanomaterials are categorized based on their dimensions: zero-dimensional (0D), one-dimensional (1D), two-dimensional (2D), and three-dimensional (3D) nanostructured materials (see Figure 14) [130]. This emphasis on precise design and careful structuring is motivated by the goal of overcoming challenges in various areas. Whether in wastewater treatment, energy production, conversion or storage, the targeted manipulation of these materials holds the potential to bring about transformative advances.

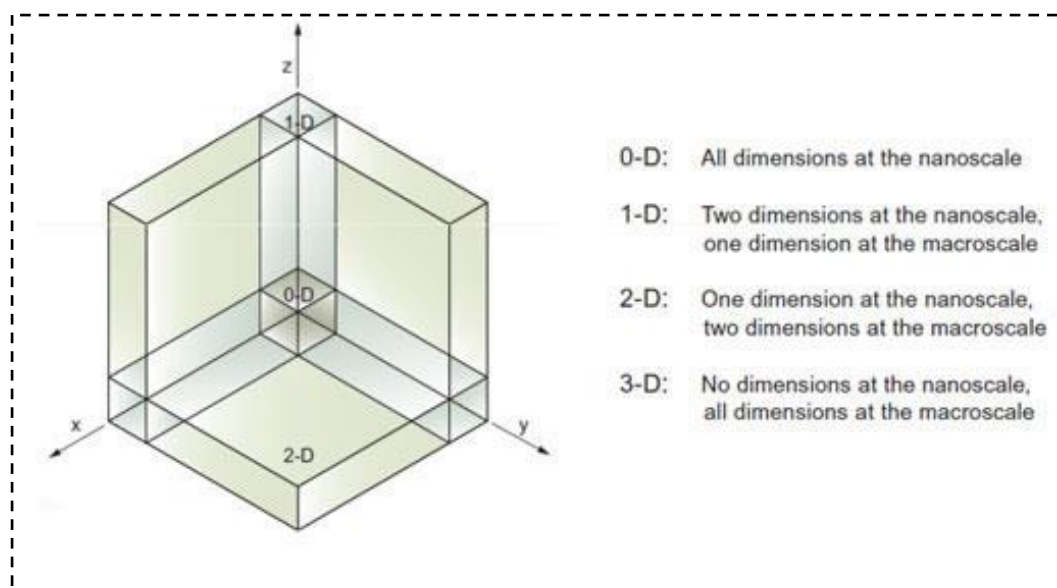


**Figure 14.** Taxonomy of nanoscale dimensions. (Source: Tallinn University of Technology).

Among the diverse families of nanomaterials, 2D nanomaterials have emerged as a particularly fascinating class characterized by a variety of fascinating properties. In short, this category is discussed in the following section.

### 1.5.1 Two-Dimensional (2D) Materials

2D materials include a specific class of substances in which one dimension operates at the nanoscale, while the remaining two dimensions exceed this threshold. Over the past 16 years, intensive study of these materials has increased significantly, particularly those composed of layered compounds characterized by robust intralayer bonds and sensitive van der Waals forces between layers. As the electronics field experiences rapid growth mainly due to advances in silicon technology [131], scientists have been working hard to develop new materials that could revolutionize the technology of electronic devices while solving the complex problems of heat dissipation.

In 2004, A.K. Geim and K.S. Novoselov of the University of Manchester reached a significant milestone with the successful isolation of graphene, the groundbreaking 2D material [132]. Their groundbreaking efforts earned them the Nobel Prize in 2010. Graphene, a crystalline carbon allotrope, has a zero bandgap and a two-dimensional atomic structure with a hexagonal arrangement at the atomic scale. In this structure, each carbon atom forms four bonds: three  $\sigma$  bonds ( $sp^2$  hybridized) with its neighboring atoms and one  $\pi$  bond oriented perpendicular to the plane. This fundamental structural unit serves as the basis for other carbon allotropes, including graphite, fullerene, nanotubes, and nanocones, making graphene the precursor to all carbon-based nanomaterials.

The discovery of graphene has sparked an explosion of research in the field and opened a new chapter in the study of other 2D materials. Scientists have created monolayers, bilayers, and materials with some layers that resemble graphene [133]. Along with other inventions, they have also created nanoribbons [134], single-walled and multi-walled nanotubes [135] and more. The unique ability of these materials to adjust their energy bandgap has enabled their use in a wide range of fields including electronics, optoelectronics, semiconductors, batteries, composite industries, solar energy, communications and more.

The 2D materials space experienced even greater expansion with the introduction of  $Ti_3C_2T_x$ , a notable member of the MXenes family. This groundbreaking development took place at Drexel University in 2011. Subsequently, similar to graphene, silicene formed as the first member of the MXenes group in 2012 [136]. This was the beginning of a series of discoveries that revealed various MXenes materials, which now include a diverse range of over 30 different 2D types. A quick examination of the dimensional database confirms the significant increase in research into 2D materials in recent years (Figure 15).

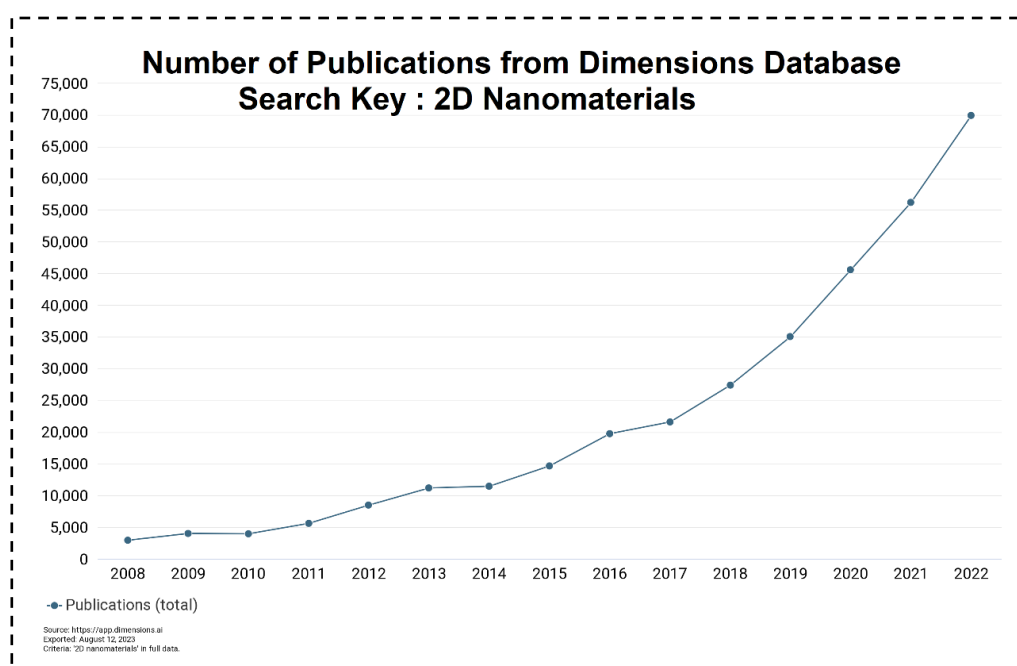


**Figure 15.** Annual publications on 2D nanomaterials over the past decade.

The important surface-to-volume ratio of 2D materials as well as the exceptional occurrence of electron confinement enable precise modification of properties. High thermal conductivity, remarkable charge carrier mobility even at ambient temperature, and atomically thin properties are all found in 2D materials, which also enable simplified processing techniques. Due to their exceptional mobility, 2D materials are more sensitive to conductivity. This is because surface-generated supports respond dynamically to photoeffects. This intriguing property positions them at the forefront of high-gain

photodetector applications, spanning areas such as optical communications, optoelectronic devices, and biomedical imaging.

Furthermore, their wide electromagnetic absorption range, ranging from infrared to ultraviolet [137] makes 2D materials central components in high-performance photonics and optics. Their ability to maintain low absorption (<10%) yet exhibit high conductivity makes them invaluable for transparent electronic applications, including solar cells and liquid crystal devices [138]. Beyond their remarkable electrical and photonic properties, 2D materials exhibit outstanding mechanical properties. These materials are characterized by their remarkable flexibility and have a breaking strength 200 times higher than that of steel [139], making them crucial for reinforcing polymers in composites.

## 1.5.2 Synthesis Approaches for 2D Materials

Two approaches are used in the synthesis of 2D materials: the *top-down* and the *bottom-up* approach [140]. A comprehensive overview of various *top-down* and *bottom-up* approaches is shown in Figure 16. In the coming discussion, we will briefly examine these approaches and highlight their specific features.

### 1.5.2.1 Top-Down Approach

In the top-down approach, the process begins with bulk materials, layers of which are carefully stripped or peeled away using various techniques to obtain atomically thin 2D layers. A notable example of this approach is peeling off layers of graphite using adhesive tape, creating the ultra-thin monoatomic layer called graphene, which is made up of graphitic carbon atoms. In addition to the methods shown in Figure 16, the transition from 3D bulk structures to 2D structures is achieved through a variety of other strategies. These include, in particular, liquid phase peeling [141], ion intercalation/peeling [142] and physicochemical peeling [143]. Among these, chemical exfoliation stands out as a widely preferred top-down approach to producing materials with small dimensions. Several other top-down techniques are used, including mechanical milling [144] and lithography, including techniques such as ion beam lithography, electron beam lithography and photolithography [145]. In parallel to these methods, approaches such as sputtering [146], the arc discharge process [147] and laser ablation [148] are used.

### 1.5.2.2 Bottom-up Approach

In the bottom-up approach, atoms are cleverly joined together, similar to sewing, to create atomically thin 2D material structures. Numerous bottom-up techniques are used, including molecular beam epitaxy, chemical vapor deposition (CVD), physical vapor deposition (PVD), hydrothermal and solvothermal methods, and template-based methods [149]. Bottom-up approaches are known for their

ability to produce high-quality 2D structures and find application across a spectrum of 2D materials. In particular, they play an important role in the design of two-dimensional metal-organic frameworks (MOFs), coordination polymers (CPs), and covalent organic frameworks (COFs) [150].

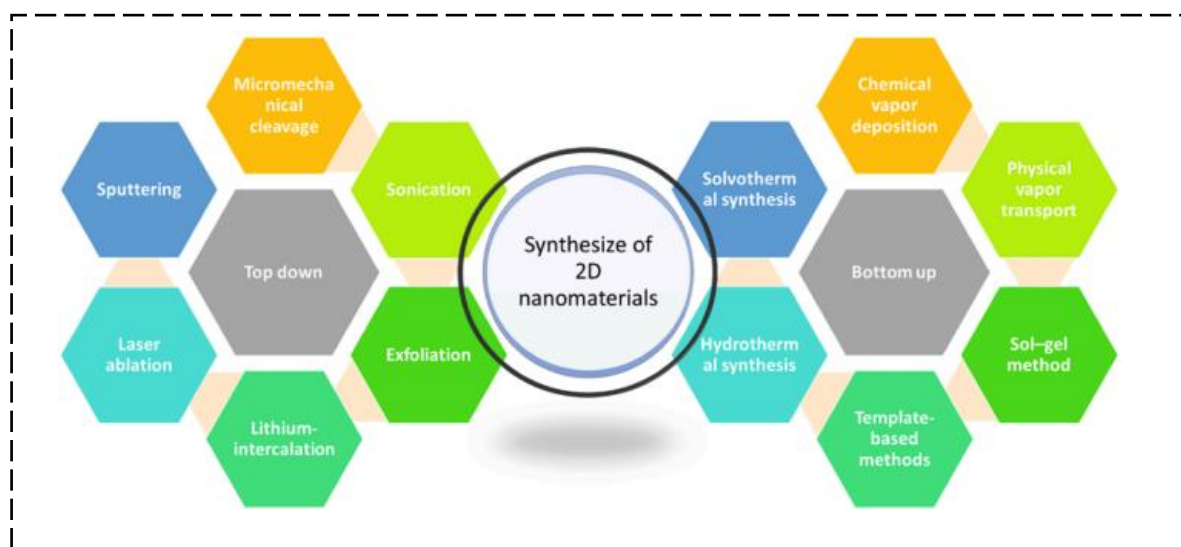


**Figure 16.** Widely utilized top-down and bottom-up approaches to synthesize the 2D materials. After Ref [151].

### 1.5.3 Categorization of 2D Materials

Due to their finely tunable energy bandgap and remarkable intrinsic properties, 2D materials have become key players in a spectrum of innovative fields, including electronics, optoelectronics, semiconductors, spintronics, spin caloritronics, batteries, composite industries, solar energy utilization and communication systems, and a range of other applications [152]. Numerous subclasses within this material category, such as silicene [153], germanene [154], hexagonal boron nitride (*h*-BN) [155], stanene [156], phosphorene [157] and single-layer transition metal dichalcogenides (SL-TMDs) [158] were included Focus of intensive and extensive research efforts.

These 2D materials form the elementary building blocks for critical components in low-dimensional devices. Based on this, we can divide 2D materials into three main families accordingly: the *graphene family*, a large class that includes graphene, *h*-BN, BCN, fluorographene, graphene oxide, and more; the *2D chalcogenide family*, an ensemble that includes MoS<sub>2</sub>, WSe<sub>2</sub>, ZrS<sub>2</sub>, NbSe<sub>2</sub>, Bi<sub>2</sub>Se<sub>3</sub>, etc.; and finally the family of *2D oxides*, a broad category that includes hydroxides such as Eu(OH)<sub>2</sub> and layered Cu oxides, MoO<sub>3</sub>, WO<sub>3</sub> and others, making a fascinating representation as shown in Figure 17.

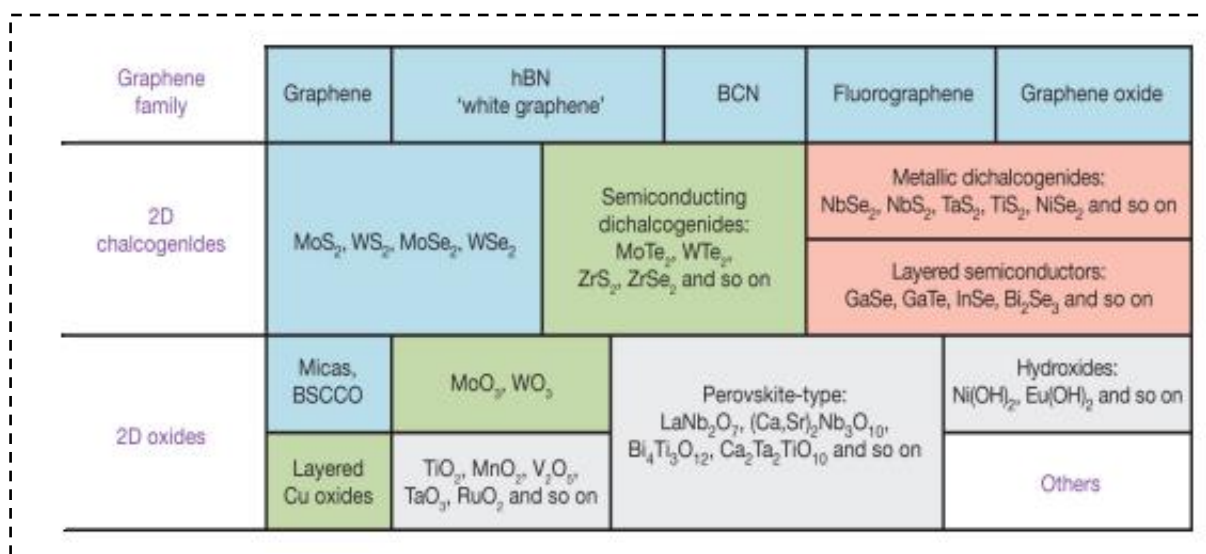


**Figure 17.** Schematic illustration of the different 2D nanomaterials families. After Ref [151].

The group of 2D chalcogenides containing group VIA elements is currently one of the most important groups and offers a wide range of materials, crystal structures and properties. This has attracted increasing attention due to their large bandgap, abundance, and special properties, including high mobility and efficient absorption in the visible and ultraviolet regions. 2D chalcogenides, either in their monolayers, bilayers, or multilayers, can be further categorized based on their chemistry and stoichiometry, as shown in Figure 18. These materials are made up of atomic planes, which are self-contained units with no dangling bonds present on surfaces. This special property facilitates the isolation of individual layers from the main material and shows the remarkable potential of these compounds [159].

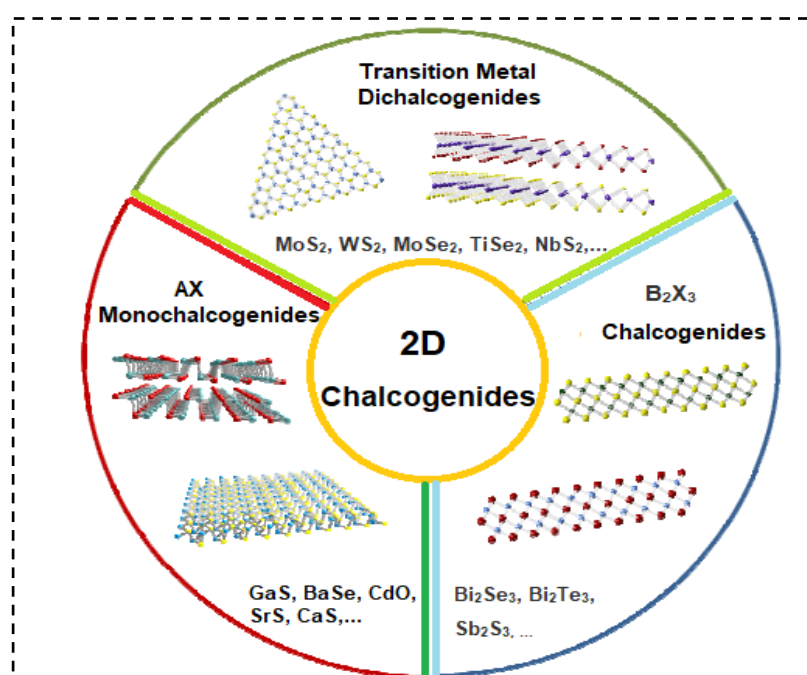


**Figure 18.** Categorization of 2D chalcogenides. After Ref [159].

A significant subgroup within the chalcogenide family are the AX monochalcogenide monolayers, essentially the II-VI group, which have also attracted considerable attention from researchers in recent years. This lattice arrangement has a honeycomb structure consisting of A-X bonds (where A means a cationic element from the group of II elements and X is the chalcogen elements (S, Se and Te), and is endowed with the  $D_{3h}$  point group symmetry. Each atom forms a vertex through  $sp$  hybridization.

In Figure 19 we show a visualization of the hexagonal structure of SrS, a prototype of the II-VI family. This symmetry is similar to other known monolayers, including graphene, silicon and BN.

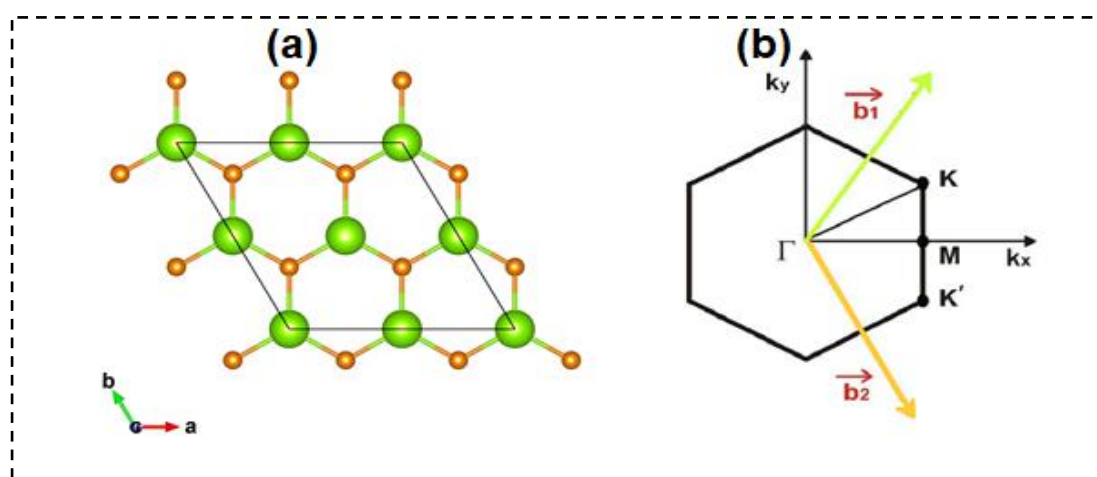


**Figure 19.** **a)** The Unit cell of the monolayer SrS, which adopts a hexagonal structure. Green spheres represent the Sr atoms, while orange spheres depict the chalcogen S atoms. The image was generated using VESTA software [76]. **b)** The first Brillouin zone of a hexagonal crystal, with the irreducible wedge identified by their common names, and the reciprocal base vectors labeled as  $b_1$ , and  $b_2$ .

Similar to their traditional 3D II-VI compounds, density functional theory (DFT) was also used to predict the novel 2D counterparts. For example, the 2D monolayers BeO, MgO, CaO, ZnO, CdO, CaS, SrS, SrSe, BaTe and HgTe were found to have strong dynamic and thermal stability and are suitable for use in UV optoelectronics [160]. The CdO monolayer has also shown promising optoelectronic capabilities suitable for visible light photocatalysis [161]. Recently, Abdullah et al. [162] showed that the combination of Be with O results in different thermal and optical properties, including high heat capacity and an active optical response observed in the UV. Interestingly, SrS and SrSe showed good thermal and dynamic stability and exhibited shallow valence bands that became highly spin polarized when doped with holes, making them excellent options for realizing Stoner ferromagnetism [160]. More recently, Yari et al. [163] found that doping the SrS monolayer with Cr induces a pronounced HMF character and increases the thermoelectric quality factor ( $ZT$ ) to 0.9 at temperatures above 500 K, making this monolayer suitable for spintronic and spin caloritronic nanodevices.



Reviewing the existing literature, the need to develop a diluted SrS monolayer-based magnetic semiconductor appears to be extremely promising. If we focus our attention on SrS as the original compound, the study of dimensionality reduction becomes extremely compelling. The aim of this study is to understand the unique influence of dimensionality reduction on various properties of SrS, particularly in the context of Fe doping compared to co-doping process.

Therefore, a bibliographic review of bulk SrS, monolayer SrS and their doped or co-doped structures is required.

## 1.6 An Overview of Bibliography

In the last decade, spintronics and its derivatives, including spin caloritronics, have come to the forefront of research and include both bulk (3D) and two-dimensional (2D) structures. In particular, the group of II-VI semiconductors based on transition metals (TM) proves to be a central component. With the ability to cover the properties of metalloids and semiconductors, these materials have a wide range of properties and applications by simply changing their composition. Their characterization, structural phase transition, synthesis techniques, magnetic behavior, electrical and optical responses, thermoelectric characteristics, and a variety of other properties have all been the subject of extensive research [164, 165].

In the following discourse, we discuss some of the groundbreaking work carried out on the TM-based II-VI semiconductor SrS, highlighting both the 3D and 2D forms.

- The binary compound SrS has been subject to thorough investigation, both experimentally and theoretically, in which it is confirmed that this compound shows *p*-type semiconductor properties with an indirect bandgap in both its 3D bulk structure and its 2D monolayer counterpart [73, 75, 82, 166-172].
- Xiao et al. [173] have examined the thermoelectric characteristics of bulk SrS, while Yari et al. [174] and Rajput et al. [175] have directed their attention towards examining the thermoelectric quality at the monolayer level. The collective findings underscored the promising potential of SrS for application in thermoelectric devices, with the *ZT* value approaching unity.
- The electronic structure, half-metallicity, and ferromagnetic properties of doped-SrS have been subject to theoretical investigations by Bourega et al. [176], Doumi et al. [64, 65], and Hamidane et al. [177] utilizing an ab-initio study. The combined results have demonstrated a large half-metallic bandgap and a stabilization of the ferromagnetism through exchange interactions between the host and magnetic dopants. These results underline how well these compounds might work as spintronic device materials.

- Hamidane et al. [66] conducted ab-initio calculations on the  $\text{Sr}_{1-x}\text{Mn}_x\text{S}$  bulk systems ( $0.25 \leq x \leq 0.75$ ). Their study revealed that the introduction of Mn into the host SrS induced alterations in the band structure and density of states. Interestingly, these changes enhanced the optical characteristics with increasing Mn concentrations, induced a significant magnetic moment, and preserved the material's semiconducting nature.
- In his research, Hoat [100] explored the electro-magnetic properties of SrS doped with first-row transition metals, maintaining a constant concentration of  $x = 0.25$ . His findings indicated that among all materials, only five, including  $\text{Sr}_{0.75}\text{Fe}_{0.25}\text{S}$ , could potentially serve as candidates for spintronics, primarily due to the presence of a considerable half-metallic bandgap.
- The hole doping at the anion site (with P and As) and cation site (with Al and Ga) of SrS monolayer was first investigated by Lin et al. [172], where they observed that the doping strategy resulted in an increase in the magnetic moment and the spin-polarization.
- In a recent study, Yari et al. [164] demonstrated the existence of magnetism in SrS monolayer through hole doping with Cr. Through a comprehensive exploration of its electronic, magneto-optical, and thermoelectric properties via a DFT approach, he confirmed the suitability of this monolayer for applications in spintronics, spin caloritronics, and spin-based optoelectronics devices.

Besides these, diverse nanostructures involving doping magnetic elements into SrS have been grown experimentally using different techniques such as sol-gel route [178], electrochemical deposition [179], solid-state diffusion [180], and others [181-183].

## 1.7 Simulation Studies and Their Scope

Broadly speaking, the study of structures involves two main approaches: theoretical and experimental. However, the advancement of computing capabilities has led to a distinct path known as Computational Condensed Matter Physics. This innovative approach acts as a mediator and connects the areas of theory and experiment. The development of computational resources has greatly facilitated deeper exploration of matter across different dimensions and length scales. Computer simulations are becoming increasingly common in condensed matter physics, both at the macroscopic and mesoscopic scales. Macroscopic systems are systems that are both measurable and observable, while mesoscopic systems deal with systems ranging from nanometers to micrometers.

Computer simulations are sometimes referred to as computer experiments because they share many similarities with laboratory experiments. The beginning of a computer simulation involves constructing an idealized model of a particular physical system. An algorithm or method is then defined to implement this model on a computing platform. By executing a computer program, the physical system is simulated and the basic ideas of the computer experiment are summarized. This digital experiment serves as a link between theoretical models and laboratory studies.

### 1.7.1 Possible Simulation Approaches

A variety of simulation methods have proven invaluable in gaining insight into the field of condensed matter physics, generally categorized as follows:

- **Classical Molecular Dynamics:** This method employs classical (Newtonian) mechanics [184], enabling the dynamic representation of systems.
- **Quantum Monte Carlo:** Characterized by a stochastic approach, Quantum Monte Carlo stands as an almost exact method for determining the many-body wavefunction [185], providing a robust avenue for exploration.
- **Ab-initio Method:** Grounded in computer simulation, this approach addresses the quantum mechanical Schrödinger equation [186], providing a complete solution.

Based on independent electronic structure computations, classical molecular dynamics is a powerful and well-established technique for studying many-body condensed matter systems [184]. The interatomic potential approximation is a fundamental question in any molecular dynamics scheme. Typically, the molecular dynamics method entails predetermining these potentials.

Quantum Monte Carlo (QMC) is revealed as a stochastic technique for calculating the ground state parameters of quantum systems by solving the Schrödinger wave equation. The QMC technique has shown promise in a number of fields with Schrödinger-like Hamiltonians, including solids, quantum liquids, nuclear matter, spin systems, and ab-initio quantum chemistry. Using significant sampling techniques is a key component of QMC approaches. This involves using a trial vector, based on "zero-variance property", which indicates that faster convergence toward the exact eigenvector is caused by a tighter alignment between the trial vector and the exact one, resulting in less statistical fluctuations [185].

Finally, ab-initio methods utilize first-principles to compute material properties by numerically solving the quantum mechanical Schrödinger equation [186]. These methods serve as primary tools for conducting research in condensed matter physics, materials science, quantum chemistry, and molecular chemistry. The level of accuracy predominantly depends on how accurately one can solve

the electronic problem. Among the most accurate based-methods, the Density Functional Theory (DFT). Density Functional Theory (DFT)-based methods include techniques that directly solve the eigenvalues and eigenfunctions of the molecular electronic Hamiltonian ( $H$ ) using basis set methods.

In Chapter 2, a detailed study of the DFT approach and the techniques used in this dissertation is presented. The application of DFT has proven crucial for studying a wide range of ground state properties, spanning both bulk and low-dimensional structures. Therefore, in this context, we adopted a theoretical approach to thoroughly investigate the systems selected for our study.

## 1.8 Conclusion

Finally, this chapter provides an introduction to II-VI bulk 3D materials and their corresponding 2D monolayer derivatives, followed by a detailed literature review of their properties and applications. Due to their remarkable electronic properties, characteristic structures, dimensionality, high carrier mobility, and tunable band gaps, these materials have attracted great interest as potential alternatives in various fields. Advances in storage technology and the constant pursuit of environmentally friendly solution materials provide the scientific community with numerous new opportunities to explore phenomena, concepts and technologies in the fields of spintronics, spin caloritronics and spin-based optoelectronics. Dilute magnetic semiconductors (DMS), obtained by incorporating transition metals into II-VI semiconductors, hold enormous potential for development into small-sized, low-power, and high-capacity memory systems. Through its comprehensive discussions, this chapter contributed significantly to the selection of suitable host semiconductors and dopants for our dissertation. We specifically chose to focus on Fe-doped SrS, using two different strategies to improve its properties: co-doping in the 3D form and dimensionality reduction to the 2D monolayer form. These approaches aim to improve a wide range of properties including structural, electronic, magnetic, mechanical, optical and thermoelectric properties.

## References for Chapter 1

- [1] Wolf, S. A., Awschalom, D. D., Buhrman, R. A., Daughton, J. M., von Molnár, V. S., Roukes, M. L., & Treger, D. M. (2001). Spintronics: a spin-based electronics vision for the future. *Science*, 294(5546), 1488-1495.
- [2] Petsagkourakis, I., Tybrandt, K., Crispin, X., Ohkubo, I., Satoh, N., & Mori, T. (2018). Thermoelectric materials and applications for energy harvesting power generation. *Science and technology of advanced materials*, 19(1), 836-862.
- [3] Linder, J., & Robinson, J. W. (2015). Superconducting spintronics. *Nature Physics*, 11(4), 307-315.
- [4] Misiorny, M., Hell, M., & Wegewijs, M. R. (2013). Spintronic magnetic anisotropy. *Nature Physics*, 9(12), 801-805.
- [5] Gerlach, W., & Stern, O. (1922). Der experimentelle nachweis der richtungsquantelung im magnetfeld. *Zeitschrift für Physik*, 9(1), 349-352.
- [6] Tedrow, P. M., & Meservey, R. (1973). Spin polarization of electrons tunneling from films of Fe, Co, Ni, and Gd. *Physical Review B*, 7(1), 318.
- [7] Dyakonov, M. I., & Perel, V. I. (1972). Spin relaxation of conduction electrons in noncentrosymmetric semiconductors. *Soviet Physics Solid State, USSR*, 13(12), 3023-3026.
- [8] Vorob'ev, L. E., Ivchenko, E. L., Pikus, G. E., Farbshteĭn, I. I., Shalygin, V. A., & Shturbin, A. V. (1979). Optical activity in tellurium induced by a current. *Soviet Journal of Experimental and Theoretical Physics Letters*, 29, 441.
- [9] Aronov, A. G., & Pikus, G. E. (1976). Spin injection into semiconductors. *Soviet Physics Semiconductors-Ussr*, 10(6), 698-700.
- [10] Johnson, M., & Silsbee, R. H. (1985). Interfacial charge-spin coupling: Injection and detection of spin magnetization in metals. *Physical review letters*, 55(17), 1790.
- [11] Baibich, M. N., Broto, J. M., Fert, A., Van Dau, F. N., Petroff, F., Etienne, P., & Chazelas, J. (1988). Giant magnetoresistance of (001) Fe/ (001) Cr magnetic superlattices. *Physical review letters*, 61(21), 2472.
- [12] Binasch, G., Grünberg, P., Saurenbach, F., & Zinn, W. (1989). Enhanced magnetoresistance in layered magnetic structures with antiferromagnetic interlayer exchange. *Physical review B*, 39(7), 4828.
- [13] Parkin, S., Wolf, S. A., Harris, J. S., Zhang, S., & Smith, D. J. (1997). The Application of Spintronics.
- [14] Hu, J., & Wu, R. (2014). Giant magnetic anisotropy of transition-metal dimers on defected graphene. *Nano letters*, 14(4), 1853-1858.
- [15] Choudhuri, I., Bhauriyal, P., & Pathak, B. (2019). Recent advances in graphene-like 2D materials for spintronics applications. *Chemistry of Materials*, 31(20), 8260-8285.
- [16] Hirohata, A., & Takanashi, K. (2014). Future perspectives for spintronic devices. *Journal of Physics D : Applied Physics*, 47(19), 193001.

- [17] The 12<sup>th</sup> international workshop on Spin Caloritronics "Spin Caloritronics XII", (2023), Tsukuba center for institutes, Japan.
- [18] The German Physical Society (DPG), (1845), Bad Honnef, Germany.
- [19] The Spin and Heat In Nanoscale Electronic System (S.H.I.N.E.S), (n.d.), US.
- [20] Seebeck, T. J. (1822). Magnetic polarization of metals and minerals. *Abhandlungen der Deutschen Akademie der Wissenschaften zu Berlin*, 265, 1822-1823.
- [21] Peltier, J. C. A. (1834). *Nouvelles expériences sur la calorité des courans électriques*.
- [22] Lenz, E. (1838). Einige versuche im gebiete des galvanismus. *Annalen der Physik*, 120(6), 342-349.
- [23] Joule, J. P. (1841). XXXVIII. On the heat evolved by metallic conductors of electricity, and in the cells of a battery during electrolysis. *The London, Edinburgh, and Dublin Philosophical Magazine and Journal of Science*, 19(124), 260-277.
- [24] Thomson, W. (1857). 4. on a mechanical theory of thermo-electric currents. *Proceedings of the Royal society of Edinburgh*, 3, 91-98.
- [25] Slack, G. A., & Rowe, D. M. (1995). CRC handbook of thermoelectrics.
- [26] Tritt, T. M. (2002). Thermoelectric materials: Principles, structure, properties, and applications.
- [27] Ioffe, A. F. (1957). Semiconductor Thermoelements, and Thermoelectric. *Cool-ingInfosearch Ltd.: London, UK*.
- [28] Snyder, G. J., & Snyder, A. H. (2017). Figure of merit ZT of a thermoelectric device defined from materials properties. *Energy & Environmental Science*, 10(11), 2280-2283.
- [29] Lenoir, B., Michenaud, J. P., & Dauscher, A. (2010). Thermoélectricité : des principes aux applications. *Technique de l'ingénieur*.
- [30] Guazzagaloppa, J. (2019). *Matériaux super-isolants thermiques à propriétés thermoélectriques intégrées* (Doctoral dissertation, Université Montpellier).
- [31] Jund, P., Viennois, R., Tao, X., Niedziolka, K., & Tédénac, J. C. (2012). Physical properties of thermoelectric zinc antimonide using first-principles calculations. *Physical Review B*, 85(22), 224105.
- [32] He, J., & Tritt, T. M. (2017). Advances in thermoelectric materials research: Looking back and moving forward. *Science*, 357(6358), eaak9997.
- [33] Wang, Y., Rogado, N. S., Cava, R. J., & Ong, N. P. (2003). Spin entropy as the likely source of enhanced thermopower in Na<sub>x</sub>Co<sub>2</sub>O<sub>4</sub>. *Nature*, 423(6938), 425-428.
- [34] Dresselhaus, M. S., Chen, G., Tang, M. Y., Yang, R. G., Lee, H., Wang, D. Z., & Gogna, P. (2007). New directions for low-dimensional thermoelectric materials. *Advanced materials*, 19(8), 1043-1053.
- [35] Yang, J., Xi, L., Qiu, W., Wu, L., Shi, X., Chen, L., & Singh, D. J. (2016). On the tuning of electrical and thermal transport in thermoelectrics: an integrated theory–experiment perspective. *NPJ Computational Materials*, 2(1), 1-17.
- [36] Zebarjadi, M., Joshi, G., Zhu, G., Yu, B., Minnich, A., Lan, Y., & Chen, G. (2011). Power factor enhancement by modulation doping in bulk nanocomposites. *Nano letters*, 11(6), 2225-2230.

- [37] Biswas, K., He, J., Blum, I. D., Wu, C. I., Hogan, T. P., Seidman, D. N., & Kanatzidis, M. G. (2012). High-performance bulk thermoelectrics with all-scale hierarchical architectures. *Nature*, *489*(7416), 414-418.
- [38] Cahill, D. G., Watson, S. K., & Pohl, R. O. (1992). Lower limit to the thermal conductivity of disordered crystals. *Physical Review B*, *46*(10), 6131.
- [39] Pizzi, G., Volja, D., Kozinsky, B., Fornari, M., & Marzari, N. (2014). BoltzWann: A code for the evaluation of thermoelectric and electronic transport properties with a maximally localized Wannier functions basis. *Computer Physics Communications*, *185*(1), 422-429.
- [40] Nolas, G. S., Sharp, J., & Goldsmid, J. (2001). *Thermoelectrics: basic principles and new materials developments* (Vol. 45). Springer Science & Business Media.
- [41] Oh, M. W., Wee, D. M., Park, S. D., Kim, B. S., & Lee, H. W. (2008). Electronic structure and thermoelectric transport properties of AgTlTe: First-principles calculations. *Physical Review B*, *77*(16), 165119.
- [42] Snyder, G. J., & Ursell, T. S. (2003). Thermoelectric efficiency and compatibility. *Physical review letters*, *91*(14), 148301.
- [43] Slachter, A., Bakker, F. L., Adam, J. P., & van Wees, B. J. (2010). Thermally driven spin injection from a ferromagnet into a non-magnetic metal. *Nature Physics*, *6*(11), 879-882.
- [44] Flipse, J., Bakker, F. L., Slachter, A., Dejene, F. K., & Van Wees, B. J. (2012). Direct observation of the spin-dependent Peltier effect. *Nature nanotechnology*, *7*(3), 166-168.
- [45] Sharma, S., & Pandey, S. K. (2015). Applicability of two-current model in understanding the electronic transport behavior of inverse Heusler alloy: Fe<sub>2</sub>CoSi. *Physics Letters A*, *379*(38), 2357-2361.
- [46] Ioffe, A. F., Stil'Bans, L. S., Iordanishvili, E. K., Stavitskaya, T. S., Gelbtuch, A., & Vineyard, G. (1959). Semiconductor thermoelements and thermoelectric cooling. *Physics Today*, *12*(5), 42-42.
- [47] Zhang, K. H., Xi, K., Blamire, M. G., & Egdell, R. G. (2016). P-type transparent conducting oxides. *Journal of Physics: Condensed Matter*, *28*(38), 383002.
- [48] Facchetti, A., & Marks, T. J. (2010). Transparent electronics. *From Synthesis to Applications*.
- [49] Pierson, H. O. (1996). *Handbook of refractory carbides and nitrides: properties, characteristics, processing and applications*. William Andrew.
- [50] Markoc, H. (2008). Handbook of Nitride Semiconductors and Devices. *Wiley-Vch Verlag GmbH & Co. KGaA*, *155*(156), 10.
- [51] Grundmann, M., Schein, F. L., Lorenz, M., Böntgen, T., Lenzner, J., & von Wenckstern, H. (2013). Cuprous iodide—ap-type transparent semiconductor: History and novel applications. *physica status solidi (a)*, *210*(9), 1671-1703.
- [52] Allen, M. J., Tung, V. C., & Kaner, R. B. (2010). Honeycomb carbon: a review of graphene. *Chemical reviews*, *110*(1), 132-145.
- [53] Cheng, J., Fan, D., Wang, H., Liu, B., Zhang, Y., & Yan, H. (2003). Chemical bath deposition of crystalline ZnS thin films. *Semiconductor science and technology*, *18*(7), 676.

- [54] Choi, J. Y., Kim, K. J., Yoo, J. B., & Kim, D. (1998). Properties of cadmium sulfide thin films deposited by chemical bath deposition with ultrasonication. *Solar energy*, 64(1-3), 41-47.
- [55] Liu, M. L., Wang, Y. M., Huang, F. Q., Chen, L. D., & Wang, W. D. (2007). Optical and electrical properties study on p-type conducting  $\text{CuAlS}_{2+x}$  with wide band gap. *Scripta Materialia*, 57(12), 1133-1136.
- [56] Han, Y., Siol, S., Zhang, Q., & Zakutayev, A. (2017). Optoelectronic properties of strontium and barium copper sulfides prepared by combinatorial sputtering. *Chemistry of materials*, 29(19), 8239-8248.
- [57] Newhouse, P. F., Hersh, P. A., Zakutayev, A., Richard, A., Platt, H. A. S., Keszler, D. A., & Tate, J. (2009). Thin film preparation and characterization of wide band gap  $\text{Cu}_3\text{TaQ}_4$  (Q= S or Se) p-type semiconductors. *Thin Solid Films*, 517(7), 2473-2476.
- [58] Hiramatsu, H., Kamioka, H., Ueda, K., Ohta, H., Kamiya, T., Hirano, M., & Hosono, H. (2006). Opto-electronic properties and light-emitting device application of widegap layered oxychalcogenides:  $\text{LaCuOCh}$  (Ch= chalcogen) and  $\text{La}_2\text{CdO}_2\text{Se}_2$ . *Physica status solidi (a)*, 203(11), 2800-2811.
- [59] Kawazoe, H., Yasukawa, M., Hyodo, H., Kurita, M., Yanagi, H., & Hosono, H. (1997). P-type electrical conduction in transparent thin films of  $\text{CuAlO}_2$ . *Nature*, 389(6654), 939-942.
- [60] Woods-Robinson, R., Han, Y., Zhang, H., Ablekim, T., Khan, I., Persson, K. A., & Zakutayev, A. (2020). Wide bandgap chalcogenide semiconductors. *Chemical reviews*, 120(9), 4007-4055.
- [61] Sedighi, M., Nia, B. A., Hamad, A. H., & Othman, M. S. (2020). Electronic and optical properties of SrS nanosheet in 001 and 101 directions. *Computational Condensed Matter*, 22, e00445.
- [62] Hou, X. Y., Cheng, Y., Hu, C. E., Piao, C. G., & Geng, H. Y. (2020). Thermoelectric properties of strontium sulfide via first-principles calculations. *Solid State Communications*, 305, 113755.
- [63] Yazdanmehr, M., Sadeghi, H., Tehrani, M. K., Hashemifar, S. J., & Mahdavi, M. (2018). Effects of nanostructuring on luminescence properties of SrS: Ce, Sm phosphor: an experimental and phenomenological study. *Optical Materials*, 75, 304-313.
- [64] Doumi, B., Mokaddem, A., Dahmane, F., Sayede, A., & Tadjer, A. (2015). A novel theoretical design of electronic structure and half-metallic ferromagnetism in the 3d (V)-doped rock salts SrS, SrSe, and SrTe for spintronics. *RSC advances*, 5(112), 92328-92334.
- [65] Doumi, B., Mokaddem, A., Temimi, L., Beldjoudi, N., Elkeurti, M., Dahmane, F., ... & Ishak-Boushaki, M. (2015). First-principle investigation of half-metallic ferromagnetism in octahedrally bonded Cr-doped rock-salt SrS, SrSe, and SrTe. *The European Physical Journal B*, 88, 1-9.
- [66] Hamidane, N., Baaziz, H., Baddari, K., & Charifi, Z. (2020). First-principles investigation of the structural, electronic, magnetic, thermodynamic and optical properties of the cubic  $\text{Sr}_{1-x}\text{Mn}_x\text{S}$  ternary alloys. *Computational Condensed Matter*, 23, e00458.
- [67] Khare, A., Mishra, S., Kshatri, D. S., & Tiwari, S. (2017). Optical properties of rare earth doped SrS phosphor: a review. *Journal of Electronic Materials*, 46, 687-708.



- [68] Kim, J., Choi, J., & Kang, Y. (2023). First-principles study of SrTe and BaTe: Promising wide-band-gap semiconductors with ambipolar doping. *Current Applied Physics*, 48, 90-96.
- [69] Salome, P. M., Vermang, B., Ribeiro-Andrade, R., Teixeira, J. P., Cunha, J. M., Mendes, M. J., ... & Sadewasser, S. (2018). Passivation of interfaces in thin film solar cells: Understanding the effects of a nanostructured rear point contact layer. *Advanced Materials Interfaces*, 5(2), 1701101.
- [70] Yogeswari, M., & Kalpana, G. (2012). Half-metallic ferromagnetism in alkaline earth selenides by first principles calculations. *Computational materials science*, 54, 219-226.
- [71] Zeng, L., Zhang, J., You, L., Zheng, H., Liu, Y., Ouyang, L., & Luo, J. (2016). Enhanced thermoelectric performance in PbSe-SrSe solid solution by Mn substitution. *Journal of Alloys and Compounds*, 687, 765-772.
- [72] Mera, A., Mahmood, Q., & Rouf, S. A. (2022). Quantum ferromagnetism in transition metals doped II-VI semiconductors for spintronic applications: A merging technology. *Solid State Communications*, 352, 114835.
- [73] Syassen, K. (1985). Pressure-induced structural transition in SrS. *Physica Status Solidi. A, Applied Research*, 91(1), 11-15.
- [74] Janotti, A., & Van de Walle, C. G. (2009). Fundamentals of zinc oxide as a semiconductor. *Reports on progress in physics*, 72(12), 126501.
- [75] Syassen, K. (1986). Ionic monochalcogenides under pressure. *Physica B+ C*, 139, 277-283.
- [76] Momma, K., & Izumi, F. (2011). VESTA 3 for three-dimensional visualization of crystal, volumetric and morphology data. *Journal of applied crystallography*, 44(6), 1272-1276.
- [77] Setyawan, W., & Curtarolo, S. (2010). High-throughput electronic band structure calculations: Challenges and tools. *Computational materials science*, 49(2), 299-312.
- [78] Li, W. M., Ritala, M., Leskelä, M., Lappalainen, R., Soinen, E., Niinistö, L., & Benoit, J. (1999). Improved blue luminescence in Ag-codoped SrS: Ce thin films made by atomic layer epitaxy and ion implantation. *Applied physics letters*, 74(16), 2298-2300.
- [79] Dos Santos, D. O. A., Giordano, L., Barbará, M. A. S. G., Portes, M. C., Pedroso, C. C. S., Teixeira, V. C., & Rodrigues, L. C. V. (2020). Abnormal co-doping effect on the red persistent luminescence SrS: Eu<sup>2+</sup>, RE<sup>3+</sup> materials. *Dalton Transactions*, 49(45), 16386-16393.
- [80] Labidi, S., Labidi, M., Meradji, H., Ghemid, S., & Hassan, F. E. H. (2011). First principles calculations of structural, electronic, optical and thermodynamic properties of PbS, SrS and their ternary alloys Pb<sub>1-x</sub>Sr<sub>x</sub>S. *Computational Materials Science*, 50(3), 1077-1082.
- [81] Chen, Y., Fan, S. W., & Xu, P. (2022). Defect induced ambipolar conductivity in wide-bandgap semiconductor SrS: Theoretical perspectives. *Applied Physics Letters*, 121(25).
- [82] Zheng, H., Li, X. B., Chen, N. K., Xie, S. Y., Tian, W. Q., Chen, Y., Hong, X., Zhang, S.B., & Sun, H. B. (2015). Monolayer II-VI semiconductors: A first-principles prediction. *Physical Review B*, 92(11), 115307.

- [83] Fang, M., Wang, H., Tan, X., Cheng, B., Zhang, L., & Xiao, Z. (2008). One-dimensional hollow SrS nanostructure with red long-lasting phosphorescence. *Journal of alloys and compounds*, 457(1-2), 413-416.
- [84] Uğur, Ş. U. L. E., Güler, E., Güler, M., Özdemir, A. L. P. T. U. Ğ., & Uğur, G. Ö. K. A. Y. (2022). Analyzing the electronic and optical properties of bulk, unstrained, and strained monolayers of SrS<sub>2</sub> by DFT. *Physica E: Low-dimensional Systems and Nanostructures*, 143, 115403.
- [85] Jain, M. K. (1991). *Diluted magnetic semiconductors*. World Scientific.
- [86] Oliver, M. R., Kafalas, J. A., Dimmock, J. O., & Reed, T. B. (1970). Pressure dependence of the electrical resistivity of EuO. *Physical Review Letters*, 24(19), 1064.
- [87] Janisch, R., Gopal, P., & Spaldin, N. A. (2005). Transition metal-doped TiO<sub>2</sub> and ZnO—present status of the field. *Journal of Physics: Condensed Matter*, 17(27), R657.
- [88] Asahi, H., & Horikoshi, Y. (Eds.). (2019). *Molecular Beam Epitaxy: Materials and applications for electronics and optoelectronics*. John Wiley & Sons.
- [89] Jiles, D. A. D. C., & Atherton, D. (1983). Ferromagnetic hysteresis. *IEEE Transactions on magnetics*, 19(5), 2183-2185.
- [90] De Groot, R. A., Mueller, F. M., van Engen, P. V., & Buschow, K. H. J. (1983). New class of materials: half-metallic ferromagnets. *Physical review letters*, 50(25), 2024.
- [91] GOUS, M. H. (2018). *Calcul des propriétés structurales, élastiques, électroniques et magnétiques des semi-conducteurs magnétiques dilués à base de MgS et des alliages demi-heusler demi-métalliques CoVTe et RuVTe* (Doctoral dissertation).
- [92] Néel, L. (1952). Antiferromagnetism and ferrimagnetism. *Proceedings of the Physical Society. Section A*, 65(11), 869.
- [93] Morrish, A. H. (2001). *The physical principles of magnetism* (p. 696).
- [94] Moriya, T. (1960). Anisotropic superexchange interaction and weak ferromagnetism. *Physical review*, 120(1), 91.
- [95] Peterson, C. (1987). A mean field theory learning algorithm for neural network. *Complex systems*, 1, 995-1019.
- [96] Kumar, R., Rani, A., & Alshaikhi, A. A. (2023). Electronic and Magnetic Properties of Cr and V Doped CaZ (Z= S, Se). *Crystals*, 13(7), 1069.
- [97] Ghazal, W., Mamoun, S., Kanoun, M. B., Goumri-Said, S., & Merad, A. E. (2023). Electronic, magnetic and optical properties of Cr and Fe doped ZnS and CdS diluted magnetic semiconductors: revised study within TB-mBJ potential. *Optical and Quantum Electronics*, 55(4), 310.
- [98] Sajjad, M., Zhang, H. X., Noor, N. A., Alay-e-Abbas, S. M., Younas, M., Abid, M., & Shaukat, A. (2014). Theoretical investigation of structural, electronic, and magnetic properties of V-doped MgSe and MgTe semiconductors. *Journal of Superconductivity and Novel Magnetism*, 27, 2327-2336.

- [99] Li, J., Xu, X., Zhou, Y., Zhang, M., & Luo, X. (2013). First-principles investigation on the electronic and magnetic properties of cubic  $\text{BeO} \cdot 75\text{MnO} \cdot 25\text{X}$  ( $\text{X} = \text{S}, \text{Se}, \text{Te}$ ). *Journal of alloys and compounds*, 575, 190-197.
- [100] Hoat, D. M. (2020). DFT prediction of structural, electronic and magnetic properties of  $\text{SrO} \cdot 75\text{TMO} \cdot 25\text{S}$  (TM is 3 d transition metals). *Philosophical Magazine Letters*, 100(3), 95-104.
- [101] Shinya, H., Fukushima, T., Masago, A., Sato, K., & Katayama-Yoshida, H. (2018). First-principles prediction of the control of magnetic properties in Fe-doped GaSb and InSb. *Journal of Applied Physics*, 124(103902).
- [102] Zhang, H. W., Wei, Z. R., Li, Z. Q., & Dong, G. Y. (2007). Room-temperature ferromagnetism in Fe-doped, Fe-and Cu-codoped ZnO diluted magnetic semiconductor. *Materials Letters*, 61(17), 3605-3607.
- [103] Bourouis, C., & Meddour, A. (2012). First-principles study of structural, electronic and magnetic properties in  $\text{Cd}_{1-x}\text{Fe}_x\text{S}$  diluted magnetic semiconductors. *Journal of magnetism and magnetic materials*, 324(6), 1040-1045.
- [104] Singh, J., & Verma, N. K. (2012). Synthesis and characterization of Fe-doped CdSe nanoparticles as dilute magnetic semiconductor. *Journal of superconductivity and novel magnetism*, 25, 2425-2430.
- [105] Mahmood, Q., Javed, A., Murtaza, G., & Alay-e-Abbas, S. M. (2015). Study of the  $\text{ZnO} \cdot 75\text{MO} \cdot 25\text{Te}$  ( $\text{M} = \text{Fe}, \text{Co}, \text{Ni}$ ) diluted magnetic semiconductor system by first principles approach. *Materials Chemistry and Physics*, 162, 831-838.
- [106] Li, T., Wang, W., Shi, Q., Zhang, J., & Zhao, L. (2022). Transition from ferromagnetism to superparamagnetism in diluted magnetic Fe (II)-doped ZnSe microspheres. *Journal of Magnetism and Magnetic Materials*, 543, 168625.
- [107] Amari, S. (2021). Physical properties of Mn-and Fe-doped CaS: A DFT insights. *Computational Condensed Matter*, 27, e00559.
- [108] Raiss, A. A., Sbai, Y., Bahmad, L., & Benyoussef, A. (2015). Magnetic and magneto-optical properties of doped and co-doped CdTe with (Mn, Fe): Ab-initio study. *Journal of Magnetism and Magnetic Materials*, 385, 295-301.
- [109] Sukkabot, W. (2020). Theoretical Investigation of Electronic and Magnetic Optical Properties of CdS Doped and Co Doped With Transition Metals (Mn, Fe, and Cu): Spin Density Functional Theory. *IEEE Transactions on Magnetics*, 56(9), 1-6.
- [110] Paranchich, S. Y., Paranchich, L. D., Andriichuk, M. D., Makogonenko, V. N., Mel' nichuk, T. A., Tanasyuk, Y. V., & Romanyuk, V. R. (2007). Effect of Fe, Co, and Cr impurities on the thermoelectric properties of  $\text{Cd}_x\text{Hg}_{1-x}\text{Se}$ . *Inorganic Materials*, 43, 338-343.
- [111] Yogeswari, M., & Kalapana, G. (2011). Ab initio electronic structure calculations of half-metallic ferromagnetism in calcium chalcogenides doped with B, C and N. *Modern Physics Letters B*, 25(18), 1537-1548.

- [112] Singh, R. (2013). Unexpected magnetism in nanomaterials. *Journal of Magnetism and Magnetic Materials*, 346, 58-73.
- [113] Coey, J. M. D. (2005).  $d^0$  ferromagnetism. *Solid State Sciences*, 7(6), 660-667.
- [114] Ghose, S., Rakshit, T., Ranganathan, R., & Jana, D. (2015). Role of Zn-interstitial defect states on  $d^0$  ferromagnetism of mechanically milled ZnO nanoparticles. *Rsc Advances*, 5(121), 99766-99774.
- [115] Peng, H., Xiang, H. J., Wei, S. H., Li, S. S., Xia, J. B., & Li, J. (2009). Origin and enhancement of hole-induced ferromagnetism in first-row  $d^0$  semiconductors. *Physical review letters*, 102(1), 017201.
- [116] Yu, D., Liu, Y., Sun, L., Wu, P., & Zhou, W. (2016). Density functional study on the hole doping of single-layer SnS<sub>2</sub> with metal element X (X= Li, Mg, and Al). *Physical Chemistry Chemical Physics*, 18(1), 318-324.
- [117] Lu, Y. L., Dong, S., Zhou, W., Zhao, H., & Wu, P. (2016). Nonmagnetic 2p-block elements (B, C, N, and O)-doped AgCl for potential halide spintronic applications: A first-principles perspective. *Physics Letters A*, 380(37), 2968-2973.
- [118] Ando, K. (2006). Seeking room-temperature ferromagnetic semiconductors. *Science*, 312(5782), 1883-1885.
- [119] Tabassum, M., Zia, Q., Zhou, Y., Reece, M. J., & Su, L. (2021). A review on advances in doping with alkali metals in halide perovskite materials. *SN Applied Sciences*, 3, 1-15.
- [120] Chang, S., Fu, J., Sun, X., Bai, G., Liu, G., Wang, K., & Tang, M. (2021). Tailoring Luminescent Properties of SrS: Ce by Modulating Defects: Sr-Deficiency and Na<sup>+</sup> Doping. *ArXiv preprint arXiv: 2111.11622*.
- [121] Yang, H. C., Gong, B. C., Liu, K., & Lu, Z. Y. (2018). The melilite-type compound (Sr<sub>1-x</sub>, Ax) <sub>2</sub>MnGe<sub>2</sub>S<sub>6</sub>O (A= K, La) being a room temperature ferromagnetic semiconductor. *Science bulletin*, 63(14), 887-891.
- [122] Yang, L., Li, X., Liu, J., Xiong, S., Ma, X., Liu, P., ... & Chen, H. (2019). Lithium-doping stabilized high-performance P<sub>2</sub>-Na<sub>0.66</sub>Li<sub>0.18</sub>Fe<sub>0.12</sub>Mn<sub>0.7</sub>O<sub>2</sub> cathode for sodium ion batteries. *Journal of the American Chemical Society*, 141(16), 6680-6689.
- [123] Krithiga, R., Sankar, S., & Subhashree, G. (2014). Room temperature diluted magnetism in Li, Na and K co-doped ZnO synthesized by solution combustion method. *Superlattices and Microstructures*, 75, 621-633.
- [124] Pazhanivelu, V., Selvadurai, A. P. B., Kannan, R., & Murugaraj, R. (2016). Room temperature ferromagnetism in Ist group elements codoped ZnO: Fe nanoparticles by co-precipitation method. *Physica B: Condensed Matter*, 487, 102-108.
- [125] Gu, H., Jiang, Y., & Yan, M. (2012). Defect-induced room temperature ferromagnetism in Fe and Na co-doped ZnO nanoparticles. *Journal of alloys and compounds*, 521, 90-94.

- [126] Yakout, S. M. (2018). Pure and Gd-based Li, Na, Mn or Fe codoped ZnO nanoparticles: insights into the magnetic and photocatalytic properties. *Solid State Sciences*, 83, 207-217.
- [127] Napagoda, M., Jayathunga, D., & Witharana, S. (2022). Introduction to nanotechnology. In *Nanotechnology in Modern Medicine* (pp. 1-17). Singapore: Springer Nature Singapore.
- [128] Masciangioli, T., & Zhang, W. X. (2003). Environmental technologies at the nanoscale, *Environ. Sci. Technol.*, 37(5).
- [129] Xuejing, L., Fulai, Z., Yu, W., Yichao, Z., Yaling, W., Yiyu, F., & Wei, F. (2021). Preparation and photoelectric properties of germanium sulphoselenide photodetector. *CHEMICAL JOURNAL OF CHINESE UNIVERSITIES-CHINESE*, 42(8), 2661-2667.
- [130] Pedireddy, S., Lee, H. K., Tjiu, W. W., Phang, I. Y., Tan, H. R., Chua, S. Q., ... & Ling, X. Y. (2014). One-step synthesis of zero-dimensional hollow nanoporous gold nanoparticles with enhanced methanol electrooxidation performance. *Nature Communications*, 5(1), 4947.
- [131] Sze, S. M., & Ng, K. K. (1981). *Physics of semiconductor devices*, John wiley & sons. *New York*, 68.
- [132] Zhou, H., Yu, W. J., Liu, L., Cheng, R., Chen, Y., Huang, X., & Duan, X. (2013). Chemical vapour deposition growth of large single crystals of monolayer and bilayer graphene. *Nature communications*, 4(1), 2096.
- [133] Celis, A., Nair, M. N., Taleb-Ibrahimi, A., Conrad, E. H., Berger, C., De Heer, W. A., & Tejeda, A. (2016). Graphene nanoribbons: fabrication, properties and devices. *Journal of Physics D: Applied Physics*, 49(14), 143001.
- [134] Mousa, M. S. (2018, February). Comparison between single-walled CNT, multi-walled CNT, and carbon nanotube-fiber pyrograf III. In *IOP Conference Series: Materials Science and Engineering* (Vol. 305, p. 012025). IOP Publishing.
- [135] Streetman, B. G., & Banerjee, S. (2000). *Solid-state electronic devices* (Vol. 4). New Jersey: Prentice hall.
- [136] Springborg, M., & Sarkar, P. (2003). Structural and electronic properties of thin chains of Ag. *Physical Review B*, 68(4), 045430.
- [137] Naguib, M., Kurtoglu, M., Presser, V., Lu, J., Niu, J., Heon, M., & Barsoum, M. W. (2011). Two-dimensional nanocrystals produced by exfoliation of Ti<sub>3</sub>AlC<sub>2</sub>. *Advanced materials*, 23(37), 4248-4253.
- [138] Rubab, A., Baig, N., Sher, M., & Sohail, M. (2020). Advances in ultrathin borophene materials. *Chemical Engineering Journal*, 401, 126109.
- [139] Reina, A., Jia, X., Ho, J., Nezich, D., Son, H., Bulovic, V., & Kong, J. (2009). Large area, few-layer graphene films on arbitrary substrates by chemical vapor deposition. *Nano letters*, 9(1), 30-35.
- [140] Gupta, A., Sakhivel, T., & Seal, S. (2015). Recent development in 2D materials beyond graphene. *Progress in Materials Science*, 73, 44-126.
- [141] Lee, C., Wei, X., Kysar, J. W., & Hone, J. (2008). Measurement of the elastic properties and intrinsic strength of monolayer graphene. *Science*, 321(5887), 385-388.

- [142] Parvez, K. (2019). Two-dimensional nanomaterials: Crystal structure and synthesis. In *Biomedical Applications of Graphene and 2D Nanomaterials* (pp. 1-25). Elsevier.
- [143] Zhang, P., Zhao, F., Long, P., Wang, Y., Yue, Y., Liu, X., & Feng, W. (2018). Sonication-assisted liquid-phase exfoliated  $\alpha$ -GeTe: a two-dimensional material with high Fe 3+ sensitivity. *Nanoscale*, *10*(34), 15989-15997.
- [144] Eng, A. Y. S., Ambrosi, A., Sofer, Z., Simek, P., & Pumera, M. (2014). Electrochemistry of transition metal dichalcogenides: strong dependence on the metal-to-chalcogen composition and exfoliation method. *Acs Nano*, *8*(12), 12185-12198.
- [145] Gao, E., Lin, S. Z., Qin, Z., Buehler, M. J., Feng, X. Q., & Xu, Z. (2018). Mechanical exfoliation of two-dimensional materials. *Journal of the Mechanics and Physics of Solids*, *115*, 248-262.
- [146] Deepika, Li, L. H., Glushenkov, A. M., Hait, S. K., Hodgson, P., & Chen, Y. (2014). High-efficient production of boron nitride nanosheets via an optimized ball milling process for lubrication in oil. *Scientific reports*, *4*(1), 7288.
- [147] Winter, A., Ekinci, Y., Gölzhäuser, A., & Turchanin, A. (2019). Freestanding carbon nanomembranes and graphene monolayers nanopatterned via EUV interference lithography. *2D Materials*, *6*(2), 021002.
- [148] Servalli, M., Celebi, K., Payamyar, P., Zheng, L., Položij, M., Lowe, B., & Schlüter, A. D. (2018). Photochemical creation of covalent organic 2D monolayer objects in defined shapes via a lithographic 2D polymerization. *ACS nano*, *12*(11), 11294-11306.
- [149] Corbella, C., Portal, S., Saadi, M. A. S. R., Solares, S. D., Kundrapu, M. N., & Keidar, M. (2019). Few-layer flakes of molybdenum disulphide produced by anodic arc discharge in pulsed mode. *Plasma Research Express*, *1*(4), 045009.
- [150] Gupta, D., Chauhan, V., & Kumar, R. (2022). Sputter deposition of 2D MoS<sub>2</sub> thin films-A critical review from a surface and structural perspective. *Inorganic Chemistry Communications*, 109848.
- [151] Coogan, Á., & Gun'ko, Y. K. (2021). Solution-based “bottom-up” synthesis of group VI transition metal dichalcogenides and their applications. *Materials Advances*, *2*(1), 146-164.
- [152] Chakraborty, G., Park, I. H., Medishetty, R., & Vittal, J. J. (2021). Two-dimensional metal-organic framework materials: Synthesis, structures, properties and applications. *Chemical Reviews*, *121*(7), 3751-3891.
- [153] Baig, N. (2022). Two-dimensional nanomaterials: A critical review of recent progress, properties, applications, and future directions. *Composites Part A: Applied Science and Manufacturing*, 107362.
- [154] Streetman, B. G., & Banerjee, S. (2000). *Solid-state electronic devices* (Vol. 4). New Jersey: Prentice hall.
- [155] Miró, P., Audiffred, M., & Heine, T. (2014). An atlas of two-dimensional materials. *Chemical Society Reviews*, *43*(18), 6537-6554.
- [156] Nathanael J. R., & David, C. (2014). Beyond Graphene: Stable Elemental Monolayers of Silicene and Germanene. *ACS Applied Materials & Interfaces*, *6* (10), 7743-7750

- [157] Beiranvand, R., & Valedbagi, S. (2015). Electronic and optical properties of h-BN nanosheet: A first principles calculation. *Diamond and Related Materials*, 58, 190-195.
- [158] Zhu, F. F., Chen, W. J., Xu, Y., Gao, C. L., Guan, D. D., Liu, C. H. & Jia, J. F. (2015). Epitaxial growth of two-dimensional stanene. *Nature materials*, 14(10), 1020-1025.
- [159] Reich, E. S. (2014). Phosphorene excites materials scientists. *Nature*, 506(7486), 19.
- [160] Li, X., Lin, B., Li, H., Yu, Q., Ge, Y., Jin, X., & Xiao, J. (2018). Carbon doped hexagonal BN as a highly efficient metal-free base catalyst for Knoevenagel condensation reaction. *Applied Catalysis B: Environmental*, 239, 254-259.
- [161] Cain, J. D., Hanson, E. D., Shi, F., & Dravid, V. P. (2016). Emerging opportunities in the two-dimensional chalcogenide systems and architecture. *Current Opinion in Solid State and Materials Science*, 20(6), 374-387.
- [162] Hoat, D. M., Naseri, M., Vu, T. V., Rivas-Silva, J. F., Hieu, N. N., & Coccoletzi, G. H. (2020). Structural, electronic and optical properties of CdO monolayer and bilayers: Stacking effect investigations. *Superlattices and Microstructures*, 145, 106644.
- [163] Abdullah, B. J., Azeez, Y. H., & Abdullah, N. R. (2023). A first-principles study on electronic structure, optical and thermal properties of BeX (X= C, N and O) monolayers. *Solid State Communications*, 361, 115080.
- [164] Yari, A., Boochani, A., & Rezaee, S. (2021). Electronic, optical, magneto-optical, and thermoelectric properties of the SrS graphene-like under Cr impurity. *Chemical Physics*, 551, 111355.
- [165] Vij, A., Gautam, S., Chae, K. H., Brajpuriya, R., & Lochab, S. P. (2012). Study of the electronic structure and luminescence of Mn-doped SrS phosphors. *Journal of the Korean Physical Society*, 61, 1604-1608.
- [166] Tholkappiyan, R., Satheesh Kumar, R., Mohamed Azarudeen, L., Anand Kumar, G., Vishista, K., & Hamed, F. (2016). Facile Synthesis of Cr-Doped SrS Phosphor: An Investigations on Structural, Vibrational, Morphological and Photoluminescence Properties. *Materials Focus*, 5(4), 342-346.
- [167] Souadkia, M., Bennecer, B., Kalarasse, F., & Mellouki, A. (2011). Ab initio calculation of vibrational and thermodynamic properties of SrX (S, Se, Te) in the B1 (NaCl) and B2 (CsCl) structures. *Computational materials science*, 50(5), 1701-1710.
- [168] Khenata, R., Baltache, H., Rérat, M., Driz, M., Sahnoun, M., Bouhafs, B., & Abbar, B. (2003). First-principle study of structural, electronic and elastic properties of SrS, SrSe and SrTe under pressure. *Physica B: Condensed Matter*, 339(4), 208-215.
- [169] Xiao-Cui, Y., Ai-Min, H., Jie, Y., Yong-Hao, H., Gang, P., Chun-Xiao, G., & Guang-Tian, Z. (2008). Theoretical prediction for structural stabilities and optical properties of SrS, SrSe and SrTe under high pressure. *Chinese Physics Letters*, 25(5), 1807.
- [170] Rached, D., Rabah, M., Benkhattou, N., Soudini, B., & Abid, H. (2004). Electronic and structural properties of strontium chalcogenides SrS, SrSe and SrTe. *physica status solidi (b)*, 241(11), 2529-2537.

- [171] Ouhe, J., Laiyu, L., & Xiangrong, C. (2007). Transition phase and elastic properties of SrS via first-principles calculations. *Journal of Atomic and Molecular Physics*, 24 (2), 424-426.
- [172] Lin, H. F., Lau, W. M., & Zhao, J. (2017). Magnetism in the p-type Monolayer II-VI semiconductors SrS and SrSe. *Scientific Reports*, 7(1), 45869.
- [173] Hou, X. Y., Cheng, Y., Hu, C. E., Piao, C. G., & Geng, H. Y. (2020). Thermoelectric properties of strontium sulfide via first-principles calculations. *Solid State Communications*, 305, 113755.
- [174] Yari, A., Boochani, A., & Rezaee, S. (2020). Thermoelectric and optical properties of the SrS graphene by DFT. *Philosophical Magazine*, 100(24), 3108-3124.
- [175] Rajput, K., & Roy, D. R. (2020, May). Investigation on the thermoelectric properties of single & bilayers of SrS. In *AIP Conference Proceedings* (Vol. 2220, No. 1). AIP Publishing.
- [176] Bourega, A., Doumi, B., Mokaddem, A., Sayede, A., & Tadjer, A. (2019). Electronic structures and magnetic performance related to spintronics of Sr<sub>0.875</sub>Ti<sub>0.125</sub>S. *Optical and Quantum Electronics*, 51(12), 385.
- [177] Hamidane, N., Baaziz, H., Ocah, H. Y., Baddari, K., Uğur, Ş., Uğur, G., & Charifi, Z. (2020). Ab initio full-potential study of the structural, electronic, and magnetic properties of the cubic Sr<sub>0.75</sub>Ti<sub>0.25</sub>X (X= S, Se, and Te) ternary alloys. *Journal of Superconductivity and Novel Magnetism*, 33, 3263-3272.
- [178] Kavitha, V., & Rani, M. P. (2023). An Investigation of the Luminescence and Hemocompatibility Properties of Eu<sup>3+</sup> Doped SrS Synthesized Via Sol–Gel Route. *Brazilian Journal of Physics*, 53(4), 100.
- [179] Samuel, S. O., Frank, M. L. E., Ogberohwo, E. P., Ekpekpko, A., Zhimwang, J. T., & Ikhiyoa, I. L. (2023). Influence of deposition voltage on strontium sulphide doped silver for optoelectronic application. *East European Journal of Physics*, (1), 189-196.
- [180] Chawla, P., Lochab, S. P., & Singh, N. (2010). Optical characterization of Bi doped SrS nanophosphors. *Materials Research Bulletin*, 45(7), 783-786.
- [181] Kumar, V., Pitale, S. S., Biggs, M. M., Nagpure, I. M., Ntwaeaborwa, O. M., & Swart, H. C. (2010). Synthesis of Ce<sup>3+</sup> doped SrS nanocrystalline phosphors using a simple aqueous method. *Materials Letters*, 64(6), 752-754.
- [182] Zhao, Y., Rabouw, F. T., Puffelen, T. V., Walree, C. A. V., Gamelin, D. R., de Mello Donegá, C., & Meijerink, A. (2014). Lanthanide-doped CaS and SrS luminescent nanocrystals: a single-source precursor approach for doping. *Journal of the American Chemical Society*, 136(47), 16533-16543.
- [183] Game, D. N., Ingale, N. B., & Omanwar, S. K. (2017). Synthesis and photoluminescence properties of Eu<sup>2+</sup> doped CaS and SrS phosphor for phosphor converted white light emitting diodes. *Journal of Materials Science: Materials in Electronics*, 28, 915-922.
- [184] Rapaport, D. C. (2004). *The art of molecular dynamics simulation*. Cambridge university press.
- [185] Williamson, A. J., Hood, R. Q., & Grossman, J. C. (2001). Linear-scaling quantum Monte Carlo calculations. *Physical Review Letters*, 87(24), 246406.



[186] Burke, K. (2012). Perspective on density functional theory. *The Journal of chemical physics*, 136(15), 150901.

# Chapter 2

## Theory and Computational Techniques

This chapter presents a fundamental *theoretical formulation* to address the challenges of the many-body problem through the application of density functional theory (DFT) and a *computational formulation* for ab-initio calculations. It also describes the software and methods used in the calculations carried out as part of our study for this dissertation.

### 2.1 Introduction

The host material investigated in this work is a semiconductor. The study of a semiconductor or any solid begins with the study of an ideal crystal at the atomic level at a temperature of 0°C. This crystal is made up of a series of atoms (or ions) that occupy precise positions and repeat periodically to form the material. The study is based on the interaction between electrons themselves and with nuclei. Due to the nature of particles (electrons and nuclei), their study requires the use of quantum mechanics, which requires solving the Schrödinger equation to determine the total energy of the system. All properties of materials can be determined by using appropriate computational tools to solve their quantum mechanical problem. This theory governs the electronic structure, which is responsible for other solid-state properties such as optical, electrical, magnetic, mechanical properties, etc. Electrons and nuclei form a highly complex N-body system, which makes solving the Schrödinger equation extremely difficult or even impossible. Various methods have been proposed to solve this problem. The method that has proven to be extremely successful and is the most widely used is density functional theory (DFT). With the introduction of density functional theory (DFT), it becomes possible to describe the particle system (nuclei and electrons) on the basis of fundamental data: lattice parameters and atomic numbers of the elements.

This theory allows us to gain insights into the composition of materials and predict their potential applications, thereby helping experimentalists develop novel devices. The study of the fundamental properties of atoms, molecules, solids and systems with reduced dimensions in their ground states forms

a central focus in the field of condensed matter physics. The fundamental understanding of the electronic structure of materials depends on solving the Schrödinger wave equation. This equation effectively illustrates the behavior of uncomplicated systems (such as the hydrogen atom problem), and numerical solutions are only possible for a limited number of atoms and molecules. However, when complex systems are involved, solving this equation and then estimating physical properties becomes extremely challenging. Although we know how to solve the problem, we still lack powerful tools to find the solution. Over the past century, there have been significant changes in the way we solve the Schrödinger wave equation for systems with many particles. The first breakthrough came in 1928 when Hartree approximated the wave function for many particles and gave an exact energy value for the hydrogen atom (-13.6 eV) [1]. Thereafter, efforts were made to find a better wave function using Slater determinants, but dealing with large systems remained difficult due to the need for extensive computational resources. The real progress came when three-dimensional electron density theories and energy function methods were introduced. This approach not only reduced computational effort but also proved remarkably accurate.

This chapter examines the development of this theory and provides a detailed explanation of the Kohn-Sham approach and the approximations used for exchange and correlation.

## 2.2 Theoretical Formulation

### 2.2.1 Many Body Problem within Schrödinger Wave Equation

Here we introduce the basics of many-body quantum mechanics. We begin by explaining the basic principles of quantum mechanics and the properties of wave functions. These ideas will later help us reformulate the problem in terms of electron density. We start with the Born-Oppenheimer approximation and other simplifications to solve the Schrödinger wave equation for systems with many particles. Finally, we examine how density functional theory (DFT) is formulated and applied to study various properties of materials in different dimensions, from bulk materials to low-dimensional structures. In their solid state, materials are composed of electrons, which have tiny mass and negative charge, and nuclei, which carry significant mass and positive charge compared to electrons. The macroscopic properties of materials are determined solely by the positions of these electrons and nuclei. As a result, electrons in materials exhibit quantum behavior and their interactions are closely linked by quantum mechanics. The complexity of the quantum mechanical system under consideration increases significantly as the number of electrons increases, resulting in the so-called many-body problem.

To put it more precisely: If there are  $N$  nuclei/electrons, there are a total of  $N+ZN$  interacting particles. These particles come into contact with each other through electromagnetic forces. Due to the tiny size of these interacting components, the system under study must be viewed from a quantum

mechanical perspective. Traditionally, the properties of a quantum mechanical system are determined by solving the time-independent Schrödinger wave equation, which is given as follows [2]:

$$\hat{H}\psi(\vec{r}_1, \vec{r}_2, \dots, \vec{R}_1, \vec{R}_2, \dots) = E\psi(\vec{r}_1, \vec{r}_2, \dots, \vec{R}_1, \vec{R}_2, \dots) \quad (\text{eq.1})$$

Here, the variables  $\vec{r}_i, \vec{R}_i$  represent the position vectors of electrons and nuclei, respectively,  $\hat{H}$  denotes the many-body Hamiltonian,  $E$  is the eigenvalue of energy and  $\psi$  represents the eigen wave function.

The Hamiltonian ( $\hat{H}$ ) in connection with many-body problems is based exclusively on electrostatic interactions (electron-electron, electron-nucleus, nucleus-nucleus) and kinetic energies. This essential quantity can be described with the following equation:

$$\hat{H} = -\frac{\hbar^2}{2m_e} \sum_i \nabla_i^2 - \sum_I \frac{\hbar^2}{2m_I} \nabla_I^2 - \sum_{i,I} \frac{Z_I e^2}{|\vec{r}_i - \vec{R}_I|} + \frac{1}{2} \sum_{i \neq j} \frac{e^2}{|\vec{r}_i - \vec{r}_j|} + \frac{1}{2} \sum_{I \neq J} \frac{Z_I Z_J e^2}{|\vec{R}_I - \vec{R}_J|} \quad (\text{eq.2})$$

The indices  $i$  and  $j$  are used for electrons and  $I$  and  $J$  for nuclei. On the left side of the equation provided, the first two terms represent the kinetic energy of electrons and nuclei, respectively. The remaining three terms characterize the energies associated with interactions: electron-nucleus, electron-electron, and internuclear Coulomb interactions. If we assume atomic units denoted as ( $\hbar^2 = e^2 = m = 4\pi\epsilon_0 = 1$ ), the Hamiltonian is further simplified to:

$$\hat{H} = -\frac{1}{2} \sum_i \nabla_i^2 - \sum_I \frac{1}{2m_I} \nabla_I^2 - \sum_{i,I} \frac{Z_I}{|\vec{r}_i - \vec{R}_I|} + \frac{1}{2} \sum_{i \neq j} \frac{1}{|\vec{r}_i - \vec{r}_j|} + \frac{1}{2} \sum_{I \neq J} \frac{Z_I Z_J}{|\vec{R}_I - \vec{R}_J|} \quad (\text{eq.3})$$

In terms of the operators, Eq.3 can be formulated as follows:

$$\hat{H} = \hat{T}_e + \hat{T}_N + \hat{V}_{eN} + \hat{V}_{ee} + \hat{V}_{NN} \quad (\text{eq.4})$$

Our goal is to investigate the many-body Schrödinger wave equation for a complex system using various techniques and approximations. To simplify this Hamiltonian, we use the Born-Oppenheimer approximation, which separates electronic and nuclear motions.

### 2.2.1.1 The Born-Oppenheimer Approximation (1927)

The forces on electrons and nuclei due to their electrical charge are comparably strong, leading to similar changes in their momenta due to these forces. This means that their impulses are comparable in size. Due to the significant difference in mass between nuclei and electrons, the velocities of the nuclei are significantly slower than those of the electrons. Consequently, we can assume that the nuclei are essentially stationary. This allows us to first solve the Hamiltonian for the electronic ground state and

determine the energy of the system in this configuration before dealing with nuclear motion. This separation between electronic and nuclear motion is called the Born-Oppenheimer (BO) approximation [3]. The separation between electronic and nuclear motion allows us to represent the complete wave function as a multiplication of electronic and nuclear wave functions, like this:

$$\psi(\vec{r}, \vec{R}) = \varphi(\vec{r}, \vec{R})\chi(\vec{R}) \quad (\text{eq.5})$$

Where  $\chi(\vec{R})$  represents a nuclear wave function and  $\varphi(\vec{r}, \vec{R})$  represents an electronic wave function that corresponds to certain nuclear positions. As a result, the Schrödinger wave equation for an electronic Hamiltonian takes the following form:

$$\hat{H}_e(\vec{R})\varphi(\vec{r}, \vec{R}) = (\hat{T}_e + \hat{V}_{ee}(\vec{r}) + \hat{V}_{eN}(\vec{r}, \vec{R}))\varphi(\vec{r}, \vec{R}) = \varepsilon_n(\vec{R})\varphi(\vec{r}, \vec{R}) \quad (\text{eq.6})$$

This produces a series of normalized eigenfunctions  $\varphi(\vec{r}, \vec{R})$  and eigenvalues  $\varepsilon_n(\vec{R})$  that depend on the kernel positions  $\vec{R}$ . For each solution, there is a kernel eigenvalue equation:

$$(\hat{T}_N + \hat{V}_{NN}(\vec{r}) + \varepsilon_n(\vec{R}))\chi(\vec{R}) = E\chi(\vec{R}) \quad (\text{eq.7})$$

Since many of the desired properties can be derived from the ground state wave function and the energy of the system, our focus is on finding a technique to determine the ground state corresponding to the lowest energy state of the system. The variational principle provides a method of reaching the ground state by minimizing the total energy of the system.

### 2.2.1.2 Variational Principle: Ground State of the System

Using the variational principle, the energy calculation derived from an approximate wave function  $\psi(\vec{r})$  acts as an upper bound on the true ground state energy  $E_0$ . Let us consider a system that exists in a state  $|\psi\rangle$ . The energy is estimated by evaluating the expectation value of the Hamiltonian and is represented as follows:

$$E(\psi) = \frac{\langle \psi | \hat{H} | \psi \rangle}{\langle \psi | \psi \rangle} \quad (\text{eq.8})$$

By using the estimated value of the energy expectation ( $E$ ) in the state  $|\psi\rangle$ , it becomes possible to approximate the eigenvalue and eigenfunction of energy using the variational principle.

$$\delta E(\psi) = 0 \quad (\text{eq.9})$$

The variational principle helps approximate the ground state energy of a system. Therefore it is important for ground state calculations. However, the techniques for implementing this principle can vary depending on the approach used to estimate the wave function and associated energy for the system. Numerous approximations have been developed to find the optimal wave function that corresponds to the antisymmetry property and includes various electron interactions within the system. To estimate the desired wave function, the Hartree and Hartree-Fock approximations are used, which will be discussed in more detail below.

### 2.2.1.3 Independent Electrons Approximations

#### a) Hartree Approach (1928)

The Born-Oppenheimer approximation simplified the complexity of the Schrödinger wave equation, but the challenge remained due to electron-electron interactions. Hartree addressed this complexity by treating electrons as separate entities, resulting in the Hartree approximation [1]. In this approach, the overall wave function is represented as a product of individual one-electron wave functions. Consequently,

$$\varphi(\vec{r}, \vec{R}) = \varphi_1(\vec{r}_1, \vec{R})\varphi_2(\vec{r}_2, \vec{R}) \dots \varphi_M(\vec{r}_M, \vec{R}) \quad (\text{eq.10})$$

$$= \prod_{k=1}^M \varphi_k(\vec{r}_k, \vec{R}) \quad (\text{eq.11})$$

This is known as the Hartree product. Here the functions  $\varphi_k(\vec{r}_k, \vec{R})$  are also called orbitals and must satisfy the condition of being orthonormal to each other, which can be expressed as  $\int dr \varphi_k^*(r)\varphi_k'(r) = \delta_{kk'}$ . This approximation does not satisfy the antisymmetry principle, also known as Pauli's exclusion principle [4]. This principle states that the wave function describing fermions must exhibit antisymmetry when exchanging any set of spatial and spin coordinates. Therefore, Hartree theory requires adjustments, a role that Hartree-Fock theory takes on.

#### b) Hartree-Fock Approach (1930)

The emergence of the Pauli exclusion principle led to the development of the Hartree-Fock method, which allowed the representation of the overall Hamiltonian for an N-electron system ( $H$ ) as the sum of individual electron Hamiltonians ( $H_i$ ), meaning  $H = \sum_i H_i$ . Furthermore, the overall wave function is expressed as a Slater determinant, which consists of individual electron wave functions. In the case of an N-electron system, the wave function can be formulated as follows:

$$\boldsymbol{\varphi} = \frac{1}{\sqrt{N!}} \begin{vmatrix} \chi_1(x_1) & \chi_2(x_2) & \cdots & \chi_N(x_N) \\ \chi_1(x_1) & \chi_2(x_2) & \cdots & \chi_N(x_N) \\ \vdots & \vdots & \ddots & \vdots \\ \chi_1(x_1) & \chi_2(x_2) & \cdots & \chi_N(x_N) \end{vmatrix} \quad (\text{eq.12})$$

The prefactor of  $\frac{1}{\sqrt{N!}}$  guarantees the fulfillment of the normalization requirement for the wave function  $\boldsymbol{\varphi}$ . The determinant represented in Eq. 12 is recognized as a Slater determinant [5]. In the equations provided previously, we switched our notation from using spatial orbitals ( $\boldsymbol{\varphi}(\mathbf{r})$ ) to introducing spin orbitals ( $\boldsymbol{\chi}(\mathbf{x})$ ). Therefore, a spin orbital is essentially the result of multiplying a spatial orbital by a spin function, represented as  $\boldsymbol{\chi}(\mathbf{x}) = \boldsymbol{\varphi}(\vec{\mathbf{r}}) \boldsymbol{\sigma}$ . Here  $\mathbf{x} = \{\vec{\mathbf{r}}, \boldsymbol{\sigma}\}$  denotes the combined set of space-spin coordinates, where  $\mathbf{r}$  stands for the space coordinate and  $\boldsymbol{\sigma}$  stands for a spin coordinate. This spin coordinate can take one of two possible values:  $\boldsymbol{\sigma}_1(\uparrow)$  or  $\boldsymbol{\sigma}_2(\downarrow)$ . This approximation gives the full energy as the Hartree-Fock energy (EHF), which is represented as follows:

This approximation gives the full energy as the Hartree-Fock energy (EHF), which is represented as follows:

$$E_{HF} = \langle \chi_i | \mathbf{h} | \chi_i \rangle + \frac{1}{2} \sum_{ij} \langle \chi_i \chi_j | \frac{1}{r_{ij}} | \chi_i \chi_j \rangle - \frac{1}{2} \sum_{ij} \langle \chi_i \chi_j | \frac{1}{r_{ij}} | \chi_i \chi_j \rangle \quad (\text{eq.13})$$

In the context of the first term,  $\mathbf{h}$  represents the one-electron operator and can be formulated as follows:

$$\mathbf{h}(i) = T_e + V_{ee} = -\frac{1}{2} \nabla_i^2 - \sum_A \frac{Z_A}{R_{Ai}} \quad (\text{eq.14})$$

The second term refers to a two-electron system and its integral form is as follows:

$$\begin{aligned} \left\langle \chi_i \chi_j \left| \frac{1}{r_{ij}} \right| \chi_i \chi_j \right\rangle &= \sum_{ij} \int dx dx' \frac{\chi_i^*(x) \chi_j^*(x') \chi_i(x) \chi_j(x')}{|\vec{\mathbf{r}} - \vec{\mathbf{r}}'|} \\ &= \sum_{ij} \int dx dx' \frac{|\chi_i(x)|^2 |\chi_j(x')|^2}{|\vec{\mathbf{r}} - \vec{\mathbf{r}}'|} \\ &= \sum_{ij} J_{ij} \end{aligned} \quad (\text{eq.15})$$

Where  $J_{ij}$  is called the Coulomb integral. The third term also refers to a two-electron system and its integral form is as follows:

$$\begin{aligned} \left\langle \chi_i \chi_j \left| \frac{1}{r_{ij}} \right| \chi_j \chi_i \right\rangle &= \sum_{ij} \int dx dx' \frac{\chi_i^*(x) \chi_j^*(x') \chi_j(x) \chi_i(x')}{|\vec{\mathbf{r}} - \vec{\mathbf{r}}'|} \\ &= \sum_{ij} K_{ij} \end{aligned} \quad (\text{eq.16})$$

Where  $K_{ij}$  is identified as **Exchange Integral**.

This approximation misses the Coulomb correlation, causing the total electronic energy to deviate from the exact solution. Consequently, the Hartree-Fock energy constantly exceeds the exact energy, and this deviation is called the correlation energy [6]. In addition to the Coulomb correlation, solving the Schrödinger wave equation presents another major challenge, known as the 3N variable problem. These problems of correlation energy and complexity due to 3N variables have been addressed by an innovative method called density functional theory (DFT), which is examined in the next subsection.

#### 2.2.1.4 Early Density Functional Theories: The Thomas-Fermi Model

First, in 1927, Thomas and Fermi (TF) suggested that atoms could be imagined as uniformly distributed clouds of negatively charged electrons surrounding nuclei in a six-dimensional phase space that includes momentum and coordinates. This represented a significant simplification of the complicated many-body problem. It is instructive to explore the basic concepts of the TF approximation before delving into a more precise theory, namely **density functional theory (DFT)**. The Thomas Fermi method [7] takes a different approach based on the electron density within the system. This method assumes that electrons move in an external potential. The main goal is to calculate the potential  $V(\vec{r})$  and the electron density  $n(\vec{r})$ . Electrons are assumed to be uncorrelated and their kinetic energy is estimated using a local approximation based on the behavior of free electrons. The potential can be found by solving the Poisson equation, and the requirement for a constant chemical potential leads to the Thomas-Fermi equation for  $n(\vec{r})$ . Although this method is not successful for real systems, it serves as a prototype for density functional theory because it focuses on the electron density  $n(\vec{r})$ , which is expressed as:

$$n(\vec{r}) = N \int d\vec{r}_2 \dots \dots d\vec{r}_N |\psi(\vec{r}, \vec{r}_2, \dots \dots \vec{r}_N)|^2 \quad (\text{eq.17})$$

The resulting energy functional includes classical expressions for nucleus-nucleus and electron-electron potentials, which were represented as follows:

$$E_{TF}[n(\vec{r})] = \frac{3}{10} (3\pi^2)^{\frac{2}{3}} \int n^{\frac{5}{3}}(\vec{r}) d\vec{r} - Z \int \frac{n(\vec{r})}{\vec{r}} d\vec{r} + \frac{1}{2} \iint \frac{n(r_1)n(r_2)}{\vec{r}_{12}} d\vec{r}_1 d\vec{r}_2 \quad (\text{eq.18})$$

This model provides a good solution to the Schrödinger equation, but a clear relationship between  $n(\vec{r})$  and  $\psi(\vec{r})$  is required. A refined version of the Thomas-Fermi model was introduced by incorporating exchange effects via an exchange functional. However, this theory still gave inaccurate results for systems with many particles. The problem was finally solved when Hohenberg and Kohn showed that knowledge of the ground state electron density  $n(\vec{r})$  for any electronic system, independent of interactions, uniquely defines the system.



### 2.2.1.5 Density Functional Theory: An Ab-initio Approach (1964)

This model provides a good solution to the Schrödinger equation, but a clear relationship between  $\mathbf{n}(\vec{\mathbf{r}})$  and  $\psi(\vec{\mathbf{r}})$  is required. A refined version of the Thomas-Fermi model was introduced by incorporating exchange effects via an exchange functional. However, this theory still gave inaccurate results for systems with many particles. The problem was finally solved when Hohenberg and Kohn showed that knowledge of the ground state electron density  $\mathbf{n}(\vec{\mathbf{r}})$  for any electronic system, independent of interactions, uniquely defines the system.

- **Theorem I:** In a system of interacting particles under an external potential  $V_{ext}(\vec{\mathbf{r}})$ , the ground state density  $\mathbf{n}_0(\vec{\mathbf{r}})$  uniquely determines the external potential.
- **Theorem II:** Using the electron density  $\mathbf{n}(\vec{\mathbf{r}})$ , a universal functional for the energy  $\mathbf{E}[\mathbf{n}]$  can be set up that is applicable to any external potential  $V_{ext}$ . For a given  $V_{ext}$ , the ground state energy of the system is the minimum value of the energy functional, and the corresponding electron density  $\mathbf{n}(\vec{\mathbf{r}})$ , which minimizes this functional, is the exact ground state density. Thus, the total energy of the system can be expressed as:

$$E[\mathbf{n}] = F[\mathbf{n}] + \int d^3\vec{\mathbf{r}} V_{ext}(\vec{\mathbf{r}}) \mathbf{n}(\vec{\mathbf{r}}) \quad (\text{eq.19})$$

The function  $F[\mathbf{n}] = T[\mathbf{n}] + V_{ee}[\mathbf{n}]$  includes both the kinetic energy and all electron-electron interactions. This functional is universal and independent of external potential. Therefore, ideally it should remain consistent across all systems. However, the theorems do not provide a method to determine the exact structure of this functional. Therefore, practical applications require approximations where the functional must be approximated for feasible calculations.

### 2.2.1.6 The Kohn-Sham Formalism (1965)

The Kohn-Sham equation [10] represents the Schrödinger wave equation for a fictitious system consisting of non-interacting particles, typically electrons. This constructed system yields the same density as any given set of interacting particles. The Kohn-Sham equation is characterized by a locally effective (imaginary) external potential in which the non-interacting particles move. This potential is usually referred to as  $V_{KS}(\vec{\mathbf{r}})$  or  $V_{eff}(\vec{\mathbf{r}})$  and is called the Kohn-Sham potential. Since the particles in the Kohn-Sham system are non-interacting fermions, the Kohn-Sham wave function becomes a single Slater determinant formed from a collection of orbitals. The practical implementation of DFT was proposed by Kohn and Sham. The concept of the Kohn-Sham approach is to replace the interacting many-body system with a complementary system of non-interacting particles that have the same ground state. Consequently, the total energy functional can be expressed as:

$$E[\mathbf{n}] = \int d^3\vec{r} V_{ext}(\vec{r}) n(\vec{r}) + T_s(\mathbf{n}) + \frac{1}{2} \int d^3\vec{r} d^3\vec{r}' \frac{n(\vec{r})n(\vec{r}')}{|\vec{r}-\vec{r}'|} + E_{xc} \quad (\text{eq.20})$$

Where  $V_{ext}$  is the external potential;  $T_s$  is the kinetic energy term of the hypothetical non-interacting electrons; The third term is the classical electrostatic energy (Hartree) of the electrons and all the many body effects are summarized in the exchange correlation energy term  $E_{xc}$ . By minimizing the Kohn-Sham energy function with respect to the electron density  $n(\vec{r})$ , a Kohn-Sham equation is derived that is similar to the Schrödinger equation:

$$H_{KS}(\vec{r})\psi_i(\vec{r}) = \left[ -\frac{1}{2}\nabla^2 + V_{KS}(\vec{r}) \right] \psi_i(\vec{r}) = \varepsilon_i \psi_i(\vec{r}) \quad (\text{eq.21})$$

The potential  $V_{KS}$ , in the above equation is an effective potential that includes the external potential  $V_{ext}$ , the Hartree potential  $V_H$ , which is represented by the integral of  $\int d^3\vec{r}' \frac{n(\vec{r}')}{|\vec{r}-\vec{r}'|}$  and the exchange correlation potential  $V_{XC} = \frac{\delta E_{XC}[\mathbf{n}]}{\delta n(\vec{r})}$ , where electrons move independently of each other.  $\psi_i$  represents the eigenfunctions corresponding to the eigenvalues  $\varepsilon_i$ . Consequently, the Kohn-Sham Hamiltonian in Eq.21 can be expressed as:

$$H_{KS}(\vec{r}) = -\frac{1}{2}\nabla^2 + V_{ext}(\vec{r}) + V_H(\vec{r}) + V_{XC}(\vec{r}) \quad (\text{eq.22})$$

This  $H_{KS}$  is related to the functional derivative of energy as follows:

$$\frac{\delta E}{\delta \psi_i^*(\vec{r})} = H_{KS}\psi_i(\vec{r}) \quad (\text{eq.23})$$

The Kohn-Sham equations are theoretically precise. However, the functional form of  $E_{XC}[\mathbf{n}(\vec{r})]$  remains unknown and requires further approximations. The total energy contribution is made up of four terms (Eq. 22): the kinetic energy ( $-\frac{1}{2}\nabla^2$ ), and the called the effective potential ( $V_{eff}(\vec{r})$ ), that englobes the classical Coulomb potential ( $V_{ext}(\vec{r})$ ), the Hartree potential ( $V_H(\vec{r})$ ) and the exchange correlation potential ( $V_{XC}(\vec{r})$ ). The exchange correlation potential ( $V_{XC}(\vec{r})$ ) includes a variety of many-body and quantum effects. Let us briefly discuss these terms one by one.

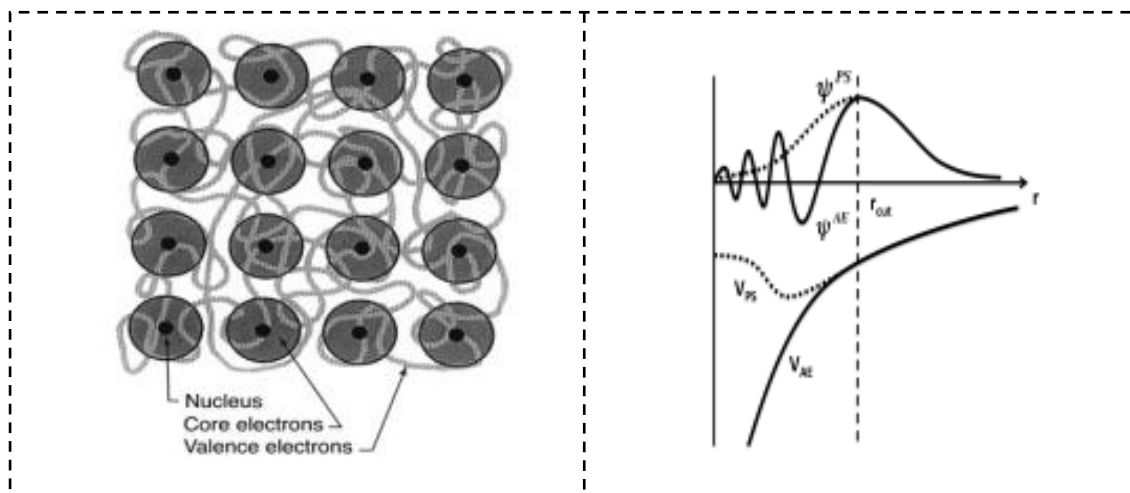
- **Kinetic Energy**

Kohn and Sham introduced a series of orbitals from which electron density can be calculated. It is important to note that these Kohn-Sham orbitals generally do not directly represent actual electron density. However, the connection between the Kohn-Sham orbitals and real electronic wave functions is that both give the same charge density. To calculate the kinetic energy term, the Kohn-Sham orbitals are used, as shown below:

$$T_s[n] = \sum_{i=1}^N \int d\vec{r} \cdot \psi_i^*(\vec{r}) \left(-\frac{1}{2} \nabla^2\right) \psi_i(\vec{r}) \quad (\text{eq.24})$$

- **Coulomb Potential: Substituted with a Pseudopotential**

The  $V_{ext}(\vec{r})$  term characterizes the interaction of the electron with various atomic nuclei present, which essentially boils down to the Coulomb potential. To deal with this aspect, a technique is used in which the Coulomb potential is replaced by a pseudopotential [10]. It is generally accepted that core electrons are minimally involved in bond formation and most material properties depend primarily on valence electrons. Therefore, it is more practical to focus on valence electrons. These valence electrons experience the Coulomb potential, which is exerted by an inert ionic nucleus (pseudonucleus, consisting of core and core electrons). Consequently, the system is simplified to handle fewer electrons, as shown in Figure 1(a). Essentially, a pseudopotential serves as an approximation for the total nuclear potential. The effectiveness of a pseudopotential depends on how closely it reproduces the actual results. When creating a pseudopotential, it is necessary to ensure that the all-electron wave function agrees with the pseudowave function within a certain limiting radius, as shown in Figure 1(b).



(a) Pseudopotential model: The movement of external electrons occurs within a stable configuration of chemically inert ionic nuclei that include both core and core electrons [11].

(b) Schematic representation of an atomic all-electron wave function (solid line) next to the corresponding atomic pseudo-wave function (dashed line), accompanied by its corresponding external Coulomb potential and pseudopotential [11].

**Figure 1.** Pseudo potential approach – pseudo wave function and pseudo potential representation.

- **Hartree Potential**

The Hartree potential describes the Coulomb repulsion experienced by the electron (at position  $\vec{r}$ ), as shown in the Kohn-Sham equations. This repulsion is determined by the total charge density encompassing all electrons (positioned at  $\vec{r}'$ ) within the given scenario. The expression for the Hartree potential is as follows:

$$V_H = \int d^3 \vec{r}' \frac{n(\vec{r}')}{|\vec{r} - \vec{r}'|} \quad (\text{eq.25})$$

To solve the KS equation we need the Hartree potential, which is closely linked to the charge density of the system. To determine the charge density, we rely on single-particle wave functions, which can only be obtained by solving the KS equations. This leads us to a challenge of solving a set of self-consistent equations. This process involves one iteration starting with an initial set of single-particle wave functions to derive the effective potential. The solution obtained using this method is called a self-consistent solution. The approach to solving this complicated equation is systematically shown in Figure 2.

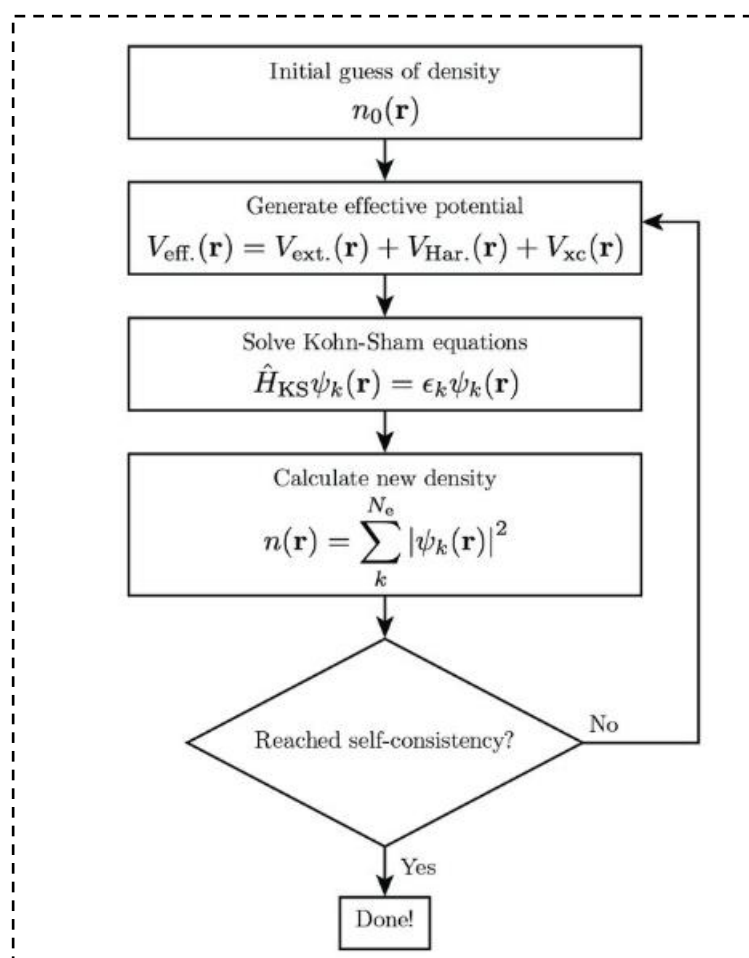


**Figure 2.** Flowchart illustrating the various steps within the Kohn-Sham iterative loop in Density Functional Theory (DFT) codes.

- **Exchange-Correlation Potential**

The most important potential term in KS equations is  $V_{xc}$ , which is used to account for exchange and correlation effects. In the following sections, we first deal with the elucidation of exchange and correlation. We then move on to discussing various approximations that are essential for estimating exchange and correlation.

### 2.2.1.7 Exchange and Correlation

#### 2.2.1.7.1 Exchange-correlation Hole

The principle of orbital antisymmetry dictates that electrons with the same spin must inhabit different orthogonal orbitals, requiring spatial separation between them. This results in a reduced electron density called an exchange hole, which results in reduced repulsion and consequently reduced system energy. This phenomenon causes the electrons to move away from each other, effectively eliminating the self-interaction inherent in the Hartree energy. Consequently, the exchange energy refers to the interaction between an exchange hole and the electron density over a certain range. Electrons with different spins can share the same orbit, but their mutual negative charge forces them to stay at a distance from each other. This electronic adjustment results in reduced electron density around each electron, resulting in lower attraction energy. This phenomenon is called the correlation hole [12]. The XC hole is predominantly determined by the exchange component at higher electron densities because of the Pauli exclusion principle, which is more pronounced when electrons are close to each other. However, at lower electron densities, the correlation component becomes more important and becomes comparable to the exchange component. Since a significant portion of the kinetic energy and the long-range Hartree energy are treated separately, the remaining XC energy can be reasonably approximated as a local or semi-local function of electron density. Furthermore, the shape of the XC hole is assumed to be spherically symmetric in three dimensions. The local XC energy per electron is therefore the electrostatic interaction energy between an electron at position  $\vec{r}$  and the XC hole density at position  $\vec{r}'$  expressed as:

$$E_{xc}[n] = \frac{1}{2} \int n(\vec{r}) d\vec{r} \int \frac{n_{xc}(\vec{r}, \vec{r}')}{|\vec{r} - \vec{r}'|} d\vec{r}' \quad (\text{eq.26})$$

Where  $n_{xc}(\vec{r}, \vec{r}')$  denotes the average coupling factor of the exchange correlation hole,

$$n_{xc}(\vec{r}, \vec{r}') = \int_0^1 n_{xc}^\lambda(\vec{r}, \vec{r}') d\lambda \quad (\text{eq.27})$$

Here  $\lambda$  is the range –separation parameter.

Consequently, it becomes possible to define the exchange correlation density as follows:

$$\epsilon_{xc}[\mathbf{n}(\vec{r})] = \frac{1}{2} \int \frac{n_{xc}(\vec{r}, \vec{r}')}{|\vec{r} - \vec{r}'|} d\vec{r}' \quad (\text{eq.28})$$

The exchange-correlation hole can be divided into two parts: the exchange hole (Fermi hole) and the correlation hole (Coulomb hole),

$$\mathbf{n}_{xc}(\vec{r}, \vec{r}') = \mathbf{n}_x(\vec{r}, \vec{r}') + \mathbf{n}_c(\vec{r}, \vec{r}') \quad (\text{eq.29})$$

The exchange hole,  $\mathbf{n}_x$  can be characterized using the Hartree-Fock expression for energy,

$$E_x[\mathbf{n}(\vec{r})] = \frac{1}{2} \int \mathbf{n}(\vec{r}) d\vec{r} \int \frac{n_x(\vec{r}, \vec{r}')}{|\vec{r} - \vec{r}'|} d\vec{r}' \quad (\text{eq.30})$$

Therefore, the exchange-correlation functional can be formulated as follows:

$$E_{xc}[\mathbf{n}(\vec{r})] = \int \mathbf{n}(\vec{r}) \epsilon_{xc}[\mathbf{n}(\vec{r})] d\vec{r} \quad (\text{eq.31})$$

By clearly understanding the specific structure of the exchange-correlation density, we can approach the exact ground state. In the next section, we will examine various approximations aimed at estimating the effects of exchange and correlation.

### 2.2.1.7.2 Exchange-Correlation Energy Approximation

In order to determine the exact ground state of a system, knowledge of the exact exchange correlation functional is crucial. Unfortunately, obtaining the exact formula is a difficult task. To fill this gap, various approximations have been developed, including the local density approximation (LDA), the generalized gradient approximation (GGA), the hybrid GGA, the meta-GGA, the Tran-Blaha modified Becke-Johnson function (TB- mBJ) and more. In the following subsection, we will discuss LDA, GGA, TB-mBJ and HSE approximations in detail.

#### a) Local Density Approximation (LDA)

The local density approximation (LDA) [13] is considered one of the oldest, simplest and yet most important exchange-correlation functionals. In this approach, the actual exchange-correlation energy of a system is approximated by the exchange-correlation energy of a uniform electron gas with the same density. This uniform gas represents the only system for which the exact form of the exchange-correlation energy is known. The LDA relies solely on local density, resulting in a total energy expression:

$$E_{xc}^{LDA}[\mathbf{n}(\vec{r})] = \int \mathbf{n}(\vec{r}) \epsilon_{xc}^{hom}[\mathbf{n}(\vec{r})] d\vec{r} \quad (\text{eq.32})$$

In this context,  $\epsilon_{xc}^{hom}$  denotes the exchange-correlation energy density of a homogeneous electron gas characterized by the electron density  $\mathbf{n}(\vec{r})$ , while the exchange-correlation potential is obtained as an energy functional derivative, as shown below:

$$V_{xc}^{LDA}[\mathbf{n}(\vec{r})] = \frac{\delta E_{xc}^{LDA}[\mathbf{n}(\vec{r})]}{\delta \mathbf{n}(\vec{r})} \quad (\text{eq.33})$$

LDA has been extended to include spin-polarized systems through the local **spin-polarized density approximation (LSDA)**, which is expressed as follows:

$$E_{xc}^{LDA}[\mathbf{n}_{\uparrow}(\vec{r}), \mathbf{n}_{\downarrow}(\vec{r})] = \int \mathbf{n}(\vec{r}) \epsilon_{xc}^{hom}[\mathbf{n}_{\uparrow}(\vec{r}), \mathbf{n}_{\downarrow}(\vec{r})] d\vec{r} \quad (\text{eq.34})$$

As already mentioned, the energy associated with the exchange hole  $\mathbf{n}_x$  can be obtained from the exact analytical formula of Dirac [14]:

$$E_x[\mathbf{n}(\vec{r})] = -\frac{3}{4} \left( \frac{9}{4\pi^2} \right)^{\frac{1}{3}} \frac{1}{r_s} \approx \frac{-0.4582}{r_s} \quad (\text{eq.35})$$

Where  $r_s$  is the Seitz radius.

The local density approximation (LDA) provides a reasonably accurate estimate of the exchange energy and typically remains within a 10% margin of error. However, the correlation energy, which is usually much smaller, is often overestimated by a factor of two. Interestingly, these two errors partially compensate for each other. LDA is found to be quite reliable in predicting ionization energies of atoms, dissociation energies of molecules, and cohesion energies, with accuracy ranging between 10% and 20%. Surprisingly, LDA achieves an astonishingly precise accuracy of about 2% for bond lengths in both molecules and solids. Nevertheless, there are cases where LDA is inadequate, for example in systems that are strongly influenced by electron-electron interactions, such as heavy fermions. To overcome the limitations of LDA, the next natural progression is to include not only the density  $\mathbf{n}(\vec{r})$  at a given point  $\mathbf{r}$  but also *the charge density gradient*  $\nabla \mathbf{n}(\vec{r})$  to account for inhomogeneous nature of true electron density. This advance leads to the development of the **generalized gradient approximation (GGA)** for exchange-correlation energy, a more sophisticated approach that increases the accuracy of the calculations.

### b) Generalized Gradient Approximation (GGA)

Hohenberg and Kohn proposed an improvement to LDA [15, 16] by incorporating a higher-order density gradient expansion term, called the gradient expansion approximation (GEA). However, the GEA is unable to reproduce the essential features of the exchange correlation hole associated with the LDA and loses its physical meaning. This is evident in the violation of the sum rules and the lack of

restrictions on the negative exchange gap [17]. Despite these shortcomings, it provides a way to construct the exchange correlation hole for GGA [15] by using a real space cutoff of the GEA exchange hole. By introducing an analytical function called gain function  $F_{xc}[\mathbf{n}(\vec{r}), \nabla \mathbf{n}(\vec{r})]$ , one can modify the LDA energy density to obtain the GGA exchange-correlation energy:

$$E_{xc}^{GGA}[\mathbf{n}(\vec{r})] = \int \mathbf{n}(\vec{r}) \epsilon_{xc}^{GGA}[\mathbf{n}(\vec{r})] F_{xc}[\mathbf{n}(\vec{r}), \nabla \mathbf{n}(\vec{r})] d\vec{r} \quad (\text{eq.36})$$

When the energy functional is expressed in integral form, the general expression for  $E_{xc}^{GGA}[\mathbf{n}(\vec{r})]$  takes the following form:

$$V_{xc}^{GGA}[\mathbf{n}(\vec{r})] = \frac{\delta E_{xc}^{GGA}}{\delta \mathbf{n}(\vec{r})} = \mathbf{n}(\vec{r}) \frac{d\epsilon_{xc}^{GGA}[\mathbf{n}(\vec{r})]}{d\mathbf{n}(\vec{r})} + \epsilon_{xc}^{GGA}[\mathbf{n}(\vec{r})] \quad (\text{eq.37})$$

If we include the consideration of spin variables, the expression for the energy functional in the framework of the generalized gradient approximation (GGA) becomes:

$$E_{xc}^{GGA}[\mathbf{n}_{\uparrow}(\vec{r}), \mathbf{n}_{\downarrow}(\vec{r})] = \int \mathbf{n}(\vec{r}) \epsilon_{xc}^{GGA}[\mathbf{n}_{\uparrow}(\vec{r}), \mathbf{n}_{\downarrow}(\vec{r}), \nabla \mathbf{n}_{\uparrow}(\vec{r}), \nabla \mathbf{n}_{\downarrow}(\vec{r})] d\vec{r} \quad (\text{eq.38})$$

Perdew and Wang introduced a diverse set of GGA methods, one of which stood out and was later simplified to become known as the **PBE** functional, which bears the names of its creators: *Perdew, Burke, and Ernzerhof* [18]. GGA methods represented a significant advance over LDA because they took into account not only the local electron density but also its gradients. PBE in particular gained widespread recognition due to its simplicity and impressive accuracy. Its main features include considerations of the local electron density, its gradient and second-order gradients within the gain factors  $F(x)$  and  $F(c)$ . This multifaceted approach has made PBE the first choice for researchers in various fields due to its ability to accurately describe a wide range of materials and their properties. However, it is important to recognize the limitations of LDA and GGA. Despite their advances, these methods are often inadequate when attempting to predict the band gaps in semiconductors or to capture the complicated electronic structures of highly correlated systems such as Mott insulators. In the field of DFT, the exchange-correlation energy plays an indispensable role. It encompasses the complex quantum mechanical effects arising from electron-electron interactions, an aspect not explicitly considered in LDA and GGA. Therefore, accurate estimation of this energy component is of paramount importance for ensuring the reliability of DFT calculations.

In addition, a revised version of the PBE function, known as *revPBE* [19], emerged to address specific cases where improvements were required. It simplifies the mathematical formulation of the exchange energy while maintaining the accuracy of the original PBE function. Recently, a new GGA approximation for the exchange energy functional was introduced by *Wu and Cohen* aptly called it the *WC approximation* [20]. This innovation has made significant progress in improving the calculation of



structural properties in solid materials. What sets WC apart is its commendable computational efficiency and its unique property of being parameter-free, which represents a significant advance in the field of DFT. These developments highlight ongoing efforts to refine exchange-correlation functional in DFT, with a focus on improving its accuracy and applicability in the study of a variety of materials and phenomena in the fields of condensed matter physics and materials science.

*c) Modified Becke and Johnson Potential (mBJ)*

While the two previously detailed approximations provide accurate predictions for structural properties, their performance deteriorates when it comes to electronic properties, particularly bandgap widths. The gaps calculated using LDA or GGA are often significantly underestimated. To resolve this discrepancy, an approach was developed in 2006 by Becke and Johnson that aims to correct the energy gap values calculated by LDA and GGA [21]. A later development by Tran and Blaha in 2007 led to the modified Tran-Blaha potential (TB-mBJ), an adaptation of the Becke-Johnson exchange potential [22]. This change has the form:

$$V_{x,\sigma}^{mBJ}(\vec{r}) = cV_{x,\sigma}^{BR}(\vec{r}) + (3c - 2) \frac{1}{\pi} \sqrt{\frac{5}{12} \frac{2t_{\sigma}(\vec{r})}{n_{\sigma}(\vec{r})}} \quad (\text{eq.39})$$

Where,

$n_{\sigma}(\vec{r}) = \sum_{i=1}^N |\psi_i|^2$  is the electron density.

$t_{\sigma}(\vec{r}) = \frac{1}{2} \sum_{i=1}^N |\psi_i^* \nabla \psi_i|^2$  is the kinetic energy density.

And 
$$V_{x,\sigma}^{BR}(\vec{r}) = -\frac{1}{b_{\sigma}(\vec{r})} (1 - e^{-x_{\sigma}(\vec{r})} - \frac{1}{2} x_{\sigma}(\vec{r}) e^{-x_{\sigma}(\vec{r})}) \quad (\text{eq.40})$$

is the Becke-Roussel potential [23], which was proposed to model the Coulomb potential arising from exchange holes.

The term in Eq.40 is determined using the following equation:

$$\frac{x_{\sigma}(\vec{r}) e^{-2x_{\sigma}(\vec{r})/3}}{x_{\sigma}(\vec{r}) - 2} = \frac{2}{3} \frac{\pi^2}{\pi^3} \frac{n_{\sigma}^{5/3}(\vec{r})}{Q_{\sigma}(\vec{r})} \quad (\text{eq.40})$$

Where

$$Q_{\sigma}(\vec{r}) = \frac{1}{6} (\nabla^2 n_{\sigma}(\vec{r}) - 2\gamma D_{\gamma}(\vec{r})) \quad (\text{eq.41})$$

With

$$D_{\sigma}(\vec{r}) = 2t_{\sigma}(\vec{r}) - \frac{1}{4} \frac{|\nabla n_{\sigma}|^2}{n_{\sigma}(\vec{r})} \quad (\text{eq.42})$$

The  $\gamma$  parameter is empirically determined by the least squares fitting of the Hartree-Fock exchange energy.

The  $b_{\sigma}$  term is expressed by the following relationship:

$$b_{\sigma}(\vec{r}) = \left( \frac{x_{\sigma}^3(\vec{r}) e^{-x_{\sigma}(\vec{r})}}{8\pi n_{\sigma}(\vec{r})} \right)^{\frac{1}{3}} \quad (\text{eq.43})$$

Or  $\sigma$  represents the notation for spin.

The change is reflected in the inclusion of the parameter “c” in the functional formula. It is worth noting that setting  $c = 1$  restores the Becke-Johnson function. The proposed representation for “c” has the following form:

$$c = \alpha + \beta \left( \frac{1}{V_{cell}} \int \frac{\nabla n(\vec{r})}{n(\vec{r})} d\vec{r} \right)^{1/2} \quad (\text{eq.44})$$

$\alpha$  and  $\beta$  are parameters that can be adjusted (with the values  $\alpha = -0.012$  and  $\beta = 1.023$  (Bohr)<sup>1/2</sup> in the WIEN2K code [24]), while  $V_{cell}$  denotes the volume of the unit cell within the studied system.

It is important to highlight that the mBJ exchange potential involves the exchange of electron holes. This exchange potential has been self-consistently integrated into the WIEN2K code [24]. In addition, the correlation potential is given, which is determined using one of the GGA versions. In our calculations we used the PBE-GGA correlation potential.

#### d) *Heyd-Scuseria-Ernzerhof Functional (HSE)*

Hybrid functionals belong to a class of approximations for the exchange-correlation energy functional within the DFT. They combine a portion of the exact exchange from Hartree-Fock theory with the remaining exchange-correlation energy from other sources, which can be either an “ab-initio” or empirical. The exact exchange energy functional is expressed in terms of Kohn-Sham orbitals rather than density and is therefore given the name implicit density functional. Axel Becke introduced the hybrid approach in 1993 [25]. Incorporating Hartree-Fock (HF) exchange, also known as exact exchange, provides a straightforward method to improve the accuracy of various molecular property calculations. These properties include atomization energies, bond lengths, and vibrational frequencies, which are often inadequately, represented using basic “ab-initio” functionals [26]. A widely used variant is the Heyd-Scuseria-Ernzerhof function (HSE) [27].

The Heyd-Scuseria-Ernzerhof (HSE) exchange-correlation function [27] uses a failure function-tested Coulomb potential to calculate the exchange energy component with the aim of improving the computational efficiency. The HSE functionals are known for their ability to improve the precision of traditional semi-local functionals such as PBE, particularly when dealing with semiconductor bandgaps. In addition, they offer lower computational cost compared to other hybrid functions. The exchange-correlation energy has the following formula:

$$E_{xc}^{\omega PBEh} = \alpha E_x^{HF,SR}(\omega) + (1 - \alpha) E_x^{PBE,SR}(\omega) + E_x^{PBE,LR}(\omega) + E_c^{PBE}(\omega) \quad (\text{eq.45})$$

In this context, “ $\alpha$ ” represents the mixing parameter, while “ $\omega$ ” serves as an adjustable parameter that determines the short-range nature of the interaction. Commonly used values of “ $\alpha = 1/4$ ” and “ $\omega = 0.2$ ” (often referred to as HSE06) have shown favorable results for most systems. The HSE exchange-correlation functional simplifies to the PBE0 hybrid functional when “ $\omega = 0$ ”. Here “ $E_x^{HF,SR}(\omega)$ ” stands for the short-range Hartree-Fock exact exchange functional, “ $E_x^{PBE,SR}$ ” and “ $E_x^{PBE,LR}$ ” denotes the short-range or long-range components of the PBE exchange function and “ $E_c^{PBE}(\omega)$ ” represents the PBE [18] correlation function.

## 2.2.2 Augmented Plane Wave (APW) Basis Set

While the value of pseudopotentials in computing electronic structures is undeniable, there is a growing trend to explore alternative methods for certain specific reasons. While pseudopotentials are highly efficient, they have limitations in capturing information that is inherently encoded near the atomic nucleus. In this context, the concept of Augmented Plane Waves (APW) is gaining importance and is proving to be a promising alternative. In the coming sections, we begin by introducing the Augmented Plane Wave (APW) method. We will then examine its improvements, including the Linearized Augmented Plane Wave (LAPW) method, Augmented Plane Waves coupled with local orbitals (APW+LO), and the Full Potential Linearized Augmented Plane Wave (FP-LAPW) approach.

### 2.2.2.1 Augmented Plane Wave (APW) Method

The Augmented Plane Wave (APW) method, originally developed by Slater [28] in 1937 to solve the Kohn-Sham equations, is based on a fundamental concept: the division of space into two different regions, as shown in Figure 3. In the inner region we encounter non-overlapping spheres, each centered on atomic locations, affectionately known as “*muffin tin*” spheres (abbreviated as *MT* spheres). These spheres have a characteristic radius called  $R_{mt}$ . Within these limits, electrons assume a relatively free state that we can describe with plane waves. Here the potential exhibits spherical symmetry and the wave functions naturally assume radial shapes. Conversely, in the second region we are faced with what we call the “*intermediate region*”, which represents the unoccupied space woven between the *muffin tin*

balls. Within this region, electrons form strong bonds with the atomic nuclei, which resemble the behavior of free atoms. The potential remains constant and wave functions take the form of plane waves [29]. This fascinating duality in treatment allows the APW method to effectively capture the complex interplay between the behavior of free and bound electrons within a crystalline structure.

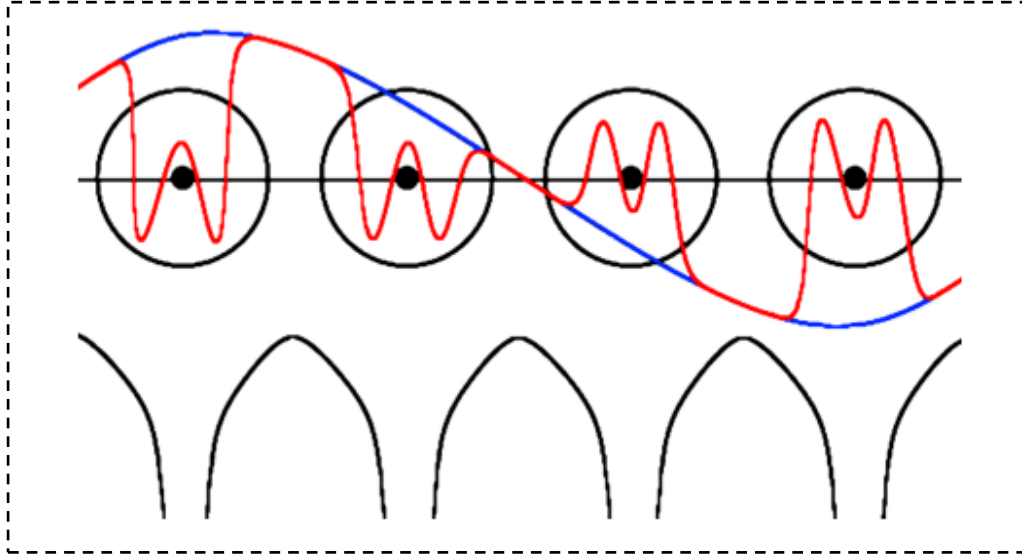


**Figure 3.** Illustration of *muffin tin* spheres and the *interstitial region* where potential singularities occur at the core positions. The Augmented Plane Waves (APW), shown in red lines, must transition smoothly exactly at the boundaries of the spheres and coincide with the plane waves in the interstitial region, shown by the blue line. This image was taken from the FLEUR user manual [30].

According to the Muffin-Tin approximation, the wave function  $\psi(\vec{r})$  takes the following specific form:

$$\begin{cases} \psi(\vec{r}) = \sum_{lm} A_{lm} U_l(\vec{r}) Y_{lm}(\vec{r}) & \vec{r} < R_{mt} \\ \psi(\vec{r}) = \frac{1}{\sqrt{\Omega}} \sum_G C_G e^{i(\vec{G}+\vec{K})\vec{r}} & \vec{r} > R_{mt} \end{cases} \quad (\text{eq.46})$$

Where  $\Omega$  is the volume of the unit cell,  $A_{lm}$  and  $C_G$  are development coefficients,  $Y_{lm}(\vec{r})$  is spherical harmonics and  $U_l(\vec{r})$  is the regular solution of the radial part of the Schrödinger equation, given by:

$$\left\{ -\frac{d^2}{dr^2} + \frac{l(l+1)}{r^2} + V(\vec{r}) - E_l \right\} r U_l(\vec{r}) = 0 \quad (\text{eq.47})$$

In this equation,  $V(\vec{r})$  denotes the spherical component of the potential enclosed in the sphere, often referred to as the *muffin tin* potential. Meanwhile,  $E_l$  represents the energy of linearization. These radial functions defined by this equation have orthogonality with respect to each nuclear eigenstate within the sphere. It is worth noting that this orthogonality property disappears at the spherical boundary [31], as explained by the following Schrödinger equation:

$$(E_2 - E_1)\vec{r}U_1U_2 = U_2 \frac{d^2\vec{r}U_1}{d\vec{r}^2} - U_1 \frac{d^2\vec{r}U_2}{d\vec{r}^2} \quad (\text{eq.48})$$

Where  $U_1$  and  $U_2$  are radial solutions corresponding to energies  $E_1$  and  $E_2$ , respectively.

Slater's method introduces a key concept: plane waves serve as solutions to the Schrödinger equation when the potential remains constant, as it does in the interstitial region. In contrast, radial functions emerge as solutions when dealing with a spherical potential, and this is also true when  $E_l$  represents an eigenvalue. While this approximation proves to be extremely effective for materials with cubic or face-centered structures, its applicability for asymmetric materials is limited. To maintain the continuity of the function  $\psi(\vec{r})$  at the surface of the MT sphere, the coefficients  $A_{lm}$  must be expressed as  $C_G$  coefficients associated with plane waves within the interstitial region. These coefficients can be expressed explicitly as follows:

$$A_{lm} = \frac{4\pi i^l}{\sqrt{\Omega} U_l(R_{mt})} \sum_G C_G J_l(|\vec{K} + \vec{G}| R_{mt}) Y_{lm}^*(\vec{K} + \vec{G}) \quad (\text{eq.49})$$

The reference point is set at the center of a sphere with a radius of  $R_{MT}$ . Consequently, the coefficients are expressed as plane wave coefficients, denoted  $C_G$ . The energy parameters  $C_G$  are referred to as coefficients of variation in the APW method. This alignment ensures that the functions indexed by  $G$  are compatible with the radial functions within the spheres, leading to the concept of Augmented Plane Waves (APW). These APW functions specifically serve as solutions to the Schrödinger equation for energies represented by  $E_l$  alone. Therefore, it is imperative that the energy value  $E_l$  matches that of the  $G$ -indexed energy band. This condition means that energy bands (for a given  $k$ -point) cannot be obtained by a simple diagonalization process. Instead, it becomes necessary to treat the secular determinant as a function of energy to decipher the complicated energy band structure.

The inherent challenge within the APW method arises from the presence of the parameter  $E_l$  in the denominator of the  $U_l$  function ( $R_{MT}$ ). This parameter can take the value zero at the surface of the MT sphere, resulting in a discontinuity between the radial functions and the plane wave functions. To address this problem, several modifications to the APW method have been introduced, the most famous being developed by Koelling [32] and Andersen [33]. Andersen's modification involves a novel approach. The aim is to represent the wave functions within the spheres by creating a linear combination of the radial functions  $U_l(\vec{r})$  and their derivatives with respect to the energy  $E_l$ . This representation is formulated as follows:  $U_l(\vec{r}) = \frac{dU_l}{dE_l}$ , which gave rise to the LAPW (*Linearized Augmented Plane Wave*) method. This adjustment effectively bridges the gap and ensures a seamless transition between radial and plane wave functions, improving the overall accuracy and versatility of the method.

### 2.2.2.2 Linearized Augmented Plane Wave (LAPW) Method

Once the fundamental functions and their derivatives are continuous and adapt to their status as radial functions with a fixed energy  $E_l$ , we introduce a more adaptable and precise framework for understanding the band structure of solids - the LAPW (Linear Augmented Plane Wave) method. The LAPW method was a remarkable success, especially after Andersen's refinements of linearization techniques. Below we outline some key principles of the LAPW method. More details can be found in the work of Singh [34]. Within the LAPW method, especially in the atomic MT region, wave functions take the form of a linear combination involving radial solutions  $U_l(\vec{r})Y_{lm}(\vec{r})$  and their derivatives, denoted as  $\dot{U}_l(\vec{r})Y_{lm}(\vec{r})$ , related to energy fluctuations. These functions  $U$  are defined according to Eq. 48 from the APW method. In addition, it is important that the derivative functions  $\dot{U}$  satisfy a certain condition:

$$\left\{-\frac{d^2}{d\vec{r}^2} + \frac{l(l+1)}{\vec{r}^2} + V(\vec{r}) - E_l\right\} \vec{r} \dot{U}_l(\vec{r}) = \vec{r} U_l(\vec{r}) \quad (\text{eq.50})$$

LAPWs are plane waves in the intermediate zone of the unit cell that reach the numerical radial functions inside the spheres, under the condition that the functions and their derivatives are continuous at the boundary as described in Eq.51:

$$\psi(\vec{r}) = \begin{cases} \sum_{lm} [A_{lm} U_l(\vec{r}) + B_{lm} \dot{U}_l(\vec{r})] Y_{lm}(\vec{r}) & \vec{r} < R_{mt} \\ \frac{1}{\sqrt{\Omega}} \sum_G C_G e^{i(\vec{G}+\vec{K})\vec{r}} & \vec{r} > R_{mt} \end{cases} \quad (\text{eq.51})$$

Where the coefficients  $B_{lm}$  corresponding to the function  $U_l(\vec{r})$  are of the same type as the  $A_{lm}$  coefficients.

As with the APW method, LAPW functions are plane waves only in the interstitial region. Within spheres, LAPW functions are more suitable than APW functions. If  $E_l$  differs slightly from the band energy  $E$ , a linear combination will actually reproduce the radial function better than APW functions consisting of a single radial function. Consequently, the  $U_l$  function can be developed as a function of its derivative and the energy  $E$ :

$$U_l(E, \vec{r}) = U_l(E_l, \vec{r}) + (E - E_l) \dot{U}_l(E, \vec{r}) + \mathbf{0}(E - E_l)^2 \quad (\text{eq.52})$$

So that  $(E - E_l)^2$  represents the energy squared error.

While this approach in the LAPW method guarantees the continuity of the wave function at the *MT* sphere boundary, it is worth noting that these calculations may experience a reduction in precision in

terms of computational accuracy compared to the APW method. The LAPW method leads to an error in the wave functions on the order of  $(E-E_l)^2$  and another error in the band energies on the order of  $(E-E_l)^4$ . Despite these errors, the LAPW wave functions serve as a robust basis for capturing all valence bands within a relatively wide energy range, all with a single energy value  $E_l$ . In cases where this is not possible, splitting the energy window into two parts provides a significant simplification compared to the APW method. When  $U_l$  takes a zero value at the surface of the MT sphere, its derivative  $\dot{U}_l$  is generally non-zero, which effectively solves the continuity problem at the surface of the MT sphere within the LAPW method. Takeda and Kubler [35] introduced a generalized version of the LAPW method using  $N$  radial functions and their  $(N-1)$  derivatives. Each radial function is associated with its unique parameter  $E_{li}$ , effectively mitigating the error associated with linearization. The default LAPW method is called when  $N=2$  and  $E_{l1}$  is close to  $E_{l2}$ . However, for  $N>2$  these errors can be further reduced. Unfortunately, using higher order derivatives to achieve convergence requires significantly longer computation times. Singh [36] modified this approach by introducing local orbitals into the basis set without increasing the plane wave energy limit, which provided a more efficient strategy to deal with convergence while maintaining computational efficiency.

- **Role of Linearization Energies  $E_l$**

The extended wave functions  $U_l$  and  $\dot{U}_l$  must satisfy the condition of orthogonality with respect to the core states within the MT sphere. However, this condition is only met if there are no nuclear states with the same quantum number “ $l$ ”. Consequently, there is a risk of fusion of semi-nuclear states with valence states. The problem of non-orthogonality between certain nuclear states is still not addressed by the APW method, and the introduction of the LAPW method requires careful selection of the energy  $E_l$ . Therefore, an adjustment of  $E_l$  is required to facilitate the calculation. In such cases, the ideal solution is to apply local orbital expansion. However, it is important to note that this option may not be available in all software programs. In such cases, selecting the largest possible MT sphere radius is crucial. Ultimately, the different  $E_l$  values should be defined independently of each other. Energy bands correspond to different orbitals. For precise electronic structure calculations,  $E_l$  should be chosen as close as possible to the energy of the band when both have the same quantum number “ $l$ ”.

### 2.2.2.3 Development of LAPW into Local Orbitals

The primary goal of the LAPW method is to obtain precise band energies close to the linearization energies  $E_l$  [33]. For most materials it is sufficient to choose these energies near the center of the band. However, this approach is not always feasible because there are materials for which a single  $E_l$  value is not sufficient to calculate all energy bands. This is particularly relevant for materials with  $4f$  orbitals [37, 38] and transition metals [39, 40]. It highlights the fundamental problem of the semi-nuclear state,

which lies between the valence and the nuclear state. To address this challenge, multiple energy windows are often used or, alternatively, local orbital expansion is used.

### 2.2.2.3.1 LAPW+LO Method

The development of the LAPW method to local orbitals involves modifying the orbitals within their basis set to eliminate the need for multiple energy windows. This is achieved by introducing a third category of basic functions. The underlying principle is to treat all energy bands within a single energy window. Singh [36] articulated local orbitals as a linear combination of two radial functions corresponding to two different energies, along with the derivative of one of these functions with respect to the energy:

$$\psi(\vec{r}) = \begin{cases} [A_{lm}U_l(\vec{r}, E_{l,1}) + B_{lm}\dot{U}_l(\vec{r}, E_{l,1}) + C_{lm}U_l(\vec{r}, E_{l,2})]Y_{lm}(\vec{r}) & \vec{r} < R_{mt} \\ 0 & \vec{r} > R_{mt} \end{cases} \quad (\text{eq.53})$$

The coefficients  $C_{lm}$  have the same nature as the previously defined coefficients  $A_{lm}$  and  $B_{lm}$ .

A local orbital is defined for a given  $l$  and  $m$  and also for a particular atom, since within the unit cell all atoms must be taken into account, not just the inequivalent ones. In addition to addressing the half-core states, local orbitals can also be used to improve the basis set for conduction bands. This improvement to the LAPW method has been crucial to its widespread success, as it extends the applicability of this linearization approach to a significantly broader range of compounds.

### 2.2.2.3.2 APW+LO Method

The problem encountered with the APW method was the energy dependence of the entire basis set. While the LAPW+LO method managed to eliminate this energy dependence, it came with the disadvantage of using a larger base, which imposed significant limitations on both the APW and LAPW+LO methods. Sjösted, Nordström, and Singh [41] achieved a significant improvement by developing a hybrid basis that combines the advantages of the APW and LAPW+LO methods. This approach is referred to as APW+LO and requires only a slightly higher plane wave cutoff energy compared to the APW method. A standard APW basis is used and  $U_l(\vec{r})$  is taken into account for a fixed energy  $E_l$ , thereby retaining the advantages of linearizing the eigenvalue problem. However, since a fixed energy basis does not provide a satisfactory description of the eigenfunctions, local orbitals are introduced to ensure variational flexibility in the radial basis functions.

An APW+LO basis is defined by the combination of two types of wave functions:

- Plane waves (APW) with a set of fixed energies  $E_l$ :



$$\psi(\vec{r}) = \begin{cases} \sum_{lm} [A_{lm} U_l(\vec{r}) + B_{lm} \dot{U}_l(\vec{r})] Y_{lm}(\vec{r}) & \vec{r} < R_{mt} \\ \frac{1}{\frac{1}{\sqrt{\Omega}} \sum_G c_G e^{i(\vec{G} + \vec{k})\vec{r}}} & \vec{r} > R_{mt} \end{cases} \quad (\text{eq.54})$$

- Local orbitals different from those of the LAPW+LO method, defined as:

$$\psi(\vec{r}) = \begin{cases} \sum_{lm} [A_{lm} U_l(\vec{r}, E_l) + B_{lm} \dot{U}_l(\vec{r}, E_l)] Y_{lm}(\vec{r}) & \vec{r} < R_{mt} \\ \mathbf{0} & \vec{r} > R_{mt} \end{cases} \quad (\text{eq.55})$$

A mixed basis can be used in calculations, including both LAPW and LAPW+LO components, taking into account different atoms and even different values of the quantum number 'l'. Typically, this approach assigns orbitals that exhibit slower convergence with the number of plane waves, such as the 3d-states in transition metals or atoms with a smaller MT sphere size to the APW+LO basis. Meanwhile, the remaining components are described on the LAPW basis [42].

#### 2.2.2.4 FP-LAPW Method

The Full Potential Linearized Augmented Plane Wave (FP-LAPW) method [43] does not make any approximations regarding the shape of the potential or the charge density. Instead, they are developed into lattice harmonics within individual atomic spheres and represented as a Fourier series in the interstitial regions. This property is the origin of the method's name, “*full-potential*”. In particular, this approach ensures the continuity of the potential at the surface of the MT sphere and can be expressed in the following comprehensive form:

$$V(\vec{r}) = \begin{cases} \sum_{lm} V_{lm}(\vec{r}) Y_{lm}(\vec{r}) & \vec{r} < R_{mt} \\ \sum_K V_K e^{i\vec{k}\vec{r}} & \vec{r} > R_{mt} \end{cases} \quad (\text{eq.56})$$

Likewise, the charge density develops in the following way:

$$n(\vec{r}) = \begin{cases} \sum_{lm} n_{lm}(\vec{r}) Y_{lm}(\vec{r}) & \vec{r} < R_{mt} \\ \sum_K n_K e^{i\vec{k}\vec{r}} & \vec{r} > R_{mt} \end{cases} \quad (\text{eq.57})$$

In addition to the basic principles of the APW method, several variants and extensions have been developed. These include the Soler-Williams formulation of the LAPW [44], ELAPW [45, 46] and QAPW [47, 48] methods, each of which provides improved accuracy, flexibility, precision and computational efficiency compared to the standard LAPW method. This makes them valuable tools for electronic structure calculations for various types of materials and systems.

Furthermore, when dealing with low-dimensional systems, it is possible to extend the division of the unit cell to explicitly include semi-infinite vacuum regions, each with tailored plane wave

amplification [49]. This approach enables efficient calculations for low-dimensional systems such as surfaces and thin films. In addition, an extension to one-dimensional setups was developed for addressing atom chains [50]. A large number of software projects have been developed to implement the LAPW method and its many variants. Some notable examples of these software codes are: Elk [51], Exciting [52], Flair [53], FLEUR [30], HiLAPW [54] and WIEN2k [42]. These software packages provide valuable resources for researchers working on the calculation of electronic structures. They provide a comprehensive toolbox for exploring the properties and behaviors of various materials, increasing the versatility and effectiveness of computational investigations in this area. Software programs such as VASP [55] and Quantum Espresso [56] adopt the pseudopotential approach alongside plane wave and projector-augmented waves (PAW). This approach is characterized by its user-friendly properties, requires fewer user control parameters and provides a streamlined development process. The use of plane waves also contributes to the simplicity of the code by simplifying various expressions in the software. A basic description of this method follows.

### 2.2.3 Projector Augmented Wave (PAW) Method

Several approaches have emerged to solve the Schrödinger equation. Among the prominent electronic structure techniques, we can divide them into two main groups: (i) linear methods, exemplified by the previously discussed Augmented Plane Wave (APW) method by Andersen [28], and (ii) the pseudopotential method, which is based on norm-conserving pseudopotentials of the first principle, which were developed by Hamann, Schluter and Chiang [57]. The pseudopotential method, in combination with a plane wave basis set, offers the advantage of formal simplicity. However, when it comes to first-row elements or systems containing  $d$  or  $f$  electrons, even pseudopotentials can become very “hard”. In such cases, practicality requires the use of either extensive or complicated basis sets instead of plane waves. Furthermore, the treatment of semi-nuclear states as valence states, which is often required for early transition metal and alkaline earth metal elements, leads to the use of hard pseudopotentials, which limits their transferability.

Vanderbilt's ultrasoft pseudopotentials [58, 59] significantly alleviated this problem by relaxing the norm conservation condition typically imposed on the pseudopotential approach. This approach also allows economical treatment of first-row elements and transition metal.

Car and Parrinello introduced a combination of density functional theory and molecular dynamics techniques [60] in which both electronic structure and atomic dynamics are solved simultaneously using Newton's equations. This approach simplifies structure determination and facilitates the dynamic evolution of atomic structures. The Car-Parrinello method was originally used in the context of the pseudopotential for plane waves. However, there is growing interest in applying this technique to all-

electron (AE) methods, which enable efficient handling of first-row elements and transition metals. AE methods provide insights into the behavior of the wave function near the nucleus, a feature not provided by the pseudopotential approach and which is crucial for various experimental techniques. Nevertheless, it is important to emphasize that up to this point, no low-energy molecular dynamics simulation [61] that rivals the quality of simulations using the pseudopotential approach has been performed.

In this context, the concept of “Projector Augmented Wave” (PAW) functions was developed. Blöchl introduced the “Projector Augmented Wave” (PAW) method [62], which combines and extends the advantageous aspects of pseudopotential and LAPW methods through the use of projector functions. Basically, the PAW method matches partial wave functions derived from isolated atoms with pseudo partial waves, using specially designed projector functions that closely mimic the all-electron solution. In this framework, PAW datasets are generated that allow the recovery of full core electron wave functions, similar to the LAPW approach but with significantly reduced computational effort, approaching the efficiency of pseudopotentials (the basic concept of the PAW method is schematically presented in Figure 4). In simpler terms, valence wave functions exhibit fast oscillations near ionic nuclei due to the need to maintain orthogonality to the core states. This presents a challenge because accurately describing these wave functions requires a large number of Fourier components or, in the case of grid-based methods, an exceptionally fine grid. The PAW method addresses this problem by converting these rapidly oscillating wave functions into smoother counterparts, making them more computationally tractable. In addition, it provides a way to calculate the properties of all electrons based on these smoothed wave functions. This approach is somewhat similar to a transition from the Schrödinger picture to the Heisenberg picture.

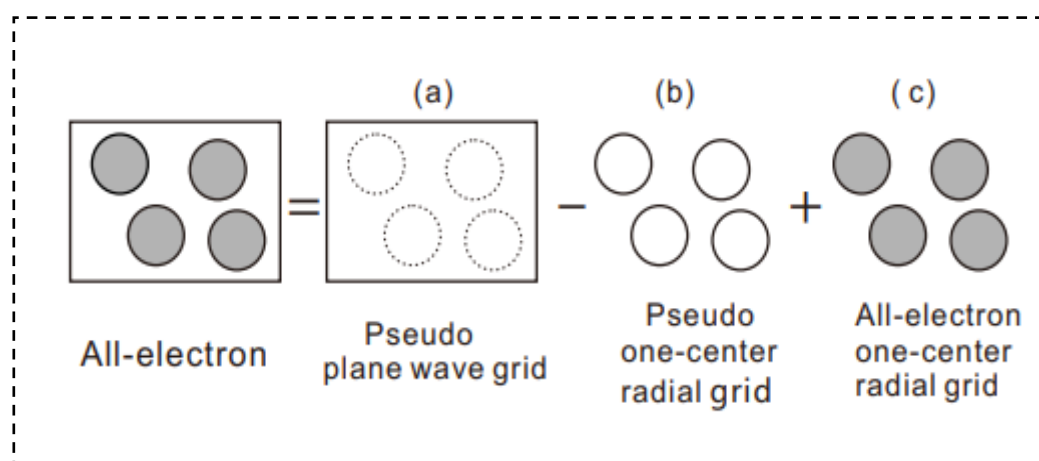


**Figure 4.** A schematic representation of the PAW method is shown. (a) Pseudo-quantities are established using a uniform, flat wave grid covering the entire space. (b) Pseudowave functions are reconstructed inside spheres and the respective single-center terms are subtracted. (c) The all-electron wave functions are reconstructed and the corresponding single-center energies are included. After Ref [63].

In the Hilbert space, the wave functions (AE) are transformed into a new, so-called pseudo (PS) Hilbert space. The linear transformation denoted by  $\zeta$  converts the hypothetical pseudo wavefunction  $|\tilde{\psi}\rangle$  into the real all-electron wavefunction  $|\psi\rangle$ :

$$|\psi\rangle = \zeta|\tilde{\psi}\rangle \quad (\text{eq.58})$$

The “all-electron” wave function, which represents a single-body Kohn-Sham wave function, should not be confused with the many-body wave function. To ensure that  $|\tilde{\psi}\rangle$  and  $|\psi\rangle$  differ mainly in the regions around the ion nuclei, we can express it as follows:

$$\zeta = \mathbf{1} + \sum_R \tilde{\zeta}_R \quad (\text{eq.59})$$

The non-zero  $\tilde{\zeta}_R$  values of are restricted to certain spherical augmentation regions  $\Omega_R$  surrounding the atom R. It is advantageous to represent the pseudowave function around each atom as an expansion of pseudopartial waves:

$$|\tilde{\psi}\rangle = \sum_i |\tilde{\phi}_i\rangle c_i \text{ within } \Omega_R \quad (\text{eq.60})$$

Due to the linearity of the operator  $\zeta$ , the coefficients  $c_i$  can be expressed as an inner product with a set of projector functions, denoted as  $|p_i\rangle$ :

$$c_i = \langle p_i | \tilde{\psi} \rangle \quad (\text{eq.61})$$

Where  $\langle p_i | \tilde{\phi}_j \rangle = \delta_{ij}$ .

The all-electron partial waves, denoted as  $|\phi_i\rangle = \zeta|\tilde{\phi}_i\rangle$ , are usually chosen as solutions of the Kohn-Sham-Schrödinger equation for an isolated atom. The transformation  $\zeta$  is thus characterized by three components: a set of all-electron partial waves  $|\phi_i\rangle$ , a set of pseudo-partial waves  $|\tilde{\phi}_i\rangle$ , and a set of projector functions  $|p_i\rangle$ , and so it can also be expressed explicitly as :

$$\zeta = \mathbf{1} + \sum_i (|\phi_i\rangle - |\tilde{\phi}_i\rangle) \langle p_i | \quad (\text{eq.62})$$

Using this transformation, we can derive the all-electron wave function (AE) from the pseudo wave function (PS) by:

$$|\psi\rangle = |\tilde{\psi}\rangle + \sum_i (|\phi_i\rangle - |\tilde{\phi}_i\rangle) \langle p_i | \tilde{\psi} \rangle \quad (\text{eq.63})$$

Outside the augmentation regions, the pseudo partial waves agree with the all-electron partial waves. Within the spheres, they can take any smooth continuation, including linear combinations of polynomials or Bessel functions.

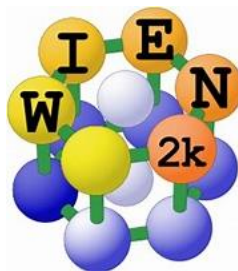
## 2.3 Computational Formulation

The main goal of practical DFT formulations is the numerical solution of the Kohn-Sham equations for systems consisting of multiple atoms. Density functional theory (DFT) calculations have quickly become a standard tool for a variety of materials modeling applications in physics, chemistry, materials science, and various engineering disciplines. The development of open-source electronic structure code packages, mainly based on the LAPW method or the pseudopotential method, has significantly enriched the toolbox for conducting detailed ab-initio materials studies. These joint efforts have produced well-structured shared codes that incorporate numerous state-of-the-art methods. A crucial aspect of code development is the validation process, with most collaborative teams incorporating internal testing as an integral part of their development processes. Additionally, the availability of multiple independently developed codes provides opportunities for extensive testing and validation.

In this dissertation, we leverage the capabilities of two commercial software packages, WIEN2k [42] and VASP [55], to perform our DFT calculations. This section provides a detailed introduction to these two codes.

### 2.3.1 WIEN2k Code

The WIEN2K simulation code comes from the Institute of Materials Chemistry at the Vienna University of Technology and was first developed in 1990 by *P. Blaha, K. Schwartz, P. Sorintin and S.B. Trickey* [24, 64]. Since its inception, this code has been continually revised and updated multiple times, resulting in various versions known by their year of release, such as WIEN93, WIEN95, WIEN97, etc. In our work, we used the 2014 WIEN2K version to study the 3D bulk structures.



WIEN2K is a computational software for calculating the Schrödinger wave equation for periodic materials in three-dimensional (3D), two-dimensional (2D) and one-dimensional (1D) configurations. It is coded primarily in FORTRAN90 and runs on the LINUX operating system. It consists of a collection of standalone programs linked together via C-SHELL SCRIPT. These programs are responsible for performing electronic structure calculations in solid-state materials using the principles of density functional theory (DFT). WIEN2K supports a wide range of function types and uses the FP-

LAPW method. It performs self-consistent calculations for all electrons, including both core and valence electrons, resulting in exceptionally accurate results.

The code's capabilities extend to fundamental electronic structure calculations, structure optimization methods, spin-polarized/spin-orbit-based systems, phonons, and the simulation of various spectroscopic methods. For applications such as X-ray absorption or electron energy loss spectroscopy, WIEN2K considers excitonic effects by introducing a core hole on the relevant atom, thus enabling the precise modeling of various spectral features. Furthermore, WIEN2K offers the opportunity to go beyond the limits of DFT by leveraging advanced many-body perturbation theories such as the GW approximation [65] and the Bethe-Salpeter approach (BSE) [66].

### 2.3.2 VASP Code

VASP, or the Vienna Ab-initio Simulation Package, is a powerful computational tool written primarily in FORTRAN. It is designed to perform ab initio quantum mechanical molecular dynamics (MD) of essentially small atom systems (approximately up to 100-200 atoms) using Vanderbilt pseudopotentials [58, 59] or the PAW method [62] combined with a plane wave basis set. While the core methodology of atoms focuses on DFT, VASP also considers post-DFT corrections, including hybrid functionals (such as HSE [27], PBE0 [26] or B3LYP [67]) that integrate DFT with Hartree–Fock (HF) exchange as well as advanced techniques such as the GW method for many-body perturbation theory [65] and dynamic electronic correlations within the random phase approximation (RPA) [68].



Originally, VASP was based on code developed by *Mike Payne*, which also laid the foundation for CASTEP [69]. Later, VASP was brought to the University of Vienna, Austria by *Jürgen Hafner* in July 1989. The main program was created by *Jürgen Furthmüller*, who came to the Institute for Materials Physics in January 1993 together with *Georg Kresse*. The further development of VASP is currently being driven forward by *Georg Kresse*. Recent extensions include the adaptation of methods commonly used in molecular quantum chemistry for use in periodic systems. The latest version of VASP is version 6.4.2, which became available on July 20, 2023. In our work, we used VASP version 6.2.1 to study the 2D monolayer structures.

A more detailed description of the basic programs of the WIEN2K and VASP codes, step calculations, and possible properties can be found in Appendix B.

### 2.3.3 BoltzTraP2 Code

BoltzTraP2, an acronym for Boltzmann Transport Properties, is a widely used software package known for its ability to simulate and calculate the thermoelectric properties of materials. This code uses a contemporary approach that leverages smoothed Fourier interpolation of periodic functions and Onsager transport coefficients for extended systems and enables the careful calculation of a material's semi-classical Boltzmann transport equation (discussed in Chapter 1). It relies on crucial inputs including band- and  $k$ -dependent quasiparticle energies, intraband optical matrix elements, and scattering rates. BoltzTraP2 interfaces seamlessly with WIEN2K and VASP and provides versatile access through both a command line interface (via the `btp2` command line interface) and a Python module [70].

The approach is based on expressing the quasiparticle energies and their derivatives for each band as Fourier series representations:

- Quasi-particle energies  $\check{\epsilon}_k$  are represented as follows:

$$\check{\epsilon}_k = \sum_{\Lambda} c_{\Lambda} \sum_{R \in \Lambda} \exp(i\mathbf{k} \cdot \mathbf{R}) \quad (\text{eq.64})$$

Where  $\Lambda$  represents sets of symmetry-equivalent lattice vectors.

- Derivatives of quasi-particle energies  $\check{\nabla} \epsilon_k$  are expressed as:

$$\check{\nabla} \epsilon_k = i \sum_{\Lambda} c_{\Lambda} \sum_{R \in \Lambda} \mathbf{R} \exp(i\mathbf{k} \cdot \mathbf{R}) \quad (\text{eq.65})$$

BoltzTraP was originally inspired by Shankland's concept [71], which proposed determining coefficients by minimizing a roughness function while ensuring accurate reproduction of the calculated quasiparticle energies. This requirement implies that the number of coefficients should exceed the number of calculated points.

The derivatives can also be derived from optical intraband matrix elements [72]:

$$\nabla \epsilon_k = -\langle \psi_k | \mathbf{p} | \psi_k \rangle \quad (\text{eq.66})$$

In BoltzTraP2, the Shankland algorithm [71] is extended to ensure that the coefficients reproduce not only the quasiparticle energies but also their derivatives, as expressed in Eq.66. This involves minimizing the Lagrangian:

$$I = \frac{1}{2} \sum_R \mathbf{c}_R \rho_R + \sum_k [\lambda_k (\epsilon_k - \check{\epsilon}_k) + \sum_a \lambda_{a,k} \nabla_a (\epsilon_k - \check{\epsilon}_k)] \quad (\text{eq.67})$$

The Fourier coefficients ( $\mathbf{c}_R$ ) are adjusted according to the constraints and the Lagrange multipliers ( $\lambda_k$  and  $\lambda_{a,k}$ ) are chosen to satisfy these constraints. Here, the index  $a$  denotes the three Cartesian directions, indicating that each calculated derivative introduces three Lagrange multipliers, as in Eq. 66.  $\rho_R$  is defined by Pickett et al. [73] as roughness function as follows:

$$\rho_R = \left(1 - c_1 \frac{R}{R_{min}}\right)^2 + c_2 \left(\frac{R}{R_{min}}\right)^6 \quad (\text{eq.68})$$

BoltzTraP2 uses the rigid band approximation (RBA) to calculate transport coefficients. This assumption implies that changes in temperature or doping level do not alter the underlying band structure. Furthermore, BoltzTraP2 is often associated with the Constant Relaxation Time Approximation (CRTA), which states that the Seebeck coefficient and the Hall coefficient are unaffected by the scattering rate [74]. This allows their determination on an absolute scale, taking into account doping and temperature fluctuations within a single analysis. However, it is important to note that under CRTA only electrical conductivity ( $\sigma$ ) and electronic thermal conductivity ( $\kappa_e$ ) are reported, both of which depend on relaxation time ( $\tau$ ) as a parameter. In order to accurately estimate  $\kappa_l$  and derive precise values for  $\sigma$  and  $\kappa_e$  independently of  $\tau$ , alternative methods are examined in Chapter 3.

## 2.4 Conclusion

In summary, density functional theory (DFT) is a powerful computational tool for solving electronic structures in many-body systems. In this chapter, we have introduced the theoretical foundations underlying density functional theory. This includes discussions of the various approximations commonly used to solve the Schrödinger equation, as well as descriptions of possible implementations. Additionally, we have provided a brief overview of various software codes designed to solve different types of problems.



## References for Chapter 2

- [1] Hartree, D. R. (1928, January). The wave mechanics of an atom with a non-Coulomb central field. Part I. Theory and methods. In *Mathematical Proceedings of the Cambridge Philosophical Society* (Vol. 24, No. 1, pp. 89-110). Cambridge university press.
- [2] Schrödinger, E. (1926). Quantization as an eigenvalue problem. *Annalen der Physik*, 79(4), 361-376.
- [3] Born, M., & Oppenheimer, R. (1927). Zur Quantentheorie der Molekeln *Annalen der Physik*, v. 84.
- [4] LI, S. (1968). *chiff, Quantum Mechanics. M cG raw-H ill, New York.*
- [5] Slater, J. C. (1930). Note on Hartree's method. *Physical Review*, 35(2), 210.
- [6] Löwdin, P. O. (1955). Quantum theory of many-particle systems. I. Physical interpretations by means of density matrices, natural spin-orbitals, and convergence problems in the method of configurational interaction. *Physical Review*, 97(6), 1474.
- [7] Thomas, L. H. (1927, January). The calculation of atomic fields. In *Mathematical proceedings of the Cambridge philosophical society* (Vol. 23, No. 5, pp. 542-548). Cambridge University Press.
- [8] Hohenberg, P., & Kohn, W. (1964). Inhomogeneous electron gas *phys. rev.* 136. B864.
- [9] Xiao, H. (2015). *First principles based multiparadigm modeling of electronic structures and dynamics.* California Institute of Technology.
- [10] Payne, M. C., Teter, M. P., Allan, D. C., Arias, T. A., & Joannopoulos, A. J. (1992). Iterative minimization techniques for ab initio total-energy calculations: molecular dynamics and conjugate gradients. *Reviews of modern physics*, 64(4), 1045.
- [11] Cohen, M. L. (2001). Nanotubes, nanoscience, and nanotechnology. *Materials Science and Engineering: C*, 15(1-2), 1-11.
- [12] Rajagopal, A. K., & Callaway, J. (1973). Inhomogeneous electron gas. *Physical Review B*, 7(5), 1912.
- [13] Ceperley, D. M., & Alder, B. J. (1980). Ground state of the electron gas by a stochastic method. *Physical review letters*, 45(7), 566.
- [14] Zhang, R., Zhao, C., Huo, Y., Han, Y., Hong, J., Liu, Y., ... & Ai, Y. (2022). Theoretical calculation of toxic/radioactive metal ion capture by novel nanomaterials. In *Emerging Nanomaterials for Recovery of Toxic and Radioactive Metal Ions from Environmental Media* (pp. 313-379). Elsevier.
- [15] Perdew, J. P., & Wang, Y. (1992). Accurate and simple analytic representation of the electron-gas correlation energy. *Physical review B*, 45(23), 13244.
- [16] Hood, R. Q., Chou, M. Y., Williamson, A. J., Rajagopal, G., & Needs, R. J. (1998). Exchange and correlation in silicon. *Physical Review B*, 57(15), 8972.
- [17] Koch, W., & Holthausen, M. C. (2015). *A chemist's guide to density functional theory.* John Wiley & Sons.

- [18] Perdew, J. P., Burke, K., & Ernzerhof, M. (1996). Generalized gradient approximation made simple. *Physical review letters*, 77(18), 3865.
- [19] Zhang, Y., & Yang, W. (1998). Comment on “Generalized gradient approximation made simple”. *Physical Review Letters*, 80(4), 890.
- [20] Wu, Z., & Cohen, R. E. (2006). More accurate generalized gradient approximation for solids. *Physical Review B*, 73(23), 235116.
- [21] Long, R., & English, N. J. (2009). Magnetic properties of first-row element-doped ZnS semiconductors: A density functional theory investigation. *Physical Review B*, 80(11), 115212.
- [22] Wei, S. H., & Zhang, S. B. (2002). Chemical trends of defect formation and doping limit in II-VI semiconductors: The case of CdTe. *Physical Review B*, 66(15), 155211.
- [23] Stevanović, V., Lany, S., Zhang, X., & Zunger, A. (2012). Correcting density functional theory for accurate predictions of compound enthalpies of formation: Fitted elemental-phase reference energies. *Physical Review B*, 85(11), 115104.
- [24] Tran, F. (2018). WIEN2k: An Augmented Plane Wave Plus Local Orbitals Program for Calculating Crystal Properties.
- [25] Becke, A. D. (1993). A new mixing of Hartree–Fock and local density-functional theories. *The Journal of chemical physics*, 98(2), 1372-1377.
- [26] Perdew, J. P., Ernzerhof, M., & Burke, K. (1996). Rationale for mixing exact exchange with density functional approximations. *The Journal of chemical physics*, 105(22), 9982-9985.
- [27] Heyd, J., Scuseria, G. E., & Ernzerhof, M. (2003). Hybrid functionals based on a screened Coulomb potential. *The Journal of chemical physics*, 118(18), 8207-8215.
- [28] Slater, J. C. (1937). Wave functions in a periodic potential. *Physical Review*, 51(10), 846.
- [29] Cottenier, S. (2002). Density Functional Theory and the family of (L) APW-methods: a step-by-step introduction. *Instituut voor Kern-en Stralingsfysica, KU Leuven, Belgium*, 4(0), 41.
- [30] Blügel, S., & Bihlmayer, G. (2006). Full-potential linearized augmented planewave method. *Computational nanoscience: do it yourself*, 31, 85-129.
- [31] Slater, J. C. (1964). Energy band calculations by the augmented plane wave method. In *Advances in quantum chemistry* (Vol. 1, pp. 35-58). Academic Press.
- [32] Koelling, D. D., & Arbman, G. O. (1975). Use of energy derivative of the radial solution in an augmented plane wave method: application to copper. *Journal of Physics F: Metal Physics*, 5(11), 2041.
- [33] Singh, D. J., & Nordstrom, L. (2006). *Planewaves, Pseudopotentials, and the LAPW method*. Springer Science & Business Media.
- [34] Singh, D. (1994). *Planes Waves, Pseudopotentials and the LAPW*.
- [35] Takeda, T., & Kubler, J. (1979). Linear augmented plane wave method for self-consistent calculations. *Journal of Physics F: Metal Physics*, 9(4), 661.
- [36] Singh, D. (1991). Ground-state properties of lanthanum: Treatment of extended-core states. *Physical Review B*, 43(8), 6388.

- [37] Singh, D. J. (1991). Adequacy of the local-spin-density approximation for Gd. *Physical Review B*, 44(14), 7451.
- [38] Goedecker, S., & Maschke, K. (1990). Alternative approach to separable first-principles pseudopotentials. *Physical Review B*, 42(14), 8858.
- [39] Singh, D., & Krakauer, H. (1991). H-point phonon in molybdenum: Superlinearized augmented-plane-wave calculations. *Physical Review B*, 43(2), 1441.
- [40] Singh, D. J., Schwarz, K., & Blaha, P. (1992). Electric-field gradients in YBa<sub>2</sub>Cu<sub>3</sub>O<sub>7</sub>: Discrepancy between experimental and local-density-approximation charge distributions. *Physical Review B*, 46(9), 5849.
- [41] Sjöstedt, E., Nordström, L., & Singh, D. J. (2000). An alternative way of linearizing the augmented plane-wave method. *Solid state communications*, 114(1), 15-20.
- [42] Madsen, G. K., Blaha, P., Schwarz, K., Sjöstedt, E., & Nordström, L. (2001). Efficient linearization of the augmented plane-wave method. *Physical Review B*, 64(19), 195134.
- [43] Hamann, D. R. (1979). Semiconductor charge densities with hard-core and soft-core pseudopotentials. *Physical Review Letters*, 42(10), 662.
- [44] Soler, J. M., & Williams, A. R. (1989). Simple formula for the atomic forces in the augmented-plane-wave method. *Physical Review B*, 40(3), 1560.
- [45] Krasovskii, E. E., Yaresko, A. N., & Antonov, V. N. (1994). Theoretical study of ultraviolet photoemission spectra of noble metals. *Journal of electron spectroscopy and related phenomena*, 68, 157-166.
- [46] Krasovskii, E. E. (1997). Accuracy and convergence properties of the extended linear augmented-plane-wave method. *Physical Review B*, 56(20), 12866.
- [47] Smrčka, L. (1984). Linearized augmented plane wave method utilizing the quadratic energy expansion of radial wave functions. *Czechoslovak Journal of Physics B*, 34(7), 694-704.
- [48] Petrů, J., & Smrčka, L. (1985). Quadratic augmented plane wave method for self-consistent band structure calculations. *Czechoslovak Journal of Physics B*, 35(1), 62-71.
- [49] Krakauer, H., Posternak, M., & Freeman, A. J. (1979). Linearized augmented plane-wave method for the electronic band structure of thin films. *Physical Review B*, 19(4), 1706.
- [50] Mokrousov, Y., Bihlmayer, G., & Blügel, S. (2005). Full-potential linearized augmented plane-wave method for one-dimensional systems: Gold nanowire and iron monowires in a gold tube. *Physical Review B*, 72(4), 045402.
- [51] Dewhurst, K., & Sharma, S. (2011). Development of the elk lapw code. *Max Planck Institute of Microstructure Physics*. Available online: <https://elk.sourceforge.io> (accessed on 16 September 2021).
- [52] Gulans, A., Kontur, S., Meisenbichler, C., Nabok, D., Pavone, P., Rigamonti, S., ... & Draxl, C. (2014). Exciting: a full-potential all-electron package implementing density-functional theory and many-body perturbation theory. *Journal of Physics: Condensed Matter*, 26(36), 363202.

- [53] Vlachoudis, V. (2009). FLAIR: a powerful but user friendly graphical interface for FLUKA. In *Proc. Int. Conf. on Mathematics, Computational Methods & Reactor Physics, Saratoga Springs, New York* (176).
- [54] Weinert, M., Schneider, G., Podloucky, R., & Redinger, J. (2009). FLAPW: applications and implementations. *Journal of Physics: Condensed Matter*, 21(8), 084201.
- [55] Kresse, G., & Furthmüller, J. (1996). Efficient iterative schemes for ab initio total-energy calculations using a plane-wave basis set. *Physical review B*, 54(16), 11169.
- [56] Giannozzi, P., Baroni, S., Bonini, N., Calandra, M., Car, R., Cavazzoni, C., ... & Wentzcovitch, R. M. (2009). QUANTUM ESPRESSO: a modular and open-source software project for quantum simulations of materials. *Journal of physics: Condensed matter*, 21(39), 395502.
- [57] Hamann, D. R., Schlüter, M., & Chiang, C. (1979). Norm-conserving pseudopotentials. *Physical Review Letters*, 43(20), 1494.
- [58] Laasonen, K., Car, R., Lee, C., & Vanderbilt, D. (1991). Implementation of ultrasoft pseudopotentials in ab initio molecular dynamics. *Physical Review B*, 43(8), 6796.
- [59] Moroni, E. G., Kresse, G., Hafner, J., & Furthmüller, J. (1997). Ultrasoft pseudopotentials applied to magnetic Fe, Co, and Ni: From atoms to solids. *Physical Review B*, 56(24), 15629.
- [60] Car, R., & Parrinello, M. (1985). Unified approach for molecular dynamics and density-functional theory. *Physical review letters*, 55(22), 2471.
- [61] Rapaport, D. C. (2004). *The art of molecular dynamics simulation*. Cambridge university press.
- [62] Blöchl, P. E. (1994). Projector augmented-wave method. *Physical review B*, 50(24), 17953.
- [63] Shishkin, M., & Kresse, G. (2006). Implementation and performance of the frequency-dependent G W method within the PAW framework. *Physical Review B*, 74(3), 035101.
- [64] Blaha, P., Schwarz, K., Madsen, G. K., Kvasnicka, D., & Luitz, J. (2001). wien2k. *An augmented plane wave+ local orbitals program for calculating crystal properties*, 60(1), 9501031.
- [65] Jiang, H., & Blaha, P. (2016). G w with linearized augmented plane waves extended by high-energy local orbitals. *Physical Review B*, 93(11), 115203.
- [66] Laskowski, R., & Blaha, P. (2010). Understanding the L 2, 3 x-ray absorption spectra of early 3 d transition elements. *Physical Review B*, 82(20), 205104.
- [67] Kim, K., & Jordan, K. D. (1994). Comparison of density functional and MP2 calculations on the water monomer and dimer. *The Journal of Physical Chemistry*, 98(40), 10089-10094.
- [68] Kaltak, M., Klimeš, J., & Kresse, G. (2014). Cubic scaling algorithm for the random phase approximation: Self-interstitials and vacancies in Si. *Physical Review B*, 90(5), 054115.
- [69] Madsen, G. K., Carrete, J., & Verstraete, M. J. (2018). BoltzTraP2, a program for interpolating band structures and calculating semi-classical transport coefficients. *Computer Physics Communications*, 231, 140-145.

- [70] Euwema, R. N., Stukel, D. J., Collins, T. C., DeWitt, J. S., & Shankland, D. G. (1969). Crystalline interpolation with applications to Brillouin-zone averages and energy-band interpolation. *Physical Review*, 178(3), 1419.
- [71] Shankland, D. G. (1971). Fourier transformation by smooth interpolation. *International Journal of Quantum Chemistry*, 5(S5), 497-500.
- [72] Koelling, D. D., & Wood, J. H. (1986). On the interpolation of eigenvalues and a resultant integration scheme. *Journal of Computational Physics*, 67(2), 253-262.
- [73] Pickett, W. E., Krakauer, H., & Allen, P. B. (1988). Smooth Fourier interpolation of periodic functions. *Physical Review B*, 38(4), 2721.
- [74] Singh, D. J., & Mazin, I. I. (1997). Calculated thermoelectric properties of La-filled skutterudites. *Physical Review B*, 56(4), R1650.

# Chapter 3

## Effect of Doping and CO-Doping on the SrS Bulk Properties

*The first part of this work has been published in Journal of Solid State Communications 361, 115060, (2023). The second part of this work has been published in Journal of Materials Science in Semiconductor Processing 165, 107684, (2023).*

In the first part of this chapter, we discussed the spin-resolved properties of pure bulk SrS (3D) doped with iron (Fe) at different concentrations: 0%, 12.5%, 25%, 50%, and 75% Fe. In the second part, we focused on the Fe concentration of 12.5%. Here, we conducted further investigations by co-doping the compound with three different alkali metals, namely Li, Na, and K. This allowed us to thoroughly investigate the optical and thermoelectric properties. We also compared the properties of the singly-doped and co-doped systems and evaluated the improvements achieved.

### 3.1 Structural, Mechanical, Electronic, and Magnetic Properties of mono-doped SrS: Fe Alloys

#### 3.1.1 Introduction

Against the backdrop of ever-increasing information needs and improved social connectivity in today's world, the 21<sup>st</sup> century has witnessed an unprecedented rise in technological advancement. This progress has been particularly evident in the significant development of high-performance computing systems and mobile devices. These advances have facilitated the seamless processing of large data sets, providing a robust response to the ongoing need for comprehensive data collection and storage methods [1].

The discipline of spintronics, which utilizes both electronic charge and spin properties, is at the forefront of technological innovation. It has enormous potential to pave the way for a new era characterized by fast, logically controlled and energy efficient data storage solutions [2]. The fabrication of dilute magnetic semiconductors (DMSs) characterized by high Curie temperatures ( $T_c$ ), thereby

enabling the control of magnetism at ambient conditions by carrier and gate voltages, represents a key milestone in the realization of an excellent candidate for semiconductor spintronic technology [3, 4]. Recently, Fe-based DMSs have attracted great scientific curiosity. They are at the forefront of research due to their tantalizing potential as ferromagnetic semiconductors, promising impressive properties such as elevated Curie temperatures, minimal power consumption, and suitability for high-speed spin-based devices [5]. This intriguing potential has led researchers to delve deeper into the intricacies of the ferromagnetic mechanism in Fe-based strain gauges. Their joint efforts reinforce the amazing promise of iron to not only achieve semimetallicity at room temperature, but also to exhibit significant magnetic moment and mechanical robustness - especially when integrated into the group of II-VI chalcogenides [6–12].

As an archetypal member of the II-VI chalcogenide family, strontium sulfide (SrS) has attracted the attention of both the scientific community and the industrial sector alike due to its properties, which are discussed in detail earlier in Chapter 1. Various theoretical and experimental aspects work has been carried out on SrS alloyed with different proportions of magnetic transition elements (with  $3d$ -orbitals) (see Section 1.6 of Chapter 1), but none has focused on conducting a detailed study on Fe-doped SrS at different concentrations. Furthermore, systematic studies on their elastic and mechanical properties are lacking. In this section of the chapter, we used a first-principles approach to investigate how doping concentration affects the structural, mechanical, electronic, and magnetic properties of Fe-doped rock-salt SrS. Our testing covers concentrations of 0%, 12.5%, 25%, 50% and 75% to ensure thorough analysis.

### 3.1.2 Computational Details

The computations discussed in this section were carried out using the Full-Potential Linearized Augmented Plane Wave (FP-LAPW) method [13] and the WIEN2k code [14]. The Generalized Gradient Approximation (GGA) as proposed by Perdew, Burke, and Ernzerhof (PBE96) [15] was utilized to address the exchange and correlation effects in order to determine the structural and mechanical properties. In addition to GGA-PBE, we optimized the results for electronic and magnetic properties by applying the Tran-Blaha modified Becke-Johnson (TB-mBJ) method [16], which is renowned for its excellent alignment with experimental data.

In the FP-LAPW method, two regions take up space. The atomic sites are surrounded by non-overlapping spheres with *muffin-tin* radii ( $R_{MT}$ ) in the first region, and the interstitial region (IR) lying between the spheres is the second region. Spherical harmonics are used to extend the basis functions, electron densities and potentials within the spheres up to a maximum angular momentum of  $l_{max}=10$ . They are expressed in a Fourier series with a Fourier charge density in the interstitial region expanded

to  $G_{max}=16 (a.u.)^{-1}$  and *cutoff* radius  $R_{MT} \cdot K_{max}=8$ . The last parameter,  $K_{max}$ , is the size of the largest wave vector used for the plane wave expansion of the eigenfunctions and controls the size of the basis set used.  $R_{MT}$  stands for smallest *muffin-tin* radius. The studied  $Sr_{1-x}Fe_xS$  alloys ( $x = 0, 0.125, 0.25, 0.50$  and  $0.75$ ) have *muffin-tin* radii for the constituent atoms that are 2.4, 2.3 and 2.1 atomic units for Sr, Fe and S, respectively. We used the following electronic configurations to represent the valence states of these atoms in our calculations: Sr [ $5s^2$ ], Fe [ $3d^6 4s^2$ ], and S [ $3s^2 3p^4$ ]. Brillouin zone sampling for SrS and  $Sr_{1-x}Fe_xS$ , respectively, is performed using an  $(8 \times 8 \times 8)$  and  $(4 \times 4 \times 4)$  gamma-centered  $k$ -point mesh to ensure computational efficiency. In successive iterations, self-consistency is considered to be achieved when the integrated energy and charge difference is less than  $10^{-4}$  Ry.

The elastic, mechanical and anisotropic properties of the compounds were investigated using the the Charpin method in conjunction with the WIEN2K code [17]. Using this method, it is possible to obtain the independent elastic constants  $C_{11}$ ,  $C_{12}$  and  $C_{44}$ , which are suitable for describing the elastic behavior of compounds with cubic symmetry and help in determining other mechanical parameters.

### 3.1.3 Results and Discussion

#### 3.1.3.1 Structural Properties

In an ab-initio calculation, determining the structural properties is a crucial step in gaining further insight into the microscopic properties of the material. This leads to the study of other physical properties such as electronic, magnetic, etc. To proceed with the calculation of structural properties for ternary alloys at different concentrations, we studied the properties of their bare SrS. This allows for a more in-depth comparison and better understanding of the alloy properties.

As mentioned in Chapter 1, bare SrS crystallizes under ambient conditions in the cubic rock-salt structure (B1) with a space group  $Fm\bar{3}m$  (N $^\circ$ .225), in which the Sr atom occupies (0, 0, 0), and the S atom occupies (0.5, 0.5, 0.5) Wyckoff positions, respectively (see Figure 9(a) in Chapter 1).

For an investigation that captures both low and high concentrations, we used the supercell approach to construct a computationally economical and time-efficient  $(2 \times 2 \times 2)$  face-centered cubic (fcc) type supercell containing 16 atoms. This resulted in a series of rock-salt compounds,  $Sr_{1-x}Fe_xS$  ( $x = 0.125, 0.25, 0.50$  and  $0.75$ ), with one, two, four and six of the eight Sr atoms replaced by Fe atoms, which gave  $Sr_7Fe_1S_8$ ,  $Sr_6Fe_2S_8$ ,  $Sr_4Fe_4S_8$  and  $Sr_2Fe_6S_8$ , configurations, respectively. All four of these compounds retain a cubic structure and each have one of three possible space groups. In particular,  $Sr_7Fe_1S_8$  ( $x = 0.125$ ) and  $Sr_4Fe_4S_8$  ( $x = 0.50$ ) retain the fcc structure with space groups 225 ( $Fm\bar{3}m$ ) and 227 ( $Fd\bar{3}m$ ), respectively. On the other hand, both  $Sr_6Fe_2S_8$  ( $x = 0.25$ ) and  $Sr_2Fe_6S_8$  ( $x = 0.75$ ) adopt the primitive cubic system with space group 221 ( $Pm\bar{3}m$ ). We considered two possible couplings between atoms:



ferromagnetic (FM), in which the spins align in the same direction, and antiferromagnetic (AFM), in which the spins are opposite. In the case of the AFM configuration, a larger body-centered cubic (bcc) supercell with 32 atoms ( $2 \times 2 \times 2$ ) was used. Figure 1(a-d) provides a visual representation of the crystal structure for the singly-doped SrS: Fe systems with the stable ferromagnetic phase (FM).

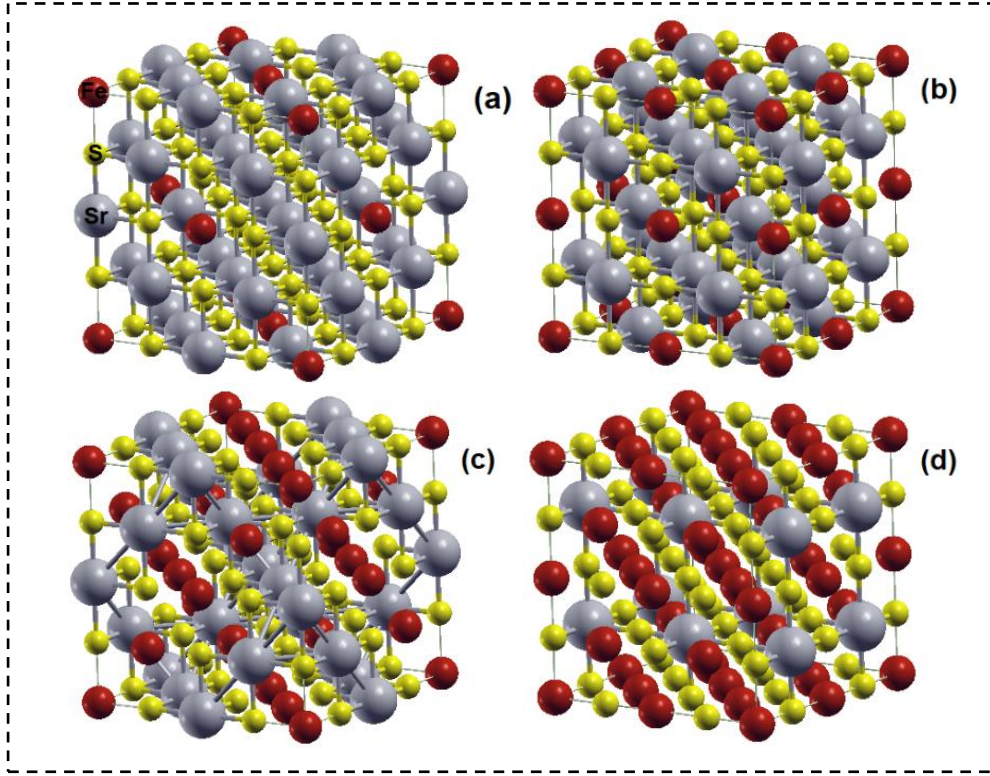


**Figure 1.** Supercell models showing the cubic structure of  $\text{Sr}_{1-x}\text{Fe}_x\text{S}$  compounds with different  $x$  values (a)  $x = 0.125$ , (b)  $x = 0.25$ , (c)  $x = 0.50$  and (d)  $x = 0.75$ . The Sr atom is shown in gray color, iron in red color, and sulfur in yellow color.

The procedure for determining the structural properties near equilibrium involves evaluating the total energy of the systems for different lattice parameter values using the empirical Birch-Murnaghan equation of state (EOS) [18] as described by:

$$E(V) = E_0 + B_0 V_0 \left[ \frac{1}{B'_0(B'_0-1)} \left( \frac{V}{V_0} \right)^{1-B'_0} + \frac{1}{B'_0} \frac{V}{V_0} - \frac{1}{B'_0-1} \right] \quad (\text{eq.1})$$

Where  $E_0$ ,  $B_0$ ,  $B'_0$ , and  $V_0$ , respectively, stand for the minimum energy, bulk modulus, the first derivative of the bulk modulus, and volume at the equilibrium state.

The bulk modulus is determined at the minimum of the  $E(V)$  curve by the following relationship:

$$B = V \frac{\partial^2 E}{\partial V^2} \quad (\text{eq.2})$$

The volume is determined as a function of pressure by:

$$V(P) = V_0 \left( 1 + \frac{B_0' P}{B_0} \right)^{-\frac{1}{B_0'}} \quad (\text{eq.3})$$

During the optimization process, we performed calculations in both spin-unpolarized and spin-polarized states. The variation of the total energy with volume for the four ternary compounds in the three configurations—ferromagnetic (FM), anti-ferromagnetic (AFM), and non-magnetic (NM)—using the GGA-PBE is shown in Figure 2. Based on Figure 2, it is clear that the ferromagnetic phase is the most stable and therefore favorable for all compounds because it has a significantly lower total energy compared to the anti-ferromagnetic and non-magnetic phases.

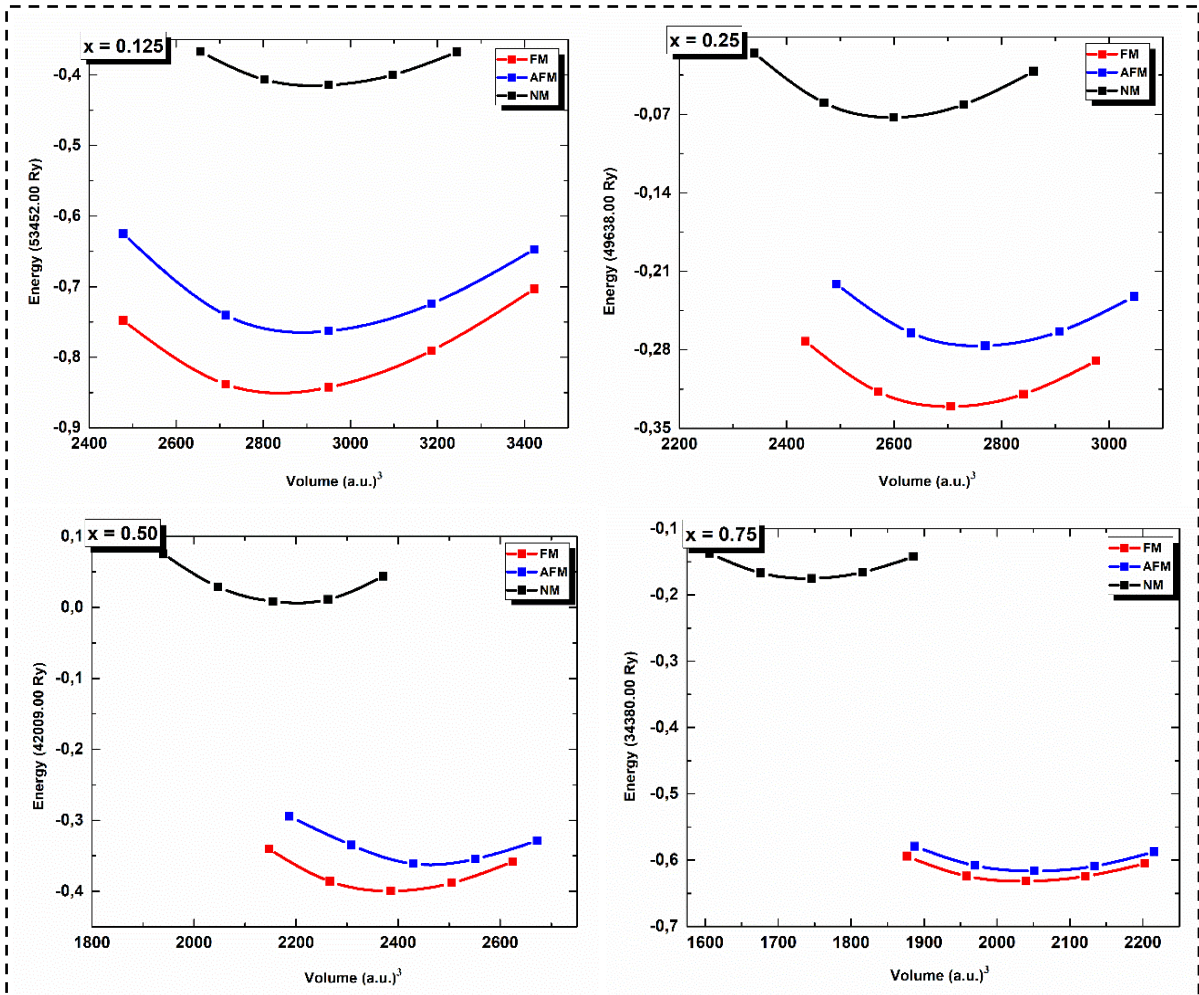


**Figure 2.** Change in total energy with volume for  $\text{Sr}_{1-x}\text{Fe}_x\text{S}$  compounds ( $x = 0.125, 0.25, 0.50,$  and  $0.75$ ) in spin-polarized and unpolarized states.

The results obtained from the E(V) curves - lattice parameters ' $a$ ' and bulk modulus ' $B$ ' of the equilibrium unit cell for our binary compound SrS as well as for the four ternary compounds in the FM stable phase are summarized in Table 1, which provides a comparison between our results and previous experimental and theoretical results for pristine SrS. It is worth noting that there are no results in the literature that can be compared with our results for the ternary compounds. Therefore, our results serve as a reference point for other theoretical investigations and highlight the need for experimental validation.

**Table 1**

The optimized lattice parameters  $a$  (Å), bulk moduli  $B$  (GPa), and formation energies  $E_f$  (eV/atom) for binary SrS and ternary  $\text{Sr}_{1-x}\text{Fe}_x\text{S}$  ( $x = 0.125, 0.25, 0.50, \text{ and } 0.75$ ) compounds.

Compound	$a$			$B$			$E_f$		
	Our work	Exp	Others	Our work	Exp	Others	Our work	Exp	Others
<b>SrS</b>	6.059	6.024 <sup>a</sup>	6.061 <sup>b</sup> 6.050 <sup>c</sup>	48.273	58 <sup>a</sup>	47.184 <sup>b</sup> 48.300 <sup>c</sup>	-	-	-
<b>Sr<sub>0.875</sub>Fe<sub>0.125</sub>S</b>	5.949	-	-	50.244	-	-	-4.384	-	-
<b>Sr<sub>0.75</sub>Fe<sub>0.25</sub>S</b>	5.852	-	5.779 <sup>d</sup>	52.410	-	59.522 <sup>d</sup>	-4.324	-	1.558 <sup>d</sup>
<b>Sr<sub>0.50</sub>Fe<sub>0.50</sub>S</b>	5.612	-	-	60.329	-	-	-4.301	-	-
<b>Sr<sub>0.25</sub>Fe<sub>0.75</sub>S</b>	5.336	-	-	73.687	-	-	-4.422	-	-

<sup>a</sup> Ref [19], <sup>b</sup> Ref [20], <sup>c</sup> Ref [21], <sup>d</sup> Ref [22].

Examination of the data from this table shows a slight deviation between the calculated lattice constant and bulk modulus of SrS compared to experimental values [19]. The PBE method shows a tendency to overestimate the cell parameter by about 0.5% and underestimate the bulk modulus by about 18.3%. Such discrepancies are consistent with the well-known trend of the PBE method. However, our results show excellent agreement with theoretical literature values using the PBE exchange potential [20, 21]. Furthermore, the estimated values for the ternary compound  $\text{Sr}_{0.75}\text{Fe}_{0.25}\text{S}$  are largely in agreement with the theoretically proposed values by Hoat [22].

Replacing strontium with iron results in a gradual reduction in the lattice constant as the concentration increases from 12.5% to 75%. This suggests a reduction in the size of the structure due to the smaller ionic radius of the substituted dopant  $\text{Fe}^{2+}$  (0.55 Å) compared to the bare cation  $\text{Sr}^{2+}$  (1.26 Å). At the same time, there is an increase in the compression modulus, which means that the structures become harder as Fe concentration increases. This behavior is consistent with findings from a study of similar transition metal-doped SrS using the GGA-PBE function within the FP-LAPW approach [20].

Thermodynamic process analysis allows us to assess the difficulties in doping ordered structures and obtain further information about the stability of the systems under consideration. Fe-doped SrS thermodynamic stability was evaluated by calculating the formation energy ( $E_f$ ) with the following formula:

$$E_f = E_{doped} - xE^b(\text{Sr}) - yE^b(\text{Fe}) - zE^b(\text{S}) \quad (\text{eq.4})$$

$E_{doped}$  denotes the total energy of the doped systems.  $E^b(\text{Sr})$ ,  $E^b(\text{Fe})$ , and  $E^b(\text{S})$  refer to the per-atom energies of bulk Sr, Fe, and S, respectively. The variables "x," "y," and "z" represent the amounts of Sr, Fe and S atoms present in the unit cell.

The formation energy results are presented in Table 1, where a negative and lower value of  $E_f$  indicates a higher degree of stability and simplicity in the doping process. Notably, all compounds exhibit negative  $E_f$  values, confirming their thermodynamic stability and suggesting their feasibility for synthesis under ambient conditions. The negative sign means that when these compounds form, thermal energy is released into the environment, indicating an exothermic reaction.

Regarding the  $E_f$  values, the order is as follows:  $E_f(\text{Sr}_{0.25}\text{Fe}_{0.75}\text{S}) < E_f(\text{Sr}_{0.875}\text{Fe}_{0.125}\text{S}) < E_f(\text{Sr}_{0.75}\text{Fe}_{0.25}\text{S}) < E_f(\text{Sr}_{0.50}\text{Fe}_{0.50}\text{S})$ , indicating that  $\text{Sr}_{0.25}\text{Fe}_{0.75}\text{S}$  is the easiest to synthesize, with the system appearing most stable at  $x = 0.75$ . Comparing our  $E_f$  value for  $\text{Sr}_{0.75}\text{Fe}_{0.25}\text{S}$  (-4.324 eV) with the previously published value using GGA-WC (-1.558 eV) [22], we find that the estimated value using GGA-PBE is 21% lower. This discrepancy can be attributed to differences in both the XC energy function used and the computational inputs.

### 3.1.3.2 Mechanical Properties

After examining the structural properties, we looked intensively at the mechanical properties. This step allowed us to not only verify the mechanical stability of the compounds but also investigate the elastic properties in the polycrystalline state and study their anisotropic responses. In our dissertation, all of the compounds we examined showed cubic symmetry. This property allowed us to rely on only three independent elastic constants ( $C_{11}$ ,  $C_{12}$ , and  $C_{44}$ ) to thoroughly characterize their mechanical properties. Determining the elastic constant requires the establishment of three equations to be solved, which are generated by applying three different types of deformation:

The first step involves calculating the bulk modulus  $B$ :

$$B = \frac{1}{3}(c_{11} + 2c_{12}) \quad (\text{eq.5})$$

The second step involves applying a tetragonal stress tensor at constant volume to derive  $C_{11} - C_{12}$ :

$$\boldsymbol{\varepsilon} = \begin{pmatrix} \sigma & 0 & 0 \\ 0 & \sigma & 0 \\ 0 & 0 & \frac{1}{(1-\sigma)^2} - 1 \end{pmatrix} \quad (\text{eq.6})$$

Where  $\boldsymbol{\varepsilon}$  represents the strain and  $\sigma$  represents the applied stress.

Within this stress, the total energy is given by:

$$E(\sigma) = E(0) + 3(C_{11} - C_{12})V_0\sigma^2 + 0(\sigma)^3 \quad (\text{eq.7})$$

Where:

- $E(0)$ : is the energy of the unstrained system.
- $V_0$  : is the volume of the unstrained system.

The third step involves applying a rhombohedral stress tensor at constant volume to calculate the  $C_{44}$  constant, which is given by the following expression

$$\boldsymbol{\varepsilon} = \frac{\sigma}{3} \begin{pmatrix} 1 & 1 & 1 \\ 1 & 1 & 1 \\ 1 & 1 & 1 \end{pmatrix} \quad (\text{eq.8})$$

The elastic constants can finally be determined and must satisfy the convergence criteria of Born-Huang [23] to be in the mechanically stable states and are provided as follows:

$$\begin{aligned} C_{11} - C_{12} &\geq 0; & C_{11} &\geq 0 \\ C_{11} + 2C_{12} &\geq 0; & C_{44} &\geq 0 \end{aligned} \quad (\text{eq.9})$$

The obtained values for the elastic constants  $C_{11}$ ,  $C_{12}$  and  $C_{44}$  of our binary and ternary compounds with some theoretical comparison values for the binary compound are listed in Table 2. For the ternary compounds, the existing literature lacks experimental and theoretical studies for possible comparisons.

According to the results reported in Table 2 and the stability criteria of Born [23], we find that the studied compounds met all the criteria for mechanical stability, indicating that they are mechanically stable.

**Table 2**

The calculated values of elastic constants  $C_{ij}$  (GPa), bulk modulus  $B$  (GPa), shear modulus  $G$  (GPa), Young's modulus  $E$  (GPa), Pugh  $B/G$  ratio, Poisson's ratio  $\nu$ , Zener anisotropy factor  $A$ , longitudinal  $v_l$  (m/s), transverse  $v_t$  (m/s), and average  $v_m$  (m/s) elastic sound velocities, Debye  $\theta_D$  (K) and melting  $T_m$  (K) temperatures of SrS and  $\text{Sr}_{1-x}\text{Fe}_x\text{S}$  ( $x = 0.125, 0.25, 0.50, \text{ and } 0.75$ ) compounds.

Parameters	SrS	$\text{Sr}_{0.875}\text{Fe}_{0.125}\text{S}$	$\text{Sr}_{0.75}\text{Fe}_{0.25}\text{S}$	$\text{Sr}_{0.50}\text{Fe}_{0.50}\text{S}$	$\text{Sr}_{0.25}\text{Fe}_{0.75}\text{S}$
$C_{11}$	110.817 100.4 <sup>e</sup> 113.9 <sup>f</sup>	93.703 -	95.651 -	112.295 -	145.268 -
$C_{12}$	19.049 17.2 <sup>g</sup> 15.75 <sup>e</sup>	28.448 -	30.823 -	34.381 -	37.706 -
$C_{44}$	32.811 26.88 <sup>e</sup> 30.3 <sup>f</sup>	12.970 -	16.509 -	26.983 -	8.396 -
<b>B</b>	49.638	50.201	52.432	60.352	73.671
<b>G</b>	37.535	18.959	21.705	31.268	19.576
<b>B/G</b>	1.322	2.647	2.415	1.930	3.763
<b>E</b>	46.935	50.517	57.219	79.989	53.949
$\nu$	0.198	0.332	0.318	0.279	0.377
<b>A</b>	0.715	0.397	0.509	0.692	0.156
$v_l$	3281	3227	3326	3631	3466
$v_t$	1240	1617	1718	2010	1535
$v_m$	1576	1814	1923	2239	1733
$\theta_D$	251	228	246	298	243
$T_m$	1198	1107	1118	1217	1412

<sup>e</sup> Ref [24], <sup>f</sup> Ref [25], <sup>g</sup> Ref [26].

Notably,  $C_{11}$ , which refers to unidirectional compression along the [100] direction, is higher than  $C_{44}$  which represents shear deformation in the [010] direction. This suggests that these compounds are more susceptible to deformation under shear deformation than under unidirectional compressive deformation. The trend observed in the  $C_{11}$  values shows a decrease in the transition from the binary SrS compound to the ternary alloy with 12.5% Fe concentration. There is then a steady increase in the  $C_{11}$  values as the Fe concentration increases from 12.5% to 75%. In contrast,  $C_{12}$  shows a steady increase with increasing concentration. On the other hand, when moving from SrS to 12.5% Fe,  $C_{44}$  initially decreases and then experiences an increase up to 50% Fe before decreasing from 50% to 75% Fe concentration. This highlights the significant influence of Fe concentration on the elastic constants of

the single crystal and implies that a higher Fe concentration reduces the shear along [010], which could affect the mechanical stability of the compounds.

Our analysis suggests that the non-monotonic fluctuation of  $C_{11}$  and  $C_{44}$  is due to the transition of fcc to primitive cubic symmetry. Yang et al. [27] observed a similar behavior in  $C_{44}$  when they studied the influence of  $3d-4d$  element concentration on the elastic properties of an Mg solid solution using first-principles calculations. However, they did not provide an explanation for the anomaly that accompanied the sudden increase in  $C_{44}$ .

Understanding the mechanical properties of a compound not only allows assessment of its mechanical stability, but also enables comprehensive quantification of properties related to mechanical behavior, such as: hardness, brittleness, ductility, stiffness, chemical bonding and anisotropy. In practical applications, materials are often in a polycrystalline state. However, ab-initio studies typically focus on materials in their single crystal form. Voigt, Reuss, and Hill [28–30] have proposed approximations to predict the elastic behavior of polycrystalline materials based on the elastic constants calculated for single-crystal counterparts.

The hardness of a material is determined by its polycrystalline bulk moduli ( $B$ ) and shear moduli ( $G$ ). The compression modulus is estimated using Eq.5, while the shear modulus is defined by the following relationships using the Voigt-Reuss-Hill approximations [28-30]:

$$G_V = \frac{C_{11} - C_{12} + 3C_{44}}{5} \quad (\text{eq.10})$$

$$G_R = \frac{5(C_{11} - C_{12})C_{44}}{4C_{44} + 3(C_{11} - C_{12})} \quad (\text{eq.11})$$

Here,  $G_V$  represents the Voigt shear modulus corresponding to the upper limit of the values of  $G$ , and  $G_R$  represents the Reuss shear modulus for cubic crystals corresponding to the lower values.

The average of these two moduli represents the Hill shear modulus ( $G_H$ ) and is given by the following equation:

$$G_H = \frac{G_R + G_V}{2} \quad (\text{eq.12})$$

The values of  $B$  range from 49.638 to 73.671 GPa and  $G$  range from 18.959 to 37.535 GPa, as listed in Table 2. This indicates that the pristine SrS with the lower  $B$  modulus value is the softest and that  $\text{Sr}_{0.875}\text{Fe}_{0.125}\text{S}$  is less resistant to shear deformation compared to all other compounds. The trend for  $B$  is consistent and gradually increases with concentration. On the other hand,  $G$  can exhibit non-monotonic behavior, decreasing in the transition from pure to ternary alloy (from SrS to 12.5% Fe), increasing in the range of 12.5% to 50% Fe, and then decreasing sharply in the range of 50% up to 75% Fe. This

variation can be attributed to the non-monotonic elastic constants that contribute to such fluctuations. It is noteworthy that the  $B$  values calculated from the elastic constants agree closely with those obtained by the Birch-Murnaghan EOS fitting (see Table 1), confirming the accuracy of our calculations.

The brittle/ductile behavior can be predicted by the Pugh ratio ( $B/G$ ) [31], which relates the bulk and shear moduli to a critical value of 1.75. The material is considered brittle if the  $B/G$  value is less than 1.75; otherwise, it is ductile. As indicated in Table 2, the  $B/G$  ratio for pristine SrS is below the critical value of 1.75, classifying it as a brittle material, while for our four alloys it is above the critical value, classifying them as ductile materials.

The stiffness of a material is quantified by the Young modulus ( $E$ ), which establishes the relationship between the compression modulus and the shear modulus and is expressed as follows:

$$E = \frac{9BG}{3G+B} \quad (\text{eq.13})$$

As Table 2 shows, the Young modulus actually exhibits a pattern similar to the shear modulus due to their interdependence. The addition of Fe to the SrS host matrix leads to an increase in stiffness, highlighting the reinforcing capacity of iron. A high modulus of elasticity indicates a material's ability to withstand stress. Of the compositions examined, the one with 50% iron content is expected to have the highest stiffness and the one with 12.5% iron content is expected to have the lowest stiffness.

We also calculated Poisson's ratio ( $\nu$ ), a quantitative measure of the type of chemical bond present in the material. This relationship can be expressed in terms of volume and shear modulus using Eq.14.

$$\delta = \frac{3B-2G}{2(3B+G)} \quad (\text{eq.14})$$

If  $\nu$  exceeds 0.25, the chemical bond is said to be ionic; if it falls below 0.25, it is considered covalent [32]. According to the  $\nu$  values listed in Table 2, all ternary alloys have a  $\nu$  value in the range of 0.3. This implies that the bonding in the compounds  $\text{Sr}_{0.875}\text{Fe}_{0.125}\text{S}$ ,  $\text{Sr}_{0.75}\text{Fe}_{0.25}\text{S}$ ,  $\text{Sr}_{0.50}\text{Fe}_{0.50}\text{S}$  and  $\text{Sr}_{0.25}\text{Fe}_{0.75}\text{S}$  is mainly ionic. On the other hand, the value for binary SrS is below 0.25, indicating its covalent nature.

The anisotropy of a material is determined using the Zener anisotropy factor ( $A$ ). This factor gives a numerical indication of the extent to which a compound deviates from isotropy and is calculated using the following equation [33]:

$$A = \frac{2c_{44}}{c_{11}-c_{12}} \quad (\text{eq.15})$$



If the factor  $A$  is equal to one, this indicates perfect isotropy. When  $A$  is less than one, the material is harder in the [100] direction, and when  $A$  is greater than one, it is harder in the diagonal [111] direction [33]. As can be seen in Table 2, all compounds exhibit deviations from unity, showing their anisotropic nature with optimal stiffness in the diagonal direction [100]. The trend in  $A$  closely follows that of  $C_{44}$  due to their interdependence. The greater the deviation from unity, the more pronounced the degree of anisotropy. This means that the iron-enriched compound (75% Fe) has the highest degree of anisotropy, while the 0% iron compound (SrS) has the lowest degree.

To provide a more comprehensive understanding of the elastic anisotropy in the studied compounds, we used three-dimensional (3D) surface representations. These plots provide a visual representation of the variation of the polycrystalline modules across the main crystal directions. The specific mathematical formulations are listed below [34, 35]:

$$\frac{1}{B} = (S_{11} + 2S_{12})(l_1^2 + l_2^2 + l_3^2) \quad (\text{eq.16})$$

$$\frac{1}{G} = (S_{44} + 4S_0J) \quad (\text{eq.17})$$

$$\frac{1}{E} = S_{11} - 2(S_{11} - S_{12} - \frac{S_{44}}{2})(l_1^2 l_2^2 + l_2^2 l_3^2 + l_1^2 l_3^2) \quad (\text{eq.18})$$

Where  $S_{11}$ ,  $S_{12}$ ,  $S_{44}$  are the elastic compliance constants;  $l_1^2$ ,  $l_2^2$ , and  $l_3^2$  are the direction cosines; and  $J$  is quantified by:

$$J = \sin^2\theta \cdot \cos^2\theta + 0.125 \cdot \sin^4\theta (1 - \cos 4\varphi) \quad (\text{eq.19})$$

$\theta$  and  $\varphi$  are Euler angles.

Figures 3(a-c) and Figures 4(a-c) illustrate the 3D contour plots of the bulk, shear and Young's moduli for SrS and  $\text{Sr}_{1-x}\text{Fe}_x\text{S}$  ( $x = 0.125, 0.25, 0.50$  and  $0.75$ ), respectively. The obvious spherical shape in the 3D contour plots of linear compressibility of cubic systems, as shown in Figure 3(a) and Figures 4(a1-a4) confirm their isotropic nature. When examining the shear and Young moduli in Figures 3(b-c) and 4(b1-b4)/ (c1-c4), their 3D representations deviate from a perfect sphere, indicating anisotropic properties. This anisotropy is more pronounced in the compound with the highest iron content (75%). Notably, the Young modulus for all compounds peaks in the [100] direction and reaches a minimum in the [110] direction, which is consistent with the Zener anisotropy factor observations. However, it is important to note that the directional dependencies of the shear modulus are opposite to those of the Young's modulus.

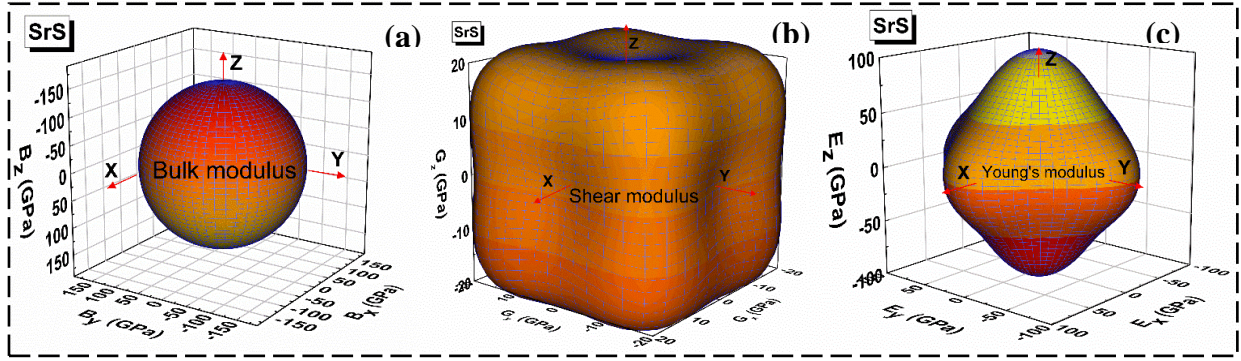


**Figure 3.** The directional dependencies of three-dimensional (3D) contour plots of (a) bulk modulus (B), (b) shear modulus (G), and (c) Young's modulus (E) for SrS pristine compound.

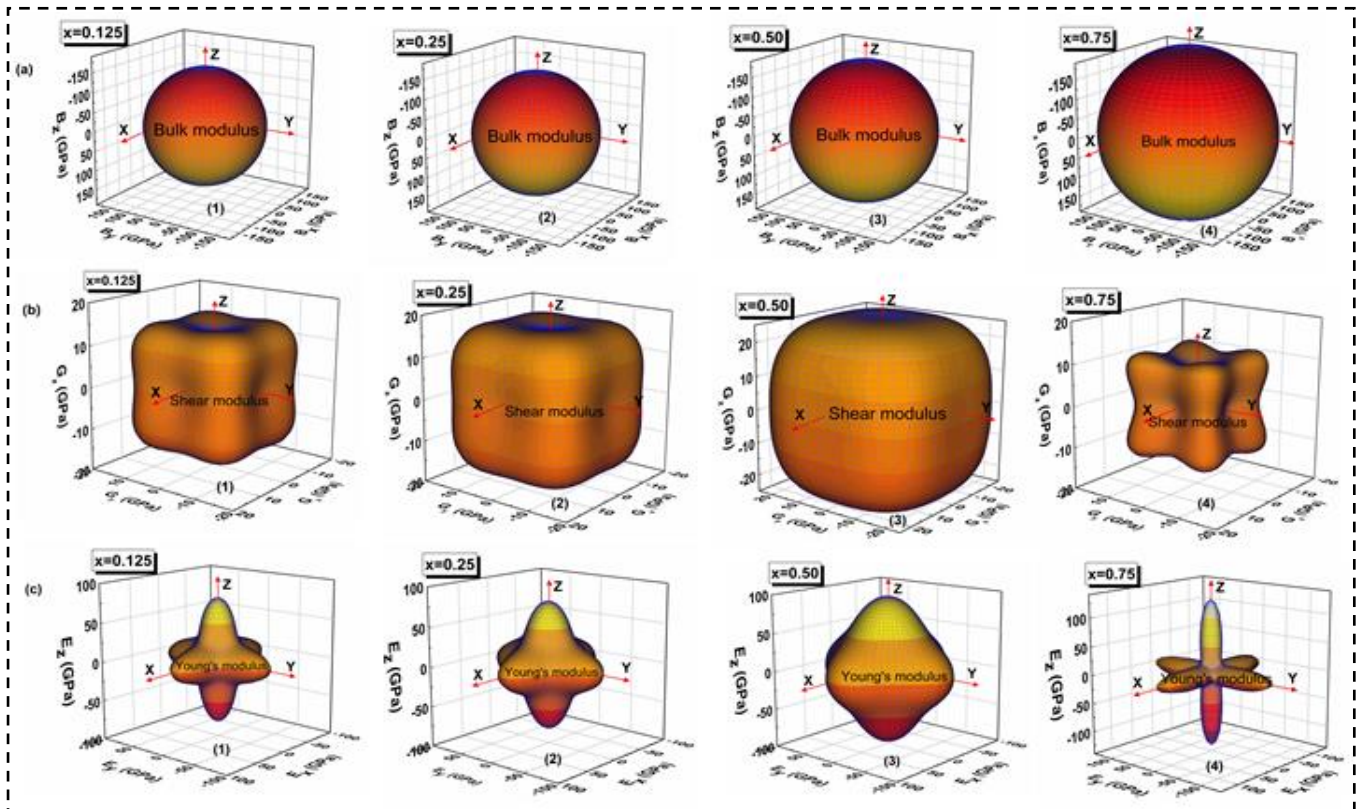


**Figure 4.** The directional dependencies of three-dimensional (3D) contour plots of (a) bulk modulus (B), (b) shear modulus (G), and (c) Young's modulus (E) for  $\text{Sr}_{1-x}\text{Fe}_x\text{S}$  compounds [(1)  $x=0.125$ , (2)  $x=0.25$ , (3)  $x=0.50$  and (4)  $x=0.75$ ].

Since mechanical behavior and thermal properties are highly correlated, the identified elastic moduli are mostly used to describe the melting point ( $T_m$ ) and the Debye temperature ( $\theta_D$ ).

The highest frequency of oscillation is related to an important physical parameter called the Debye temperature. From this temperature, important thermophysical parameters such as entropy, melting temperature and heat capacity can be calculated. According to the harmonic approach, the vibration frequency and the square root of hardness are directly related, and the Debye temperature can be used

to determine the hardness [36]. Using the data of the average speed of sound ( $v_m$ ) and the elastic constant, the Debye temperature ( $\theta_D$ ) can be calculated in a conventional way [37]:

$$\theta_D = \frac{h}{k_B} \left[ \frac{3n}{4\pi} \left( \frac{N_A \rho}{M} \right) \right]^{\frac{1}{3}} v_m \quad (\text{eq.20})$$

Here,  $h/k_B$  represents the ratio of Planck's constant to Boltzmann's constant;  $n$  stands for the number of atoms in the cell;  $N_A$  is Avogadro's number;  $\rho$  denotes the mass density;  $M$  represents the molecular weight. Additionally,  $v_m$  encompasses both transverse ( $v_t$ ) and longitudinal ( $v_l$ ) velocities, outlined as [37]:

$$v_m = \left[ \frac{1}{3} \left( \frac{2}{v_t^3} + \frac{1}{v_l^3} \right) \right]^{-\frac{1}{3}} \quad (\text{eq.21})$$

By applying the Navier equation [37] to the mass density, shear modulus, and bulk modulus, the transverse velocity ( $v_t$ ) and longitudinal velocity ( $v_l$ ) can be obtained:

$$v_t = \sqrt{\frac{G}{\rho}}; \quad v_l = \sqrt{\frac{B + \frac{4}{3}G}{\rho}} \quad (\text{eq.22})$$

The heat sensitivity of a material is indicated by its melting temperature ( $T_m$ ). Because they are stable over a wide range of temperatures, materials with a high melting point are highly desirable. To estimate the melting temperature of these materials, the empirical equation of Fine [38] is used, taking into account the elastic constant  $C_{11}$ .

$$T_m(K) = 553K + (5.911K/GPa) C_{11} \pm 300K \quad (\text{eq.23})$$

The Debye temperatures and melting temperatures are shown in Table 2 and are graphically shown in Figure 5 for better visualization. It is obvious that the melting temperature has a nonlinear variation with the Fe concentration in the compounds and shows a similar trend with the elastic constant  $C_{11}$ , reflecting the direct correlation between them, as presented in Eq.23. The  $T_m$  values obtained for all compounds are high, indicating their resistance to high-temperature treatment and their ability to maintain their solid-state structures at elevated temperatures.

In contrast to the melting temperature, the Debye temperature shows a decrease with increasing concentration from 0% to 12.5%, followed by an increasing trend at 12.5% Fe and a subsequent decreasing trend at 50% Fe. This pattern is already evident in the elastic properties results, since the Debye temperature is an average of the sound velocity that correlates with the compression modulus and in particular with the shear modulus (see equations (20)–(22)). This suggests that the shear modulus

has a stronger influence on the variation of the Debye temperature. The compound  $\text{Sr}_{0.50}\text{Fe}_{0.50}\text{S}$  has the highest value, which indicates its relatively high intrinsic hardness.

Unfortunately, direct comparison of our thermal and mechanical results with previous experimental work on this doped chalcogenide is not possible. However, it is interesting to note that our results agree with most previous first-principles calculations [39–41].

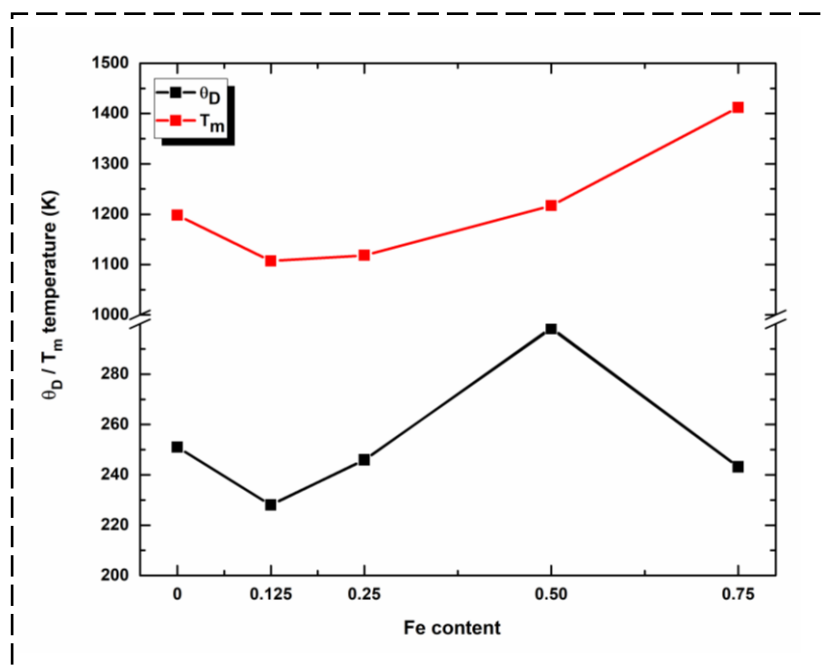
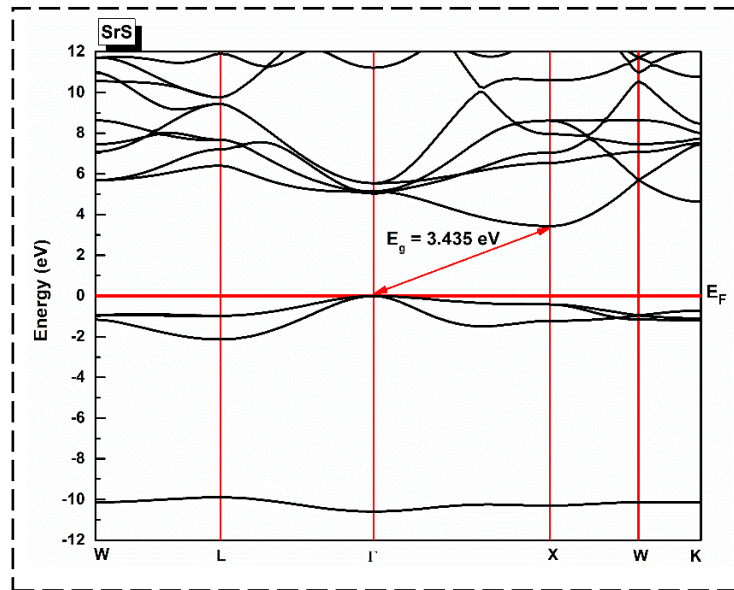


**Figure 5.** The dependence of melting temperature ( $T_m$ ) and Debye temperature ( $\theta_D$ ) on Fe content for  $\text{Sr}_{1-x}\text{Fe}_x\text{S}$  Compounds ( $x = 0, 0.125, 0.25, 0.50, \text{ and } 0.75$ ).

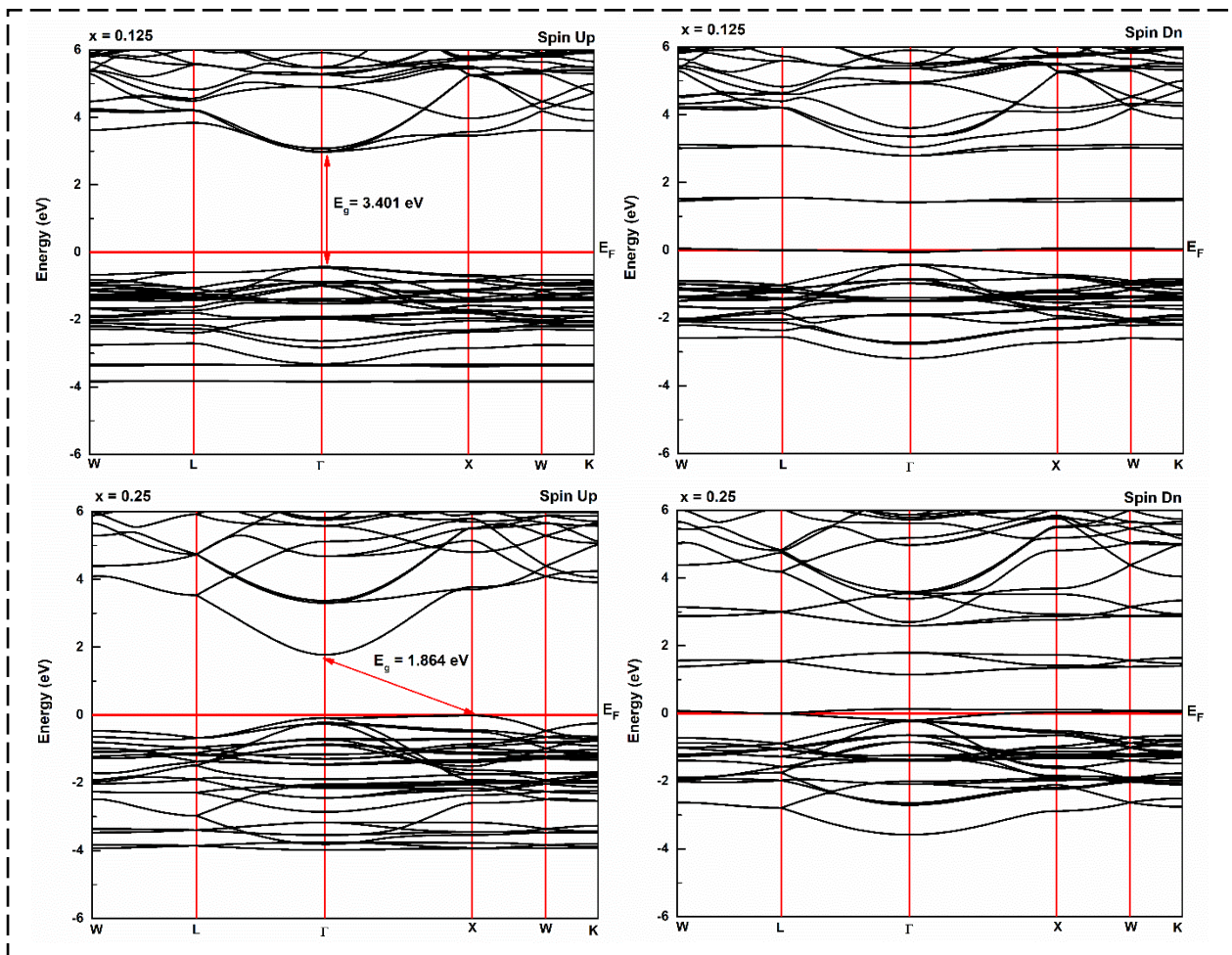
### 3.1.3.3 Electronic Properties

#### 3.1.3.3.1 Electronic Band Structure Analysis

After studying the effects of Fe doping on various properties and system stability, we will now consider how the introduction of Fe affects the electronic behavior of the SrS semiconductor. This is achieved through an analysis of spin-resolved band structures (BS), total density of states (TDOS) and partial density of states (PDOS). It is worth noting that previous studies have shown that bandgaps in materials are often slightly underestimated when using PBE-GGA, which is due to self-interaction errors [15]. An alternative is to use the mBJ exchange functional, which has been shown to provide reasonably accurate bandgap calculations that are close to experimental values. Figures 6 and 7 show the band structures along the high-symmetry points of the irreducible Brillouin zone for the host SrS and the ternary-doped  $\text{Sr}_{1-x}\text{Fe}_x\text{S}$  compounds ( $x = 0.125, 0.25, 0.5, \text{ and } 0.75$ , respectively), calculated based on their equilibrium lattice constants.



**Figure 6.** Electronic band structure of rock-salt SrS with mBJ-PBE method.





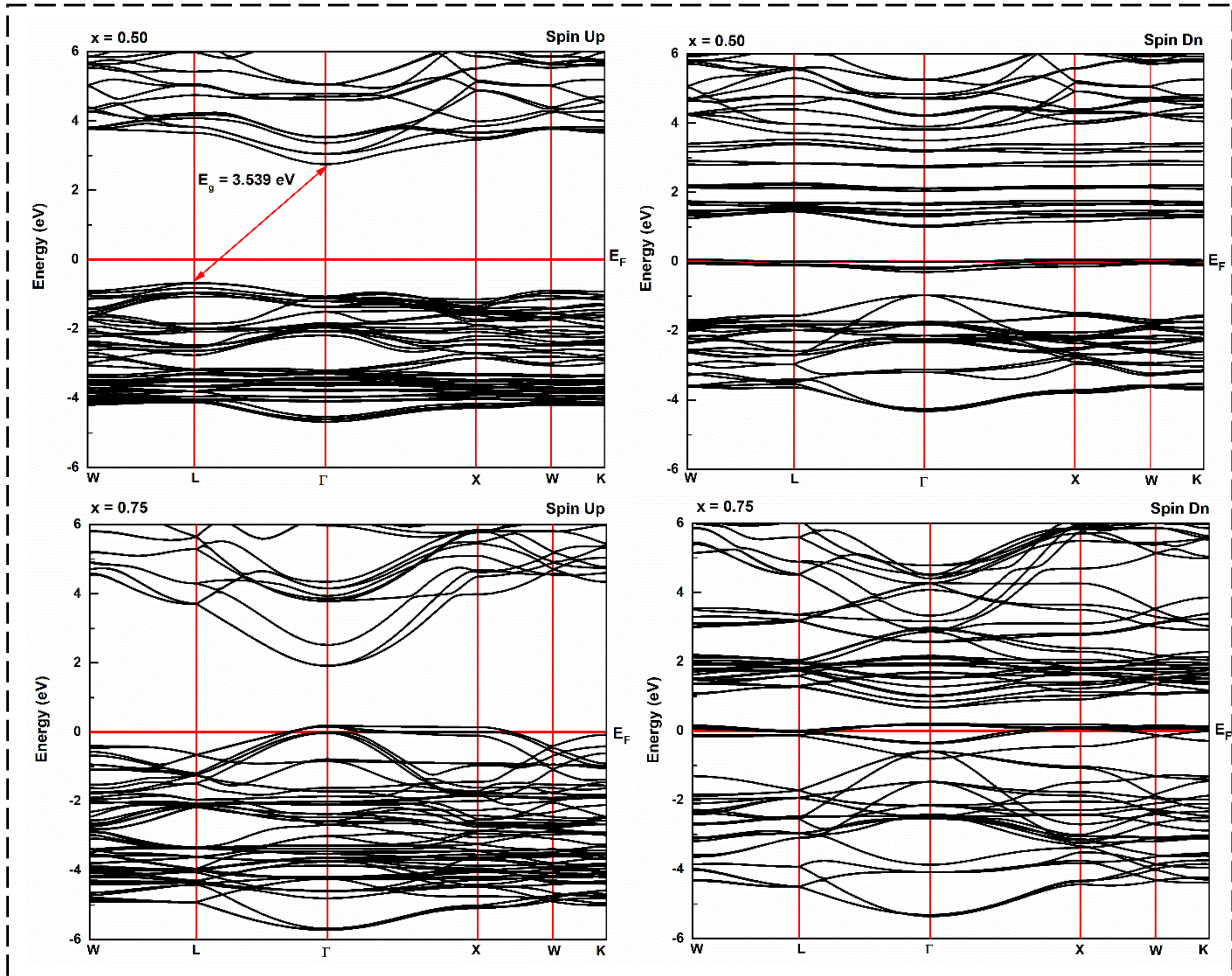


**Figure 7.** Spin-resolved electronic band Structures of  $\text{Sr}_{1-x}\text{Fe}_x\text{S}$  compounds ( $x = 0.125, 0.25, 0.50,$  and  $0.75$ ) with mBJ-PBE.

According to Figure 6, SrS has a band structure typical of a semiconductor. In an mBJ calculation, the gap is indirect in the direction  $\Gamma$ -X with a value of 3.435 eV. Compared to other theoretical calculations, this value is closer to that of Hamidane et al. [20], with a difference of 0.135 eV, than that calculated by Kaneko and Koda [43], which has a deviation of 0.419 eV. The calculated gap value is underestimated compared to the experimentally measured value. It shows a difference of 26% compared to the experimental value of Sharma et al. [42]. However, this discrepancy arises from the use of different input parameters and the well-known tendency of DFT to underestimate energy gaps compared to experimental values. Our calculations compared to other theoretical and experimental results are summarized in Table 3.

From Figure 7, which shows the spin-majority and spin-minority band structures for the ternary compounds, it can be seen that the introduction of Fe into the SrS host matrix results in a significant transformation of the electronic structure. In fact, the addition of 12.5%, 25% and 50% Fe content changes the nature of pristine SrS from a non-magnetic semiconductor to a ferromagnetic half-metal (HMF) and from ferromagnetic half-metal to magnetic metal at a higher degree of concentration (75%

Fe ). The semimetallicity in the first three concentrations arises from the fact that the majority-spin (left image) maintains the semiconducting behavior of SrS, with the Fermi level ( $E_F$ ) lying within the generated bandgap. Conversely, the minority-spin (right image) shows metallic behavior due to the overlap of some valence bands with the  $E_F$ , resulting in 100% spin-polarization. The  $\text{Sr}_{0.875}\text{Fe}_{0.125}\text{S}$  compound exhibits a direct bandgap with both the conduction band minima (CBM) and valence band maxima (VBM) located at the  $\Gamma$  symmetry point with a value of 3.401 eV. However, the scenario changes drastically with increasing concentration, with the direct bandgap transforming into an indirect bandgap located at  $\Gamma$ -X for  $\text{Sr}_{0.75}\text{Fe}_{0.25}\text{S}$ , with a transition energy gap of 1.864 eV and at L- $\Gamma$  for  $\text{Sr}_{0.50}\text{Fe}_{0.50}\text{S}$ , with a transition energy gap of 3.539 eV.

The energy gap ( $E_g$ ) is defined as the energy difference between the maximum of the valence band (VBM) and the minimum of the conduction band (CBM). Thus, the  $E_g$  is calculated for our compounds in the spin-up direction. The half-metallic gap ( $G_{\text{HM}}$ ) is another important parameter for characterizing half-metallic materials, which can be determined by the difference between the VBM and the  $E_F$  in the spin-up channel. The  $E_g$  and  $G_{\text{HM}}$  values for the three semimetallic ferromagnetic compounds are always given in Table 3. As indicated in Table 3, both  $E_g$  and  $G_{\text{HM}}$  values show nonlinear behavior with increasing iron content. The trend over the entire concentration range follows a specific order: a decrease from 12.5% to 25% Fe, followed by an increase from 25% to 50% Fe, and finally a complete disappearance between 50% and 75% Fe. This changing trend is consistent with observations made on previously studied TM-doped II-VI compounds [44, 45]. This behavior is attributed to the introduction of impurity states by Fe doping into the SrS bandgap, resulting in a sudden and significant narrowing.

At a low Fe concentration (12.5%), the impurity states shift both the VBM and CBM slightly downward, resulting in a net bandgap reduction of 0.034 eV compared to pure SrS. This downward shift is attributed to the weakened interaction between the cation Sr and the anion S due to Fe doping. When the Fe concentration increases to 25%, the impurity states broaden, resulting in a significant downward shift in the CBM and a slight upward shift in the VBM. This results in a gradual reduction in the bandgap with a net reduction of 1.537 eV. The reduced bandgap value can be attributed to the combined effects of band modification due to the convergence of energy levels of the 3d bands of the Fe atom and the 3p bands of the S atom. This leads to an exchange interaction between these bands, as described in the following section, along with strain effects caused by the doping level. When the dopant concentration increases to 50%, the bandgap begins to increase gradually and reaches a maximum of 3.539 eV. The increased concentration of impurities leads to the formation of larger defects. Consequently, a higher defect concentration along with symmetry changes from fcc to primitive cubic may contribute to the observed broadening between the 3d-Fe and 3p-S bands (see the next section for more details). At 75% Fe, VBM and CBM follow a similar pattern to the band structure at 25% Fe, further reducing the bandgap until it finally disappears. In addition to the previously mentioned factors, the resulting

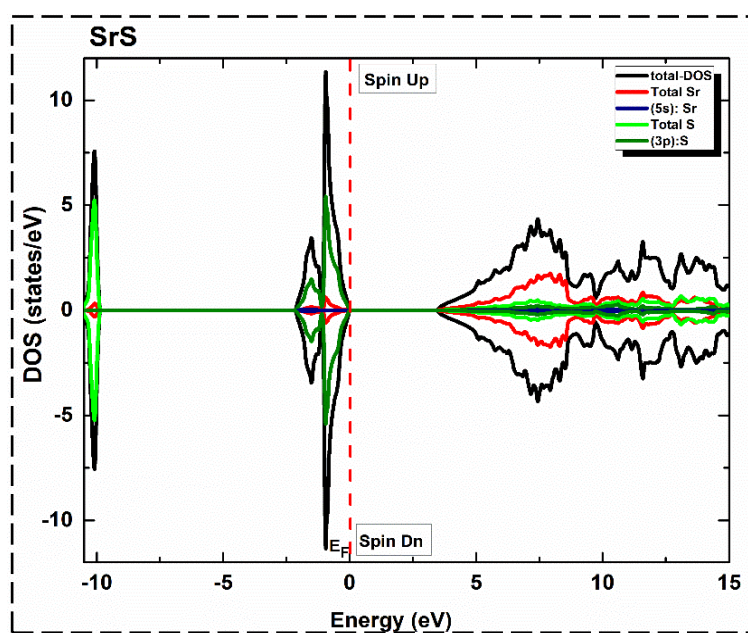
hybridization of  $3d$ -Fe with  $3p$ -S bands at the highest doping concentration could be a factor contributing to the sudden disappearance of the bandgap.

Note that our calculated  $E_g$  and  $G_{HM}$  band gaps for  $Sr_{0.75}Fe_{0.25}S$  show an underestimation compared to the previous theoretical values [22], with deviations estimated at 0.253 eV for  $E_g$  and 0.571 eV for  $G_{HM}$ . This underestimation is due to the differences in the approximation methods used (WC-based mBJ). An important point to consider is that both experimental [46] and theoretical [47] evidence have shown that a material's bandgap is directly correlated with its hardness. Consequently, the maximum bandgap observed in the  $Sr_{0.50}Fe_{0.50}S$  compound is consistent with the findings regarding its mechanical properties and Debye temperature.

### 3.1.3.3.2 Total and Partial Densities of States Analysis

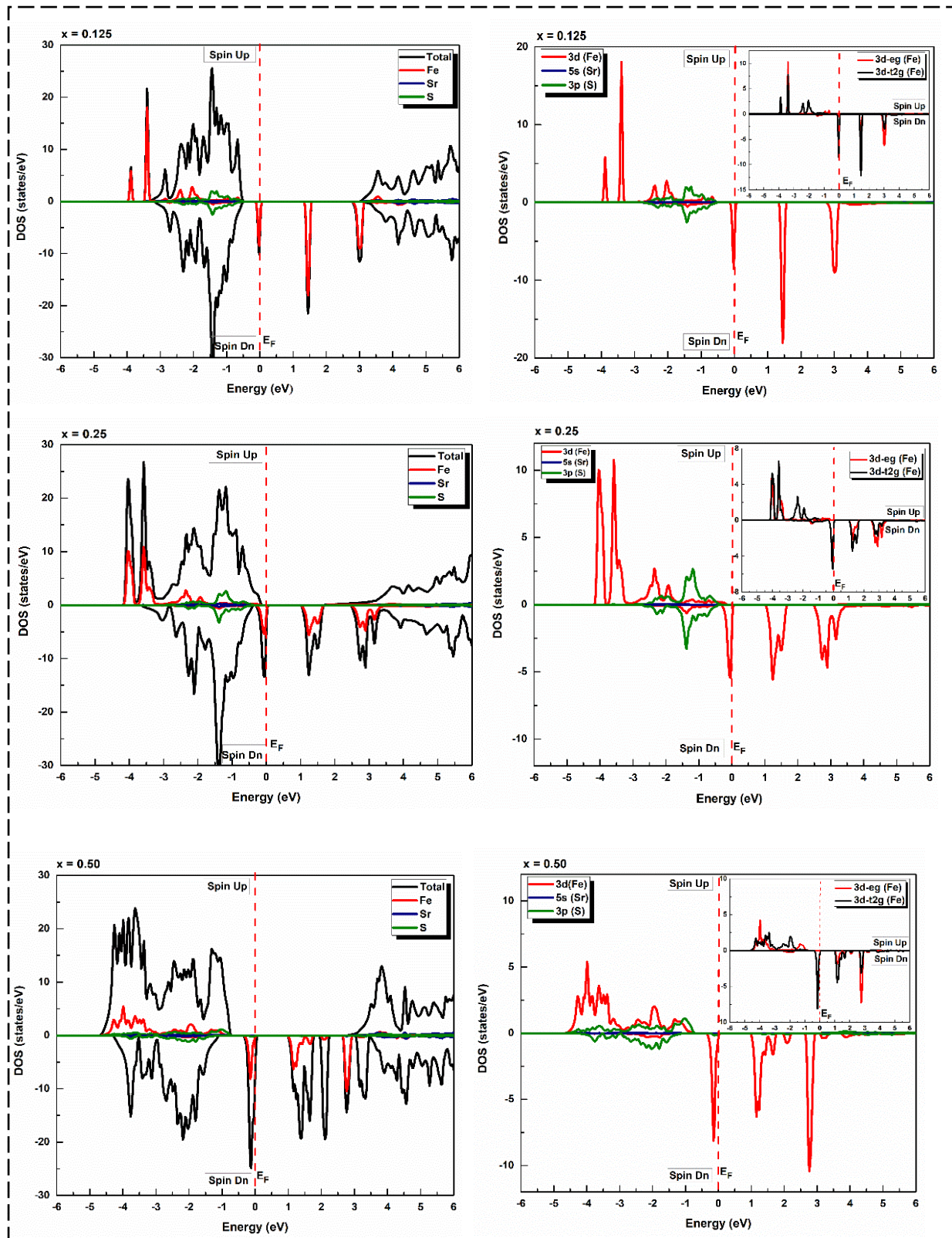
To shed light on the role of atomic states in shaping semimetallic and metallic behavior and to further investigate the underlying reasons for the bandgap wobble, we performed comprehensive calculations of the TDOS and PDOS for pristine SrS and all  $Sr_{1-x}Fe_xS$  compounds ( $x = 0.125, 0.25, 0.50$  and  $0.75$ ). The resulting curves for both spin configurations are shown in Figures 8 and 9, respectively.

From the TDOS curves in Figure 8, it can be seen that there is no polarization between the electron densities of the states for up and down spin orientations of SrS. The density of states is symmetric and indicates the non-magnetic state of the compound, in contrast to the density of states for  $Sr_{1-x}Fe_xS$ , which is asymmetric (Figure 9). This is logically attributed to the doping effect with Fe.



**Figure 8.** The Spin-resolved total and partial density of states of rock-salt SrS with mBJ-PBE method.





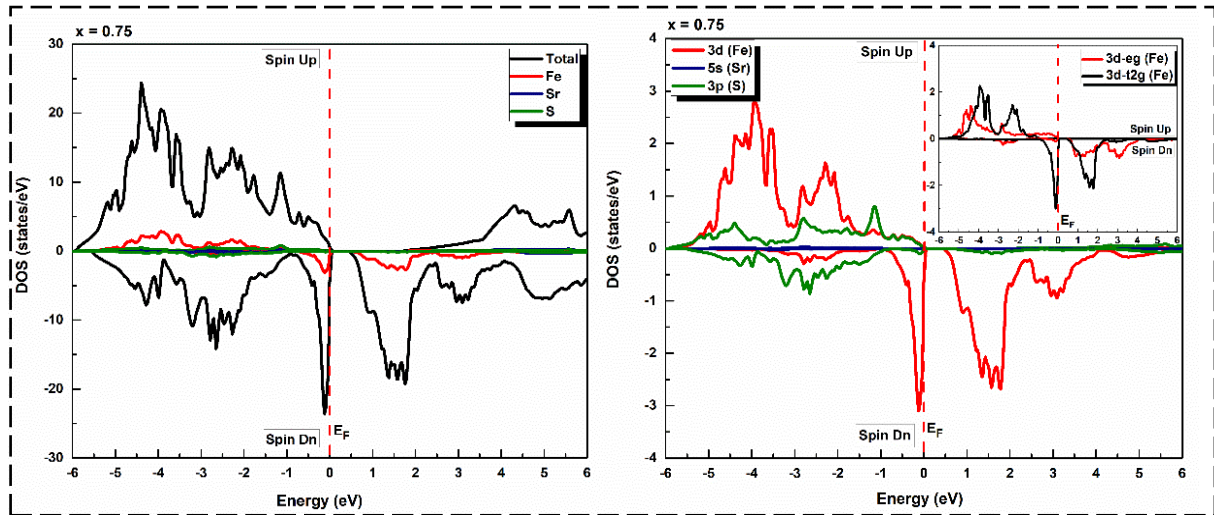


**Figure 9.** Spin-resolved total and partial densities of states of  $\text{Sr}_{1-x}\text{Fe}_x\text{S}$  compounds ( $x = 0.125, 0.25, 0.50, \text{ and } 0.75$ ) with mBJ-PBE.

From the Sr curve (Figure 8), a significant bandgap is evident, indicating the semiconductor nature of this system. This is because the CB and VB do not intersect the Fermi level ( $E_F$ ), which is defined at 0 eV. This bandgap arises mainly from the shift of the  $p$ -states of the S atom, which dominate the VBM, and the  $s$ -states of the Sr atom, which make a small contribution in both regions.

Upon closer inspection of the TDOS curves of the ternary HMF compounds (Figure 9), a clear pattern emerges. In particular, in majority-spin, the  $3d$ -Fe states and  $3p$ -S states of  $\text{Sr}_{0.875}\text{Fe}_{0.125}\text{S}$ ,  $\text{Sr}_{0.75}\text{Fe}_{0.25}\text{S}$ , and  $\text{Sr}_{0.50}\text{Fe}_{0.50}\text{S}$ , hybridize with each other, leading to the formation of a bandgap near the  $E_F$ . This configuration gives these materials a semiconductor-like character. Conversely, in minority-spin, the  $3d$ -Fe and  $3p$ -S states intersect the  $E_F$ , resulting in a distinct metallic character, confirming that these compounds are HMF with 100% spin-polarization at  $E_F$ . In the  $\text{Sr}_{0.25}\text{Fe}_{0.75}\text{S}$  compound, both majority- and minority-spin channels exhibit metallic character that is due to the formation of  $3d$ -Fe and  $3p$ -S states at the  $E_F$ . This means that  $p$ - $d$  hybridization is not particularly pronounced when the concentration of  $3d$ -Fe electrons is relatively low.

Analysis of the PDOS curves shows that for both  $\text{Sr}_{0.875}\text{Fe}_{0.125}\text{S}$ ,  $\text{Sr}_{0.75}\text{Fe}_{0.25}\text{S}$  compounds, the VB in the energy range from about  $\sim -4.14$  eV to about  $\sim -1.63$  eV is mainly derived from  $3d$ -Fe states, with a small contribution from  $3p$ -S states. In the subsequent energy range from about  $\sim -1.63$  eV to about  $\sim -0.42$  eV, the contribution comes predominantly from  $3p$ -S states. When the Fe content exceeds 25%, the contribution of  $3p$ -S states becomes prominent alongside that of  $3d$ -Fe states in the energy range from about  $\sim -4.53$  eV to about  $\sim -0.74$  eV for  $\text{Sr}_{0.50}\text{Fe}_{0.50}\text{S}$  and significantly  $\sim -5.57$  eV to about  $\sim -0.05$  eV for  $\text{Sr}_{0.25}\text{Fe}_{0.75}\text{S}$ . However, the involvement of  $5s$ -Sr states is negligible for all compounds. Conversely, in the minority-spin channel, the lower part of the CB is mainly dominated by  $3d$ -Fe states. These states start at 1.35, 1.02, 0.99, and 0.48–6 eV, respectively, and follow the order  $0.125 \rightarrow 0.25 \rightarrow$

0.50  $\rightarrow$  0.75. States at the  $E_F$  in the PDOS are predominantly attributed to the  $3d$ -Fe states, with minimal contribution from the  $3p$ -S states. These states play a crucial role in producing the ferromagnetic properties observed in the resulting compounds. The calculated PDOS values at the  $E_F$  for the studied cases are summarized in Table 3. It is generally accepted that lower densities of states at the  $E_F$  are associated with greater material stability [42]. This suggests that the compound with the highest iron content (75%) has the highest stability, which is consistent with the conclusions from the enthalpy of formation and melting point calculations.

**Table 3**

The calculated spin-majority bandgaps  $E_g$  (eV), half-metallic bandgaps  $G_{HM}$  (eV), and partial density of states (PDOS) at the Fermi level (states/eV) of  $Sr_{1-x}Fe_xS$  compounds ( $x = 0.125, 0.25, 0.50, \text{ and } 0.75$ ).

Compound	Nature of gap	Location	$E_g$			$G_{HM}$			PDOS ( $E_F$ )		
			Our work	Exp	Others	Our work	Exp	Others	3d (Fe)	5s (Sr)	3p (S)
SrS	indirect	$[\Gamma-X]$	3.435	4.32 <sup>h</sup>	3.300 <sup>b</sup> 3.016 <sup>i</sup>	-	-	-	-	-	-
Sr <sub>0.875</sub> Fe <sub>0.125</sub> S	direct	$[\Gamma-\Gamma]$	3.401	-	-	0.431	-	-	5.322	$2.806 \times 10^{-4}$	0.005
Sr <sub>0.75</sub> Fe <sub>0.25</sub> S	indirect	$[X-\Gamma]$	1.864	-	2.117 <sup>d</sup>	0.090	-	0.661 <sup>d</sup>	2.142	$3.626 \times 10^{-4}$	0.008
Sr <sub>0.50</sub> Fe <sub>0.50</sub> S	indirect	$[L-\Gamma]$	3.539	-	-	1.059	-	-	0.647	$9.056 \times 10^{-4}$	0.086
Sr <sub>0.25</sub> Fe <sub>0.75</sub> S	-	-	-	-	-	-	-	-	0.432	$1.848 \times 10^{-4}$	0.001

<sup>h</sup> Ref [42], <sup>b</sup> Ref [20], <sup>i</sup> Ref [43], <sup>d</sup> Ref [22].

A more detailed understanding of the mechanism of interaction between the introduced Fe impurity states and the anion S states is provided by crystal field theory. The electron configuration of the  $Fe^{2+}$  cation is  $[Ar] 3d^6$ . The  $Fe^{2+}$  ion forms six bonds with the ligand S atoms in an octahedral complex. According to Hund's rule and crystal field theory, each atom contributes two electrons, so a total of two electrons are added to the VB of the host semiconductor. The octahedral field created by the S anion after the introduction of Fe impurities splits the  $3d$ -Fe states into two energy-different states: a triplet  $t_{2g}$  ( $d_{xy}$ ,  $d_{yz}$  and  $d_{xz}$ ) and a doublet  $e_g$  ( $d_{z^2}$  and  $d_{x^2-y^2}$ ). Five of the six Fe electrons have majority-spin and occupy the states  $e_g$  and  $t_{2g}$ , which are below the  $E_F$ . In contrast, at the lower end of the conduction band the unoccupied  $e_g$  states are in minority spin, and third of the  $t_{2g}$  minority states are filled and raised to the  $E_F$ . Figure 10 shows a schematic diagram illustrating how the  $Fe^{2+}$  ion splits into its crystal fields in the octahedral environment.

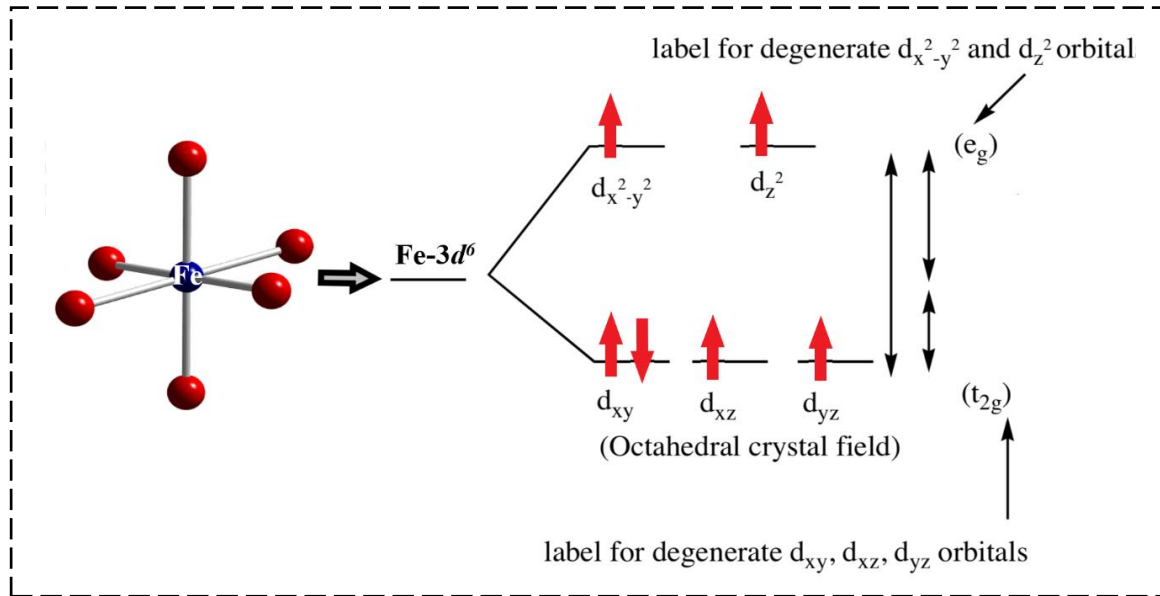


**Figure 10.** Schematic diagram of the distribution of electrons in the  $e_g$  and  $t_{2g}$  levels of the  $\text{Fe}^{2+}$  ion situated in an octahedral crystal field. After Ref [50].

The main cause of the partially filled  $\text{Fe-}t_{2g}$  states observed at the  $E_F$  is the significant  $p$ - $d$  hybridization. This hybridization also explains the two symmetrical states separation in the majority spin, which eventually causes ferromagnetism in the compounds under study to emerge and stabilize. The proposal of Zunger and Katayama [48, 49] on the ferromagnetism of octahedrally doped semiconductor systems with transition metals is similar to our observations.

Examination of the  $\text{Fe:}3d$  direct exchange splitting energy  $\Delta x(d)$ , determined by the difference ( $\Delta d_{\downarrow} - \Delta d_{\uparrow}$ ) between the respective up and down peaks, provides additional evidence for the existence of ferromagnetic alignment. This interaction arises from overlapping electron wavefunctions of neighboring atoms, resulting in an energy reduction when the electron spins align in parallel. This reduction in energy is called the direct exchange splitting energy. The calculated values are listed in Table 4. The high  $\Delta x(d)$  values confirm the consolidation of ferromagnetic alignment across all compounds.

The spin-polarization  $P$  at the  $E_F$  was determined and expressed by Eq.39 in Chapter 1. Table 4 presents the results, which strongly validate the HMF nature of the compounds  $\text{Sr}_{1-x}\text{Fe}_x\text{S}$  ( $x = 0.125, 0.25, \text{ and } 0.50$ ), showing a magnetic spin-polarization of 100%. On the other hand, the compound  $\text{Sr}_{1-x}\text{Fe}_x\text{S}$  ( $x = 0.75$ ) exhibits a 33% polarization. This is obtained from 8% of the majority-spin states and 4% of the minority-spin states that are both present at the  $E_F$ , strongly indicating that it is metallic.

**Table 4**

Calculated values of exchange-splitting  $\Delta_x(d)$ , majority-spin  $N_\uparrow(E_F)$  and minority-spin  $N_\downarrow(E_F)$  states at  $E_F$ , and the spin polarization  $P$  of  $\text{Sr}_{1-x}\text{Fe}_x\text{S}$  ( $x=0.125, 0.25, 0.50$ , and  $0.75$ ) compounds.

Compound	$\Delta_x(d)$ (eV)	$N_\uparrow(E_F)$ (states/eV)	$N_\downarrow(E_F)$ (states/eV)	$P$
<b>Sr<sub>0.875</sub>Fe<sub>0.125</sub>S</b>	4.829	0	0.06	1
<b>Sr<sub>0.75</sub>Fe<sub>0.25</sub>S</b>	4.819	0	0.05	1
<b>Sr<sub>0.50</sub>Fe<sub>0.50</sub>S</b>	6.748	0	1.33	1
<b>Sr<sub>0.25</sub>Fe<sub>0.75</sub>S</b>	5.726	0.08	0.04	0.33

### 3.1.3.4 Magnetic Properties

#### 3.1.3.4.1 Magnetic Moment

In this section, we calculated the total magnetic moment of  $\text{Sr}_{1-x}\text{Fe}_x\text{S}$  at different concentrations ( $x$ ), as well as the local magnetic moments of Sr atom, S atom, Fe impurity and the interstitial magnetic moment to clarify the cause of the induced magnetism in pristine SrS. Table 5 rearranges the collected data.

The compounds  $\text{Sr}_{0.875}\text{Fe}_{0.125}\text{S}$ ,  $\text{Sr}_{0.75}\text{Fe}_{0.25}\text{S}$  and  $\text{Sr}_{0.50}\text{Fe}_{0.50}\text{S}$  have been proven to be half-metallic ferromagnets because their total magnetic moment has an integer value of  $4 \mu_B$  per Fe atom. The unfilled  $3d$ -Fe states are responsible for this measured magnetic moment. In this case, S has  $3s^2 3p^4$  with two missing electrons in the outermost  $3p$  shell, while Fe has an electronic valence configuration of  $3d^6 4s^2$ . Two of the eight valence electrons are added to the dangling bonds of the anion (S) when incorporating Fe. The  $s$  of Fe electrons make no contribution to the magnetic moment because they are completely localized. The magnetic state is established by the remaining four  $d$  electrons of Fe, which are delocalized and fill the majority-spin while the minority-spin remains empty. The magnetic moment of the iron-rich compound (75% Fe) is characterized by a slight deviation from the expected integer value ( $4\mu_B$ ), a property that often occurs in metals.

Small permanent local magnetic moments, which show a positive sign and are indicative of parallel spin arrangements (FM), were produced on the non-magnetic sites of the Sr and S atoms as a result of  $pd$ -type electron transfer. Additionally, Table 5 indicates that the Fe atom has the largest values and contributes the most to the compounds' total magnetic moment, which decreases as concentration increases. The unfilled  $3d$  electronic states of the magnetic atom Fe are responsible for this magnetic

moment. This pattern is consistent with previous research on SrS doped with transition metals at different concentrations [44, 20]. Furthermore, the interstitial sites positively contribute to the supercell's overall magnetic moment. This suggests that ferromagnetic interaction occurs at these sites between the Fe-3d states and the corresponding 5s-3p states of Sr and Sr. When comparing the predicted magnetic moments of Sr<sub>0.75</sub>Fe<sub>0.25</sub>S in this study with those found in the body of existing literature presented in Table 5, we find consistent results [22].

#### 3.1.3.4.2 Exchange Constants

We have determined two important constants that shed light on the important role that the valence and conduction bands play in the spin-splitting exchange coupling observed in the electronic band structures of our compounds. These are the exchange constants for *s-d* and *p-d*, denoted  $N_{0\alpha}$  and  $N_{0\beta}$ , respectively, which relate to CB and VB. Assuming the standard Kondo interaction, both constants were found [60]:

$$N_{0\alpha} = \frac{\Delta E_c}{x\langle S \rangle} \quad (\text{eq.24})$$

$$N_{0\beta} = \frac{\Delta E_v}{x\langle S \rangle} \quad (\text{eq.25})$$

In this context,  $\Delta E_c = E_c^\downarrow - E_c^\uparrow$  and  $\Delta E_v = E_v^\downarrow - E_v^\uparrow$ , are the spin separation at the edges of the conduction and valence bands, respectively. The variable "x" denotes the percentage of Fe in the compound, while  $\langle S \rangle$  signifies the average magnetization of the Fe atoms.

Table 5 shows the calculated values for  $\Delta E_c$ ,  $\Delta E_v$ ,  $N_{0\alpha}$ , and  $N_{0\beta}$  of the HMF compounds Sr<sub>1-x</sub>Fe<sub>x</sub>S (x = 0.125, 0.25 and 0.50). Notably, the *s-d* exchange coupling between the CB and *d*-Fe states consistently exhibits an anti-ferromagnetic nature at all concentrations, as evidenced by the negative sign of the  $N_{0\alpha}$  constant. Conversely, the  $N_{0\beta}$  constant shows a positive value for x = 0.125 and 0.50, but a negative value for x = 0.25. This means a mixture of ferromagnetic and antiferromagnetic interactions in the *p-d* exchange between the VB and *d*-Fe levels. The overall increase in  $N_{0\alpha}$  and fluctuations in  $N_{0\beta}$  values with the increase in Fe content from 0.125 to 0.50 reinforce the targeted magnetic properties of these materials.

$N_{0\alpha}$  is generally found to be positive in most studies on half-metallic ferromagnetic/semiconductor compounds, while  $N_{0\beta}$  is invariably negative [44, 61]. In our study, this pattern is completely reversed. Changes in symmetry and quantum confinement effects may be responsible for the reversal of the sign of  $N_{0\alpha}$  [62]. In contrast, in the DMS Zn<sub>1-x</sub>Cr<sub>x</sub>Se, Mac and co-workers first predicted the positive sign of  $N_{0\beta}$  and associated this significant shift with the *d*-state position of the valence band [63]. A

comparable pattern was also recently observed at low concentrations of the ternary compounds  $\text{Cd}_{0.937}\text{TM}_{0.0625}\text{S}$  (TM = Cr, V, Cu and Sc) [64].

**Table 5**

The calculated values of total magnetic moment  $M_{\text{tot}}$  (in  $\mu_{\text{B}}$ ) per Fe atom, local magnetic moments (in  $\mu_{\text{B}}$ ) of Fe ( $M_{\text{Fe}}$ ), Sr ( $M_{\text{Sr}}$ ), and S ( $M_{\text{S}}$ ), and magnetic moment in the interstitial sites  $M_i$  ( $\mu_{\text{B}}$ ), spin-splitting edges of conduction  $\Delta E_c$  (eV) and valence  $\Delta E_v$  (eV) bands, and exchange constants  $N0_\alpha$ , and  $N0_\beta$  of  $\text{Sr}_{1-x}\text{Fe}_x\text{S}$  compounds ( $x = 0.125, 0.25, 0.50, \text{ and } 0.75$ ).

Compound	$M_{\text{tot}}$	$M_{\text{Fe}}$	$M_{\text{Sr}}$	$M_{\text{S}}$	$M_i$	$\Delta E_c$	$\Delta E_v$	$N0_\alpha$	$N0_\beta$
<b><math>\text{Sr}_{0.875}\text{Fe}_{0.125}\text{S}</math></b>	4	3.690	0.005	0.031	0.119	-3.021	0.017	-12.08	0.068
<b><math>\text{Sr}_{0.75}\text{Fe}_{0.25}\text{S}</math></b>	4; 4 <sup>d</sup>	3.680; 3.651 <sup>d</sup>	0.006; -0.001 <sup>d</sup>	0.052; 0.044	0.230; 0.089 <sup>d</sup>	-2.639	-0.977	-5.278	-1.954
<b><math>\text{Sr}_{0.50}\text{Fe}_{0.50}\text{S}</math></b>	4	3.643	0.010	0.125	0.435	-2.768	0.884	-2.768	0.884
<b><math>\text{Sr}_{0.25}\text{Fe}_{0.75}\text{S}</math></b>	3.973	3.636	0.004	0.158	0.750	-	-	-	-

<sup>d</sup> Ref [22].

### 3.1.4 Conclusion

In the first section of this chapter, we examined an in-depth study of the Fe-doped SrS semiconductor using rigorous first-principles calculations facilitated by the WIEN2K computational framework. This study involved a comprehensive investigation of the  $\text{Sr}_{1-x}\text{Fe}_x\text{S}$  compounds, where  $x$  takes values of 0, 0.125, 0.25, 0.50, and 0.75, with a focus on their behavior in the rock-salt phase. The key findings and conclusions from this endeavor are presented as follows:

1. The results of the structural properties obtained with the PBE-GGA approximation showed that the ferromagnetic phase is the most stable in all  $\text{Sr}_{1-x}\text{Fe}_x\text{S}$  compounds and that the equilibrium lattice constant of the compounds decreases with increasing Fe concentration. The enthalpy of formation values confirmed the stability of the cubic structure, with  $\text{Sr}_{0.50}\text{Fe}_{0.50}\text{S}$  being the most stable.
2. Analysis of mechanical and thermal properties confirmed that all the doped-compounds meet the criteria for mechanical stability. They exhibit ductility and anisotropy and are characterized by ionic bonding. In addition, they exhibit remarkable resistance to heat treatment. Among them,  $\text{Sr}_{0.50}\text{Fe}_{0.50}\text{S}$  showed the highest stiffness, while  $\text{Sr}_{0.875}\text{Fe}_{0.125}\text{S}$  was found to be the most flexible. Furthermore,  $\text{Sr}_{0.25}\text{Fe}_{0.75}\text{S}$  exhibited the highest degree of anisotropy.

3. The electronic properties calculated from the equilibrium lattice parameters confirm that all  $\text{Sr}_{1-x}\text{Fe}_x\text{S}$  compounds are HM ferromagnets and therefore applicable to spintronics, whereas the  $\text{Sr}_{0.25}\text{Fe}_{0.75}\text{S}$  compound shows metallic behavior.
4. For all HMF compounds, we calculated a total magnetic moment of  $4 \mu_B$  and a low local magnetic moment at the non-magnetic sites of Sr and S due to hybridization between Fe-3d and S-3p states. The exchange interactions in the compounds yielded exchange constants  $N_{0\alpha}$  and  $N_{0\beta}$  with opposite signs, confirming the existence of an opposite interaction between valence and conduction states.



## 3.2 Structural, Electronic, Magnetic, Optical, and Thermoelectric Properties of co-doped SrS: (Fe, p<sup>0</sup>) Alloys

### 3.2.1 Introduction

A key factor in the recent boom in scientific research has been the search for new materials with remarkable properties. In this regard, third-generation semiconductors – also referred to as – wide band gap (WBG) materials have emerged as a highly favorable platform for the development of high-performance optoelectronic and electronic devices [65]. SrS is a material that stands out among the others as an example with interesting properties. In addition to the features discussed previously in this Chapter, SrS is particularly known for its remarkable optical properties, which are covered in further detail in Chapter 1, Part 1.4.

Despite extensive research on pure SrS, obstacles such as the large bandgap and indirect nature limit its application in optics [66]. Chemical doping is a promising solution to this problem, as demonstrated by our previous work, where doping transition metals, particularly Fe at 12.5%, successfully induced an indirect to direct band transition. This is a promising direction to improve the optical properties and performance of spintronics.

The need for more data storage capacity makes it imperative to convert waste heat into usable electrical energy [67]. This plan is considered the best as it provides a reliable, cost-effective, clean and environmentally friendly source of renewable energy in the long term. High-performance spin-dependent thermoelectric materials lie at the intersection of thermoelectricity and spintronics, an area that requires further research and development.

In particular, the alkali metal series has shown promise in doping the SrS site. These non-magnetic elements have been shown to increase ferromagnetism and luminescence efficiency [68–70] and are non-toxic. Simultaneous doping of these elements with transition metal ions in bulk SrS will be important as it can create new systems with unique properties.

The second section of this chapter builds on our previous work and examines the structural, electronic, magnetic, optical, and transport properties of Li, Na, and K co-doped at a fixed concentration of 12.5% in SrS: Fe. Our knowledge of co-doped SrS systems is expected to grow as a result of this research, leading to the development and improvement of SrS-based materials for applications in thermoelectricity, magnetism, electronics, and optics.

### 3.2.2 Computational Details

Since our work in this section of the chapter builds on the work in the previous section, we have chosen to continue with the same data parameter settings as for the mono-doped systems, including code, basis set, approximation, and function for exchange-correlation term within the INPUT parameters. We simply enlarged the supercell to accommodate 32 atoms in a  $(2 \times 2 \times 2)$  configuration of a bcc structure in the FM case to produce the co-doped systems SrS: (Fe,  $p^0$ = Li, Na and K). This supercell contains 16 Sr atoms and 16 S atoms. We exchanged two atoms at the Sr positions to achieve a total impurity ion concentration of 12.5%. One was fixed as Fe and is located at the (0, 0, 0) position (at the corner), and the other, for  $p^0$  ions, is located in the next position at (0.5, 0, 0), i.e.  $\text{Sr}_{0.875}\text{Fe}_{0.0625}p^0_{0.0625}\text{S}$ . For the AFM configuration, we used a larger P-type supercell with 64 atoms  $(2 \times 2 \times 2)$ . To obtain trustworthy results in evaluating optical and thermoelectric properties, we also used a larger  $k$ -mesh and the TB-mBJ method [16]. We used Bardeen and Shockley's deformation potential theory [71] and Boltzmann's semi-classical theory-based BoltzTrap2 software [72] to perform a post-DFT approach to study the thermoelectric properties of the compounds.

### 3.2.3 Results and Discussion

#### 3.2.3.1 Structural Properties

The  $(2 \times 2 \times 2)$  bcc-lattice crystal of the (Fe,  $p^0$ ) co-doped SrS systems is modeled in Figures 11(a) and (b). Table 6 shows the structural parameters details of the SrFeLiS, SrFeNaS, and SrFeKS systems, including lattice parameter ( $a$ ), bulk modulus ( $B$ ), total energy differences between FM and AFM configurations ( $\Delta E = E_{\text{AFM}} - E_{\text{FM}}$ ), and Curie temperature ( $T_C$ ).

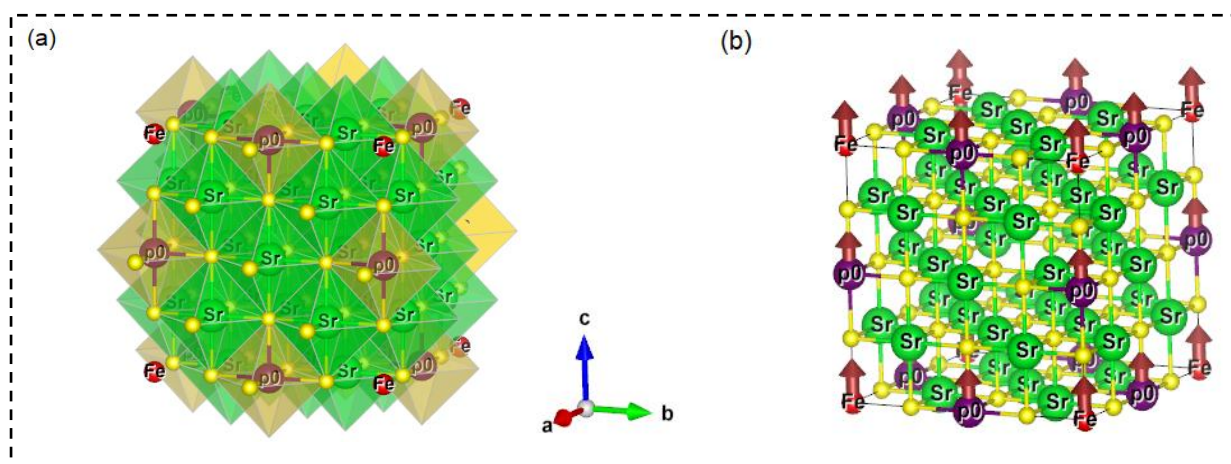


**Figure 11.** (a) Polyhedral view of the SrS: (Fe,  $p^0$ ) [ $p^0$  = Li, Na, and K] crystal structures (b) The stable FM configuration.

**Table 6**

The calculated values of crystal lattice parameter  $a$  (Å), bulk modulus  $B$  (GPa), energy difference ( $\Delta E$ ), Curie temperature ( $T_c$ ), and formation energy ( $E_f$ ) of (Fe, p<sup>0</sup>) co-doped SrS systems. The Fe mono-doped SrS data are included in the Table from the preceding section, to facilitate further analysis and comparison.

Materials	$a_0$ (Å)	$B_0$ (GPa)	$\Delta E_{AFM-FM}$ (eV)	$T_c$ (K)	$E_f$ (eV)
<b>SrFeS</b>	5.949	50.244	1.160	-	-4.384
<b>SrFeLiS</b>	5.983	48.322	0.432	1326	-5.099
<b>SrFeNaS</b>	5.994	48.107	0.435	1337	-5.087
<b>SrFeKS</b>	6.017	47.518	0.437	1341	-5.073

The AFM and FM order's energetic stability is indicated by the “-” and/or “+” signs of  $\Delta E$ . According to the simulation results in Table 6, the positive  $\Delta E$  values indicate that the co-doped SrS (Fe, p<sup>0</sup>) structures have the ability to suppress the AFM order and promote the FM order in the long term. This implies that the FM state is stabilized and gains an energetic advantage over the AFM state when Fe is combined with alkali metals (Li, Na and K).

The Curie temperature ( $T_c$ ), an important parameter for magnetic materials in spintronics, was calculated based on the energy difference  $\Delta E$ . To estimate  $T_c$ , the MFA (Mean-Field Approximation) formula was used as follows:

$$T_c^{MFA} = -\frac{2}{3nk_B} \Delta E \quad (\text{eq.26})$$

Here  $k_B$  is the Boltzmann constant and  $n$  is the number of substituted atoms.

However, it is important to keep in mind that percolation behavior, which has a significant impact on the magnetic order and leads to an overestimation of  $T_c$ , is not taken into account by MFA [73]. To overcome this limitation, we used an empirical relationship [74] that uses the ratio  $T_c/T_c^{MFA} = 0.794$  to relate the exact value of the critical temperature ( $T_c$ ) to the expected mean field value ( $T_c^{MFA}$ ). From Table 6, it is noted that all three systems have  $T_c$  above room temperature (RT) and that there is a clear trend in  $T_c$ . In particular, it increases as the atomic number ( $Z$ ) increases from Li to Na to K, suggesting that the higher the  $Z$ , the more stable the system is. This highlights how the types of alkali metal dopants (Li, Na and K) can be changed to control ferromagnetism in these systems, opening possibilities for spintronic applications. It should be noted that this is the first time these systems have been predicted and further experimental validation is required.

Table 6 shows the optimized lattice parameters and bulk modulus of the co-doped systems in the stable FM configuration. Figure 12 shows the comparison of the total energies and the cell volume. The structural parameters of monodoped SrS: Fe<sup>2+</sup> calculated in the previous section were also included to assess the feasibility of co-doping. Since the substituted Fe<sup>2+</sup> (0.55 Å) has a smaller ionic radius than the dopants Li<sup>+</sup> (0.76 Å), Na<sup>+</sup> (1.02 Å) and K<sup>+</sup> (1.38 Å), the lattice constant increases gradually with increasing  $Z$  after the co-doping procedure. This indicates grid expansion. In contrast, the values of the bulk modulus decrease slightly, indicating that the co-doped systems have lower hardness. Importantly, Figure 12 shows that the addition of Li, Na, and K results in an increase in cell volume of 0.49%, 0.64%, and 0.98%, respectively, and a consistent energy reduction of about 3% to 8%. These data clearly indicate that the co-doping process can lead to significant stabilization of the system.

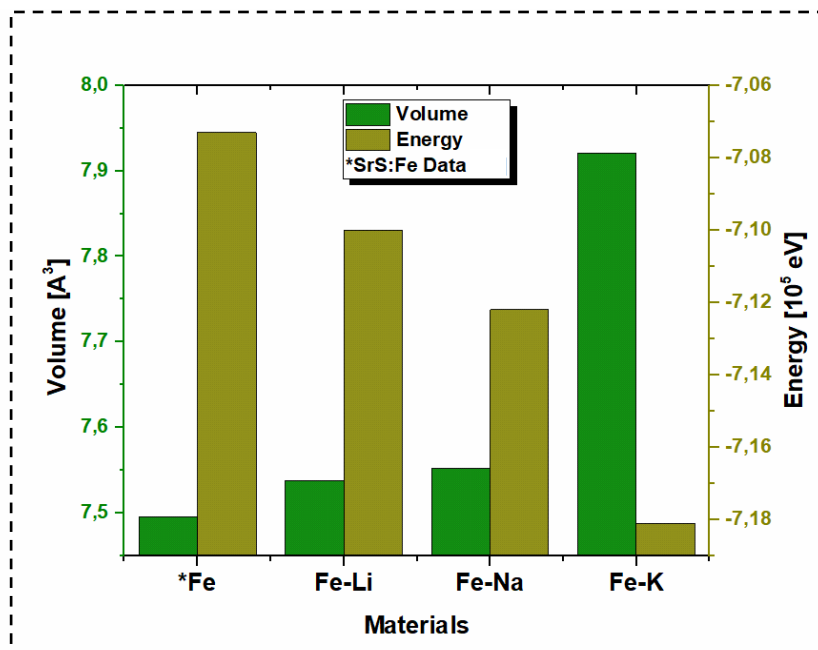


**Figure 12.** An illustration of the total energy and cell volume of the Fe-p<sup>0</sup> co-doped systems in comparison to the Fe mono-doped system.

To evaluate the thermodynamic stability of the co-doped systems, we also calculated the formation energy. Our expression was as follows:

$$E_f = E_{codoped} - aE^b(Sr) - bE^b(Fe) - cE^b(p^0) - dE^b(S) \quad (\text{eq.27})$$

The term  $E_{codoped}$  refers to the total energy of SrS co-doped with transition-alkali metals; the terms  $E^b(Sr)$ ,  $E^b(S)$ ,  $E^b(Fe)$ , and  $E^b(p^0)$  denote the energies per atom of the host atoms (Sr and S), the fixed dopant (Fe), and the associated impurity ( $p^0 = \text{Li, Na, and K}$ ); the numbers of the relevant atoms within the supercell are indicated by  $a$ ,  $b$ ,  $c$ , and  $d$ .

Table 6 shows that the estimated formation energies ( $E_f$ ) of all compounds have negative values. This suggests that these substances may be synthesized under ambient conditions and are thermodynamically stable.  $E_f(\text{Fe-Li}) < E_f(\text{Fe-Na}) < E_f(\text{Fe-K}) < E_f(\text{Fe-single})$  is the order in which the  $E$  values are found. This implies that the most difficult system to dope is the singly Fe-doped SrS, which has the highest  $E_f$ . On the other hand, the co-doped Fe-Li system has a comparatively simpler doping process as much less energy is required for its formation.

In summary, we find that the introduction of monovalent alkali metals reduces the  $E_f$  of the mono-doped system. This implies that the alkali atoms help alleviate some of the difficulties in the singly Fe-doped SrS system, which in turn leads to a more stable configuration. Therefore, the overall stability of the system is significantly improved and the doping process is simplified by (Fe, p<sup>0</sup>) co-doping.

### 3.2.3.2 Electronic Properties and Chemical Bonding Analysis

#### 3.2.3.2.1 Electronic Band Structure Analysis

Figure 13 shows the electronic band structures of the co-doped SrS systems (Fe, Li), (Fe, Na) and (Fe, K) along the high symmetry directions ( $\Lambda$ ,  $\Delta$ , and  $Z$ ) and high symmetry points ( $\Gamma$ -H-N- $\Gamma$ -P) of the first Brillouin zone (BZ).

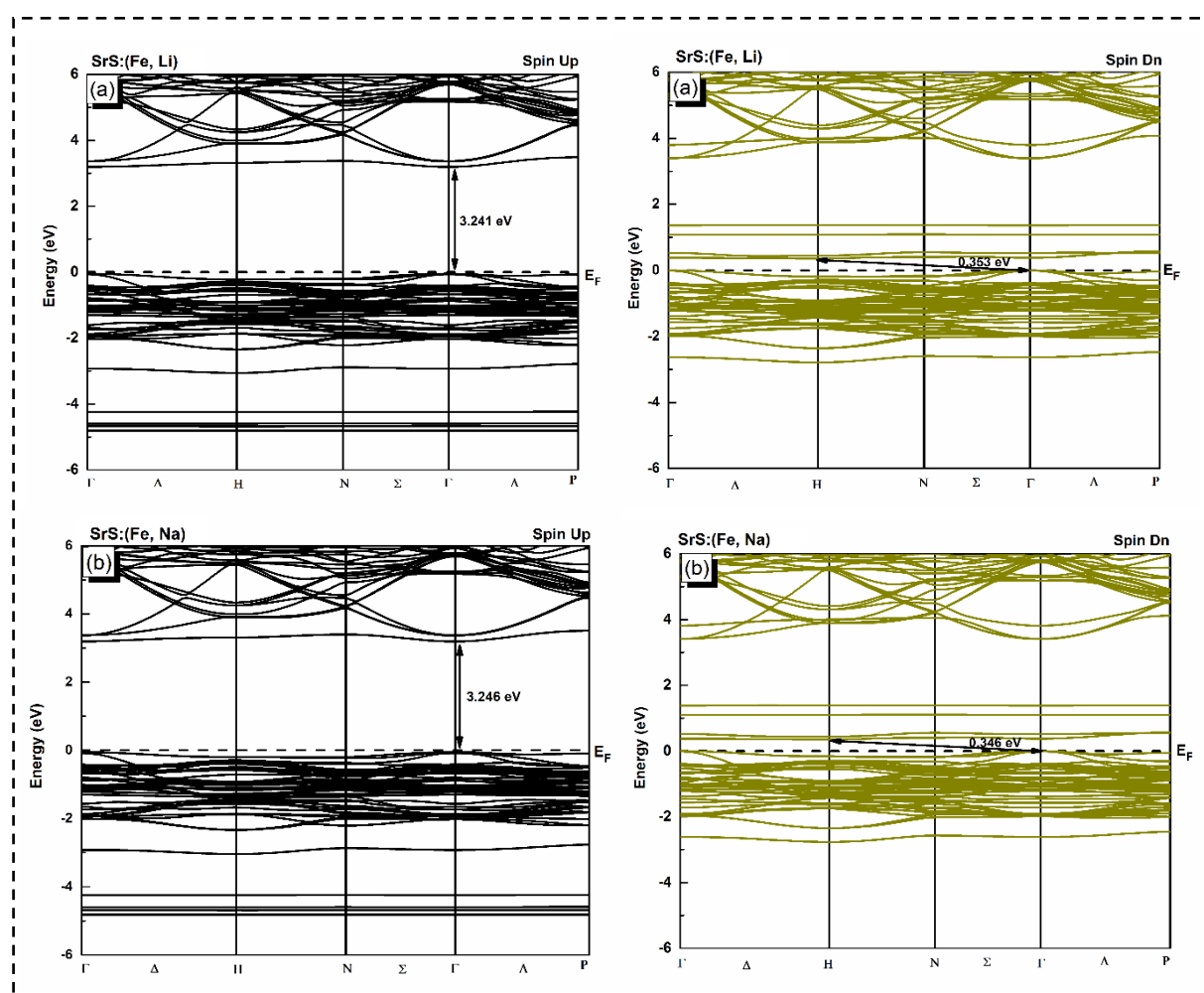
All SrS co-doped systems are half-semiconductors because the  $E_F$  is clearly empty since neither the up- nor the down-spin channels crosses it. Both the VBM and CBM are positioned at the  $\Gamma$  point for up-spin, resulting in a wide direct bandgap of 3.241 eV, 3.246 eV, and 3.182 eV for co-doping of Li, Na, and K, respectively. On the other hand, the narrower and indirect bandgap is indicated by the CBM being at the  $H$  point and the VBM being at the  $\Gamma$  point for the down-spin channel. For co-doping with Li, Na, and K, the bandgap size upon spin-down was found to decrease with  $Z$ , with values of 0.353 eV, 0.346 eV, and 0.300 eV, respectively. It is important to note that the VBM is located close to the  $E_F$  in the band structures of all three compounds, suggesting that they are  $p$ -type semiconductors. The comparatively smaller bandgap of the spin-down channel (<1 eV) facilitates thermal excitation of electrons, which improves electrical conductivity. Due to this property, these  $p$ -type HSC alloys have great potential for use in thermoelectric (TE) systems.

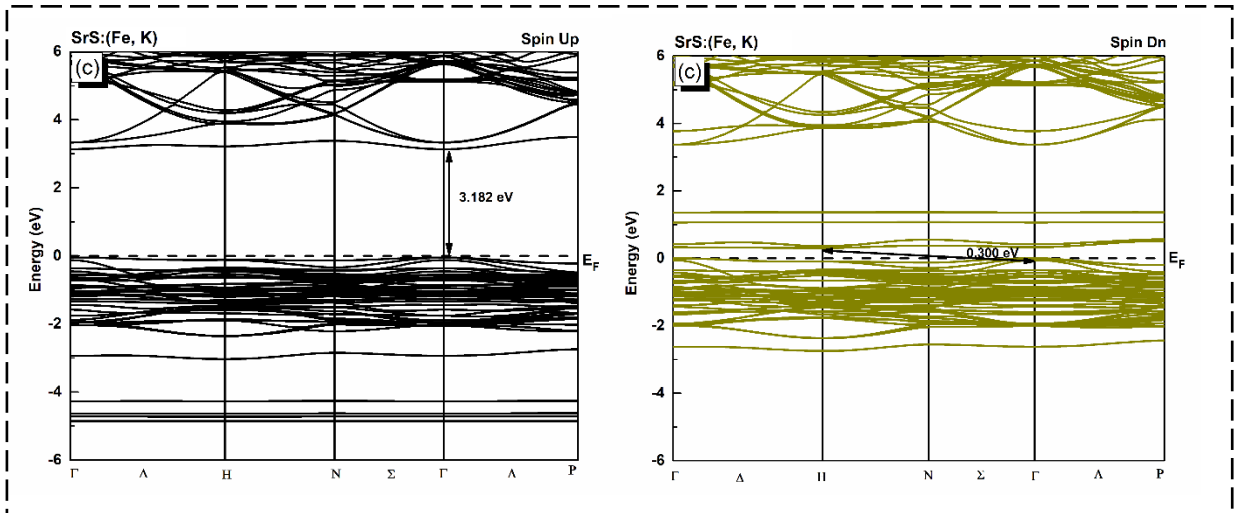
Table 7 summarizes the results for the up-spin and dn-spin channels. We find that the introduction of hole-type charge carriers through alkali doping not only maintains the semiconducting nature of the up-spin but also reduces its bandgap values compared to Fe-doped SrS, which exhibits HMF properties. It also causes a down-spin shift from the  $E_F$ , leading to conventional semiconductor behavior.

Table 7

The calculated bandgap values of co-doped SrS: (Fe,  $p^0$ ) systems. The data of Fe mono-doped SrS are included in the table from the previous section to facilitate further analysis and comparison.

Materials	Gap nature	Up-spin channel		Down-spin channel	
		Direction	Value (eV)	Direction	Value (eV)
SrFeS	HMF	$[\Gamma - \Gamma]$	3.401	-	-
SrFeLiS	HSC	$[\Gamma - \Gamma]$	3.241	$[\Gamma - H]$	0.353
SrFeNaS	HSC	$[\Gamma - \Gamma]$	3.246	$[\Gamma - H]$	0.346
SrFeKS	HSC	$[\Gamma - \Gamma]$	3.182	$[\Gamma - H]$	0.300

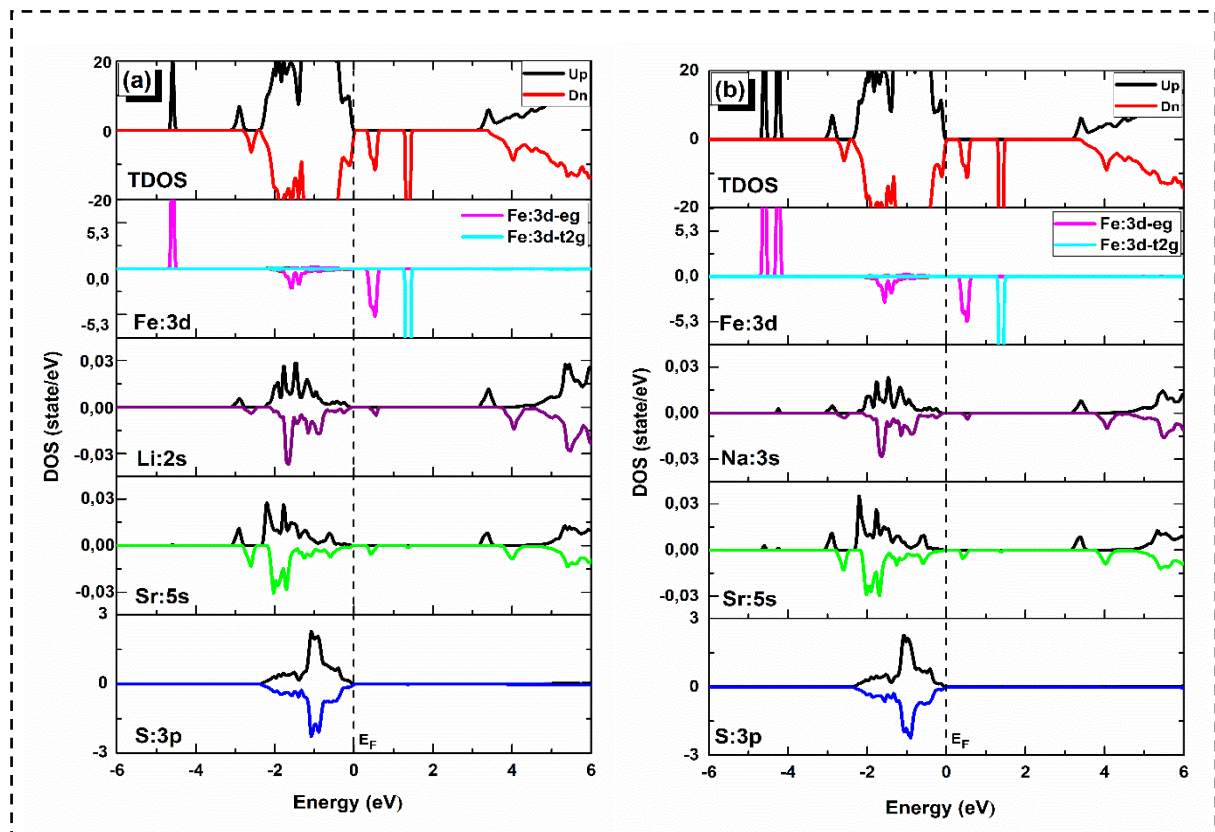




**Figure 13.** (a-c) Spin-resolved electronic band structures of (Fe, Li), (Fe, Na), and (Fe, K) co-doped SrS with mBJ-PBE method.

### 3.2.3.2.2 Total and Partial Densities of States Analysis

The spin-resolved total density of states (TDOS) and orbital-decomposed density of states (PDOS) of Sr, S, Fe, and  $p^0$  atoms are shown in Figure 14.





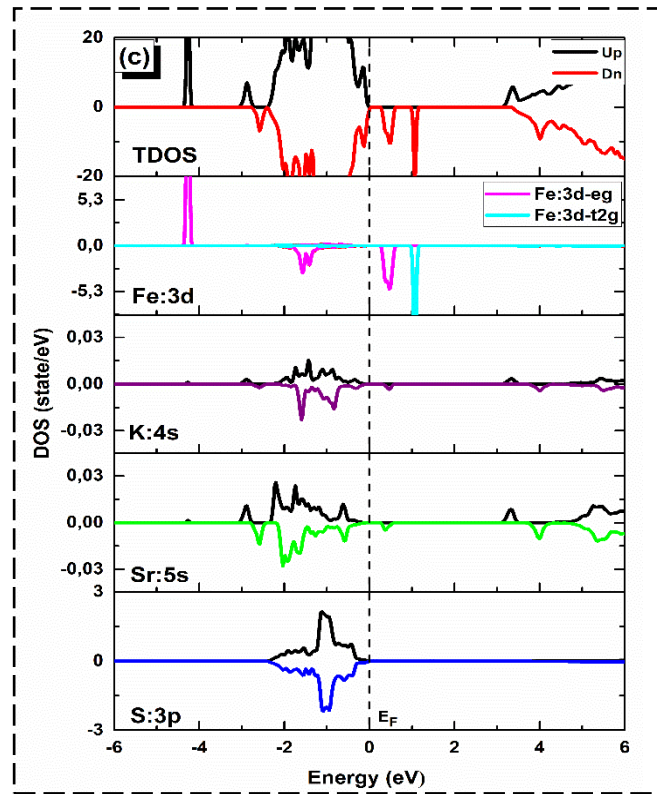


**Figure 14. (a-c)** Spin-resolved total and partial densities of states of of (Fe, Li), (Fe, Na), and (Fe, K) co-doped SrS with the mBJ-PBE method.

The asymmetry of the TDOS in both spin channels can be seen in Figures 14(a–c) and confirms the ferromagnetic nature of the materials. It can also be seen that neither spin channel exhibits an impurity state at the  $E_F$  level, highlighting the magnetic semiconductor nature of them. Fe:3d and S:3p orbitals make up the majority of the VB, while the S:3p and Fe:3d orbitals dominate the VBM, with the Sr:5s and  $p^0:s$  (Li:2s, Na:3s and K:4s) orbitals contribute very little. Fe:3d orbitals make up the majority of the CB, and Fe:3d determines the CBM, with a small contribution from Sr: 5s and  $p^0:s$  orbitals. It appears that alkali substitution contributes only slightly to the TDOS near the  $E_F$ . Ultimately, this is different from the TDOS detected by the Fe mono-doped SrS, where the compound exhibited the HMF property. We hypothesize that coupled Fe- $p^0$  doping is preferable to Fe mono-doping to achieve optimal magnetic and optical properties due to the presence of a localized energy level at the top of the CB near the  $E_F$ .

A careful examination of the PDOS shows that the Fe:3d values have shifted significantly compared to the parent compound SrS:Fe. Atomic Fe:3d levels split into  $e_g$  and  $t_{2g}$  manifolds with lower and higher energies, respectively, due to the tetrahedral crystal field. While the  $e_g$  orbital splits into the singlet  $d_{x^2-y^2}$  and  $d_{z^2}$  levels, the  $t_{2g}$  orbital splits further into the double degenerate  $d_{xz} + d_{yz}$  levels and the singlet  $d_{xy}$  level. Hund's rule states that since the 3d state of the Fe dopant has six electrons, the five up-spin electrons fill the five sub-states that lie below the  $E_F$  level in a potential range of about  $\sim -0.4$  to



-4.5 eV. Since the  $p^0$ -s states are one electron short, the addition of alkali dopants creates a hole in the system. As a result, the atoms of Li, Na and K act as acceptors. Thus, the  $p$ -type semiconductor behavior in the three compounds can be explained by the sub-states in the spin-down channels remaining unoccupied and located above the  $E_F$  level in a potential range of approximately  $\sim -0.3$  eV–1.4 eV. The  $3p$  orbitals of neighboring S atoms and the  $3d$  orbitals of Fe clearly overlap close to the  $E_F$ , suggesting strong  $pd$ -hybridization between them. This  $pd$ -hybridization is crucial for maintaining ferromagnetic order and generating magnetism in the co-doped systems in addition to band edge splitting. Another factor is the coupling chain between the states Fe: $3d_{t2g/eg}$ –Sr: $5s$ – $p^0$ : $3s$ , which exists in the energy range from about  $\sim -2$  eV to  $E_F$ .

Along with the previously defined direct exchange splitting ( $\Delta_x(\mathbf{d})$ ), we also calculated the crystal field energy ( $\Delta E_{crys}$ ), which is defined as the energy arising from the interaction of surrounding ligands with metal ions ( $E_{t2g} - E_{eg}$ ). When the  $\Delta_x(d)$  energy exceeds the  $\Delta E_{crys}$ , the energy obtained from the parallel spin alignment through direct exchange is larger than the energy difference between the  $e_g$  and  $t_{2g}$  orbitals, this can cause the material to exhibit more pronounced ferromagnetic behavior. In our case, SrFeLiS, SrFeNaS and SrFeKS have calculated  $\Delta_x(d)$  values of 6.06 eV, 6.14 eV and 5.465 eV, respectively. These values exceed their corresponding  $\Delta E_{crys}$  values of 0.672 eV, 0.713 eV and 0.436 eV. Therefore, they strongly support the parallel alignment of the spins and promote the stabilization of ferromagnetism in these systems.

A crucial parameter for understanding the electronic structure and optical properties of (Fe,  $p^0$ ) co-doped SrS is the  $d$ - $d$  transition, which is defined as the distance between up-spin occupied Fe: $3d$  states and unoccupied Fe: $3d$  states in down-spin. We gain important insights into the energy absorbed during the  $d$ - $d$  transition by quantifying the energy separation between the up-spin and down-spin states involved in this transition. Our calculations show that the co-doped SrS systems (Fe, Li), (Fe, Na), and (Fe, K) have  $d$ - $d$  transition energies of 0.300 eV, 0.346 eV, and 0.353 eV, respectively. These values show that the co-doped SrS systems absorb 0.300 eV, 0.346 eV, and 0.353 eV during the  $d$ - $d$  optical transition in the FM configuration, respectively.

### 3.2.3.2.3 Electron Density Difference and Chemical Bonding Analysis

The analysis of the electron density difference of the co-doped systems provides information about the interaction between atoms and their bonding properties. In an ionic bond, there is a significant difference in electronegativity between the bonded atoms, resulting in electron transfer and the formation of charged ions. This type of bond is predominantly ionic in nature. Conversely, a covalent bond occurs when atoms with similar electronegativity share electrons, resulting in a more balanced electron distribution and covalent character.

The 2D bond charge density distributions of the SrS: (Fe, Li), SrS: (Fe, Na), and SrS: (Fe, K) systems were plotted in the (110) plane in Figure 15. The charge density difference is represented by the color scale in the figures, with red indicating electron depletion and blue indicating electron accumulation.

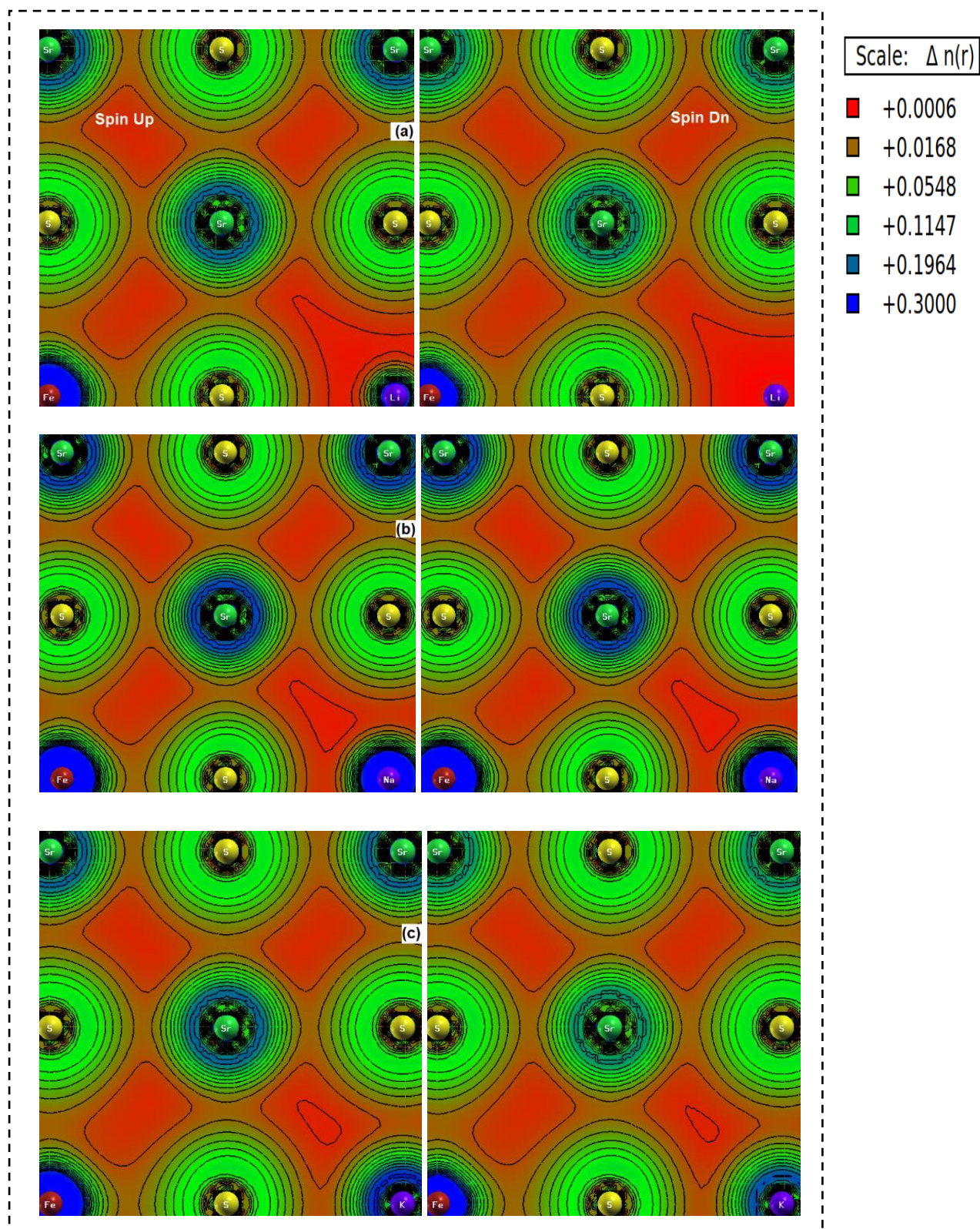


**Figure 15.** (a-c) The bonding contour profiles of electron density difference for (Fe, Li), (Fe, Na), and (Fe, K) co-doped SrS Systems, respectively.

A small amount of electrons, about  $0.016 \text{ eV}/\text{\AA}^3$  accumulates between Sr and S, Fe and S, and  $p^0$  and S, as shown in this figure. This indicates the strong ionic character of the Sr-S, Fe-S and  $p^0$ -S bonds. Interestingly, there is a larger accumulation of electrons around the Fe atom compared to the Sr atom, suggesting that Fe has a greater ability to donate or accept electrons, which affects its bonding behavior. Furthermore, the analysis showed that more charges were localized between  $p^0$  and S, reducing electron exchange between them. As a result, there is a greater concentration of free electrons generated by  $p^0$  atoms, leading to an increase in electron accumulation near  $p^0$ . For co-doping with Li, Na, and K, the electron accumulation values around  $p^0$  are about 0.05, 0.196, and  $0.3 \text{ eV}/\text{\AA}^3$ , respectively. This suggests that the ionic character of the  $p^0$ -S bond in the (Fe,  $p^0$ ) co-doped SrS system slightly improves with increasing  $Z$  of alkali metals. The doping of  $p^0$  atoms thus improves ionic bonding of SrS: (Fe,  $p^0$ ) co-doped systems.

### 3.2.3.3 Magnetic Properties

#### 3.2.3.3.1 Magnetic Moment

Table 8 summarizes the results of the total magnetic moment, the magnetic moments of Sr, S, Fe and  $p^0$ , and the magnetic moment of the interstitial region calculated by the PBE + mBJ method. The calculated  $M_{\text{TOT}}$  in all systems converges to an integral value of  $5.00 \mu_B$ , as shown in this table. The mono-doped SrS:Fe indicates a permanent magnetic moment of  $4.00 \mu_B$  in free space, which is different from this value. As mentioned in the DOS section, the total value of the magnetic moment increases to  $5.00 \mu_B$  due to the charge exchange between the Fe and  $p^0$  ions in the co-doped systems. The  $3d$  orbitals of the transition metal ion (Fe) and the interstitial region are the main sources of  $M_{\text{TOT}}$ . The nearest neighboring S and Sr atoms as well as the alkali metals contribute very little to the total value.

The  $sp-d$  hybridization between the Fe: $3d$  states and the S: $3p$ , Sr: $5s$ , and  $p^0$ : $ns$  states (where  $n$  is the number of Li, Na, and K electrons) in these compounds is responsible for the higher values of magnetic moments in the interstitial region. Due to this hybridization, the magnetic moments of the interstitial region increase and the local magnetic moments associated with the Fe atoms decrease (to about  $3.89 \mu_B$  in all compounds). This phenomenon illustrates how hybridization has a significant impact on how these compounds behave magnetically and distribute electrons.

The studied co-doped systems exhibit elevated and integer magnetic moment values, suggesting possible applications in spintronic devices.

### 3.2.3.3.2 Exchange Constants

The  $s$ - $d$  and  $p$ - $d$  exchange constants are determined using the corresponding equations (Eq. 24) (Eq. 25) described in the first section of this chapter. The calculated  $\Delta E_c$ ,  $\Delta E_v$ ,  $N_{0\alpha}$ , and  $N_{0\beta}$  are summarized in Table 8. The negative values of  $s$ - $d$  coupling suggest an attractive interaction between magnetic moments on dopant atoms and band holes, implying AFM coupling in the alkali-doped SrS:Fe systems. Conversely, the positive values of  $N_{0\beta}$  indicate that the  $p$ - $d$  coupling is repulsive, indicating FM behavior. Compared to the results of Fe single doping, the exchange constants for  $p^0$  co-doping show a slight increase. This slight increase can be attributed to the effects of additional electrons, altered hybridization, and variations in the crystal lattice and local environment. These factors collectively influence the magnetic coupling and contribute to the observed changes in exchange constants.

**Table 8**

The calculated values of total magnetic moment ( $M^{\text{tot}}$ ), interstitial magnetic moment ( $M^i$ ), magnetic moment on each Sr, S, Fe, and  $p^0$  atoms, band edges splitting  $\Delta E_c$  and  $\Delta E_v$ , and exchange constants  $N_{0\alpha}$  and  $N_{0\beta}$  of co-doped SrS systems. The data of Fe mono-doped SrS are included in the Table from the previous section for further analysis and comparison.

Materials	$M^{\text{tot}}$ ( $\mu_B$ )	$M^i$ ( $\mu_B$ )	$M^{\text{Fe}}$ ( $\mu_B$ )	$M^{\text{Sr}}$ ( $\mu_B$ )	$M^{\text{S}}$ ( $\mu_B$ )	$M^{p^0}$ ( $\mu_B$ )	$\Delta E_c$ (eV)	$\Delta E_v$ (eV)	$N_{0\alpha}$	$N_{0\beta}$
SrFeS	4	0.119	3.690	0.005	0.031	-	-3.021	0.017	-12.08	0.068
SrFeLiS	5	0.503	3.893	0.008	0.110	0.002	-2.841	0.053	-8.782	0.170
SrFeNaS	5	0.270	3.895	0.007	0.111	0.112	-2.840	0.052	-9.088	0.171
SrFeKS	5	0.268	3.892	0.007	0.112	0.005	-2.830	0.048	-9.05	0.154

### 3.2.3.4 Optical Properties

The optical behavior of a material in a medium is elucidated by examining its optical properties. Highly spin-polarized semiconductors (HSCs), which span a wavelength spectrum from ultraviolet to visible, can be treated as a continuous medium. Under optical excitation, these materials demonstrate the ability to generate fully spin-polarized electrons and/or holes. The complex dielectric function  $\epsilon(\omega)$  is a key optical property that bridges the gap between the physical process of electron transfer and the energy band structure. It reflects the linear macroscopic response of the material to electromagnetic radiation. The complex dielectric function can be expressed as:

$$\epsilon(\omega) = \epsilon_1(\omega) + i\epsilon_2(\omega) \quad (\text{eq.27})$$

Where  $\epsilon_2(\omega)$  signifies the imaginary part of the complex dielectric function and delineates optical absorption. Conversely, the real part  $\epsilon_1(\omega)$  denotes dispersion and polarized radiation.

The  $\epsilon_2(\omega)$  includes two different contributions: interband transitions (between the bands) and intraband transitions (within the bands). It can be calculated based on the band structure as follows [77]:

$$\epsilon_2(\omega) = \left(\frac{4\pi^2 e^2}{m^2 \omega^2}\right) \sum_{i,f} \int \langle i | \mathbf{M} | f \rangle^2 f_i (1 - f_f) \delta(E_f - E_i - \omega) d^3 k \quad (\text{eq.28})$$

Where  $f_i$  and  $f_n$  are the Fermi functions for initial  $|i\rangle$  and final  $|f\rangle$  states with energies  $E_i$  and  $E_f$  and  $\mathbf{M}$  is the momentum operator.

The  $\epsilon_1(\omega)$  can be derived from the imaginary part through the Kramers-Kronig relation [75], as shown below:

$$\epsilon_1(\omega) = 1 + \frac{2}{\pi} \mathbf{P} \int_0^\infty \frac{\omega' \epsilon_2(\omega')}{\omega'^2 - \omega^2} d\omega' \quad (\text{eq.29})$$

Where  $\mathbf{P}$  is the Cauchy principal value.

As  $\omega \rightarrow 0$ , the static dielectric constant ( $\epsilon_1(0)$ ) in Eq.29 simplifies to:

$$\epsilon_1(0) = \epsilon(\omega) = 1 + \frac{2}{\pi} \mathbf{P} \int_0^\infty \frac{\epsilon_2(\omega')}{\omega'} d\omega' \quad (\text{eq.30})$$

The integral part  $\int_0^\infty \frac{\epsilon_2(\omega')}{\omega'} d\omega'$  is proportional to a value of  $\frac{\pi}{2} \omega_p^2$ . The  $\omega_p$  is defined as the plasmon frequency [75] and it is given as follows:

$$\omega_p^2 = \frac{N_v e^2}{m_e^* \epsilon_0} \quad (\text{eq.31})$$

Where  $N_v$  is the valance electron density and  $m_e^*$  is the effective mass of the electrons.

From the components  $\epsilon_1(\omega)$  and  $\epsilon_2(\omega)$  of the complex dielectric function, further parameters such as the refractive index  $n(\omega)$  and the extinction coefficient  $k(\omega)$  could be calculated [75]:

$$n(\omega) = \frac{[\sqrt{\epsilon_1^2(\omega) + \epsilon_2^2(\omega)} + \epsilon_1(\omega)]^{1/2}}{\sqrt{2}} \quad (\text{eq.32})$$

$$k(\omega) = \frac{[\sqrt{\epsilon_1^2(\omega) + \epsilon_2^2(\omega)} - \epsilon_1(\omega)]^{1/2}}{\sqrt{2}} \quad (\text{eq.33})$$

We can also calculate the absorption coefficient  $\alpha(\omega)$  and the optical conductivity  $\sigma(\omega)$  using the following formulas [75]:

$$\alpha(\omega) = \sqrt{2}(\omega) [\sqrt{\epsilon_1^2(\omega) + \epsilon_2^2(\omega)} - \epsilon_1(\omega)]^{1/2} \quad (\text{eq.34})$$



$$\sigma(\omega) = \frac{\omega}{4\pi} \varepsilon_2(\omega) \quad (\text{eq.35})$$

Figure 16 shows the real and imaginary parts of the complex dielectric function, the absorption coefficient and the optical conductivity, over a photon energy range of 0–13.6 eV. In addition, for comparison purposes, we calculated the optical properties of pure SrS and Fe-doped SrS using the data from the first part of this chapter.

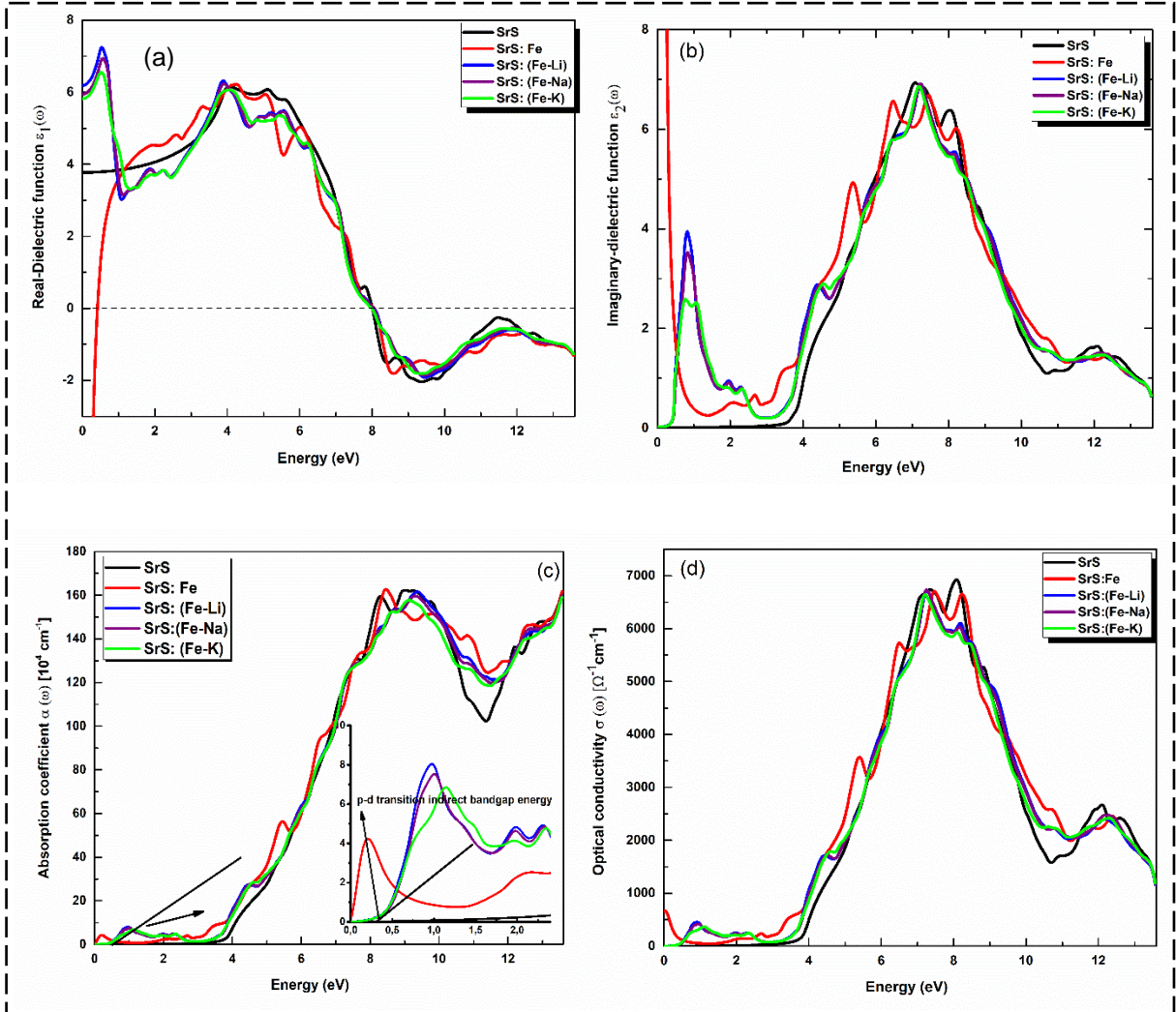


**Figure 16.** (a-d) Real part of the complex dielectric function  $\varepsilon_1(\omega)$ , Imaginary part of the complex dielectric function  $\varepsilon_2(\omega)$ , Absorption coefficient  $\alpha(\omega)$ , and Optical conductivity  $\sigma(\omega)$  spectra, respectively, of pristine SrS, Fe-single doped and (Fe,  $p^0$ ) co-doped systems.

#### a. Real and Imaginary Parts of Complex Dielectric Function

The discussion begins with an examination of the real part of the complex dielectric function. In **Figure 16(a)** we plotted the profiles of the  $\varepsilon_1(\omega)$  function for the binary, ternary, and quaternary systems. At lower energies, a notable difference is apparent between the co-doped, singly doped, and pristine SrS

systems. The static dielectric, denoted by  $\epsilon_1(0)$ , refers to the real part value at zero energy and is defined by (Eq. 30). In the case of the pristine SrS,  $\epsilon_1(0)$  starts positive and reaches a value of 3.769. After reaching this value,  $\epsilon_1(\omega)$  increases with energy until it reaches its maximum of 6.151 at 4.186 eV in the visible region.

When Fe is introduced into pure SrS, the compound shows the HMF character, which causes  $\epsilon_1(0)$  to shift towards a significantly large negative value, indicating two crucial aspects: First, this negative value means metallic behavior in this energy sector. Secondly, it results in energy loss and limited light transmission through the medium, resulting in significant reflections. However, once it reaches its minimum value, the magnitude of  $\epsilon_1(\omega)$  begins to increase and finally becomes positive at 0.416 eV, marking the first root.

When co-doping SrS:Fe with alkali metals, sharp peaks appear on the low energy side, showing high values of  $\epsilon_1(0)$  with 6.194, 5.954 and 5.822 for Li-, Na- and K-co-doped SrS:Fe, respectively. These values are significantly increased compared to pure SrS. These distinct peaks indicate the semiconducting behavior that arises upon the introduction of alkali metal ions. The significantly higher value of  $\epsilon_1(0)$  in SrFeLiS underlines its superior polarizability compared to other alloys. Beyond 0.416 eV, the  $\epsilon_1(\omega)$  profiles of the three co-doped systems follow a similar trend as the pure SrS and Fe single doping. The maximum dielectric peak for Fe mono-doping occurs at a photon energy of 4.3 eV, which corresponds to a dielectric value of 6.204.

Beyond this energy, there is no apparent disparity in the  $\epsilon_1(\omega)$  profiles of all studied systems. This suggests that the influence of alkali metal co-doping may also extend to lower energies. Subsequently, the value of  $\epsilon_1(\omega)$  decreases sharply and finally reaches negative values after 8.065 eV. These negative values imply high reflectivity and plasmonic excitation in the energy range of 8.065–13.6 eV, indicating metallic behavior of the materials. Furthermore, the  $\epsilon_1(\omega)$  values show a trend towards greater stability with increasing photon energy. This suggests that the materials' interaction with incoming high-energy photons becomes more restricted or dampened.

**Figure 16(b)** provides a visual representation of the spectra of the  $\epsilon_2(\omega)$  function. Such spectral data provide crucial insights into how materials react to incoming electromagnetic radiation. In addition, the phenomenon of interband shift is clearly illustrated, which arises from the interaction between electrons in the occupied valence band and the radiation built into the material below the  $E_F$ .

In contrast to the behavior of  $\epsilon_1(\omega)$ ,  $\epsilon_2(\omega)$  in the Fe mono-doping system shows high positive values, followed by a sharp decay, with multiple transition peaks appearing at different rates in the low energy region. These interband transitions can be attributed to the influence of impurity bands introduced by the electrons of the Fe atom. The decrease in  $\epsilon_2(\omega)$  indicates that the interaction between photons and

the material surface is minimal [76]. Prominent peaks in the  $\epsilon_2(\omega)$  spectrum of Fe-doped SrS indicate electronic transitions between occupied and unoccupied states. These transitions can be identified directly by the PDOS of each connection. The 2.0 eV peak arises from the transition between 3p-S in the VB and 3d-t<sub>2g</sub> Fe in the CB. At 2.7 eV, an electronic transition occurs between the 5s-Sr state and the 3d-t<sub>2g</sub> Fe state. The significant 5.4 eV peak is attributed to the electronic transition between the 3d-t<sub>2g</sub> orbital in the VB and the 3d-e<sub>g</sub> orbital in the CB (see Figure 9 in this chapter). The variation in the size of these dielectric peaks can be explained by the difference in the amount of photoelectron energy required for electronic transitions induced by the different dopants.

When examining the  $\epsilon_2(\omega)$  curve of pristine SrS, a prominent peak is visible in the near UV region and maximum absorption occurs in this region. The absorption edge for this binary system begins at an energy of 3.435 eV and is due to electron transitions between the S-3p states in the VB and the Sr-5s states in the CB.

For the systems SrFeLiS, SrFeNaS and SrFeKS they show clear absorption peaks in the infrared range of 0.3–1.6 eV. This means enhanced infrared absorption in the SrS and SrS:Fe systems through co-doping with one of the three alkali metal ions. It is noteworthy that co-doping with Li has the highest intensity. The absorption edges in these ordered alloys SrFeLiS, SrFeNaS, and SrFeKS manifest as energy peaks at 0.353 eV, 0.346 eV, and 0.300 eV, respectively. These peaks arise from electron transitions between the S-3p states in the VB and the Fe-3d<sub>e<sub>g</sub></sub> states in the CB. Remarkably, the positions of these energy peaks closely match the forbidden gaps of the respective alloys. This close agreement suggests that the electron transitions responsible for the absorption edges occur within the energy range defined by the forbidden gap of each material.

*sp-d* hybridization creates direct transitions from the VB to the CB, leading to the formation of shallow levels near the  $E_F$ . This reduces the bandgaps of the materials, which leads to a red shift. In the energy range of 1.6–2.7 eV, the co-doped systems exhibit higher peak intensities compared to the pure and singly doped systems, which means that the co-doping enhances the absorption of the system in the visible region. Significant peak intensities of  $\epsilon_2(\omega)$  are observed in the energy range of 3.2–11.3 eV, indicating significant absorption from the near visible to ultraviolet region. This property makes the studied materials promising for applications in energy production systems.

#### *b. Absorption Coefficient*

In addition to  $\epsilon_1(\omega)$  and  $\epsilon_2(\omega)$ , we calculated the absorption coefficient  $\alpha(\omega)$ , which is a crucial metric that quantifies the material's ability to absorb and convert photons of specific energy into a usable form. This coefficient provides valuable insight into the attenuation of incident light intensity as it passes



through a material and illustrates the process of light decay in the absorbing medium. The  $\alpha(\omega)$  curves of pristine SrS, Fe-doped, and (Fe, p<sup>0</sup>) co-doped SrS are shown in Figure 16(c).

The HMF property is evident in the absorption coefficient spectra. In the singly doped system there is a clear infrared absorption in the lower energy range from 0 to approximately 0.4 eV. However, a notable absence of infrared absorption is observed in the pure and co-doped systems. This is because the photon energy falls into the forbidden bandgap, which means transparency for infrared light. As the photon energy increases, the absorption coefficient increases rapidly, showing typical semiconductor behavior. Of all the compounds examined, the ultraviolet range has the highest absorption. The absorption spectra of these materials show prominent peaks in the UV range, which mainly occur above 9 eV photon energy. These peaks show specific values, namely 162, 163, 162, 159, and 157 [10<sup>4</sup> Cm<sup>-1</sup>], for the pristine Fe-mono-doped and Li, Na, and K co-doped SrS alloys, respectively. This indicates a significant level of absorption and minimal electron losses within this energy range for all alloys. In the visible range, the absorption values for all compounds are comparatively lower than in the UV range and almost zero for SrS. The substitution of p<sup>0</sup> also shifts the position of the absorption peaks of singly doped SrS in the infrared and visible region and results in new peaks. Consequently, a redshift occurs, which is consistent with the previous interpretation of  $\epsilon_2(\omega)$ .

Based on previously reported data, the absorption curves can be divided into two distinct regions showing improvement compared to pure SrS. SrS: (Fe, p<sup>0</sup>) compounds exhibit significant absorption compared to SrS: Fe in the first region, covering the energy range from 0 to 2.7 eV and covering the near-infrared to visible region. In the second region, which extends from 2.7 to 13.6 eV and corresponds to the near ultraviolet region, SrS:Fe absorbs more energy than SrS:(Fe, p<sup>0</sup>). These groundbreaking findings clearly demonstrate the potential of SrS: (Fe, p<sup>0</sup>) materials as highly effective hole transport materials (HTM) for use in solar cells. They are particularly characterized by their exceptional property of minimal absorption of incident sunlight, making them an ideal choice for improving solar cells efficiency. It should also be mentioned that SrS:Fe is ideal for use as a photodetector.

### *c. Optical Conductivity*

The optical conductivity  $\sigma(\omega)$  is related to the conduction of electrons, which are formed when a photon of a certain frequency interacts with a medium. Figure 16(d) shows the optical conductivities of pure, Fe-doped and (Fe, p<sup>0</sup>) co-doped SrS. The optical conductivity spectra largely agree with the shape of the imaginary part of the dielectric function. This means that by analyzing these spectra, which come from the imaginary part of the dielectric function, we can identify specific transitions that are responsible for the peaks. This is done using band-to-band decomposition as explained earlier.

$\sigma(\omega)$  of the co-doped compounds is quite intriguing and starts around the fundamental bandgap. Notably, the optical conductivity for all compounds, including the pure and singly doped ones, shows significant peaks in the photon energy range of 4–11 eV. This indicates an increased photon absorption rate in this particular energy range. Remarkably, all compounds in this region exhibit similar behavior, highlighting their comparable optical properties. The remarkably high value of optical conductivity means that these materials respond strongly to light, demonstrating their efficiency in conducting electrons when illuminated. Furthermore, the optical conductivity patterns consistently mirror those observed at  $\alpha(\omega)$ , highlighting that the absorption of photons results in an abundance of charges available for conduction. This highlights the crucial role of photon absorption in enabling charge conduction.

It is important to highlight that our optical findings for the binary system agree well with previous theoretical evaluations [20, 77, 78]. However, it is worth noting that both experimental and theoretical data are lacking for other ternary and quaternary systems, highlighting the need for experimental validation.

### 3.2.3.5 Thermoelectric Properties

As stated in Section 1.3.3 of Chapter 1 and 2.3.3 of Chapter 2, thermoelectricity is the process of converting heat into electricity through the Seebeck effect. In this scenario, it is the heat flow that induces movement of charge carriers, resulting in the generation of an electric current. The thermoelectric performance of materials can be evaluated using the dimensionless figure of merit, which is described as follows:

$$ZT = S^2\sigma T / (\kappa_e + \kappa_l) \quad (\text{eq.36})$$

In this case,  $S$  stands for the Seebeck coefficient,  $\sigma$  for the electrical conductivity,  $PF = S^2\sigma$  for the power factor,  $\kappa_e + \kappa_l$  for the total thermal conductivity (which adds the contributions of the lattice and electronic components, respectively) and  $T$  for the temperature in Kelvin.

To achieve the best thermoelectric performance, low thermal conductivity, significant Seebeck coefficient and high electrical conductivity are required. Nevertheless, the electronic component of thermal conductivity is directly related to electrical conductivity according to the Wiedemann-Franz law [79], which establishes a connection between  $\kappa_e$  and electrical conductivity via  $\kappa_e = L\sigma T$  (where  $L$  is the Lorentz number). Because of this interdependence, it is difficult to improve  $ZT$  by changing one parameter without also changing the others.

Selecting and designing thermoelectric materials, therefore, requires considering various other crucial factors. This includes aiming for a low band effective mass, which leads to a high Seebeck coefficient, without significantly impeding electrical conductivity. In BoltzTrap2's constant relaxation

time approximation (RTA), both electrical and electronic thermal conductivities, unlike the Seebeck coefficient, are dependent on relaxation time ( $\tau$ ). Therefore, determining  $\tau$  is necessary to determine their actual values. The electronic structure derived from DFT calculations serves as an important input for the estimation of this parameter. Based on the identified band structures, we determined the effective masses ( $m^*$ ) of the charge carriers at the CBM and VBM using the parabolic band approximation framework [80]. Additionally, we calculated the uniaxial deformation potentials of electrons and holes by evaluating the CBM and VBM changes.

We also performed estimates of uniaxial deformation potentials for electrons and holes obtained by calculating changes in the CBM and VBM. The deformation potential (DP), defined as the energy change of a system due to a deformation of its lattice structure along the transport direction, is described as follows:

$$E_d = \frac{\partial E_{edge}}{\partial \left(\frac{\Delta a}{a_0}\right)} \quad (\text{eq.37})$$

Where  $\partial E_{edge}$  represents the alteration in CBM and VBM for electrons and holes, respectively, and  $\frac{\Delta a}{a_0}$  denotes the uniaxial strain, ranging from -4% to 4%. The slope of the curves represents  $E_d$ .

Based on their effective masses and strain potentials, we calculated the relaxation time, for the pristine, doped and co-doped SrS systems using the deformation potential theory proposed by Bardeen and Shockley [71]. This theory provides a formula that relates  $\tau$  to temperature as follows:

$$\tau = \frac{2\sqrt{2}\pi\hbar^4 C_\alpha}{3(m^* k_b T)^{3/2} E_d^2} \quad (\text{eq.38})$$

$\hbar$  is the reduced Planck's constant,  $m^*$  is the band effective mass,  $E_d$  is the DP, and  $C_\alpha$  is the elastic constant computed via a quadratic polynomial fit of total energy fluctuation under strain as:

$$C_\alpha = \frac{1}{V_0} \frac{\partial^2 E}{\partial \left(\frac{\Delta a}{a_0}\right)^2} \quad (\text{eq.39})$$

Herein,  $V_0$  represents the equilibrium volume.

For the pure, doped, and co-doped SrS systems, the fitted curves showing edges and total energies versus strains are shown in Figures 17–20. Table 9 additionally shows the calculated values of  $m^*$ ,  $E_d$  and  $C_\alpha$ .

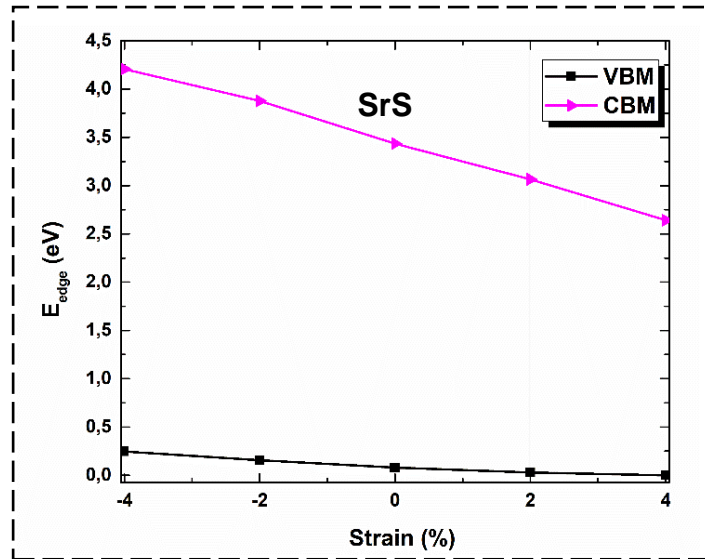
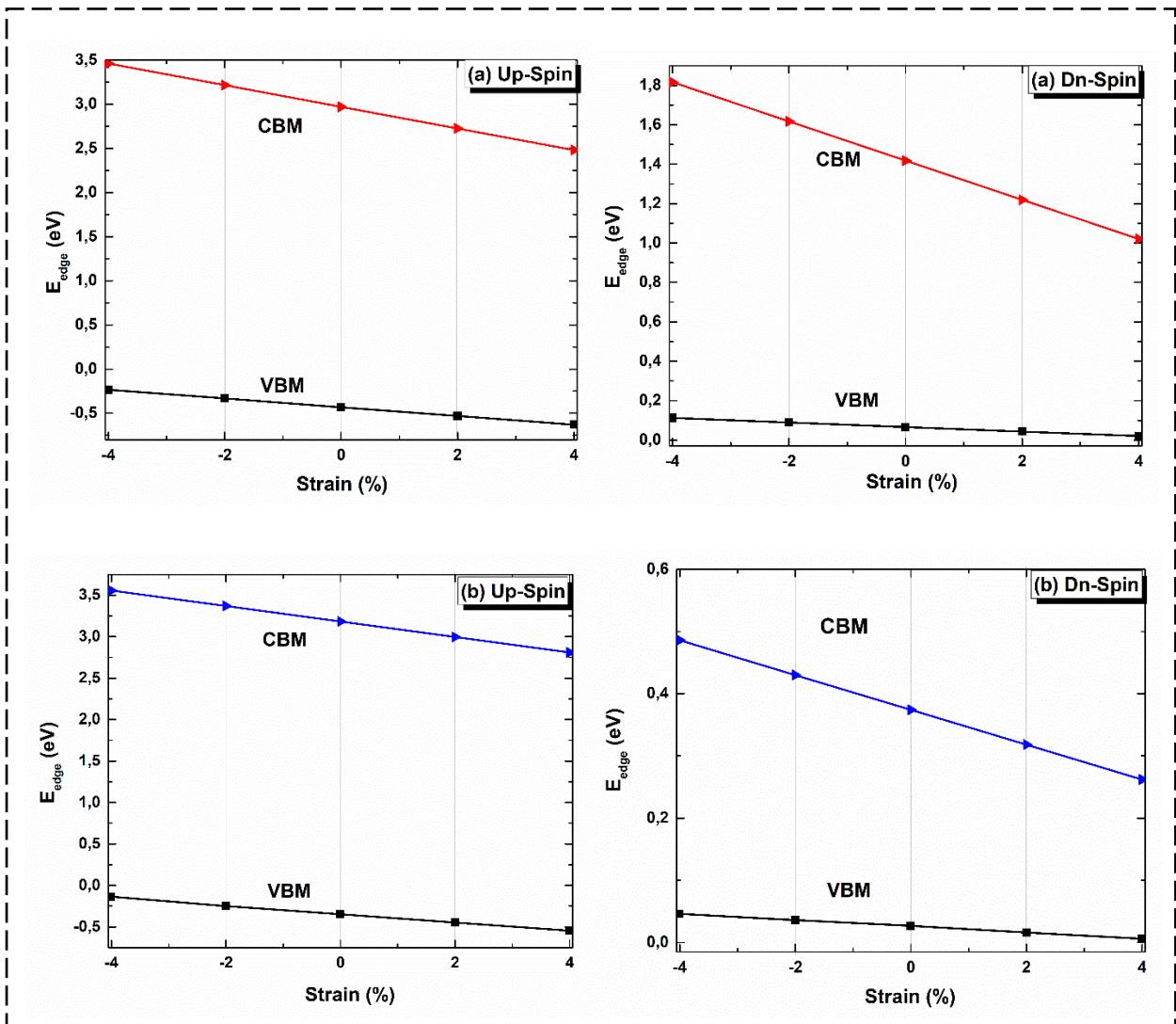
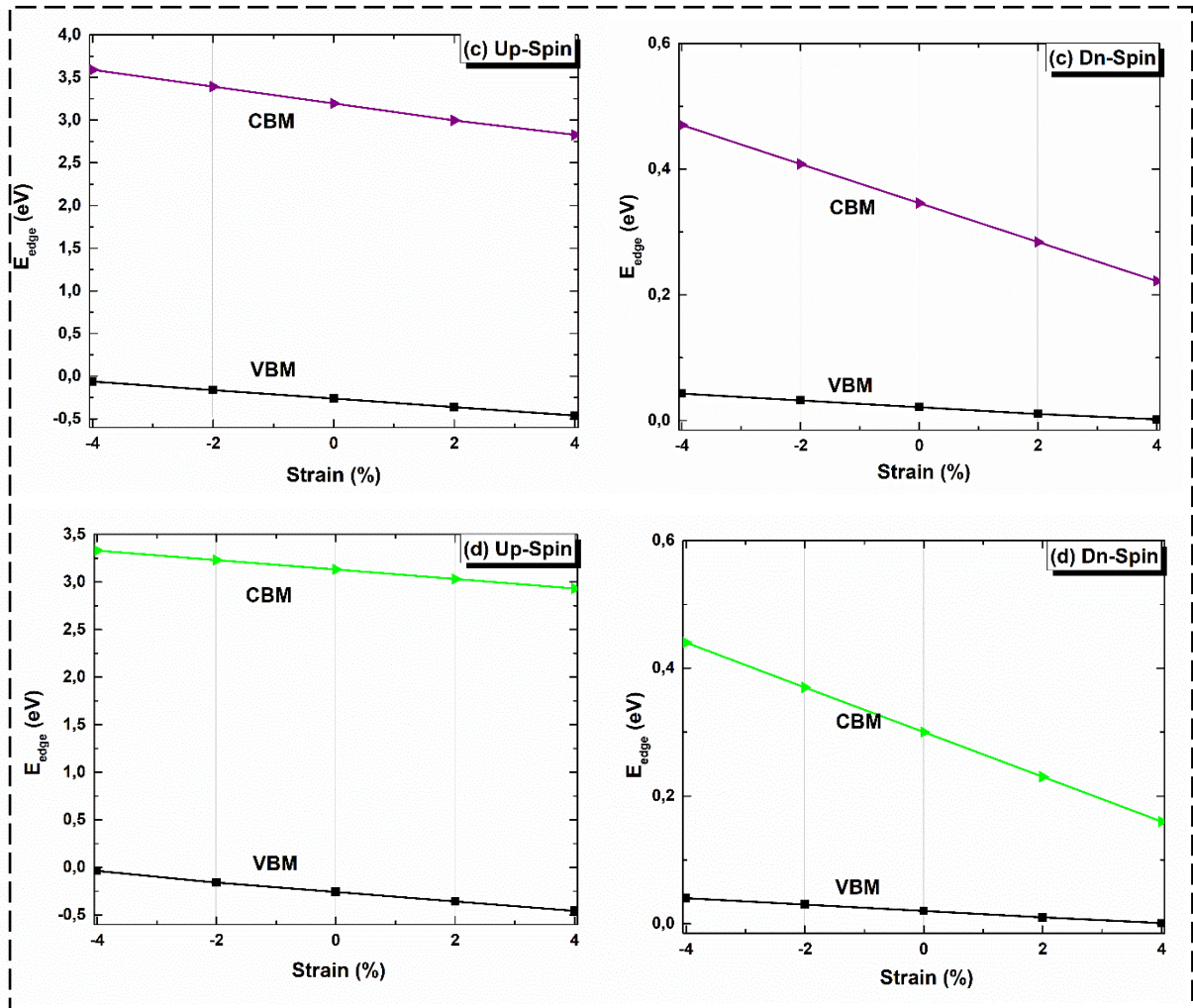
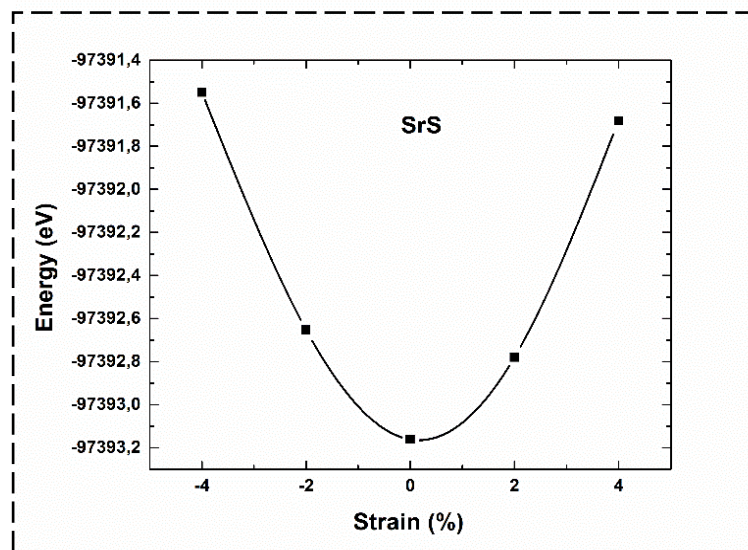


Figure.17 Band energy edge ( $E_{\text{edge}}$ ) as a function of uniaxial strain ( $\frac{\Delta a}{a_0}$ ) for the pristine SrS.





**Figure 18.** Band energy edge ( $E_{\text{edge}}$ ) as a function of uniaxial strain ( $\frac{\Delta a}{a_0}$ ) for: (a) Fe mono-doped and (b-d) (Fe, Li), (Fe, Na), and (Fe, K) co-doped systems, respectively.



**Figure 19.** Total energy as a function of uniaxial strain ( $\frac{\Delta a}{a_0}$ ) for the pristine SrS.



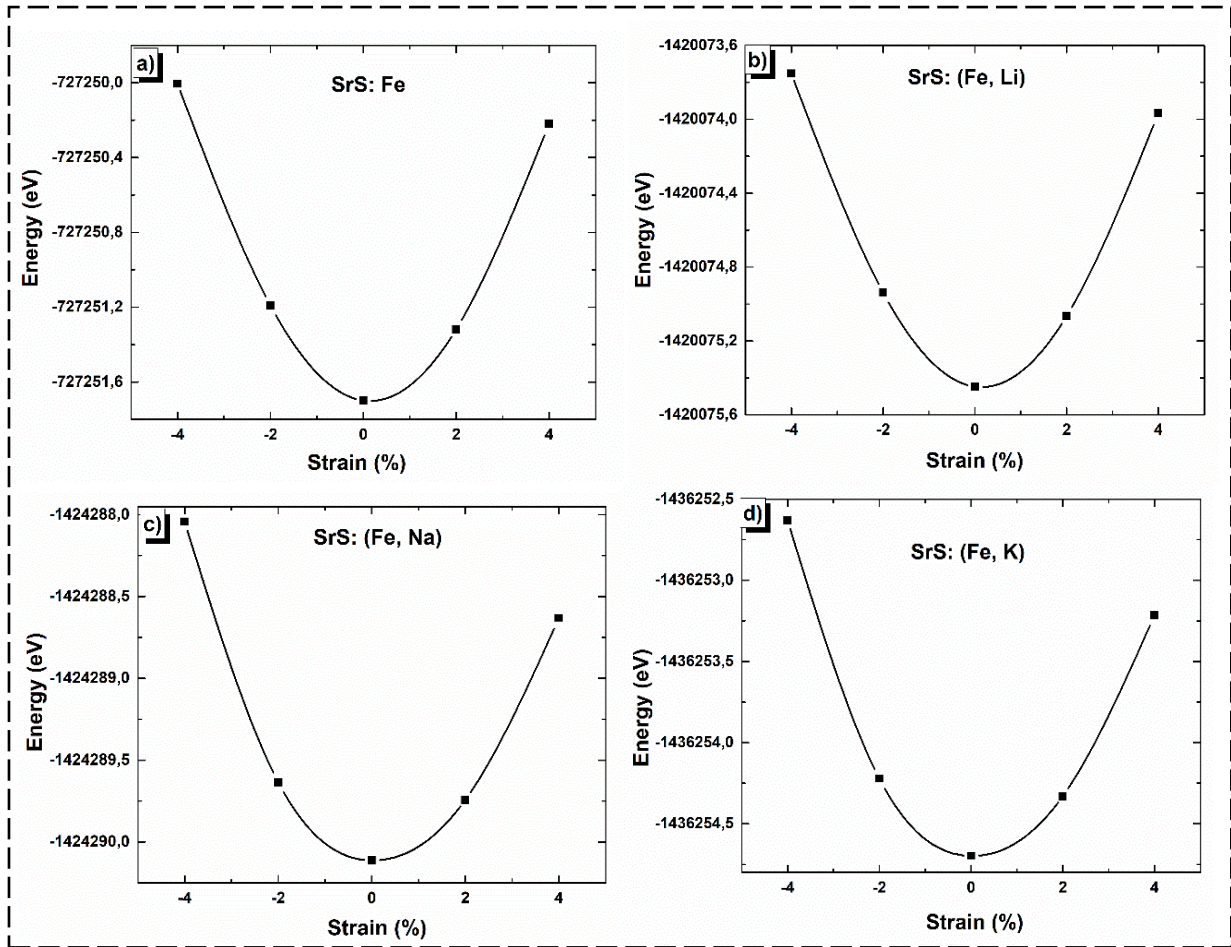


**Figure 20.** Total energy as a function of uniaxial strain ( $\frac{\Delta a}{a_0}$ ) for: **(a)** Fe mono-doped and **(b-d)** (Fe, Li), (Fe, Na), and (Fe, K) co-doped systems, respectively.

As shown in Table 9, the  $C_\alpha$  values gradually decrease as dopants are introduced into SrS and as the system goes from mono-doping to co-doping. This is consistent with an increase in atomic number within the co-doped systems. This decrease in the elastic constant can be attributed to the introduction of additional dopant atoms, which disrupt the regular lattice structure and lead to lattice defects.

On the other hand, the  $E_d$  has a stronger effect on electrons than on holes. These different effects highlight the different sensitivity of these charge carriers to external perturbations.

In addition, the  $m^*$  of the majority-electrons is smaller than that of the majority-holes. This contrast in  $m^*$  highlights the different mobilities and transport behavior of the majority electrons and holes.

Comparing our results for the pristine material with those of Hou et al. using HSE [80], we observe good agreement for all parameters. The slight differences could possibly be due to differences in the computational code or approximation methods used (VASP code).

**Table 9**

The calculated elastic constant  $C_\alpha$ , the DP constant  $E_d$ , and the effective mass  $m^*$  of the pristine, doped and co-doped SrS systems.

Materials	Carrier type	$C_\alpha$ (eV/Å <sup>3</sup> )	$E_d$ (eV)		$m^*$ (m <sub>e</sub> )	
			Up-Spin	Dn-Spin	Up-Spin	Dn-Spin
SrS	<i>p</i> -type	1.335	-6.25		0.461	
		1.347 <sup>j</sup>	-17.20 <sup>j</sup>		0.590 <sup>j</sup>	
	<i>n</i> -type	1.335	-18.55		0.170	
		1.347 <sup>j</sup>	-11.44 <sup>j</sup>		1.518 <sup>j</sup>	
SrFeS	<i>p</i> -type	0.800	-4.951	-1.150	0.538	1.363
	<i>n</i> -type	0.800	-12.25	-9.951	0.288	0.899
SrFeLiS	<i>p</i> -type	0.780	-3.452	-0.952	0.560	0.382
	<i>n</i> -type	0.780	-11.05	-3.703	0.254	0.841
SrFeNaS	<i>p</i> -type	0.696	-1.080	-0.544	0.583	0.393
	<i>n</i> -type	0.696	-9.853	-3.501	0.244	0.910
SrFeKS	<i>p</i> -type	0.644	-0.734	-0.230	0.600	0.417
	<i>n</i> -type	0.644	-5.000	-3.100	0.227	0.795

<sup>j</sup> Ref [82].

Using the obtained parameters from Table 9 and substituting them into Eq. 38, we can determine  $\tau$ . The  $\tau$  of holes (*p*-type) and electrons (*n*-type) for pure SrS as well as for majority- and minority- spins of doped and co-doped systems as a function of temperature in a range of 100–1200 K is shown in Figures 21 and 22, respectively.

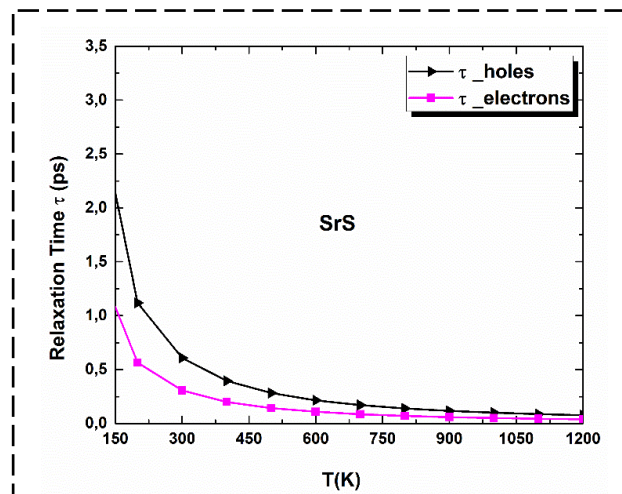


**Figure 21.** Measured relaxation time ( $\tau$ ) of holes and electrons as temperature dependence for SrS.

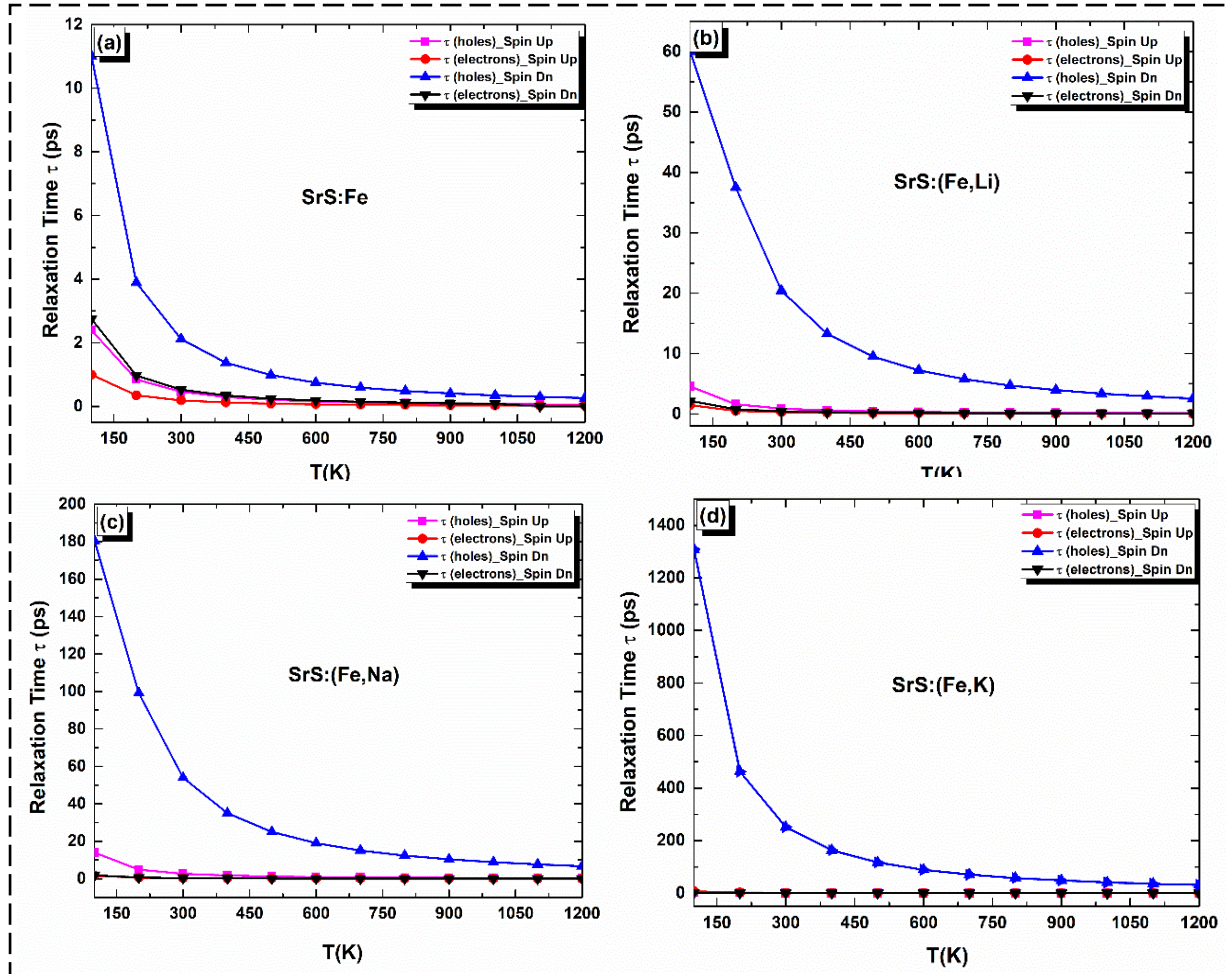


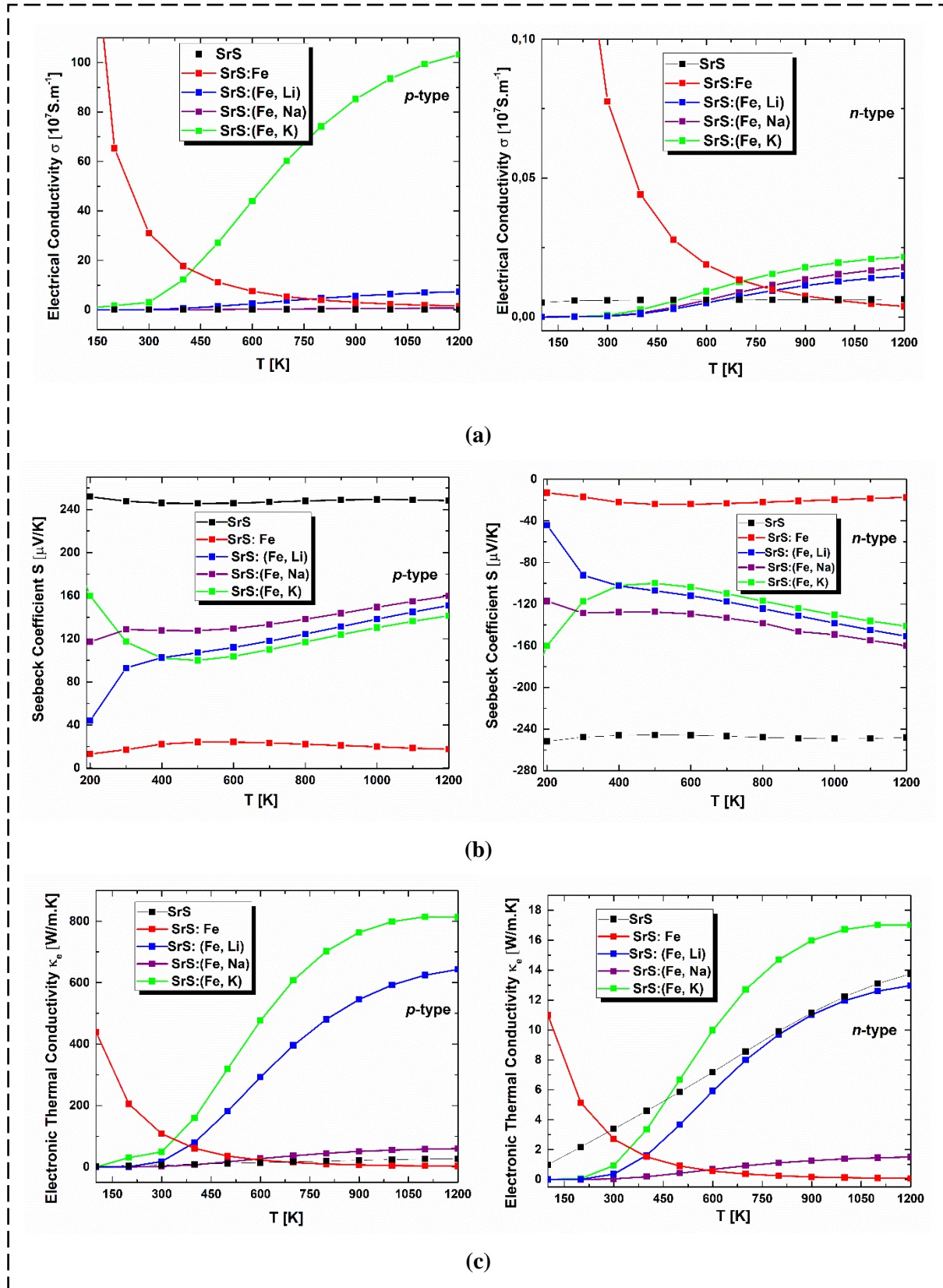
**Figure 22.** Measured spin-resolved relaxation time ( $\tau$ ) of holes and electrons as temperature dependence for (a) Fe-single doped and (b-d) (Fe,  $p^0$ ) co-doped systems, respectively.

From the figures, it can be seen that all compounds have similar variations in  $\tau$ . The intensity of  $\tau$  initially decreases before gradually varying over a high temperature range. At low temperatures, the co-doped system SrFeKS has the most significant value, followed by SrFeNaS, SrFeLiS, SrFeS and then SrS. This trend can largely be attributed to the low deformation potential values of the SrFeKS material compared to other materials (since  $\tau$  is inversely proportional to the square of  $E_d$ , the impact of this contribution will be particularly significant). The relaxation time of HSC compounds is ten times longer than that of HMF compound. Consequently, we expect high electrical conductivity and consequently high  $ZT$  in all  $p$ -type co-doped systems.

Our calculated  $\tau$  values for pristine SrS appear to be higher than those of Hou et al. [80], who obtained values in the order of  $10^{-14}$ s. This is also due to the difference in the computational code or approximation methods used



After determining  $\tau$ , we calculated the spin-dependent transport properties, including  $\sigma$ ,  $S$ ,  $\kappa$ , and ZT, for both holes and electrons in all systems, independent of  $\tau$ . The results are shown in Figure 23 (a-e).



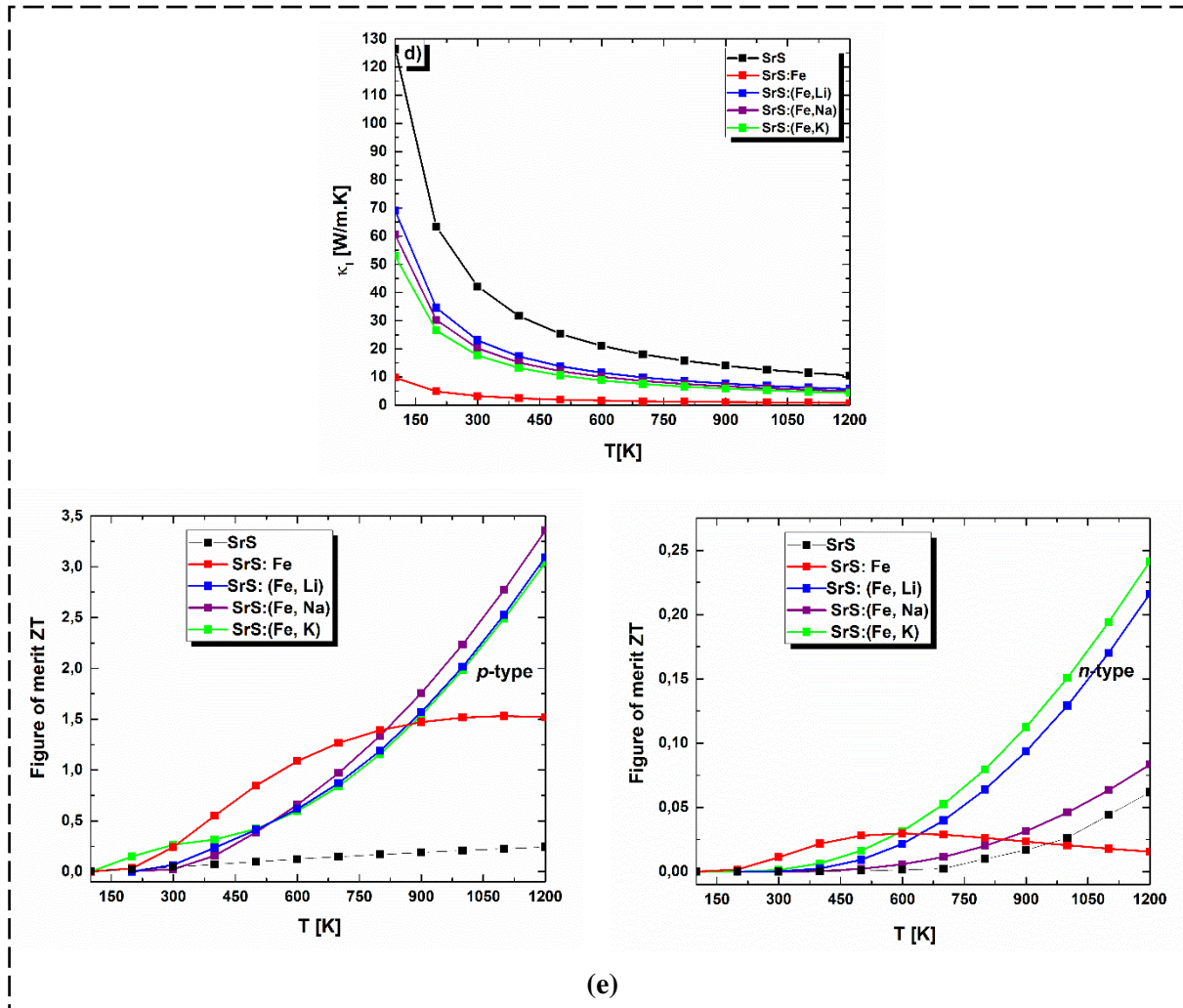


**Figure.23** Temperature dependent thermoelectric properties (a) electrical conductivity ( $\sigma$ ), (b) Seebeck coefficient ( $S$ ), (c) electronic thermal conductivity ( $\kappa_e$ ), (d) lattice thermal conductivity ( $\kappa_l$ ), and (e) figure of merit ( $ZT$ ) for both  $p$ -type and  $n$ -type of pristine, Fe-single doped and (Fe,  $p^0$ ) co-doped SrS systems.

#### a. Electrical Conductivity

Electrical conductivity ( $\sigma$ ) refers to the movement of free electrons within materials. It generally depends on the mobility of the charge carriers, which is influenced by impurities and defects. Electrons move from the hot to the cold region in a material, and as a result of this phenomenon, electricity is generated. For an effective thermoelectric device, materials must have high electrical conductivity. Materials are categorized as either conductors or semiconductors according to energy band theory. Conductors have freely moving electrons for conduction, while semiconductors require the supply of external energy to enable charge movement. Our analysis uses the two-current model to study the

temperature-dependent changes in spin-based transport properties. The plots of  $\sigma$  for  $p$ -type and  $n$ -type are shown in Figure 23(a) versus temperature up to 1200 K.

In the two-current model, electrical conduction is determined by taking into account the currents in both spin channels [81]. This means that the total electrical conductivity is the sum of the respective values for each spin channel, expressed by the equation:  $\sigma = \sigma_{\uparrow} + \sigma_{\downarrow}$  [82].

Examining the curves, it is clear that the electronic conductivity of pure material is almost independent of temperature for both  $p$ -type and  $n$ -type carriers. This observation is consistent with the findings of Hou et al. [80] and Rajput et al. [83]. Conversely, the curves for the co-doped systems all show a gradual increase with increasing temperature, which is characteristic of semiconductors. On the other hand, the conductivity of mono-Fe-doped SrS gradually decreases with increasing temperature, a behavior typical for metallic materials. Notably, the conductivity of  $p$ -type compounds exceeds that of the corresponding  $n$ -type compounds, which may be due to the longer relaxation time in  $p$ -type systems compared to  $n$ -type systems. For  $p$ -type carriers, the maximum conductivity reaches  $103.1 \times 10^7 \text{ S.m}^{-1}$  for SrS: (Fe, K), followed by  $7.4 \times 10^7 \text{ S.m}^{-1}$  for SrS: (Fe, Li), then  $0.7 \times 10^7 \text{ S.m}^{-1}$  for SrS: (Fe, Na),  $1.6 \times 10^7 \text{ S.m}^{-1}$  for SrS: Fe and a minimum of  $0.0125 \times 10^7 \text{ S.m}^{-1}$  for pristine SrS, all at 1200 K.

#### *b. Seebeck Coefficient*

The Seebeck coefficient ( $S$ ), commonly known as thermo-power, is quantified as the voltage produced in an open circuit between two points where there is a uniform temperature difference of 1 K. The magnitude of this coefficient varies with the temperature level at which the thermal gradient is introduced. An essential Seebeck coefficient is essential for optimizing thermoelectric devices. In the two-current model, the total Seebeck coefficient can be understood as the average of the up-spin and down-spin coefficients, weighted by their respective electrical conductivities as  $S = \sigma_{\uparrow} S_{\uparrow} + \sigma_{\downarrow} S_{\downarrow} / \sigma_{\uparrow} + \sigma_{\downarrow}$  [82]. The variation of the Seebeck coefficient with temperature is shown in Figure 23(b).

The sign of the Seebeck coefficient basically determines the type of majority charge carriers in the system. Figure 23(b) shows that both types of carriers exist in our considered series of materials: (i) materials with a positive Seebeck coefficient region have holes as the majority charge carriers, and (ii) materials in the negative Seebeck coefficient region have electrons as the majority of charge carriers. The Seebeck coefficients of  $p$ -type and  $n$ -type SrS, SrS: Fe and SrS: (Fe,  $p^0$ ) alloys show similar trends. In the range of 200–500 K, the absolute values of  $S$  for both carrier types in pure SrS initially decrease with increasing temperature, reaching a minimum of  $245 \mu\text{V K}^{-1}$  at 500 K and then decreasing with temperature until they reach a maximum of  $249 \mu\text{V K}^{-1}$  at 1200 K, which is comparable to previous results [80, 83]. For the HMF compound,  $S$  increases gradually, reaches a maximum of  $24.29 \mu\text{V K}^{-1}$  at 500 K, and then slowly decreases at temperatures between 500 and 1200 K. Based on these results,

we can conclude that doping iron in SrS is not preferable as it reduces its Seebeck coefficient, showing that pure semiconductors have better voltage generation compared to HMF compounds. For Li- and Na-co-doped systems,  $S$  increases with increasing temperature, indicating a high Seebeck coefficient at high temperatures. Conversely, co-doping with K initially decreases  $S$  in the range of 200–500 K, followed by a linear decrease to match the trend of pristine and other co-dopants. The simultaneous doping of Li, Na and K in SrS:Fe significantly increases the absolute value of  $S$ , approaching 151.15, 160.29 and 150.24  $\mu\text{VK}^{-1}$  at 1200 K, respectively. The variation of  $S$  values can be attributed to the differences in the bandgap values.

### c. Thermal Conductivity

Optimization of thermoelectric materials also depends on a crucial factor known as thermal conductivity ( $\kappa$ ). This factor refers to the transfer of energy in the form of heat due to temperature differences within a material. The total thermal conductivity ( $\kappa = \kappa_e + \kappa_l$ ) includes both the electronic ( $\kappa_e$ ) and the lattice contribution ( $\kappa_l$ ). As already described,  $\kappa_e$  is closely linked to electronic conductivity via the Wiedemann-Franz law [79]. Therefore, a good thermoelectric material requires low thermal conductivity without compromising electrical conductivity.  $\kappa_e$  is calculated using the BoltzTrap2 code as described in Eq. 38 in Chapter 1 in the framework of the two-current model [82]. Conversely,  $\kappa_l$  is determined by the Slack equation. This equation specifically accounts for the heat conduction enabled by acoustic phonons through an anharmonic flip-scattering process and can be expressed as [84]:

$$\kappa_l = A \frac{\bar{M} \theta_D^3 V^{1/3}}{\gamma^2 T n^{2/3}} \quad (\text{eq.40})$$

Herein  $\bar{M}$  is the average atomic mass,  $V$  is the average volume per atom,  $n$  is the number of atoms in the unit cell, and  $\gamma$  is the Grüneisen parameter calculated by the expression proposed by Julian [87] as

$$\gamma = \frac{9 - 12 \left(\frac{v_t}{v_l}\right)^2}{2 + 4 \left(\frac{v_t}{v_l}\right)^2}, \text{ in which } v_l \text{ and } v_t \text{ are the longitudinal and transversal sound velocities, respectively.}$$

The constant factor  $A$  is determined by the Grüneisen parameter and can be calculated using the formula:

$$A = \frac{2.43 \times 10^7}{1 - \frac{0.514}{\gamma} + \frac{0.228}{\gamma^2}}.$$

Figures 23(c-d) show the evolution of  $\kappa_e$  and  $\kappa_l$  as a function of temperature for all series of materials discussed in this study. The curves representing  $\kappa_e$  in Figure 23(c) show a significant increase with increasing temperature for both  $p$ -type and  $n$ -type semiconductor materials in their pristine and HSC forms. This is due to the increase in electron energy, which increases the mobility of the charge carriers and consequently leads to higher electrical conductivity. Notably, the  $p$ -type alloys exhibit

higher  $\kappa_e$  values compared to their corresponding  $n$ -type counterparts. In contrast, for the HMF alloy,  $\kappa_e$  decreases rapidly and remains constant at high temperatures.

For comparison,  $p$ -type SrS: (Fe, K) has the highest  $\kappa_e$ , followed by SrS: (Fe, Li), then SrS: (Fe, Na), SrS and finally the SrS: Fe compound at 1200 K. The order is different for  $n$ -type carriers, where they are SrS: (Fe, K), SrS, SrS: (Fe, Li), SrS: (Fe, Na) and finally SrS: Fe. The behavior of  $\kappa_e$  mirrors that of  $\sigma$  and follows the proportionality presented in the Wiedemann-Franz law [79] for  $p$ -type carriers. For the  $n$ -type carriers, all compounds follow the law except SrS, which is consistent with Rosenberg's observation [88] that the Wiedemann-Franz law holds at both low and high temperatures, but may not hold at intermediate temperatures. Our results are not consistent with those of Hou et al. [80], which could also be due to the differences in the parameters used.

To gain deeper insights into the temperature sensitivity of thermal conductivity, we plotted the curves of  $\kappa_l$  in Figure 23(d), which clearly shows that  $\kappa_l$  decreases with increasing temperature. From 100 K to 1200 K, the  $\kappa_l$  decreases from 126.51 W/m.K to 10.54 W/m.K for pristine SrS, from 69.04 W/m.K to 5.76 W/m.K for SrS: (Fe, Li), from 60.92 W/m.K to 5.04 W/m K for SrS: (Fe, Na), from 53.12 W/m K to 4.42 W/m K for SrS: (Fe, K ) and from 9.64 W/m K to 0.82 W/m K for SrS: Fe. This trend shows that higher temperatures lead to greater phonon scattering, resulting in reduced  $\kappa_l$ . This behavior of suppressed lattice thermal conductivity is desirable for improving the thermoelectric efficiency.

Our original values are overestimated compared to previous literature work (2.60 W/m.K at 1200 K) [80]. This can be attributed to the use of ShengBTE [87], which uses a fully iterative solution of the BTE and considers second and third order force constants instead of the Slack equation. This overestimation of  $\kappa_l$  can be clarified by considering the influence of inaccurately estimated  $\gamma$  in the Slack equation, as mentioned in [88].

#### d. Figure of Merit

Using the collected  $\sigma$ ,  $S$ ,  $\kappa_e$ , and  $\kappa_l$  data, we estimated the dimensionless quality factor ( $ZT$ ) to evaluate the practical thermal efficiency of our compounds. The temperature-dependent  $ZT$  diagrams are shown in Figure 23(e). Upon careful analysis, we found that the  $ZT$  values for  $p$ -type SrS, SrS:Fe, and SrS:(Fe,  $p^0$ ) compounds outperform their  $n$ -type counterparts within the same material, reflecting the superior thermoelectric performance of  $p$ -type compounds underlines in comparison to their  $n$ -type carriers. Furthermore, it is evident that temperature has a significant influence on the thermoelectric behavior of these compounds. At 300 K,  $ZT$  remains relatively low and has values of 0.04, 0.24, 0.07, 0.02 and 0.3 for pristine SrS, SrS: Fe, SrS: (Fe, Li), SrS: (Fe, Na) and SrS: (Fe, K) in  $p$ -type doping carriers. However, when temperatures increase to 1200 K, the

maximum ZT values reach 0.24, 1.51, 3.11, 3.34, and 3.03 for *p*-doped carriers, maintaining the same order. In contrast, the maximum ZT value for *n*-doped carriers reaches 0.06, 0.02, 0.22, 0.08 and 0.24 at 1200 K. This discrepancy can be due to the significantly higher electrical conductivity and electronic thermal conductivity of *p*-type carriers compared to their *n*-type counterparts.

Furthermore, these impressive ZT values, which exceed one for *p*-type carriers, are largely due to the semiconductor nature of the narrow bandgap co-doped alloys. These results suggest that the HSC compounds are promising for high-temperature thermoelectric applications, especially compared to the HMF alloy. Furthermore, it shows that co-doping is more effective than mono-doping to achieve the best thermoelectric performance for binary SrS. It should be emphasized that the ZT values we calculated for SrS show slight deviations from those reported by Hou et al. [80] (0.08 for *p*-type and 0.15 for *n*-type). These deviations were explained in the respective section.

### 3.2.4 Conclusion

In the second section of this chapter, we examined an in-depth study of the three newly designed  $p^0$  alkali metals ( $p^0 = \text{Li, Na, and K}$ ) co-doped into SrS:Fe compounds at a selected doping level of 12.5% using rigorous ab-initio calculations within the PBE and PBE+mBJ methods. This study included a comprehensive investigation of the effects of co-doping on various properties, including structural, electronic, magnetic, optical, and thermoelectric properties. The key findings and conclusions from this endeavor are presented as follows:

1. The results of the structural properties obtained with the PBE-GGA approximation have shown that the lattice constant  $a$  ( $\text{\AA}$ ) increases gradually with the atomic number ( $Z$ ), while the bulk modulus  $B$  (GPa) progressively decreases. Substitution of alkali metals in SrS:Fe has been shown to increase the overall stability of the system, facilitate the doping process, and strengthen ionic bonds. Calculations of the differences in total energies ( $\Delta E$ ) confirmed the stability of the co-doped systems in the ferromagnetic (FM) state, with a higher Curie temperature ( $T_c$ ) being observed compared to room temperature. Among the co-doped systems, SrS: (Fe, K) in particular has the highest  $T_c$ , making it a promising candidate for spintronic applications.
2. The electronic properties showed that all compounds were characterized as *p*-type semiconductors (HSCs), and it was observed that the energy gap became smaller in the co-doped systems compared to the semi-metallic (HM) SrS:Fe compound.
3. In all compounds, we calculated a total magnetic moment of  $5 \mu_B$ , which is increased compared to mono-doping, and a low local magnetic moment was created at the non-magnetic sites due to *sp-d* hybridization.

4. The analysis of optical properties in terms of dielectric function, absorption coefficient and optical conductivity has shown that all three types of alkali metal ions have the ability to enhance the infrared absorption of the SrS:Fe system and generate new peaks in the visible region and leads to a redshift. This property makes the materials ideal for solar cells applications.
5. The analysis of the thermoelectric properties clearly showed that the  $p$ -type ZT values were significantly superior to those of the  $n$ -type ZTs. In particular, the  $p$ -type SrS: systems (Fe-Li, Na, and K) were found to be promising candidates for efficient thermoelectric materials, showing ZT values above 1 at 1200 K.

In summary, Chapter 3 with its two parts has provided comprehensive insights into one of the two methods, namely co-doping. This method proves to be a powerful tool for tailoring the properties of HMFs to meet precise application requirements.

In the next chapter of this dissertation, we will examine the second method, which focuses on dimensionality reduction.

### References for Chapter 3

- [1] Choudhuri, I., Bhauriyal, P., & Pathak, B. (2019). Recent advances in graphene-like 2D materials for spintronics applications. *Chemistry of Materials*, 31(20), 8260-8285.
- [2] Misiorny, M., Hell, M., & Wegewijs, M. R. (2013). Spintronic magnetic anisotropy. *Nature Physics*, 9(12), 801-805.
- [3] Munekata, H., Ohno, H., Von Molnar, S., Segmüller, A., Chang, L. L., & Esaki, L. (1989). Diluted magnetic III-V semiconductors. *Physical Review Letters*, 63(17), 1849.
- [4] Ohno, H., Shen, N. A., Matsukura, A. F., Oiwa, A., Endo, A., Katsumoto, S., & Iye, Y. (1996). (Ga, Mn) As: a new diluted magnetic semiconductor based on GaAs. *Applied Physics Letters*, 69(3), 363-365.
- [5] Shinya, H., Fukushima, T., Masago, A., Sato, K., & Katayama-Yoshida, H. (2018). First-principles prediction of the control of magnetic properties in Fe-doped GaSb and InSb. *Journal of Applied Physics*, 124(10), 103902.
- [6] Zhang, H. W., Wei, Z. R., Li, Z. Q., & Dong, G. Y. (2007). Room-temperature ferromagnetism in Fe-doped, Fe-and Cu-codoped ZnO diluted magnetic semiconductor. *Materials Letters*, 61(17), 3605-3607.
- [7] Murali, G., Reddy, D. A., PoornaPrakash, B., Vijayalakshmi, R. P., Reddy, B. K., & Venugopal, R. (2012). Room temperature magnetism of Fe doped CdS nanocrystals. *Physica B: Condensed Matter*, 407(12), 2084-2088.
- [8] Singh, J., & Verma, N. K. (2012). Synthesis and characterization of Fe-doped CdSe nanoparticles as dilute magnetic semiconductor. *Journal of superconductivity and novel magnetism*, 25, 2425-2430.
- [9] Bourouis, C., & Meddour, A. (2012). First-principles study of structural, electronic and magnetic properties in Cd<sub>1-x</sub>Fe<sub>x</sub>S diluted magnetic semiconductors. *Journal of magnetism and magnetic materials*, 324(6), 1040-1045.
- [10] Mahmood, Q., Javed, A., Murtaza, G., & Alay-e-Abbas, S. M. (2015). Study of the Zn<sub>0.75</sub>M<sub>0.25</sub>Te (M= Fe, Co, Ni) diluted magnetic semiconductor system by first principles approach. *Materials Chemistry and Physics*, 162, 831-838.
- [11] Li, T., Wang, W., Shi, Q., Zhang, J., & Zhao, L. (2022). Transition from ferromagnetism to superparamagnetism in diluted magnetic Fe (II)-doped ZnSe microspheres. *Journal of Magnetism and Magnetic Materials*, 543, 168625.
- [12] Amari, S. (2021). Physical properties of Mn-and Fe-doped CaS: A DFT insights. *Computational Condensed Matter*, 27, e00559.
- [13] Ernzerhof, M., & Scuseria, G. E. (2000). Perspective on “Inhomogeneous electron gas” Hohenberg P, Kohn W (1964) Phys Rev 136: B864. *Theoretical Chemistry Accounts*, 103, 259-262.



- [14] Tran, F. (2018). WIEN2k: An Augmented Plane Wave Plus Local Orbitals Program for Calculating Crystal Properties.
- [15] Perdew, J. P., Burke, K., & Ernzerhof, M. (1996). Generalized gradient approximation made simple. *Physical review letters*, 77(18), 3865.
- [16] Tran, F., & Blaha, P. (2009). Accurate band gaps of semiconductors and insulators with a semilocal exchange-correlation potential. *Physical review letters*, 102(22), 226401.
- [17] Blaha, P., Schwarz, K., Madsen, G. K., Kvasnicka, D., & Luitz, J. (2001). wien2k. *An augmented plane wave+ local orbitals program for calculating crystal properties*, 60(1).
- [18] Birch, F. (1978). Finite strain isotherm and velocities for single-crystal and polycrystalline NaCl at high pressures and 300 K. *Journal of Geophysical Research: Solid Earth*, 83(B3), 1257-1268.
- [19] Syassen, K. (1985). Pressure-induced structural transition in SrS. *Physica Status Solidi. A, Applied Research*, 91(1), 11-15.
- [20] Hamidane, N., Baaziz, H., Baddari, K., & Charifi, Z. (2020). First-principles investigation of the structural, electronic, magnetic, thermodynamic and optical properties of the cubic Sr<sub>1-x</sub>Mn<sub>x</sub>S ternary alloys. *Computational Condensed Matter*, 23, e00458.
- [21] Souadkia, M., Bennecer, B., Kalarasse, F., & Mellouki, A. (2011). Ab initio calculation of vibrational and thermodynamic properties of SrX (S, Se, Te) in the B1 (NaCl) and B2 (CsCl) structures. *Computational materials science*, 50(5), 1701-1710.
- [22] Hoat, D. M. (2020). DFT prediction of structural, electronic and magnetic properties of SrO. 75TM0. 25S (TM is 3 d transition metals). *Philosophical Magazine Letters*, 100(3), 95-104.
- [23] Guo, Y. D., Yang, Z. J., Gao, Q. H., Liu, Z. J., & Dai, W. (2008). The phase transition, and elastic and thermodynamic properties of CaS derived from first-principles calculations. *Journal of Physics: Condensed Matter*, 20(11), 115203.
- [24] Chelli, S., Touam, S., Hamioud, L., Meradji, H., Ghemid, S., & Hassan, F. E. (2015). Ab-initio study of structural, elastic, electronic and thermodynamic properties of Ba<sub>x</sub>Sr<sub>1-x</sub> ternary alloys. *Mater Sci Pol*, 33(4), 879-886.
- [25] Yan, C., Lai-Yu, L., Ou-He, J., & Qing-Quan, G. (2008). First-Principle Calculations for Transition Phase and Elastic Properties of SrS. *Communications in Theoretical Physics*, 49(6), 1611.
- [26] Khenata, R., Baltache, H., Rérat, M., Driz, M., Sahnoun, M., Bouhafs, B., & Abbar, B. (2003). First-principle study of structural, electronic and elastic properties of SrS, SrSe and SrTe under pressure. *Physica B: Condensed Matter*, 339(4), 208-215.
- [27] Yang, F., Fan, T. W., Wu, J., Tang, B. Y., Peng, L. M., & Ding, W. J. (2011). Effects of Y and Zn atoms on the elastic properties of Mg solid solution from first-principles calculations. *physica status solidi (b)*, 248(12), 2809-2815.
- [28] Voigt, W. (1928). Lehrbuch der kristallphysik (mit ausschluss der kristalloptik), edited by bg teubner and jw edwards, leipzig berlin. *Ann Arbor, Mich.*

- [29] Hill, R. (1952). The elastic behaviour of a crystalline aggregate. *Proceedings of the Physical Society. Section A*, 65(5), 349.
- [30] Reuß, A. (1929). Berechnung der fließgrenze von mischkristallen auf grund der plastizitätsbedingung für einkristalle. *ZAMM-Journal of Applied Mathematics and Mechanics/Zeitschrift für Angewandte Mathematik und Mechanik*, 9(1), 49-58.
- [31] Pugh, S. F. (1954). XCII. Relations between the elastic moduli and the plastic properties of polycrystalline pure metals. *The London, Edinburgh, and Dublin Philosophical Magazine and Journal of Science*, 45(367), 823-843.
- [32] Simunek, A., & Vackar, J. (2001). Correlation between core-level shift and bulk modulus in transition-metal carbides and nitrides. *Physical Review B*, 64(23).
- [33] Moğulkoç, Y., ÇİFTÇİ, Y., KABAK, M., & Çolakoğlu, K. (2013). First-principles study of structural, elastic and electronic properties of NdTe<sub>2</sub> and TiNdTe<sub>2</sub>. *Cumhuriyet Üniversitesi Fen Edebiyat Fakültesi Fen Bilimleri Dergisi*, 34(3), 12-28.
- [34] Nye, J. F. (1985). *Physical properties of crystals: their representation by tensors and matrices*. Oxford university press.
- [35] Fahrman, M., Hermann, W., Fahrman, E., Boegli, A., Pollock, T. M., & Sockel, H. G. (1999). Determination of matrix and precipitate elastic constants in ( $\gamma$ - $\gamma'$ ) Ni-base model alloys, and their relevance to rafting. *Materials Science and Engineering : A*, 260(1-2), 212-221.
- [36] Tohei, T., Kuwabara, A., Oba, F., & Tanaka, I. (2006). Debye temperature and stiffness of carbon and boron nitride polymorphs from first principles calculations. *Physical Review B*, 73(6), 064304.
- [37] Schreiber, E. (1973). O. L. Anderson, and N. Soga, Elastic Constants and Their Measurement.
- [38] Fine, M. E., Brown, L. D., & Marcus, H. L. (1984). Elastic constants versus melting temperature in metals. *Scripta metallurgica*, 18(9), 951-956.
- [39] Hamidane, O., Meddour, A., Gous, M. H., & Bourouis, C. (2021). Systematic, First Principle Study of Ambient Temperature Ferromagnetism and Elastic Anisotropy of Cubic Ca<sub>0.75</sub>TM<sub>0.25</sub>S (TM= Mn, Co, and Ni) Ternary Alloys: Using mBJ Functional. *Journal of Superconductivity and Novel Magnetism*, 34, 179-192.
- [40] Choutri, H., Ghebouli, M. A., Ghebouli, B., Bouarissa, N., Uçgun, E., & Ocak, H. Y. (2014). Spin-polarized investigation of ferromagnetism on magnetic semiconductors Mn<sub>x</sub>Ca<sub>1-x</sub>S in the rock-salt phase. *Materials Chemistry and Physics*, 148(3), 1000-1007.
- [41] Monir, M. E. A., Baltache, H., Khenata, R., Murtaza, G., Azam, S., Bouhemadou, A., & Ali, R. (2015). First-principles calculations of a half-metallic ferromagnet zinc blende Zn<sub>1-x</sub>V<sub>x</sub>Te. *Journal of Magnetism and Magnetic Materials*, 378, 41-49.
- [42] Sharma, G., Munjal, N., Vyas, V., Kumar, R., Sharma, B. K., & Joshi, K. B. (2013). Electron momentum density, band structure, and structural properties of SrS. *Journal of Experimental and Theoretical Physics*, 117, 747-753.

- [43] Kaneko, Y., & Koda, T. (1988). New developments in IIa–VIb (alkaline-earth chalcogenide) binary semiconductors. *Journal of Crystal Growth*, 86(1-4), 72-78.
- [44] Doumi, B., Mokaddem, A., Temimi, L., Beldjoudi, N., Elkeurti, M., Dahmane, F., & Ishak-Boushaki, M. (2015). First-principle investigation of half-metallic ferromagnetism in octahedrally bonded Cr-doped rock-salt SrS, SrSe, and SrTe. *The European Physical Journal B*, 88, 1-9.
- [45] Hamidane, O., Meddour, A., & Bourouis, C. (2019). First-principle predictions of electronic properties and half-metallic ferromagnetism in vanadium-doped rock-salt CaS. *Journal of Electronic Materials*, 48, 3276-3284.
- [46] J.C. Jamieson, Crystal structures at high pressures of metallic modifications of silicon and germanium, *Science* 139 (1963) 845–847.
- [47] Gilman, J. J. (1997). Chemical and physical “hardness”. *Materials Research Innovations*, 1(2), 71-76.
- [48] Zunger, A. (1986). Electronic structure of 3d transition-atom impurities in semiconductors. In *Solid State Physics* (Vol. 39, pp. 275-464). Academic Press.
- [49] Katayama-Yoshida, H. (1987). Spin-polarized electronic structure of interstitial 3d transition atom impurities in silicon. *International Journal of Modern Physics B*, 1(05n06), 1207-1247.
- [50] YAHI, H. (2016). *Etude des propriétés structurales, électroniques et magnétiques des semi-conducteurs magnétiques dilués Cd1–xCoxS et Cd1–xVxS* (Doctoral dissertation).
- [60] Sanvito, S., Ordejón, P., & Hill, N. A. (2001). First-principles study of the origin and nature of ferromagnetism in Ga 1– x Mn x As. *Physical Review B*, 63(16), 165206.
- [61] Hamidane, N., Baaziz, H., Ocak, H. Y., Baddari, K., Uğur, Ş., Uğur, G., & Charifi, Z. (2020). Ab initio full-potential study of the structural, electronic, and magnetic properties of the cubic Sr 0.75 Ti 0.25 X (X= S, Se, and Te) ternary alloys. *Journal of Superconductivity and Novel Magnetism*, 33, 3263-3272.
- [62] Wei, S. H., & Dalpian, G. M. (2008, February). Band coupling model of electron and hole mediated ferromagnetism in semiconductors: the case of GaN. In *Gallium Nitride Materials and Devices III* (Vol. 6894, pp. 85-95). SPIE.
- [63] Mac, W., Twardowski, A., Gaj, J. A., & Demianiuk, M. (1993). Ferromagnetic p-d exchange in Zn 1– x Cr x Se diluted magnetic semiconductor. *Physical review letters*, 71(14), 2327.
- [64] Yahi, H., Bourouis, C., & Meddour, A. (2020). First Principle Investigation on the Magnetism of Zinc Blende Structures of 3d (Cr, V, Mn, Cu, Sc)-Doped CdS. *Journal of Superconductivity and Novel Magnetism*, 33, 1917-1926.
- [65] Takahashi, K., Yoshikawa, A., & Sandhu, A. (2007). Wide bandgap semiconductors. *Verlag Berlin Heidelberg*.
- [66] Volonakis, G., Haghghirad, A. A., Milot, R. L., Sio, W. H., Filip, M. R., Wenger, B., ... & Giustino, F. (2017). Cs2InAgCl6: a new lead-free halide double perovskite with direct band gap. *The journal of physical chemistry letters*, 8(4), 772-778.

- [67] Lhermitte, C. R., & Sivula, K. (2019). Alternative oxidation reactions for solar-driven fuel production. *ACS Catalysis*, 9(3), 2007-2017.
- [68] Yu, X., Xu, X., Zhou, C., Tang, J., Peng, X., & Yang, S. (2006). Synthesis and luminescent properties of SrZnO<sub>2</sub>: Eu<sup>3+</sup>, M<sup>+</sup> (M= Li, Na, K) phosphor. *Materials Research Bulletin*, 41(8), 1578-1583.
- [69] Chang, S., Fu, J., Sun, X., Bai, G., Liu, G., Wang, K., ... & Tang, M. (2021). Tailoring Luminescent Properties of SrS: Ce by Modulating Defects: Sr-Deficiency and Na<sup>+</sup> Doping. *arXiv preprint arXiv:2111.11622*.
- [70] Yang, H. C., Gong, B. C., Liu, K., & Lu, Z. Y. (2018). The melilite-type compound (Sr<sub>1-x</sub>, Ax) <sub>2</sub>MnGe<sub>2</sub>S<sub>6</sub>O (A= K, La) being a room temperature ferromagnetic semiconductor. *Science bulletin*, 63(14), 887-891.
- [71] Madsen, G. K., Carrete, J., & Verstraete, M. J. (2018). BoltzTraP2, a program for interpolating band structures and calculating semi-classical transport coefficients. *Computer Physics Communications*, 231, 140-145.
- [72] Bardeen, J., & Shockley, W. J. P. R. (1950). Deformation potentials and mobilities in non-polar crystals. *Physical review*, 80(1), 72.
- [73] Bergqvist, L., Eriksson, O., Kudrnovský, J., Drchal, V., Korzhavyi, P., & Turek, I. (2004). Magnetic percolation in diluted magnetic semiconductors. *Physical Review Letters*, 93(13), 137202.
- [74] ASHCROFT, N., & MERMIN, N. (1976). Solid State Physics Harcourt College Publishers. *New York*.
- [75] Fox, M. (2002). Optical properties of solids. *American Journal of Physics*, 70(12), 1269–1270.
- [76] Shi, S., Ke, X., Ouyang, C., Zhang, H., Ding, H., Tang, Y., & Tang, W. (2009). First-principles investigation of the bonding, optical and lattice dynamical properties of CeO<sub>2</sub>. *Journal of Power Sources*, 194(2), 830-834.
- [77] Shaukat, A., Saeed, Y., Nazir, S., Ikram, N., & Tanveer, M. (2009). Ab initio study of structural, electronic and optical properties of Ca<sub>1-x</sub>Sr<sub>x</sub>S compounds. *Physica B: Condensed Matter*, 404(21), 3964-3972.
- [78] Sharma, S., Sharma, J., & Sharma, Y. (2016, May). DFT calculations of electronic and optical properties of SrS with LDA, GGA and mGGA functionals. In *AIP Conference Proceedings* (1728). AIP Publishing.
- [79] Singh, S., Maurya, R. K., & Pandey, S. K. (2016). Investigation of thermoelectric properties of ZnV<sub>2</sub>O<sub>4</sub> compound at high temperatures. *Journal of Physics D: Applied Physics*, 49(42), 425601.
- [80] Hou, X. Y., Cheng, Y., Hu, C. E., Piao, C. G., & Geng, H. Y. (2020). Thermoelectric properties of strontium sulfide via first-principles calculations. *Solid State Communications*, 305, 113755.
- [81] Mott, N. F. (1964). Electrons in transition metals. *Advances in Physics*, 13(51), 325-422.
- [82] Sharma, S., & Pandey, S. K. (2015). Applicability of two-current model in understanding the electronic transport behavior of inverse Heusler alloy: Fe<sub>2</sub>CoSi. *Physics Letters A*, 379(38), 2357-2361.

- [83] Rajput, K., & Roy, D. R. (2020). Structure, stability, electronic and thermoelectric properties of strontium chalcogenides. *Physica E: Low-dimensional Systems and Nanostructures*, 119, 113965.
- [84] Slack, G. A. (1973). Nonmetallic crystals with high thermal conductivity. *Journal of Physics and Chemistry of Solids*, 34(2), 321-335.
- [85] Julian, C. L. (1965). Theory of heat conduction in rare-gas crystals. *Physical Review*, 137(1A), A128.
- [86] Rosenberg, H. F. (2006). Interview with Dr. Nancy A. Lee and Dr. James J. Lee regarding Pivotal Advance: Eosinophil infiltration of solid tumors is an early and persistent inflammatory host response. *Journal of leukocyte biology*, 79(6), 1129-1130.
- [87] Marepalli, P., Mathur, S. R., & Murthy, J. Y. (2020). An unintrusive approach to the computation of derivatives: Applications in. *Thermal Behaviour and Applications of Carbon-Based Nanomaterials: Theory, Methods and Applications*, 181.
- [88] Malakkal, L., Szpunar, B., Siripurapu, R. K., Zuniga, J. C., & Szpunar, J. A. (2017). Thermal conductivity of wurtzite and zinc blende cubic phases of BeO from ab initio calculations. *Solid State Sciences*, 65, 79-87.

# Chapter 4

## Effect of Dimensionality Reduction on the Fe-Doped SrS Properties

*This part of the work is in progress.*

In the final chapter of this dissertation, we have studied the spin-resolved structural, electronic, and magnetic properties of  $\text{Sr}_{1-x}\text{Fe}_x\text{S}$  monolayers at different concentrations ( $x = 0, 0.125, 0.25, 0.50, 0.75,$  and  $1$ ). We have also compared the findings for these monolayers with those of their bulk counterparts, as examined in the initial section of Chapter 3, to get the effect of dimensionality reduction on the different properties.

### 1.1 Introduction

Two-dimensional (2D) materials have distinct properties that can differ significantly from their bulk counterparts due to their increased surface-to-volume ratio. This characteristic has provided a new foundation for hybrid device engineering, allowing us to explore and customize the materials' exceptional properties. Although extensive research is being conducted on the applications of 2D materials, many investigations are still in their early stages, and there remain numerous unresolved issues that require attention. In the realm of 2D materials, one of the most notable examples is monolayer graphene [1], which captured the significant interest of material scientists since 2004, as we discussed earlier in Chapter 1. The SrS structure, akin to graphene, exhibits a large indirect bandgap in the near-visible spectrum and a remarkably flat band in the upper valence band [2]. This rendered it particularly intriguing in the post-graphene era for various applications.

Keeping in view of these unique characteristics, in this chapter, we systematically investigate the structural, electronic and magnetic properties of SrS-to-FeS monolayers by varying the strontium ratio concentration using the powerful first-principle calculations. Until now, the study of  $\text{Sr}_{1-x}\text{Fe}_x\text{S}$  alloys has been limited to the bulk phase, as conducted for the first time in the previous chapter, with no prior

reports on the monolayer forms of  $\text{Sr}_{1-x}\text{Fe}_x\text{S}$  alloys. Therefore, this study will form a base for future theoretical and experimental investigations in this field.

## 1.2 Computational Details

The calculations presented in this chapter were performed using the Vienna Ab-initio Simulation Package (VASP) program [3, 4], within the Spin-Polarized Density Functional Theory (SPDFT) formalism and the Projector Augmented Wave (PAW) potential [5, 6]. The electron exchange-correlation functional was described by the Perdew-Burke-Ernzerhof (PBE) form of the generalized gradient approximation (GGA) [7]. To ensure accuracy, potential underestimations in bandgap and magnetic moment within GGA were cross-verified using the non-local Heyd-Scuseria-Ernzerhof hybrid functional (HSE06) [8]. In this approach, the electron-electron interaction was determined by a proportion of Hartree-Fock exchange with  $\alpha = 0.25$  and a default screening parameter of  $0.2 \text{ \AA}^{-1}$ .

To create  $\text{Sr}_{1-x}\text{Fe}_x\text{S}$  alloys, the Sr atoms were systematically replaced with Fe atoms in varying ratios ( $x$ ), corresponding to  $x = 0, 0.125, 0.25, 0.50, 0.75,$  and  $1$ . For each alloy ratio, all possible combinations of Fe atom in the SrS host matrix were considered to select the most stable configuration. To model the different crystal structures of the systems, a  $(2 \times 4 \times 1)$  supercell of 16 atoms containing one Fe atom for  $x = 0.125$  and a  $(2 \times 2 \times 1)$  supercell of 8 atoms containing one, two, and three Fe atoms for  $x = 0.25, 0.50, 0.75,$  respectively, were constructed based on a conventional SrS unit cell. Interlayer interactions between successive unit-cells were avoided by assuming a vacuum spacing of  $20 \text{ \AA}$ . A gamma scheme was used to sample the Brillouin zone (BZ), with a  $12 \times 12 \times 1$   $k$ -point mesh in the unit cells and scaled accordingly to  $6 \times 3 \times 1$  and  $6 \times 6 \times 1$   $k$ -point meshes, respectively, for the supercell simulations.

The ground state was optimized with an energy convergence criterion of  $10^{-5}$  eV between consecutive iterations. Additionally, the maximum Hellmann-Feynman force on each atom was constrained to be less than  $10^{-3}$  eV/ $\text{\AA}$  during ion relaxation. To ensure accuracy, a cutoff value of 500 eV for the plane-waves energy was employed.

For charge distribution analysis, Bader analysis [9] was applied to different concentrations. The dynamic stabilities of bare SrS and FeS monolayers were assessed via phonon band dispersion using the PHONOPY code [10]. A  $(5 \times 5 \times 1)$  supercell was used for each monolayer with a  $9 \times 9 \times 1$   $k$ -point mesh.

Ab-initio molecular dynamics simulation (AIMD) [11] was employed to investigate the thermal stabilities of the monolayers. This was conducted using a supercell of  $(6 \times 6 \times 1)$  for  $h$ -SrS and  $(5 \times 5 \times 1)$  for  $s$ -FeS at 300 K temperature, employing time steps of 1 fs.

### 1.3 Results and Discussion

#### 4.3.1 Structural Properties

The SrS monolayer is an atomically thin material, composed of a single layer with a unique planar hexagonal honeycomb lattice structure. This lattice is entirely constructed from Sr-S bonds, exhibiting space group N°187 that falls within the  $D_{3h}$  point group symmetry, akin to other well-studied monolayers like graphene, silicene, and BN. The unit cell of the SrS monolayer encompasses one Sr atom and one S atom.

In contrast, the FeS monolayer possesses a distinctive square crystal structure within the P4/mmm space group N°123. Its unit cell comprises a total of four atoms, including two Fe atoms and two S atoms. Figure 1 offers an illustrative representation of the top and side views of both the *h*-SrS and *s*-FeS configurations.

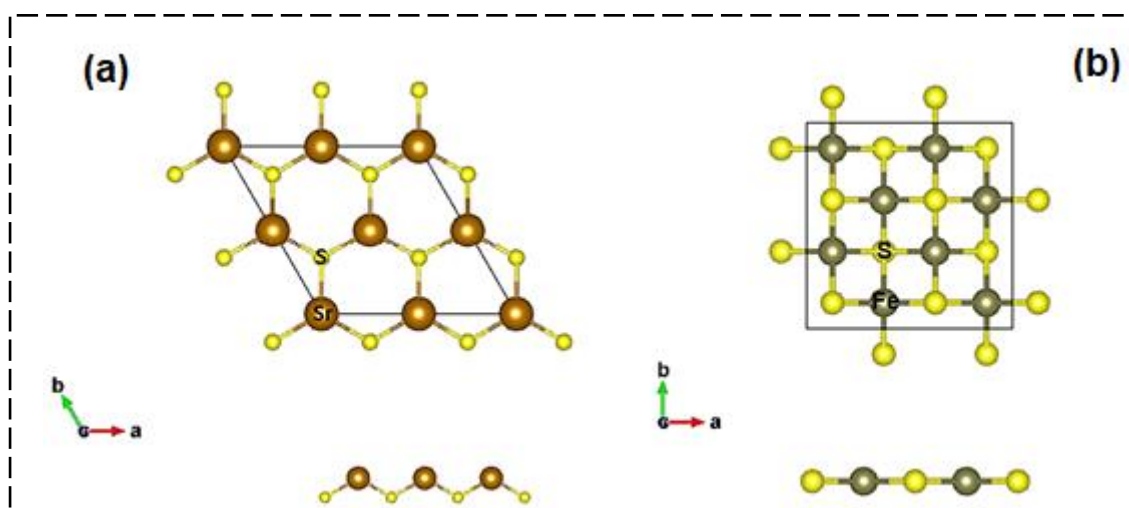


**Figure 1.** Top and side views of the repeated unit-cells of (a) the bare *h*-SrS and (b) *s*-FeS monolayers.

The structural parameters including the lattice parameters  $a$  (Å) and bond lengths  $d$  (Å) of the *h*-SrS and *s*-FeS are tabulated in Table 1. The lattice parameters were determined to be  $a = b = 4.837$  Å for *h*-SrS and 3.557 Å for *s*-FeS. On the other hand, the bond lengths were determined to be  $d_{Sr-S} = 2.793$  Å for *h*-SrS, and 2.150 Å for *s*-FeS. These values are in good agreement with those reported in the literature [12-15]. When comparing the lattice parameter of rock-salt SrS (6.059 Å) to its hexagonal structure, we observed that it is larger in bulk form than in monolayer form. This can be attributed to dimensionality reduction, where interatomic interactions result in a different equilibrium spacing compared to a monolayer.



**Table 1**

The equilibrium optimized structural parameters of bare  $h$ -SrS,  $s$ -FeS, and doped monolayers  $\text{Sr}_{1-x}\text{Fe}_x\text{S}$ : lattice constant ( $a$ ), shortest bond length ( $d$ ), formation energy ( $E_f$ ), and elastic constants ( $C_{ij}$ ).

Materials	$a=b$ (Å)	$d$ (Å)	$E_{for}$ (eV)	$C_{11}$ (N/m)	$C_{12}$ (N/m)	$C_{66}$ (N/m)
$h$ -SrS	4.837	2.793	-1.402	28.993	23.801	-
	4.76 <sup>a</sup>	2.75 <sup>a</sup>	-	-	-	-
	4.85 <sup>b</sup>	2.80 <sup>b</sup>	-	-	-	-
$\text{Sr}_{0.875}\text{Fe}_{0.125}\text{S}$	4.756	2.254	-1.176	-	-	-
$\text{Sr}_{0.75}\text{Fe}_{0.25}\text{S}$	4.581	2.283	-1.049	-	-	-
$\text{Sr}_{0.50}\text{Fe}_{0.50}\text{S}$	4.168	2.217	-0.454	-	-	-
$\text{Sr}_{0.25}\text{Fe}_{0.75}\text{S}$	4.085	2.232	-0.021	-	-	-
$s$ -FeS	3.557	2.150	-0.427	77.575	46.595	60.542
	3.56 <sup>c</sup>	2.16 <sup>c</sup>	-	-	-	-
	3.59 <sup>d</sup>	-	-	-	-	-

<sup>a</sup> Ref [12], <sup>b</sup> Ref [13], <sup>c</sup> Ref [14], <sup>d</sup> Ref [15].

We have evaluated the energy required for constructing the atomic assembly of both  $h$ -SrS and  $s$ -FeS monolayers by calculating the formation energy ( $E_f$ ) using the formula as indicated in Chapter 3.

The calculated  $E_f$  values are also indicated in Table 1. As it is seen from Table 1, the  $E_f$  values for  $h$ -SrS and  $s$ -FeS are both negative, indicating that the bare monolayers are exothermic and unlikely to decompose after formation. Moreover, the formation energy of  $h$ -SrS (-1.402 eV) is notably less than that of  $s$ -FeS (-0.427 eV), indicating that  $h$ -SrS provides a more favorable environment for doping compared to  $s$ -FeS. Hence, when preparing Fe-doped SrS samples, it is advisable to create an  $h$ -SrS environment to ensure efficient and effective doping in practical experiments.

Utilizing the Density Functional Perturbation Theory (DFPT) approach [16], we assessed the dynamic stability of the  $h$ -SrS and  $s$ -FeS monolayers by examining their phonon dispersions. In Figure 2, the phonon spectra are presented along high-symmetry lines in the first Brillouin zone. It is evident that the phonon branches do not exhibit any imaginary frequencies, indicating that both structures remain dynamically stable under ambient conditions. However, slight occurrences of negative frequencies can be addressed by further increasing the supercell size.

The phonon plots reveal that the  $h$ -SrS monolayer possesses six phonon branches, consisting of three acoustic and three optical branches. Conversely, the primitive cell of  $s$ -FeS, which contains four atoms, yields twelve phonon branches, comprising three acoustic and nine optical branches. The

maximum frequency in these monolayers reaches up to  $140\text{ cm}^{-1}$  for *h*-SrS and  $200\text{ cm}^{-1}$  for *s*-FeS, aligning with prior research findings [13, 14]. Our observations also indicate that the phonon spectra of both systems exhibit non-degeneracy along the directions of the Brillouin zone. Furthermore, we note an important phonon gap in the optical band, measuring approximately  $50\text{ cm}^{-1}$  and  $15\text{ cm}^{-1}$  for *h*-SrS and *s*-FeS, respectively.

Significantly, this phonon gap is most prominent in *h*-SrS and least in *s*-FeS, primarily attributed to disparities in the arrangement of atoms within their primitive cells. This phonon bandgap has the potential to enhance thermal conductivity through specific phonon-phonon scattering processes, suggesting that *s*-FeS may exhibit higher thermal conductivity compared to *h*-SrS.

Subsequently, Ab-initio Molecular Dynamics (AIMD) simulations were conducted to perform a comprehensive evaluation of the thermal stability of the materials. Figure 3 depicts the energy fluctuations of the *h*-SrS and *s*-FeS bare monolayers over a 3000 fs period at 300 K. The AIMD simulations revealed consistent energy values for the bare monolayers throughout the entire simulation duration. The minor energy fluctuations arise from the rippling effect induced by the increase in temperature (the change in energy interval is minimal). This observation strongly supports the assertion that both the *h*-SrS and *s*-FeS monolayers possess stable structures and exhibit good thermal stability at room temperature.

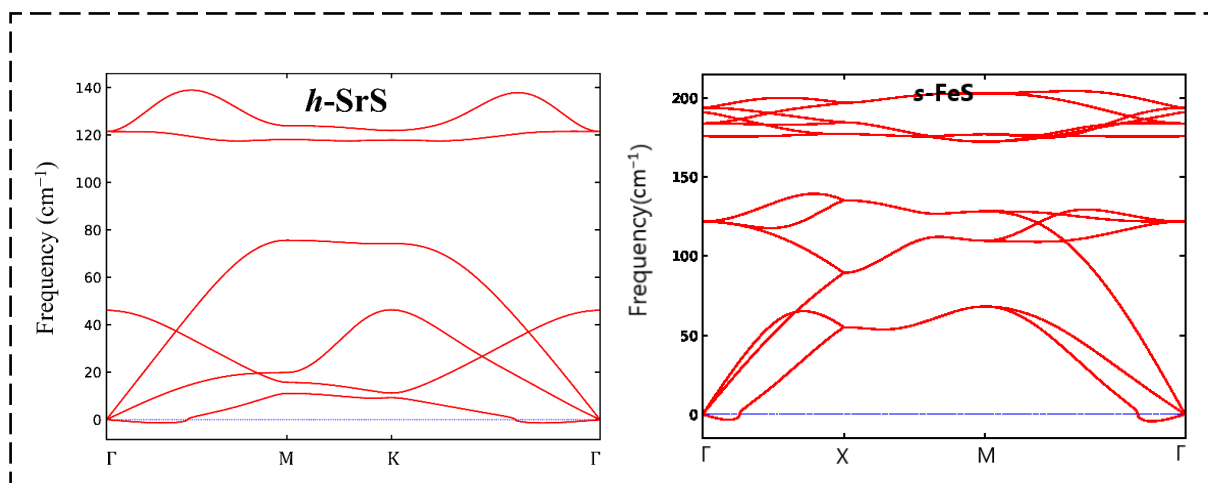


**Figure 2.** Phonon dispersion spectra of the bare *h*-SrS and *s*-FeS, respectively.

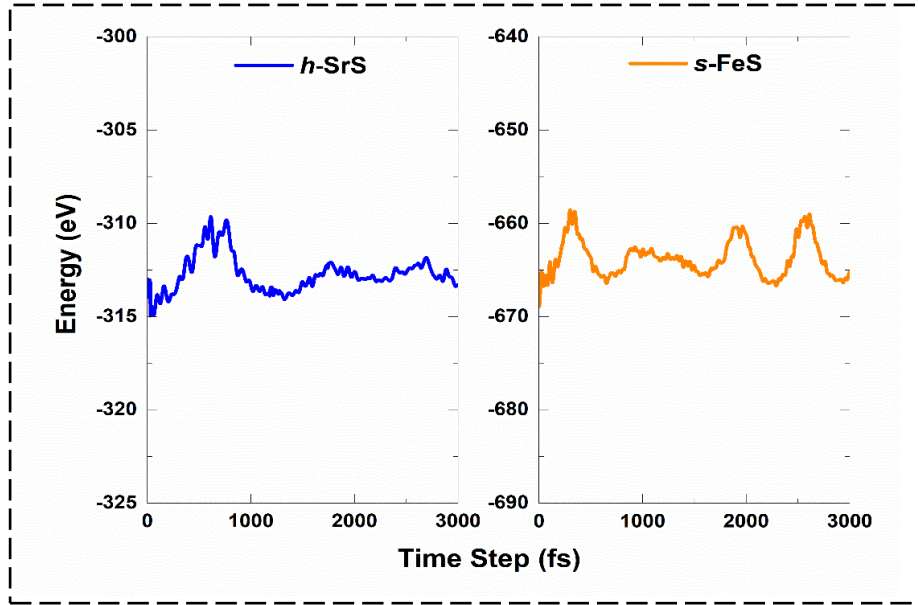


**Figure 3.** The variation of the total energy with time during AIMD simulation at 300k over a 3000 fs.

After confirming the thermodynamic, dynamic, and thermal stabilities of the pristine monolayers, we employed the widely recognized strain-energy approach [17, 18] to evaluate their mechanical stability.

By systematically varying the strain ratio ( $\varepsilon = \frac{a_i - a_0}{a_0}$ ,  $a_i$  and  $a_0$  indicate strained and strain-free lattice constants, respectively) within the range of  $-3\% \leq \varepsilon \leq 3\%$  with an incremental step size of 0.01, we acquired corresponding energy (E) values. The resulting E vs.  $\varepsilon$  data was fitted using a quadratic polynomial equation. This fitting process allowed us to extract the in-plane stiffness using the following equation:

$$C_{ij} = \frac{1}{A_0} \frac{\partial^2 E}{\partial^2 \varepsilon} \quad (\text{eq.1})$$

In this context,  $A_0$  denotes the equilibrium area of the system. A system is deemed mechanically stable when it adheres to the minimum Born criterion for elastic stability in 2D materials [19].

For hexagonal and square crystals, the mechanical stability criterion are the following [20]:

$$C_{11} > 0; \quad C_{11} > |C_{12}| \quad \text{for hexagonal structure} \quad (\text{eq.2})$$

$$C_{11} > 0; \quad C_{66} > 0; \quad C_{11} > |C_{12}| \quad \text{for square structure} \quad (\text{eq.3})$$

Upon reviewing the elastic constants detailed in Table 1, we can affirm their compliance with the aforementioned stability criteria, confirming hence the mechanical stability of these monolayers. It is worth noting that experimental validation and further theoretical investigations are still required to

validate these findings. Specifically, the elastic constant  $C_{11}$  measures a material's resistance to linear compression along the x direction [21]. Our computations revealed that the  $C_{11}$  values for the pristine monolayers are markedly elevated in comparison to the other elastic constants with the *s*-FeS boasts the highest value of 77.575 N/m, followed by *h*-SrS. This suggests that both systems are highly resistant to uniaxial stress in the x direction, and *s*-FeS is particularly highly incompressible in this direction due to its exceptionally large  $C_{11}$  value.

Following our previous work on bulk structures, we conducted spin-polarized computations involving the introduction of Fe atoms into the pure *h*-SrS structure at four key concentrations: 12.5%, 25%, 50%, and 75% Fe. In order to ensure energetically stable configurations for the resulting alloys, we explored various arrangements of the transition-metal atoms into the *h*-SrS monolayer for each alloy type, evaluating the total energy per atom. The most energetically stable configurations for each alloy are illustrated in Figure 4.

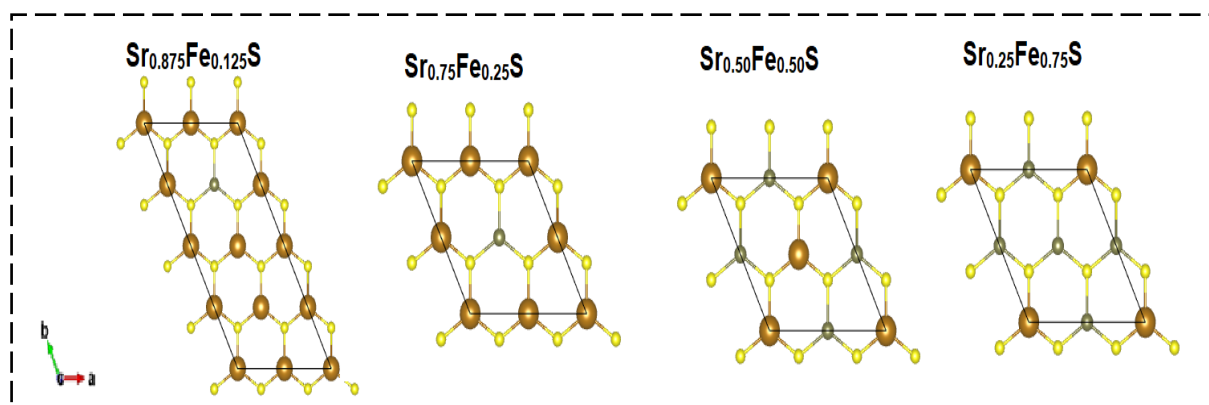


**Figure 4.** The ground-state configurations of predicted energetically stable  $\text{Sr}_{1-x}\text{Fe}_x\text{S}$  monolayers (Sr atom is designated by brown color, S by yellow, and Fe by grey).

After geometric optimization, it was observed that all the alloyed ground-state structures maintained their original hexagonal configuration, albeit with slight distortions in the shape of their unit cells. Table 1 furnishes detailed information on the lattice constants, formation energies, and bond lengths for the doped monolayer alloys. It is noteworthy that the lattice parameters consistently decrease with increasing Fe concentration in *h*-SrS. This reduction can be attributed to the disparity in ionic radii between Fe and Sr atoms. Additionally, they exhibit the same trend as their bulk counterparts, with a noticeable decrease in values from bulk to monolayer structure. This is also explained by the interatomic interactions resulting from the dimensionality reduction.

Concerning the bond lengths, the average distance between Fe and the nearest S atoms in the doped monolayers ranges from  $d_{\text{Fe-S}} = 2.217$  to  $2.283 \text{ \AA}$ , depending on the specific doping concentration. The Fe-S bonds in the doped monolayers experience compression compared to Sr-S bonds before doping.

This compression can be attributed to the relatively small difference in ionic radii between Fe and Sr atoms. However, it is noteworthy that the Fe-S bond length shows minimal variation with changes in the doping concentration, indicating the structural stability of the alloys.

The formation energy for the doped monolayers has also been computed utilizing the previously outlined formula from Chapter 3. The outcomes, detailed in Table 1, demonstrate that Fe atoms can be effectively incorporated into the monolayer *h*-SrS through an exothermic process. Upon examining the formation energies, a gradual increase is observed as the doping concentration escalates from 0.125 to 0.75. This pattern signifies that the *h*-SrS with 12.5% Fe doping displays the highest thermodynamic stability among the alloys, suggesting its most energetically favorable configuration.

Upon comparing the formation energies of monolayers to their bulk counterparts (please refer to Table 1 in Chapter 3), it becomes evident that the formation energies in 2D configurations are greater than those in 3D configurations. This leads to the conclusion that in a bulk structure, atoms establish more connections and form a higher number of bonds, ultimately resulting in increased binding energy and, consequently, lower formation energy. Moreover, the higher surface of 2D materials enables increased surface energy due to the incomplete coordination compared to the bulk counterparts; thereby contribute to a higher energy of formation.

Also in terms of comparison, the stability demonstrated through co-doping SrS: Fe with alkali metals surpasses that achieved by reducing its dimensionality. This highlights the pronounced effectiveness of co-doping method in enhancing stability in our specific case.

### 4.3.2 Electronic Properties and Bader Charge Analysis

#### 4.3.2.1 Band Structures Analysis

In Figure 5, we have depicted the band structures of both the pristine compounds and  $\text{Sr}_{1-x}\text{Fe}_x\text{S}$  monolayer alloys using the Heyd–Scuseria–Ernzerhof (HSE06) method. Additionally, we have tabulated the computed bandgap values for these compounds in Table 2, comparing them with those obtained via the GGA method. It is crucial to note that the GGA method, employed in our computational analysis, tends to underestimate the bandgap values of the materials under study. This tendency can potentially affect the precision of our findings, especially in characterizing the electronic and optical properties of the materials. To tackle this challenge, the HSE has emerged as a promising alternative due to its capability to offer more dependable and precise predictions of bandgap values.

From Figure 5, it is evident that the *h*-SrS exhibits the characteristics of a non-magnetic semiconductor, displaying an indirect bandgap of 2.825 eV within the GGA method and 3.861 eV within HSE, which aligns with earlier researches [12, 13]. Notably, the CBM is positioned at the  $\Gamma$  point of the

BZ, while the VBM is located at the M point. It is obvious when the dimensionality of SrS decreases from 3D to 2D; the bandgaps maintain indirect with the gap values increase from 3.435 eV using the mBJ to 3.861 eV using the HSE for 2D monolayer. This is expected as the lattice parameter demonstrates the opposite trend when transitioning from 3D to 2D.

In contrast, the electronic behavior of the *s*-FeS monolayer differs from that of *h*-SrS. The analysis reveals a metallic character, with the Fermi level intersecting both the valence and conduction bands, resulting in a non-magnetic metallic state according to both the GGA and HSE methods. These observations validate a previous study [14], underscoring the reliability and accuracy of the obtained results.

The introduction of Fe atoms through doping in the pristine *h*-SrS monolayer induces significant changes in its band structure. This doping introduces impurity levels within the initial bandgap, causing a notable shift in the electronic character towards a HSC character within the HSE. Notably, this alteration induced by doping leads to a distinct lowering of the position of the CBM.

As detailed in Table 2, within the GGA method, the bandgap diminishes from 2.825 eV in its pristine form to a range of 1.822–0.000 eV in up-spin channel and to 0.664–0.000 eV in down-spin channel, depending on the doping concentration of the Fe atoms. Similarly, the HSE method predicts a decrease in the bandgap from 3.861 eV to a range of 3.225–3.049 eV in up-spin channel and to 2.935–2.297 eV in down-spin channel.

The PBE results indicate that the HSC monolayers including,  $\text{Sr}_{0.875}\text{Fe}_{0.125}\text{S}$ ,  $\text{Sr}_{0.75}\text{Fe}_{0.25}\text{S}$ , and  $\text{Sr}_{0.50}\text{Fe}_{0.50}\text{S}$ , display total indirect bandgaps in [H- $\Gamma$ ], [K- $\Gamma$ ], and [ $\Gamma$ -K], respectively, while the  $\text{Sr}_{0.25}\text{Fe}_{0.75}\text{S}$  demonstrates metallic character.

However, under the application of the HSE method, it is observed that the  $\text{Sr}_{0.25}\text{Fe}_{0.75}\text{S}$  transition from a metal to HSC with a total direct bandgap of 2.263 eV in [ $\Gamma$ - $\Gamma$ ] direction, while the remaining alloys preserve their semiconducting properties within the same bandgap direction.

It is important to highlight that the effect of doping on the band structure, as observed with both the PBE and HSE methods, shows non-linear behavior with respect to the doping concentration. The variation of the total band gaps, defined as the smallest distance between the CBM and VBM of both spin channels, is tabulated in Table 2 and shown in Figure 6 for visualization.

The significant reduction in the bandgap of *h*-SrS after the incorporation of Fe atoms can be attributed to the hybridization between the orbitals of the Fe dopant atoms and the neighboring Sr/S atoms, as further explained by the partial density of states (PDOS) analysis in the following section.

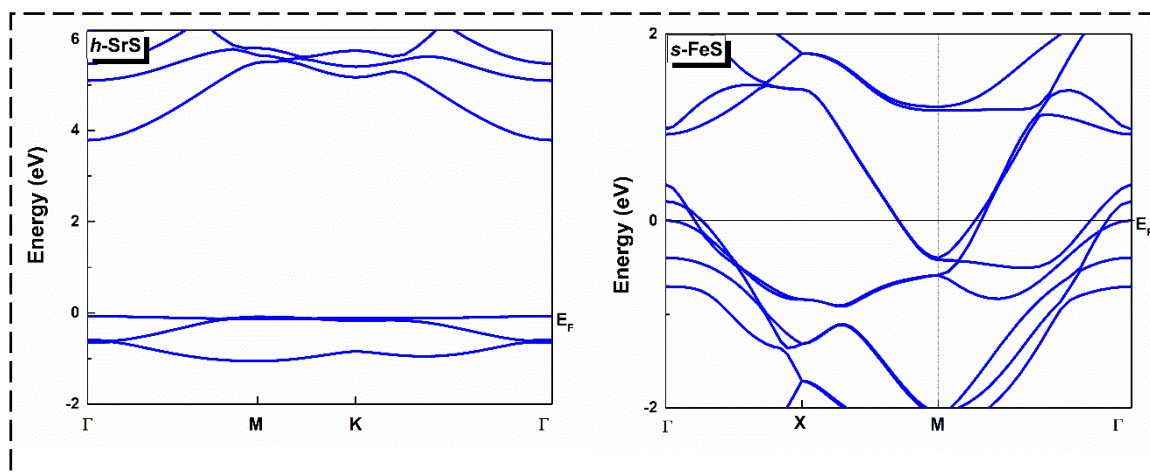
Comparing the results for doped monolayers with their bulk counterparts, we conclude that the reduction in dimensionality shifts the nature from HMF to HSC by creating a gap in the spin-down channel. In addition, the doped monolayers exhibit a particularly flat valence band, a typical feature of their 2D configurations. This flat valence band represents an important and advantageous feature to consider in thermoelectric applications.

#### 4.3.2.2 Bader Charge Analysis

Bader charge analysis provides valuable insights into the redistribution of electron charges within a material. Here, we performed Bader charge analysis to understand the partitioning of the total charge of the h-SrS monolayer into localized atomic charges after Fe dopant substitution. The results are summarized in Table 2.

The observed variation in charge transfer values is consistent with the corresponding trend of bandgap variation within the monolayers calculated using the GGA method. In the original h-SrS monolayer, both Sr and S atoms carry a net Bader charge of 1.236e, reflecting the electron transfer from Sr to S atoms caused by their different electronegativities. When doping with Fe atoms, the amount of charge transferred to the Fe atom varies from 0.399e to 0.575e to 0.609e to 0.268e for  $\text{Sr}_{0.875}\text{Fe}_{0.125}\text{S}$ ,  $\text{Sr}_{0.75}\text{Fe}_{0.25}\text{S}$ ,  $\text{Sr}_{0.50}\text{Fe}_{0.50}\text{S}$ , and  $\text{Sr}_{0.25}\text{Fe}_{0.75}\text{S}$ , respectively.

These values are lower than those in bare h-SrS, indicating a less robust interaction between Fe and the neighboring S atoms compared to that between Sr and S atoms. A reduced Bader interaction implies a weaker bond between the doped Fe ions and the neighboring atoms. This could possibly be due to changes in the electronic structure or atomic arrangement caused by the doping process.





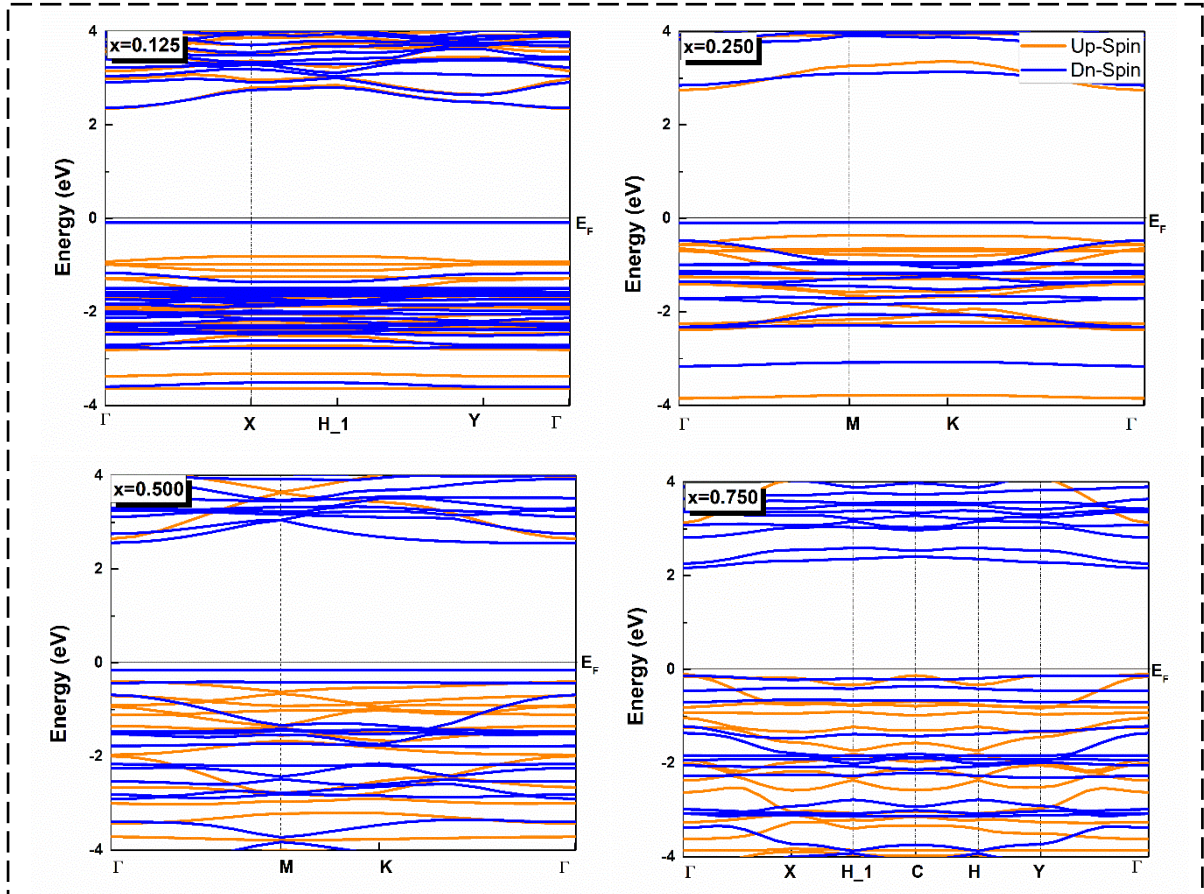


**Figure 5.** Spin-polarized electronic band structures of the bare *h*-SrS, *s*-FeS and  $\text{Sr}_{1-x}\text{Fe}_x\text{S}$  monolayer alloys calculated with the HSE06 method. The  $E_F$  is set to zero.

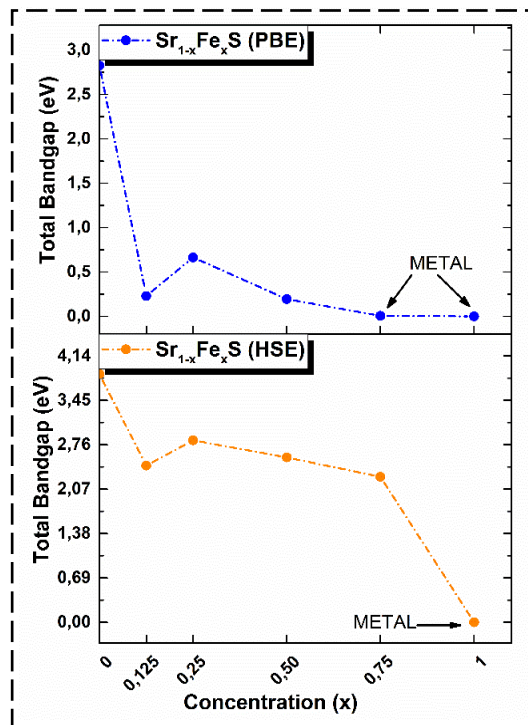


**Figure 6.** Visualization of the bandgap fluctuation of the bare *h*-SrS, *s*-FeS and  $\text{Sr}_{1-x}\text{Fe}_x\text{S}$  monolayer alloys.



**Table 2**

The calculated electronic properties of bare *h*-SrS, *s*-FeS, and doped monolayer alloys Sr<sub>1-x</sub>Fe<sub>x</sub>S, including bandgap values for up-spin channel, down-spin channel, and total gap within both PBE and HSE functionals, along with Bader charge ( $\Delta q$ ) transfer from Sr (Fe) to S atoms.

Materials	Up-spin channel		Dn-spin channel		Total gap		$\Delta q$ (e)	
	direction	Value(eV)	direction	Value(eV)	direction	Value(eV)		
<i>h</i> -SrS	PBE	[M- $\Gamma$ ]	2.825				1.236	
		[M- $\Gamma$ ] <sup>a</sup>	2.77 <sup>a</sup>					
		[M- $\Gamma$ ] <sup>b</sup>	2.54 <sup>b</sup>					
	HSE	[M- $\Gamma$ ]	3.860		[M- $\Gamma$ ]	3.860		
		[M- $\Gamma$ ]	3.74 <sup>b</sup>					
<b>Sr<sub>0.875</sub>Fe<sub>0.125</sub>S</b>	PBE	[X- $\Gamma$ ]	1.822	[H- $\Gamma$ ]	0.229	[H- $\Gamma$ ]	0,229	0.399
	HSE	[X- $\Gamma$ ]	3.154	[H- $\Gamma$ ]	2.451	[H- $\Gamma$ ]	2.435	
<b>Sr<sub>0.75</sub>Fe<sub>0.25</sub>S</b>	PBE	[M- $\Gamma$ ]	1.803	[K- $\Gamma$ ]	0.664	[K- $\Gamma$ ]	0.664	0.575
	HSE	[M- $\Gamma$ ]	3.105	[K- $\Gamma$ ]	2.935	[K- $\Gamma$ ]	2.830	
<b>Sr<sub>0.50</sub>Fe<sub>0.50</sub>S</b>	PBE	[ $\Gamma$ - $\Gamma$ ]	1.780	[ $\Gamma$ -K]	0.198	[ $\Gamma$ -K]	0.198	0.609
	HSE	[ $\Gamma$ - $\Gamma$ ]	3.050	[ $\Gamma$ -K]	2.564	[ $\Gamma$ -K]	2.564	
<b>Sr<sub>0.25</sub>Fe<sub>0.75</sub>S</b>	PBE	Metal		Metal		Metal	0.268	
	HSE	[ $\Gamma$ - $\Gamma$ ]	3.225	[ $\Gamma$ - $\Gamma$ ]	2.297	[ $\Gamma$ - $\Gamma$ ]		2.263
<i>s</i> -FeS	PBE	Metal				Metal	0.771	
		Metal <sup>c</sup>						
	HSE	Metal				Metal		

<sup>a</sup> Ref [12], <sup>b</sup> Ref [13], <sup>c</sup> Ref [14].

#### 4.3.2.3 Total and Partial Densities of States Analysis

The TDOS and PDOS of the bare *h*-SrS and *s*-FeS are visually depicted in Figure 7.

The analysis of the TDOS for the *h*-SrS bare monolayer clearly affirms its semiconducting nature. This is evident from the absence of energy states at the  $E_F$  level, signifying the presence of a bandgap between the CB and VB. Moreover, the examination reveals a distinct two peaks precisely situated at the VB edge at -0.117 eV and -0.932 eV, respectively, representing the highest occupied energy levels in the material. Further investigation via the PDOS clarifies that the VB arises mainly from the 3p<sub>z</sub> orbitals of S atom and a weak hybridization between the Sr: 5s-orbitals and the S: 3p<sub>x</sub>-orbitals, with the S orbitals providing the most substantial contributions. Conversely, the emergence of the CB in the

energy range of 3.860 to 6 eV is predominantly attributed to the 5s-orbitals of the Sr atoms, accompanied by a minor contribution of the S: 3p<sub>z</sub>-orbitals. These observations align with prior studies [13].

The TDOS of the *s*-FeS bare monolayer displays a different characteristic from that of *h*-SrS, within a sharp peak extending towards the CB edge giving a metallic character. Analysis of the PDOS of *s*-FeS reveals that the VB in the energy range from -6 eV to 4 eV is dominated by both the S: p-orbitals and the Fe: d-orbitals, within the highest contribution coming from the S: 3p<sub>z</sub> and Fe: 3d<sub>x<sup>2</sup>-y<sup>2</sup></sub>-states

In the energy range from -3.5 eV to 2.5 eV, the contribution of the S: p-states decreases and Fe: d-states dominate. Specifically, Fe: 3d<sub>xy</sub> dominates in the energy range of -3.5 eV to -2 eV, while Fe: 3dz<sup>2</sup> and Fe: 3dx<sup>2</sup>-y<sup>2</sup> dominate in the energy range of -2 eV to 1 eV, intersecting the E<sub>F</sub> level. This confirms the metallic characteristic exhibited by this bare monolayer. From 1 eV to 2.5 eV, both Fe: 3d<sub>xy</sub> and Fe: 3dz<sup>2</sup> are dominant. A minor contribution in this range comes from the S: 3p<sub>z</sub>. These findings are in agreement with the results presented in reference [14].

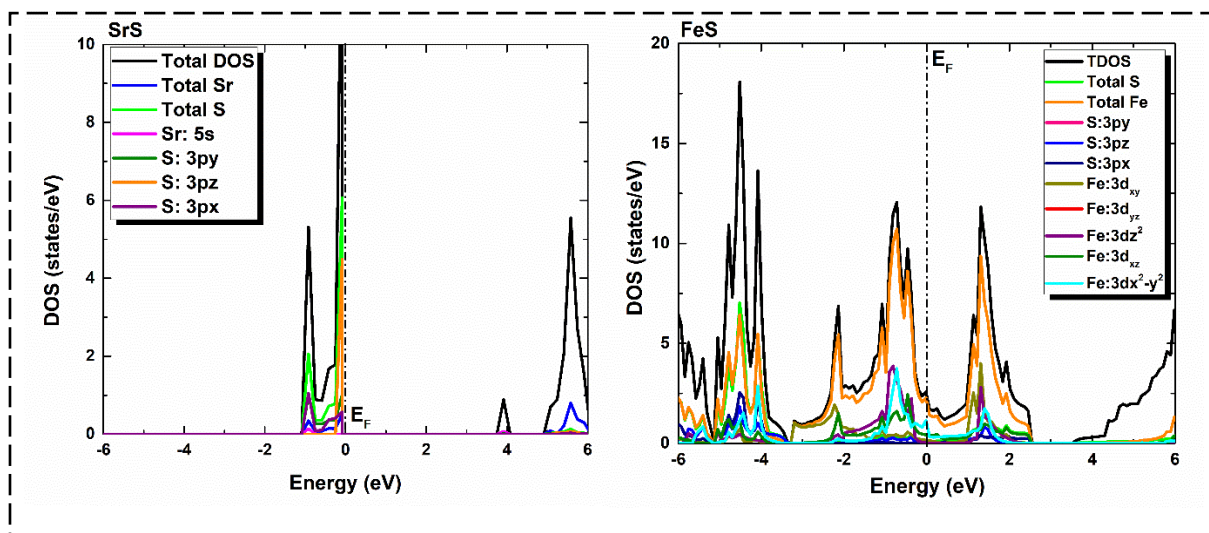


**Figure 7.** Electronic total (TDOS) and partial (PDOS) densities of states of the bare *h*-SrS and *s*-FeS monolayers.

The TDOS and PDOS of the ternary-doped monolayers at different concentrations are displayed in Figures 8 and 9, respectively.

Looking carefully at these numbers, the disparity between spin-up and spin-down TDOS in the Sr<sub>1-x</sub>Fe<sub>x</sub>S monolayers is striking. This asymmetry is in perfect agreement with the ferromagnetic ground states of all systems and confirms their magnetic nature. Furthermore, the presence of the impurity states in the minority VB, located in close proximity to the E<sub>F</sub>, confirms their *p*-type character even after doping with impurities, which is fundamental for enabling a wide range of electronic devices and technologies.

Specifically, in the majority-spin, the Fe: 3d states and S: 3p states of the four compounds hybridize with each other. This leads to the preservation and reduction of the bandgap compared to that of the bare  $h$ -SrS. In the minority-spin, the  $p$ - $d$  hybridization also shifts the 3d-Fe and 3p-S states towards the  $E_F$ , while maintaining the bandgap. This results in a distinctly HSC character for these compounds. This behavior is definitely different from that of their bulk counterparts, where the  $p$ - $d$  hybridization and the emergence of 3d states in the minority states at  $E_F$  lead to a HMF character with 100% spin-polarization.

We come to a very important conclusion in our case that is by reducing the symmetry in 2D monolayer form we can drastically change the character of the compounds.

It is also evident from the Figure 8 that with increasing the concentration of the Fe impurities from 12.5% to 75%, respectively, the  $p$ - $d$  hybridization become notably pronounced and the 5s states effect decreases, which aligns also with the bulk results.

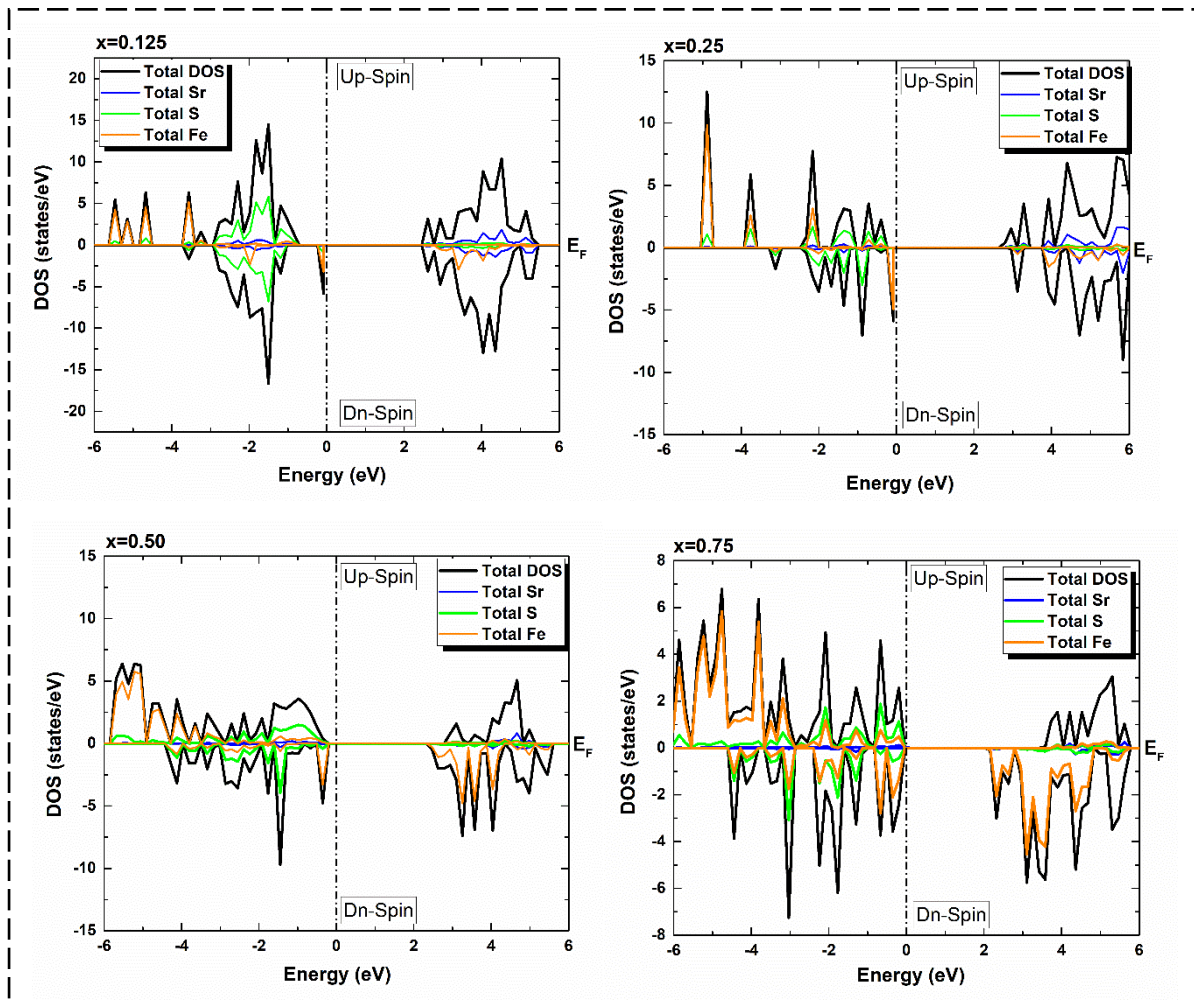


**Figure 8.** Electronic TDOS of  $\text{Sr}_{1-x}\text{Fe}_x\text{S}$  ( $x = 0.125, 0.25, 0.50, \text{ and } 0.75$ ) monolayer alloys. The positive and negative values represent the spin-up and spin-down channels, respectively.

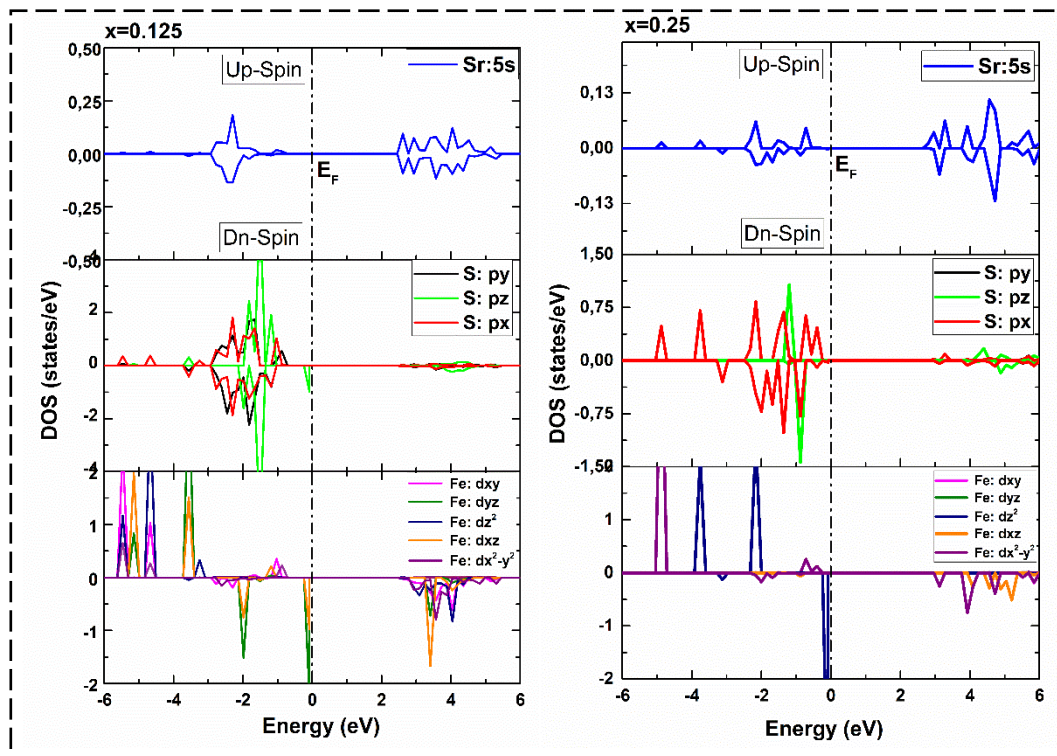
We further analyzed the PDOS of the monolayer alloys and plotted them in Figure 9. The analysis of the curves revealed that, for the  $\text{Sr}_{0.875}\text{Fe}_{0.125}\text{S}$  compound, the majority-spin VB, in the energy range of  $\sim -5$  eV to  $\sim -1$  eV is primarily derived from the  $3p_x$  and  $3p_z$  states of S atoms, and the  $3d_{xz}$ ,  $3d_{yz}$ , and  $3d_{z^2}$  of the Fe atoms, with a minor contribution coming from the 5s-states of the Sr atoms. As the Fe content reaches 25%, 50%, and 75 % Fe, the  $3d_{yz}$  and  $3d_{xz}$  of Fe atom increase and become dominant compared to the  $3p_x$  and  $3p_z$  states of S atoms and 5s-states of the Sr atoms, which decrease with increasing the concentration.

In the majority-spin CB, in the energy range of  $\sim -3$  eV to around  $\sim 6$  eV, the Sr: 5s become dominant through all the four concentrations, with a small contributions coming from  $3p_z$  and  $3p_x$  of the S atoms.

For the minority-spin channel, the VB is mainly dominated by the S:  $3p_x$  and S:  $3p_z$  states and the VBM at around -1 eV is dominated by Fe:  $3d_{xz}$  and Fe:  $3d_{yz}$  states for 12.5% Fe, by the Fe:  $3d_{z^2}$  states for 25% Fe, the Fe:  $3d_{z^2}$  states for 50% Fe, and by the Fe:  $3d_{z^2}$  and Fe:  $3d_{yz}$  for 75% Fe.

The CB on the other side, in the energy range of  $\sim -3$  eV to  $\sim 5$  eV, is dominated by the Fe:  $3d_{xz}$  states and the Fe:  $3dx^2-y^2$  and a little contribution coming from the 5s states of the Sr.

Overall, the impact of the  $p$ - $d$  hybridization on the electronic behavior is even seen at low-dimensionality, underscoring the significance of this phenomenon in influencing the bandgap and changing the character of materials.





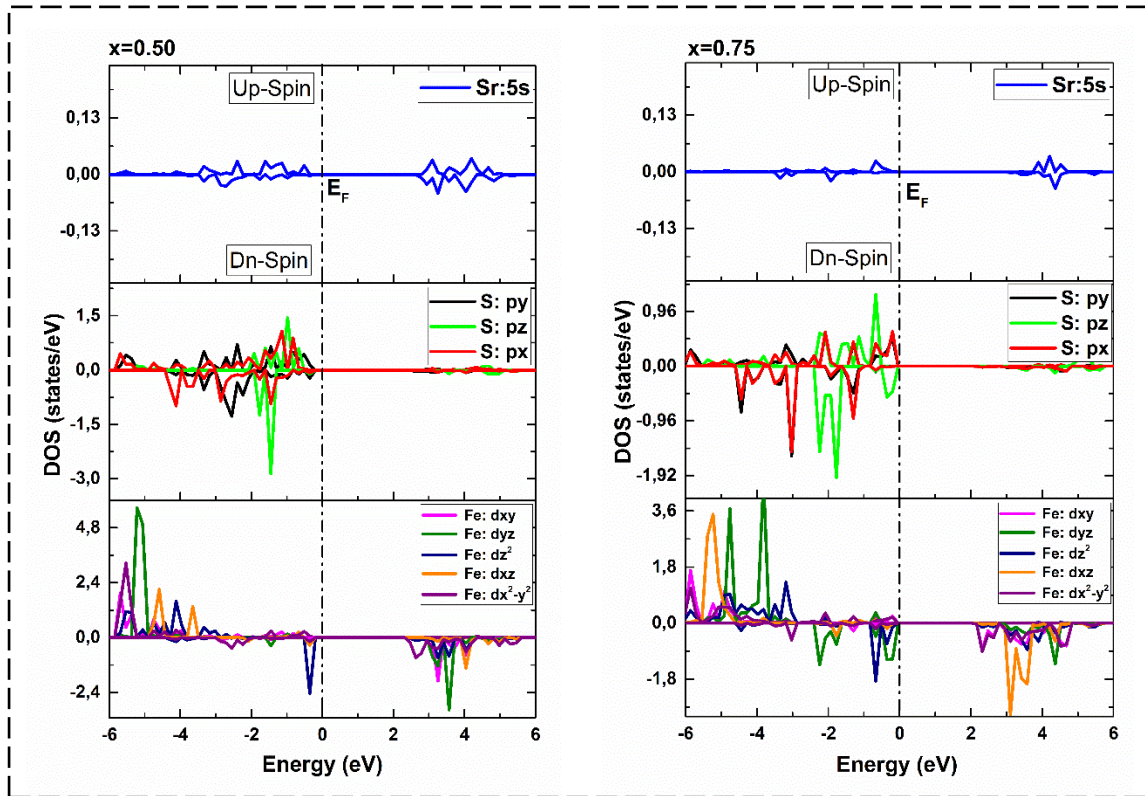


**Figure 9.** Electronic PDOS of  $\text{Sr}_{1-x}\text{Fe}_x\text{S}$  ( $x=0.125, 0.25, 0.50, \text{ and } 0.75$ ) monolayer alloys.

### 4.3.3 Magnetic Properties

The magnetic properties of the Fe-doped  $h$ -SrS monolayer alloys are evaluated based on their magnetic moments, and the outcomes are presented in Table 3.

The results revealed an integer value of the magnetic moment ( $M_{\text{TOT}}$ ) of  $4\mu_{\text{B}}$  per supercell across all concentrations. These findings align with the bulk structure results reported earlier in Table 5 of Chapter 3. The distribution of magnetic moments within the  $\text{Sr}_{1-x}\text{Fe}_x\text{S}$  monolayers conforms to Hund's rule and crystal field theory. Interaction with neighboring S ions induces a crystal field splitting, causing the  $3d$ -orbitals of the transition metal atom Fe to separate into distinct energy levels. In this context, the trigonal-bipyramidal arrangement of Fe introduces a symmetry that can be depicted using the  $D_{3h}$  point group. These levels encompass a non-degenerate orbital ' $a$ ' ( $dz^2$ ), a two-fold degenerate orbital ' $eg_1$ ' ( $d_{xy}$  and  $d_{x^2-y^2}$ ), and another two-fold degenerate orbital ' $eg_2$ ' ( $d_{xz}$  and  $d_{yz}$ ), as illustrated in Figure 10.

In the spin-up configuration of  $\text{Fe}^{2+}$  ( $d^6$ ), the ' $a$ ', ' $eg_1$ ', and ' $eg_2$ ' orbitals are situated below the  $E_{\text{F}}$  level and are fully occupied, while the ' $a$ ' orbital in the spin-down channel lies above the  $E_{\text{F}}$ . This electronic configuration can be represented as  $a \uparrow \downarrow eg_2 \uparrow \uparrow eg_1 \uparrow \uparrow$ , resulting in a  $M_{\text{TOT}}$  of  $4\mu_{\text{B}}$ .

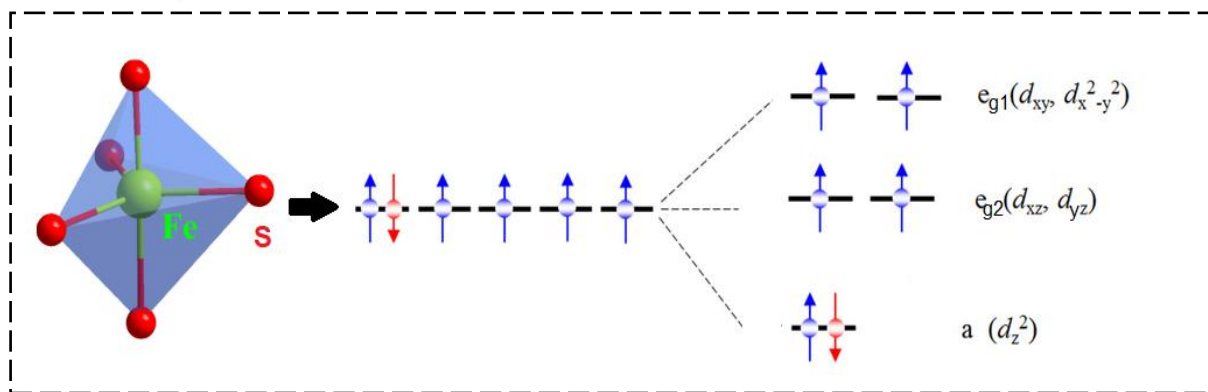


**Figure 10.** Schematic diagram representation of the crystal field splitting of the  $\text{Fe}^{2+}$  sites. Modified from [22].

Upon comparing the  $M_{\text{TOT}}$  per supercell with the local magnetic moments per atom (Table 3), it becomes evident that the primary contribution to the magnetic moment arises from the Fe atom, affirming the findings presented in the PDOS analysis. Smaller magnetic moments are attributed to the nearest neighboring Sr and S atoms, which exhibit ferromagnetic coupling with their adjacent Fe atoms due to their positive signs.

Furthermore, it was observed that the local magnetic moment of Fe displays a linear variation, where it increases with increasing doping concentration from 12.5% to 75%. This behavior suggests a strong interaction between the Fe dopants and the adjacent surrounding atoms, reinforcing the ferromagnetic order in these monolayers. It should be mentioned that this trend differs from that of the bulk structures, where the  $M^{\text{Fe}}$  shown a decrease with concentration increasing. This may be also attributed to the difference in the arrangement of the atoms and how they interact in 2D monolayer structure, where there are fewer neighboring atoms, compared to the bulk structure.

**Table 3**

Total magnetic moment ( $M_{\text{TOT}}$ ) and local magnetic moment on each Sr, S, and Fe atoms of  $\text{Sr}_{1-x}\text{Fe}_x\text{S}$  ( $x = 0.125, 0.25, 0.50,$  and  $0.75$ ) monolayer alloys.

Concentration (x)	$M^{\text{tot}} (\mu_{\text{B}})$	$M^{\text{Fe}} (\mu_{\text{B}})$	$M^{\text{Sr}} (\mu_{\text{B}})$	$M^{\text{S}} (\mu_{\text{B}})$
<b>0.125</b>	4.000	3.545	0.005	0.028
<b>0.250</b>	4.000	3.555	0.011	0.035
<b>0.500</b>	4.000	3.556	0.028	0.051
<b>0.750</b>	4.000	3.587	0.089	0.037

## 1.4 Conclusion

In this chapter, we have done a spin-resolved ab-initio study of the 2D monolayer form of  $\text{Sr}_{1-x}\text{Fe}_x\text{S}$  ( $x = 0, 0.125, 0.25, 0.50, 0.75, \text{ and } 1$ ) ordered alloys using a plane-wave pseudopotential DFT method within the VASP code. This study involved a comprehensive investigation of the effect of dimensionality reduction on different properties including the structural, electronic, and magnetic properties. The principle outcomes and conclusions are outlined as follows:

1. The outcomes of formation energies, molecular dynamics simulations, and elastic stiffness constants indicated that each of the examined bare materials, SrS (FeS), is energetically favorable and remained thermally and mechanically stable under ambient conditions. Phonon spectra calculations further demonstrated that both materials exhibited dynamic stability in their lattice structures. In terms of ground state results, it is found that SrS maintained stability in a hexagonal structure akin to graphene, while FeS shown a preference for a square structure, aligning with prior theoretical studies. When Fe impurities were introduced in the Sr-sites through doping, all four monolayers retained their structural and thermodynamic stability in the hexagonal form, as confirmed by the formation energy. Upon comparing the formation energies, it is determined that the *h*-SrS system with 12.5% Fe doping displayed the lowest energy among the doped cases, indicating its most stable composition.
2. The electronic properties analysis confirmed that both the PBE and HSE06 methods identified the bare monolayer *h*-SrS as a non-magnetic semiconductor with an indirect bandgap. On the other hand, the *s*-FeS system was identified as a non-magnetic metal. Concerning compositions, according to PBE results, three compounds namely,  $\text{Sr}_{0.875}\text{Fe}_{0.125}\text{S}$ ,  $\text{Sr}_{0.75}\text{Fe}_{0.25}\text{S}$  and  $\text{Sr}_{0.50}\text{Fe}_{0.50}\text{S}$  exhibited the behavior of HSCs, while  $\text{Sr}_{0.25}\text{Fe}_{0.75}\text{S}$  behaved as a metal. However, when the HSE06 method was applied,  $\text{Sr}_{0.25}\text{Fe}_{0.75}\text{S}$  transformed into a HSC with a direct bandgap in both spin-directions, while the other alloys maintained their semiconducting properties with an enhancement in bandgap values. We have concluded that the dimensionality affected the electronic character of these compounds that shown the HMF in bulk form.
3. In all doped monolayers, we calculated a total magnetic moment of  $4 \mu_B$ , which is consistent with the bulk structures. Additionally, low local magnetic moments on the non-magnetic sites were generated due to the *p-d* hybridization. We also observed that the local magnetic moments on Fe sites increased with increasing concentration, contrary to their bulk counterparts, confirming the strong ferromagnetic character at low dimension.

## References for Chapter 4

- [1] Novoselov, K. S., Geim, A. K., Morozov, S. V., Jiang, D. E., Zhang, Y., Dubonos, S. V., & Firsov, A. A. (2004). Electric field effect in atomically thin carbon films. *Science*, 306(5696), 666-669.
- [2] Feng, B., Ding, Z., Meng, S., Yao, Y., He, X., Cheng, P., & Wu, K. (2012). Evidence of silicene in honeycomb structures of silicon on Ag (111). *Nano letters*, 12(7), 3507-3511.
- [3] Blöchl, P. E. (1994). Projector augmented-wave method. *Physical review B*, 50(24), 17953.
- [4] Kresse, G., & Joubert, D. (1999). From ultrasoft pseudopotentials to the projector augmented-wave method. *Physical review b*, 59(3), 1758.
- [5] Kresse, G., & Furthmüller, J. (1996). Efficiency of ab-initio total energy calculations for metals and semiconductors using a plane-wave basis set. *Computational materials science*, 6(1), 15-50.
- [6] Kresse, G., & Furthmüller, J. (1996). Efficient iterative schemes for ab initio total-energy calculations using a plane-wave basis set. *Physical review B*, 54(16), 11169.
- [7] Perdew, J. P., Burke, K., & Ernzerhof, M. (1996). Generalized gradient approximation made simple. *Physical review letters*, 77(18), 3865.
- [8] Heyd, J., Scuseria, G. E., & Ernzerhof, M. (2003). Hybrid functionals based on a screened Coulomb potential. *The Journal of chemical physics*, 118(18), 8207-8215.
- [9] Bader, R. F. W., Popelier, P. L. A., & Keith, T. A. (1994). Theoretical definition of a functional group and the molecular orbital paradigm. *Angewandte Chemie International Edition in English*, 33(6), 620-631.
- [10] Jeong, H. Y., Lee, J. H., & Hayes, K. F. (2008). Characterization of synthetic nanocrystalline mackinawite: crystal structure, particle size, and specific surface area. *Geochimica et cosmochimica acta*, 72(2), 493-505.
- [11] Rapaport, D. C. (2004). *The art of molecular dynamics simulation*. Cambridge university press.
- [12] Zheng, H., Li, X. B., Chen, N. K., Xie, S. Y., Tian, W. Q., Chen, Y., & Sun, H. B. (2015). Monolayer II-VI semiconductors: A first-principles prediction. *Physical Review B*, 92(11), 115307.
- [13] Lin, H. F., Lau, W. M., & Zhao, J. (2017). Magnetism in the p-type Monolayer II-VI semiconductors SrS and SrSe. *Scientific Reports*, 7(1), 45869.
- [14] Bafekry, A., Abdolhosseini Sarsari, I., Faraji, M., Fadlallah, M. M., Jappor, H. R., Karbasizadeh, S., Nguyen, V., & Ghergherehchi, M. (2021). Electronic and magnetic properties of two-dimensional of FeX (X= S, Se, Te) monolayers crystallize in the orthorhombic structures. *Applied Physics Letters*, 118(14), 143102.
- [15] Sukhanova, E. V., Baidyshev, V. S., Manakhov, A. M., Al-Qasim, A. S., & Popov, Z. I. (2023). Hydrogen production from H<sub>2</sub>S on metal-doped FeS Mackinawite monolayer via DFT calculations. *Applied Surface Science*, 609, 155322.



- [16] Gonze, X., & Lee, C. (1997). Dynamical matrices, Born effective charges, dielectric permittivity tensors, and interatomic force constants from density-functional perturbation theory. *Physical Review B*, 55(16), 10355.
- [17] Topsakal, M., Cahangirov, S., & Ciraci, S. (2010). The response of mechanical and electronic properties of graphane to the elastic strain. *Applied Physics Letters*, 96(9).
- [18] Şahin, H., Cahangirov, S., Topsakal, M., Bekaroglu, E., Akturk, E., Senger, R. T., & Ciraci, S. (2009). Monolayer honeycomb structures of group-IV elements and III-V binary compounds: First-principles calculations. *Physical Review B*, 80(15), 155453.
- [19] Born, M., Huang, K., & Lax, M. (1955). Dynamical theory of crystal lattices. *American Journal of Physics*, 23(7), 474-474.
- [20] Shen, D., Zhao, B., Zhang, Z., Zhang, H., Yang, X., Huang, Z., & Duan, X. (2022). Synthesis of group VIII magnetic transition-metal-doped monolayer MoSe<sub>2</sub>. *ACS nano*, 16(7), 10623-10631.
- [21] Gao, X., Jiang, Y., Zhou, R., & Feng, J. (2014). Stability and elastic properties of Y–C binary compounds investigated by first principles calculations. *Journal of Alloys and Compounds*, 587, 819-826.
- [22] Wang, W., Wang, H., Xu, X., Zhu, L., He, L., Wills, E., & Xu, X. (2012). Crystal field splitting and optical bandgap of hexagonal LuFeO<sub>3</sub> films. *Applied Physics Letters*, 101(24), 241907.

# General Conclusion and Future Perspectives

In the pursuit of new materials aimed at optimizing energy usage, advancing information storage, and promoting sustainability, spintronics, optoelectronics, and thermoelectrics have captured significant attention from researchers, being regarded as pivotal technologies for the future. Identifying materials with the requisite properties for effective application across these three domains proves to be a challenging task, owing to the specific criteria set by material properties. Presently, there exists a pressing need to develop new materials that are both more abundant, less harmful, and more cost-effective than their current counterparts. In light of this, the research approach has focused on enhancing the different properties of materials that already exhibit good ferromagnetic properties for spintronics.

Dilute magnetic semiconductors (DMSs), the building blocks of spintronics, can be obtained by doping transition metals into semiconductor host matrices. Due to their high Curie temperature, low cost, ease of synthesis, and high electrical conductivity, iron (Fe) transition metal atoms are a great option for ferromagnetic dopants used in this dissertation to improve host matrix properties.

Advances in theories and improvement of computational methods such as density functional theory (DFT) in recent years have led to significant advances in the understanding and analysis of the physical properties of materials. The work of this dissertation relied on theoretical research using ab-initio calculations to contribute to the study of new materials desirable for the above applications.

First, we investigated the structural, mechanical, electronic and magnetic properties of  $\text{Sr}_{1-x}\text{Fe}_x\text{S}$  compounds ( $x = 0, 0.125, 0.25, 0.50$  and  $0.75$ ) using the FP-LAPW method and the implemented PBE/PBE+mBJ approximations in the WIEN2K code. Our aim was to understand the influence of Fe doping on various properties of binary SrS and to explore new potential semi-metallic ferromagnets (HMF) for spintronic applications. Examination of the structural properties revealed that these materials were more stable in the ferromagnetic (FM) phase than in the anti-ferromagnetic (AFM) and non-magnetic (NM) phases. The formation energies indicated their thermodynamic stability. An increase in Fe concentration led to a decrease in the lattice parameter  $a$  (Å), accompanied by an increase in the hardness  $B$  (GPa). Analysis of their mechanical properties showed that they were mechanically stable and showed greater resistance to unidirectional compression than to shear deformation. They showed high anisotropy and were stiffer in the [100] direction. They can be classified as ductile compounds. They also exhibited

ionic bonding nature and resist high temperature treatment. For the selected concentrations, the DMSs  $\text{Sr}_{1-x}\text{Fe}_x\text{S}$  ( $x = 0.125, 0.25$  and  $0.50$ ) showed a total magnetic moment of  $4 \mu_B$  and a ferromagnetic half-metallic character (HMF) due to the strong  $p$ - $d$  hybridization, making them good candidates for spintronics. In contrast,  $\text{Sr}_{1-x}\text{Fe}_x\text{S}$  ( $x=0.75$ ) showed a metallic character. Based on the obtained negative and positive exchange constants  $N_{0\alpha}$  and  $N_{0\beta}$ , it was observed that the exchange coupling between the valence band of SrS and Fe- $3d$  states is anti-ferromagnetic, whereas between the conduction band of SrS and Fe- $3d$  states, the exchange coupling is a mixture of ferromagnetic and anti-ferromagnetic.

The next step was to enhance the properties of these materials to make them more efficient. Co-doping and dimensionality reduction were the two methods used to accomplish this.

The study of co-doping initially involved selecting the dopant concentration at  $x = 0.125$  and incorporating the alkali metals Li, Na, and K alongside Fe. This was consistently done using the PBE/PBE+mBJ as incorporated in the WIEN2K code, complemented by the Boltzmann transport equations integrated into the BoltzTrap code. The investigation encompassed structural, electronic, and magnetic properties of the quaternaries with the formula  $\text{Sr}_{0.875}\text{Fe}_{0.06}\text{p}^0_{0.06}\text{S}$  ( $\text{p}^0 = \text{Li, Na, and K}$ ), followed by an examination of their optical and thermoelectric properties. The outcomes regarding structural properties revealed a gradual increase in lattice constant with atomic number ( $Z$ ), coupled with a progressive decrease in bulk modulus. Introducing alkali metal in SrS: Fe proved instrumental in maximizing the system's overall stability and reinforcing ionic bonds. Calculations of total energy differences ( $\Delta E$ ) affirmed the stability of the systems in the ferromagnetic state, with a notably higher Curie temperature ( $T_c$ ) observed compared to room temperature (RM). Notably, SrS: (Fe, K) exhibited the highest  $T_c$  among these co-doped systems. Examination of the electronic and magnetic properties revealed that all materials exhibited  $p$ -type semiconductor behavior (HSCs). In particular, it was observed that the energy gap in the co-doped systems was smaller compared to the SrS:Fe compound. A total magnetic moment of  $5 \mu_B$  was calculated, which represents an increase compared to mono-doping, and a small local magnetic moment was generated at the non-magnetic sites due to the  $sp$ - $d$  hybridization. Examination of the optical properties, including real and imaginary parts of the dielectric function, absorption coefficient, and optical conductivity, revealed that each of the three alkali metal ions contributed to enhanced infrared absorption in the SrS: Fe system and the formation of new peaks in the visible spectrum. Such a property significantly increases the suitability of these materials for applications in solar cells. Finally, the analysis of thermoelectric properties, in terms of Seebeck coefficient, electrical conductivity, thermal conductivity and merit factor, highlighted the exceptional performance of the  $p$ -type ZT values compared to their  $n$ -type and mono-doped counterparts and exceeded them 1 at 1200 K. This makes them promising candidates for high-temperature thermoelectric applications.

The dimensionality reduction method involved reducing the dimension of the ternary compounds  $\text{Sr}_{1-x}\text{Fe}_x\text{S}$  ( $x = 0, 0.125, 0.25, 0.50, 0.75,$  and  $1$ ) from their 3D bulk structures to their 2D monolayer

counterparts using a plane-wave pseudopotential (PAW) method and the PBE/PBE+HSE approximations within the VASP code. This investigation included a thorough examination of their structural, electronic, and magnetic properties. The findings from the analysis of formation energies, molecular dynamics simulations, and elastic constants indicated that each of the examined pristine materials, SrS (FeS), had favorable formation energies and maintained thermal and mechanical stabilities under normal conditions. Calculations of phonon spectra also confirmed the dynamic stability of their lattice structures. Regarding their ground state configurations, SrS was observed to remain stable in a hexagonal structure like graphene, while FeS preferred a square structure, which is consistent with previous theoretical studies. The influence of dimensionality reduction is clearly observed in the electronic properties of the doped monolayers, which exhibited a behavior that differs significantly from the HMF character observed in the bulk counterparts. According to the PBE results, Sr<sub>0.875</sub>Fe<sub>0.125</sub>S, Sr<sub>0.75</sub>Fe<sub>0.25</sub>S and Sr<sub>0.50</sub>Fe<sub>0.50</sub>S showed HSC behavior, while Sr<sub>0.25</sub>Fe<sub>0.75</sub>S behaved like a metal. However, with the application of the HSE method, Sr<sub>0.25</sub>Fe<sub>0.75</sub>S transformed into an HSC with a direct bandgap in both spin directions. Finally, we calculated a total magnetic moment of 4  $\mu_B$  in all doped monolayers, a result from *p-d* hybridization that is consistent with results in bulk structures. We also found an increase in local magnetic moments at Fe sites with concentration in contrast to their bulk counterparts, confirming the robust ferromagnetic nature at small dimensions.

In summary, both co-doping and dimensionality reduction show promising key performances for the desired applications.

In perspectives, we plan to calculate the optical and thermoelectric properties of our monolayers to enable a comprehensive comparison between 2D and 3D scales. Furthermore, it would be interesting to evaluate the reliability of other methods discussed in Chapter 1, such as inducing defects or external stimuli in SrS-based DMS.

# Appendices

## Appendix. A

This appendix contains basic equations that serve as initial steps in understanding the process of finding an appropriate basis set.

### A.1 Bloch's Theorem

In the field of solid-state systems, it is common for the units of interest to have specific translational symmetries in space. This property is suitable for the application of periodic boundary conditions (PBC) [1–3], a technique that significantly streamlines calculations for real systems. Under PBC, the system is encapsulated in a unit cell, systematically replicated throughout space and defined by the vectors  $\vec{a}_1$ ,  $\vec{a}_2$ , and  $\vec{a}_3$  [4]. This well-structured setup ensures that each grid point  $\mathbf{R}$  can be precisely constructed, facilitating detailed analysis and calculations.

$$\mathbf{R} = n_1 \vec{a}_1 + n_2 \vec{a}_2 + n_3 \vec{a}_3 \quad (\text{eq.1})$$

The Bravais lattice is characterized by three integer coefficients, namely  $n_1$ ,  $n_2$  and  $n_3$ . This grid is paired with a reciprocal grid :

$$\mathbf{G} = m_1 \vec{b}_1 + m_2 \vec{b}_2 + m_3 \vec{b}_3 \quad (\text{eq.2})$$

Each reciprocal lattice vector  $\mathbf{G}$  can be expressed as a linear combination of the reciprocal basis vectors  $\vec{b}_1$ ,  $\vec{b}_2$ , and  $\vec{b}_3$  where  $m_1$ ,  $m_2$ , and  $m_3$  are integer values. These reciprocal basis vectors are derived from their counterparts in real space.

$$\vec{b}_1 = \frac{2\pi}{\Omega} (\vec{a}_2 \times \vec{a}_3) \quad (\text{eq.3})$$

$$\vec{b}_2 = \frac{2\pi}{\Omega} (\vec{a}_3 \times \vec{a}_1) \quad (\text{eq.4})$$

$$\vec{b}_3 = \frac{2\pi}{\Omega} (\vec{a}_1 \times \vec{a}_2) \quad (\text{eq.5})$$

Here,  $\Omega = \vec{a}_1(\vec{a}_2 \times \vec{a}_3)$  represents the volume of the unit cell in real space. Both the real and reciprocal basis vectors adhere to the relationship  $\vec{a}_i \cdot \vec{b}_j = 2\delta_{ij}$ . The Schrödinger equation governing a single electron under periodic boundary conditions (PBC) is provided by [4]:

$$\left(-\frac{1}{2}\nabla^2 + V(\vec{r})\right)\psi(\vec{r}) = \epsilon\psi(\vec{r}) \quad (\text{eq.6})$$

Within a system governed by a periodic potential  $V(\vec{r})$  that adheres to  $V(\vec{r} + \vec{R}) = V(\vec{r})$ , the Bloch theorem, credited to Swiss physicist Felix Bloch in 1929 [5], postulates that all eigenstates  $\psi(\vec{r})$  of the one-electron Hamiltonian can be expressed as a composite of a plane wave phase factor  $e^{ik\vec{r}}$  and a periodic function  $u_{n,k}(\vec{r})$ . This function mirrors the precise periodicity exhibited by the Bravais lattice [4].

$$\psi_{n,k}(\vec{r}) = e^{ik\vec{r}}u_{n,k}(\vec{r}) \quad (\text{eq.7})$$

$$u_{n,k}(\vec{r} + \vec{R}) = u_{n,k}(\vec{r}) \quad (\text{eq.8})$$

In this context, the quantum numbers 'n' and 'k' refer to the band index and the Bloch wave vector in reciprocal space, respectively. It is a fundamental principle that any periodic function can be expressed as a sum of plane waves in a basis set [2]:

$$u_{n,k}(\vec{r}) = \sum_G C_{n,k,G} e^{iG\vec{r}} \quad (\text{eq.9})$$

Consequently, the one-electron wave function can be expanded as follows:

$$\psi_{n,k}(\vec{r}) = \sum_G C_{n,k,G} e^{i(G+k)\vec{r}} \quad (\text{eq.10})$$

In practical applications, the plane waves are typically truncated within a cutoff  $|\mathbf{G}_{max}|$ , which corresponds to an energy *cutoff*  $E_{cut} = |\mathbf{k} + \mathbf{G}_{max}|^2/2$ . Furthermore, the Bloch wave vectors 'k' can be confined to the Brillouin zone (BZ), which represents the first Wigner-Seitz cell in reciprocal space. This restriction is possible because all other Bloch states 'k' can be calculated by combining a Bloch state within the BZ ( $\mathbf{k}_{BZ}$ ) with an additional reciprocal lattice vector 'G' [4].

$$\mathbf{k} = \mathbf{k}_{BZ} + \mathbf{G} \quad (\text{eq.11})$$

This implies that the Bloch states (eigenvalues and eigenfunctions) exhibit periodicity in reciprocal space [4]. To streamline computational efforts, symmetry considerations come into play. Specifically, only k-points within the irreducible wedge of the Brillouin Zone (IBZ) are taken into account, each with

a corresponding weight denoted as  $\omega_k$ . With this approach, the summation over  $k$ -points for a periodic function  $F(\mathbf{k})$  spanning the entire Brillouin Zone can be simplified as follows:

$$\frac{1}{\Omega_{BZ}} \int_{BZ} d\mathbf{k} F(\mathbf{k}) = \frac{\Omega}{(2\pi)^3} \int_{BZ} d\mathbf{k} F(\mathbf{k}) = \sum_k^{BZ} F(\mathbf{k}) = \sum_k^{IBZ} \omega_k F(\mathbf{k}) \quad (\text{eq.12})$$

Here, the  $\mathbf{k}$  point grids and their associated weights  $\omega_k$  are typically generated using the Monkhorst and Pack scheme [6].  $\Omega_{BZ}$  represents the volume of the Brillouin Zone, while  $\Omega$  denotes the volume of the real-space unit cell.

The band structure of solids is represented by  $\epsilon_n(\mathbf{k})$  a function dependent on the  $\mathbf{k}$  vector for a specific band ' $n$ '. The Density of States (DOS) for each band ' $n$ ' is determined by integrating over the IBZ [4]:

$$D_n(\epsilon) = \frac{\Omega}{2\pi^3} \int_{BZ} d\mathbf{k} \delta(\epsilon - \epsilon_n(\mathbf{k})) = \sum_k^{IBZ} \omega_k (\epsilon - \epsilon_n(\mathbf{k})) \quad (\text{eq.13})$$

As a result, the total DOS, encompassing contributions from all bands, is calculated as:

$$D(\epsilon) = \sum_n D_n(\epsilon) \quad (\text{eq.14})$$

## A.2 Fourier Transformation

In physics, the Fourier transform (FT) is a powerful mathematical operation that transforms a function and provides a detailed representation of the frequencies contained in the original data. Given a three-dimensional rectangular box (a finite system) with side lengths  $L_x$ ,  $L_y$ , and  $L_z$ , any sufficiently smooth function  $f(\vec{\mathbf{r}})$  that satisfies the periodic boundary conditions can be considered [7].

$$f(\vec{\mathbf{r}} + L_x \mathbf{e}_x) = f(\vec{\mathbf{r}} + L_y \mathbf{e}_y) = f(\vec{\mathbf{r}} + L_z \mathbf{e}_z) = f(\vec{\mathbf{r}}) \quad (\text{eq.15})$$

Eq.15 can be represented as a series of Fourier as follows:

$$f(\vec{\mathbf{r}}) = \frac{1}{\Omega} F_k e^{ik\vec{\mathbf{r}}} \quad (\text{eq.16})$$

Where  $k$  represents a wave vector within the reciprocal space of the system, which has a volume  $\Omega = L_x L_y L_z$ .

$$\mathbf{k} = n_x \frac{2\pi}{L_x} \mathbf{e}_x + n_y \frac{2\pi}{L_y} \mathbf{e}_y + n_z \frac{2\pi}{L_z} \mathbf{e}_z, \quad \{n_x, n_y, n_z\} \in \text{integer} \quad (\text{eq.17})$$

Subsequently, the Fourier coefficients  $F(\mathbf{k})$  can be computed through the following process:

---

$$\mathbf{F}(\mathbf{k}) = \int_{\Omega} d\vec{r} f(\vec{r}) e^{-i\mathbf{k}\vec{r}} \quad (\text{eq.18})$$

Some frequently utilized formulas for simplifying equations:

$$\frac{1}{\Omega} \sum_{\mathbf{k}} e^{\pm i\mathbf{k}\vec{r}} = \delta(\vec{r})$$

$$\int_{\Omega} d\vec{r} e^{\pm i\mathbf{k}\vec{r}} = \Omega \delta(\mathbf{k}) \quad (\text{eq.19})$$

The principles and formulas previously discussed for the three-dimensional system can be extended and applied to a two-dimensional environment, taking the respective dimensions and coordinates into account.



## Appendix. B

This appendix provides a guide to better understand the WIEN2K and VASP codes and includes the flowchart of basic programs that serve as first steps in understanding the process of how the programs are used and executed.

### B.1 WIEN2K Code

#### 1.1 ``Master Input`` File *case.struct*: Preliminary Requirement in WIEN2K

To start DFT calculations in WIEN2K for a specific system, it is important to create a *.struct* file that represents the atom types involved in the simulation. This file, called "*case.struct*" (where "case" is the file name), serves as the main requirement in WIEN2K. The generation process is facilitated by *StructGen*, which is accessible via a web browser and the *w2web* interface or alternatively via the command line of an *xterm*. This crucial first step is to create a blank structure template into which we can enter relevant structure details such as atom symbols, lattice parameters, space group, atom positions, angles, atomic number (*Z*), and *R<sub>MT</sub>* values, which can be set either manually or automatically. After completing the *StructGen* process, the file "*case.struct*" is generated, which serves as the master input file for all subsequent programs. This step also automatically creates an input file with the atomic configurations, labeled "*case.inst*."

#### 1.2 Main Programs in WIEN2K

Once the two basic input files have been generated, the calculations are initialized using the "*init-lapw*" command. This command provides a user-friendly step-by-step guide to setting up the calculations and generating inputs for the main programs. By initializing the calculations, several automated steps are carried out seamlessly. Where 'x' represents the script for starting WIEN2k programs.

- **x nn** \_This command calculates the nearest neighbors within a specified distance.
- **x sgroup** \_ This command calculates both the point and space groups for a given structure.
- **x-symmetry** \_ This command generates space group symmetry operations, determines the point group for individual atom locations, and generates the local moment extension (LM) for lattice harmonics and local rotation matrices.

- **x lstart\_** This command generates atomic densities and defines how the orbitals are treated in band structure calculations, including considerations such as core or band states, local orbitals, etc.
- **x kgen\_** This command creates a  $k$ -network within the Brillouin zone (BZ).
- **x dstart\_** This command generates an initial density for the Self-Consistent Field (SCF) cycle.

After initializing the calculation, the SCF process is initiated and repeated until solution convergence is achieved. For non-magnetic materials, such as SrS in our case, the SCF cycle can be triggered with the “*run\_lapw*” command. For materials with ferromagnetic properties, such as Fe-doped SrS in our scenario, the “*runsp\_lapw*” command is used. The SCF cycle includes the following phases:

- **LAPW0 (POTENTIAL):** This phase generates the potential based on the calculated density.
- **LAPW1 (BANDS):** Here the valence bands, including eigenvalues and eigenvectors, are calculated.
- **LAPW2 (RHO):** This stage derives valence densities from the obtained eigenvectors.
- **LCORE:** It is responsible for computing the core states and their respective densities.
- **MIXER:** In this step, a mixing process is performed for the input and output densities to enable further iterations.

The diagram (Figure 1) clearly illustrates how the various WIEN2K programs are used and executed and provides a visual orientation for better understanding.

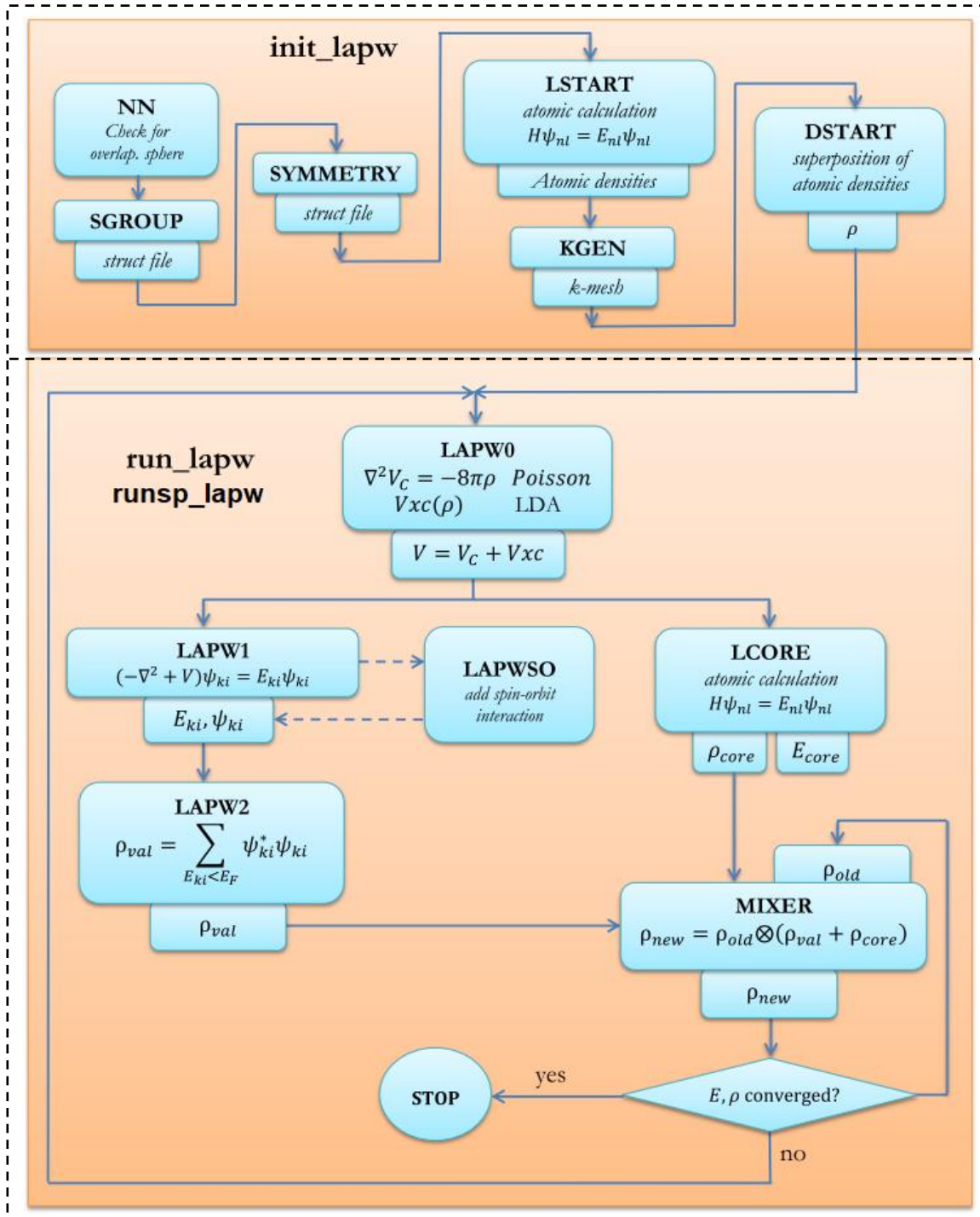


**Figure.1** The flowchart shows the program flow in the WIEN2K package.

## B.2 VASP Code

### 2.1 Main Input/Output Files in VASP

VASP searches the specified directory for four primary input files: **POSCAR**, **INCAR**, **KPOINTS**, and **POTCAR**.

- Within the **POSCAR** file we specify the placement of a single atom within a box. This file encapsulates the initial grid geometry and ion positions.
- The **INCAR** file contains tags that control the calculation. These tags are detailed in the VASP wiki under specific categories and have default values if not explicitly defined in the INCAR file. As a central input file, INCAR includes a significant portion of the key words that are essential for the calculations. This includes parameters such as the limit energy, smearing parameters, convergence criteria and more.
- The **KPOINT** file specifies the coordinates and associated weights of  $k$ -points within the Brillouin zone for sampling. It also contains information about how these  $k$ -points are created, including the method used, such as the Monkhorst-Pack scheme.
- The **POTCAR** file contains pseudopotential data and associated information for the designated atoms.

Regarding the output files, VASP generates three main files: **CONTCAR**, **OUTCAR** and **OSZICAR**.

- The **CONTCAR** includes the optimized grid geometry and ion positions.
- The **OUTCAR** file serves as the central output document in VASP and includes a comprehensive set of data generated during the calculation.
- The **OSZICAR** file provides an optimized overview of each electronic step, presenting important information on a single line. This includes the number of iterations, total energy and variation in total energy.

## 2.2 Running Calculations

Similar to the WIEN2K code, the VASP code is based on two central phases: cell relaxation and the SCF cycle. When run with the *vasp\_std* executable, VASP can be run in parallel with *mpirun*. First, the electronic charge density is determined from the POTCAR file and remains constant for the first steps. This is attributed to the iterative diagonalization of the Hamiltonian, meaning that the Kohn-Sham (KS) orbitals used to update the charge density require a warm-up period to be considered reliable. Figure 2 provides another visualization of the SCF cycle and OUTPUT file generation.

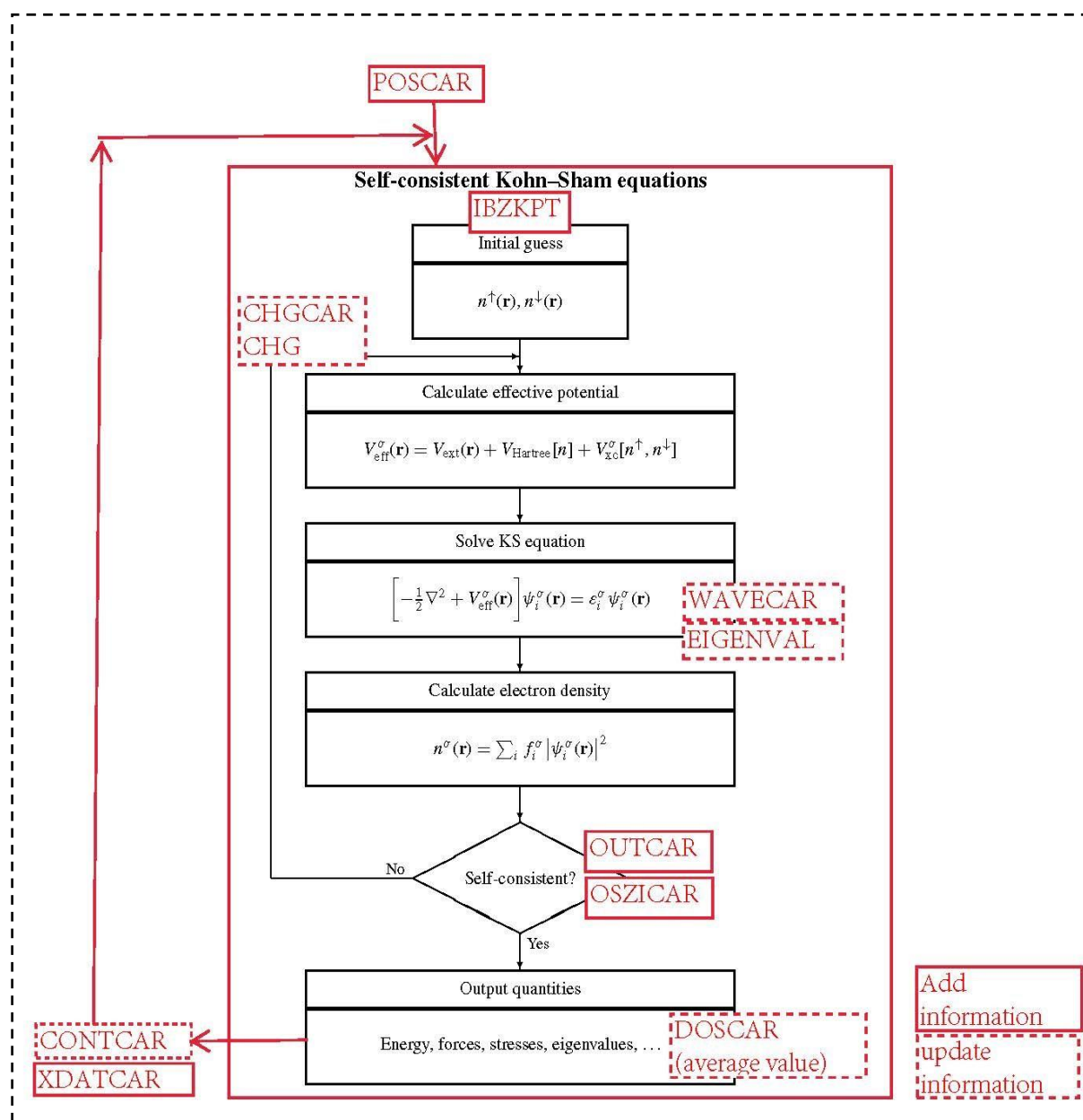


**Figure.2** Schematic representation of the self-consistent loop for solving the Kohn-Sham equation. (For the two spins, it is necessary to go through two such loops at the same time.)

### B.3 Possibilities with WIEN2K and VASP Codes

The WIEN2K and VASP codes are versatile tools for studying a wide range of properties in periodic materials. They allow researchers to determine important structural attributes such as structure type, lattice constants, bonding, bond angles, bulk modulus, formation and cohesion energies, phonon spectrum and molecular dynamics. They also enable in-depth study of electronic properties, including spin-resolved electronic band structures, densities of states (both total and projected) and magnetic moments. In addition, they facilitate the assessment of real and imaginary components of dielectric function as well as the evaluation of mechanical, thermal and electronic transport properties.

- **Structural Properties**

Ensuring a well-defined and relaxed geometry is a crucial aspect when examining crystals or surfaces. The aim is to find the geometry with the lowest energy. Since we are studying periodic systems, two very important concepts come into play: the crystal *unit cells* and the *positions of ions*, both of which define the crystal structure. Within WIEN2K, optimization is carried out using the eosfit program. This tool allows varying grid parameters up to a certain percentage. One can then graph the energy versus volume and fit this nonlinear relationship using various equations of state. WIEN2K provides options such as the Murnaghan [8] and Birch Murnaghan [9] equations of state. VASP offers various relaxation methods. Among these, the most commonly used approach is to relax the ion positions while keeping the cell shape constant, a configuration achievable with ISIF=4. Visualization was facilitated by Xcrysden [10] for WIEN2K and Vesta [11] for VASP code.

To deal with phonon spectra, an additional package called PHONOPY (included in VASP) was used [12]. This utility constructs a supercell to calculate force constants in real space using DFPT (Density Functional Perturbation Theory) [13]. The PHONOPY code is used to calculate the phonon spectrum, a process performed for all monolayers studied in this dissertation.

By applying ab-initio molecular dynamics simulations (AIMD), a better assessment of thermal stability can be achieved. AIMD is a computational approach that combines quantum mechanical principles with classical molecular dynamics to simulate the dynamic behavior of atoms and molecules in real time. Without going further into the mathematical equations that describe their method, let us simply note that the thermostat principle is to adjust the velocities of the system particles during the simulation so that the average kinetic energy of the system is equal to the kinetic energy corresponding to the target temperature. Typical AIMD simulations are limited to systems with a few hundred atoms and a total duration of ten to a thousand picoseconds [14]. To run a basic AIMD simulation in VASP (as in our case for monolayers), a simple copy of the input files along with changes to a few flags and

selecting the correct thermostat type is enough. It should be noted that the choice of thermostats to use depends on the specific requirements of the simulation and the accuracy required for the study being carried out. Various thermostats can be used to control temperature, including:

1. **Nose-Hoover Thermostat :**

This is a popular choice for maintaining a constant temperature during AIMD simulations. It uses a number of additional degrees of freedom to control the kinetic energy of the system.

2. **Langevin Thermostat :**

The Langevin thermostat adds a stochastic term to the equations of motion, simulating the effects of a heat bath. This allows the system to reach and maintain a desired temperature.

3. **Andersen Thermostat :**

The Andersen thermostat randomly selects particles and gives them a velocity that corresponds to a Maxwell-Boltzmann distribution at the desired temperature.

In this dissertation, we implemented the Nose-Hoover thermostat.

- **Electronic Properties**

After geometry relaxation, the electronic density of states (DOS) was determined by integrating the electron density over  $k$ -space. Another important electronic property, the band structure, was also estimated by locating the high symmetry points in the Brillouin zone of the solid. In our WIEN2K analysis, we used the interface tailored for the post-processing of first principles data, equipped with the essential programs for property calculation. Meanwhile, in our work with VASP, we used the VaspKit package [15] for data post-processing. VaspKit proves to be an accessible toolkit that streamlines the initial setup of calculations and enables detailed post-processing analysis to derive a variety of material properties from the raw data generated by the VASP code. (All upcoming properties are determined using the same scheme).

- **Magnetic Properties**

Evaluating magnetic properties is crucial for applications such as spintronic devices and spin-based devices. These properties have been thoroughly investigated by analyzing spin-polarized density of states diagrams and spin-resolved electronic band structures, magnetic moments, and exchange constants.

- **Mechanical Properties**

Mechanical properties are the properties of a material that describe how it reacts to applied forces or loads. These properties are important for understanding how a material behaves under different conditions, which is crucial for the design and construction of various structures and components. The most important mechanical properties include stiffness, hardness, ductility and brittleness, all of which can be determined from elastic constants. In Figure 3 we have shown the strain curve ( $\epsilon$ ), which illustrates the deformation of the material in relation to the applied stress ( $\sigma$ ). Two main regions are identified: the first is called the “*elastic region*” and is characterized by a linear variation of deformation with stress, where the deformation is reversible; when stress is removed, the material returns to its original shape. The second region is the “*plastic region*” in which the deformation is irreversible. The stress value at which the plastic region begins is called the yield point. Note that the elastic and plastic regions correspond to low and high stresses, respectively. In this dissertation, we will work in the elastic range.

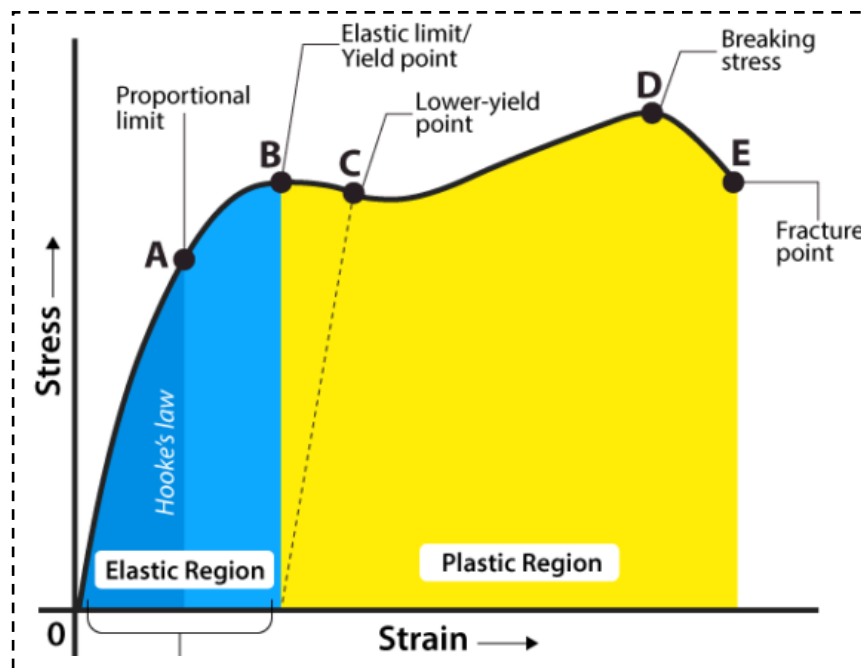


**Figure.3** Schematic Stress-Strain Curve. After Ref [16].

In the linear elastic regime, the relationship between the stress ( $\sigma$ ) and the applied strain ( $\epsilon$ ) in solids follows the generalized Hooke's law [16] and can be expressed using Voigt notation [17]:

$$\sigma_i = \sum_{j=1}^6 C_{ij} \epsilon_j \quad (\text{eq.20})$$



The strain, stress, and elastic constants are each represented as tensor of 6x6 independent components denoted by subscripts  $i$  and  $j$ . Each code handles the elastic constants in its own way. WIEN2K typically begins with a perfect crystal lattice structure. To calculate elastic constants, the program applies small deformations (strains) along various directions to the crystal lattice. For each strain applied, WIEN2K calculates the total energy of the deformed crystal structure. By fitting these energy-strain curves, it is possible to extract the elastic constants and determine all elastic moduli. Similar to WIEN2K, VASP can calculate elastic constants by applying small deformations to the crystal lattice. This is often done using the second derivative of the total energy according to the atom positions, the so-called Hessian matrix. This matrix contains information about the curvature of the energy surface, which is related to the elastic constants.

- **Optical Properties**

It is crucial to understand how materials interact with light, and their optical properties provide a valuable tool for this. These properties are characterized by the complex dielectric function  $\epsilon(\omega)$ , which determines the response of the medium to the electromagnetic field [18]:

$$\epsilon(\omega) = \epsilon_1(\omega) + i\epsilon_2(\omega) \quad (\text{eq.21})$$

Here,  $\epsilon_1$  and  $\epsilon_2$  represent the real and imaginary parts of the complex dielectric function, respectively,  $\omega$  denotes the photon frequency.

In the WIEN2K framework, the "*optic*" subroutine is employed to compute the optical properties. This subroutine calculates the components of the matrix dipole moment for each  $k$ -point and each combination of occupied and empty bands. The determination of  $\epsilon_2$  components across the Brillouin zone is accomplished by the "*joint*" subroutine, generating the file **case.joint**. Application of the **Kramers-Kronig** formula to compute the  $\epsilon_1$  components is carried out by the "*kram*" subroutine. At this stage, we specify the value of the "**scissor operator**," determined by the difference between the experimentally measured optical gap and the theoretically derived one. The resulting files include **case.epsilon**, **case.sigmak**, **case.absorption**, **case.reflection**, **case.refraction**, and **case.eloss**.

Within the VASP code, the VASPKIT package proves invaluable in determining frequency-dependent dielectric functions. This package facilitates the extraction of linear spectra by parsing the output files using FLAG 71. The resulting files are labeled with names corresponding to each specific property, including **ABSORPTION\_2D**, **OPTICAL CONDUCTIVITY\_2D**, **REFLECIION\_2D**, and **TRANSMISSION\_2D**.

- **Thermoelectric Properties**

Thermoelectric properties refer to the characteristics of a material that govern its ability to convert temperature gradients into electrical voltage or vice versa, a phenomenon known as the Seebeck effect. These properties are crucial in thermoelectric applications, which involve harnessing waste heat or providing localized cooling. Optimizing the Figure of merit ( $ZT$ ) for thermoelectric performance is a key goal in thermoelectric materials research. This parameter depends on properties like electrical conductivity ( $\sigma$ ), thermal conductivity ( $\kappa = \kappa_e + \kappa_l$ ), and the Seebeck coefficient ( $S$ ) that could be manipulated through simulation to enhance the overall performance. The thermoelectric properties are calculated using the BoltzTrap2 code [19].

## References for Appendices

- [1] Allen, M. P., & Tildesley, D. J. (2017). *Computer simulation of liquids*. Oxford university press.
- [2] Payne, M. C., Teter, M. P., Allan, D. C., Arias, T. A., & Joannopoulos, A. J. (1992). Iterative minimization techniques for ab initio total-energy calculations: molecular dynamics and conjugate gradients. *Reviews of modern physics*, 64(4), 1045.
- [3] Marsman, M. (2009). Periodic systems, plane waves, the PAW method, and hybrid functionals. *Computational Methods in Catalysis and Materials Science: An Introduction for Scientists and Engineers*, 61-76.
- [4] Ashcroft, N. W., & Mermin, N. D. (1993). Solid-state physics (brooks cole, 1976). *Cited on*, 26.
- [5] Bloch, F. (1928). Quantum mechanics of electrons in crystal lattices. *Z. Phys*, 52, 555-600.
- [6] Monkhorst, H. J., & Pack, J. D. (1976). Special points for Brillouin-zone integrations. *Physical review B*, 13(12), 5188.
- [7] Fourier, J. B. J. (1888). *Théorie analytique de la chaleur*. Gauthier-Villars et fils.
- [8] Murnaghan, F. D. (1944). The compressibility of media under extreme pressures. *Proceedings of the National Academy of Sciences*, 30(9), 244-247.
- [9] Birch, F. (1978). Finite strain isotherm and velocities for single-crystal and polycrystalline NaCl at high pressures and 300 K. *Journal of Geophysical Research: Solid Earth*, 83(B3), 1257-1268.
- [10] Kokalj, A. (1999). XCrySDen—a new program for displaying crystalline structures and electron densities. *Journal of Molecular Graphics and Modelling*, 17(3-4), 176-179.
- [11] Momma, K., & Izumi, F. (2011). VESTA 3 for three-dimensional visualization of crystal, volumetric and morphology data. *Journal of applied crystallography*, 44(6), 1272-1276.
- [12] Togo, A., Chaput, L., Tadano, T., & Tanaka, I. (2023). Implementation strategies in phonopy and phono3py. *Journal of Physics: Condensed Matter*.
- [13] Nakamura, K., Higuchi, S., & Ohnuma, T. (2018). Density functional perturbation theory to predict piezoelectric properties. *Perturbation Methods with Applications in Science and Engineering*, 2-7.
- [14] Panchmatia, P. M., Orera, A., Rees, G. J., Smith, M. E., Hanna, J. V., Slater, P. R., & Islam, M. S. (2011). Oxygen defects and novel transport mechanisms in apatite ionic conductors: combined 17O NMR and modeling studies. *Angewandte Chemie International Edition*, 50(40), 9328-9333.
- [15] Wang, V., Xu, N., Liu, J. C., Tang, G., & Geng, W. T. (2021). VASPKIT: A user-friendly interface facilitating high-throughput computing and analysis using VASP code. *Computer Physics Communications*, 267, 108033.
- [16] Hooke, C. J. (1980). The elastohydrodynamic lubrication of heavily loaded point contacts. *Journal of Mechanical Engineering Science*, 22(4), 183-187.
- [17] Voigt, W. (1910). Lehrbuch der Kristallphysik (reprinted 1928). *Teubner, Leipzig*.

- [18] Gajdoš, M., Hummer, K., Kresse, G., Furthmüller, J., & Bechstedt, F. J. P. R. B. (2006). Linear optical properties in the projector-augmented wave methodology. *Physical Review B*, 73(4), 045112.
- [19] Madsen, G. K., Carrete, J., & Verstraete, M. J. (2018). BoltzTraP2, a program for interpolating band structures and calculating semi-classical transport coefficients. *Computer Physics Communications*, 231, 140-145.